# The temperature dependence of grain boundary complexion transitions and their effect on the grain boundary character and energy distributions

Submitted in partial fulfillment of the requirements for

the degree of

Doctor of Philosophy

in

Materials Science & Engineering

Madeleine N. Kelly

B.S., Materials Science & Engineering, Carnegie Mellon University
B.S., Engineering & Public Policy, Carnegie Mellon University
M.S., Materials Science & Engineering, Carnegie Mellon University

Carnegie Mellon University
Pittsburgh, PA

August 2017

# Table of Contents

# 1 Preliminaries

## 1.1 List of Tables



## 1.2 List of Figures

## 1.3 Acknowledgements

I would first like to thank my funding sources. ONR-MURI program grant no. N00014-11-0678, the Carnegie Mellon University Materials Characterization Facility, Dean Garrett for awarding me the Bertucci fellowship that funded my last spring semester, the Joseph Goldstein Scholar award that funded my travel to the University of Manchester and my advisor Greg Rohrer.

Thank you to all of the staff in the MSE department for first hiring me as a work-study during my undergraduate years. I always received such kind words from Jeanna Pekarcik, Anita Connelly, Suzy Smith, Kelly Rockenstein, Angie Pusateri, Neetha Khan, Marygrace Antkowski and Roxann Martin that I am appreciative for.

I also have to thank Jay Whitacre for giving me my first opportunity to do research at Aquion Energy. The three summers I worked at Aquion were what made me interested in research and were what made me want to pursue a doctorate degree. I have to thank Sneha Shanbhag, Alex Mohammed, Andrew Polonsky, and Kristen Carlisle for how much they all taught me there.

Thank you to Bill Pingatore, who was always willing and so kind to help with my experiments, Jason Wolf who was always excited to talk about the projects I was working on, David Crockett and Brett Riale for helping with my IT issues, and Adam Wise for teaching me and helping with the AFM. Thank you to Tom Nuhfer for all of the microscopy collaboration, for helping me on late nights and weekends to check on my data collection on the PFIB, and for the University of Manchester referral, an opportunity that I would not have otherwise had. I thank Grace Burke and Xiangli at the University of Manchester for hosting me as well as for exchanging ideas about the PFIB and other microscopy techniques.

Next I must thank all of my collaborators. Thank you Stephanie Bojarski for starting me off on this project, our collaborative research and for answering my endless questions. Thanks to Sean Donegan for helping me write a ForTran script to convert Gwyddion file formats to be read-able in my MatLab scripts. Thanks to everyone at Dream3D, especially Michael Jackson, for helping with 3D reconstructions, Krzystof Glowinski for the tips about Dream3D pipelines, explanations of his GBCD programs and our collaboration. Thank you to Wolfgang Rheinheimer for providing us the

opportunity to work on $SrTiO_3$ and for all of the engaging discussions. Thanks to everyone at Lehigh University on this collaborative effort to explore grain boundary complexions, especially my committee member Martin Harmer as well as my other committee members Elizabeth Holm, Anthony Rollett. Thanks to the other professors in our department, Brian Webler, Chris Pistorius, Yoosuf Picard, Paul Salvador, Marc DeGraef and Robert Heard for all of the time and effort you have put in either to support my work or teach me. Thank you to my advisor, Greg Rohrer, for taking a chance on me and for all of the unending advice and support.

Thank you to my childhood friends, Carley Crawford and Amanda Holcombe for your friendships that I had long before this all began and that continue. I would also like to thank my very best undergraduate friends Marcy Held, Lisa Kessler, Abby Cryan, Emma Hartman and Ruari Egan. My memories and experiences at CMU all begin with our relationships. I want to thank my fellow undergraduate MSE friends Dana Lee and Hannah Shepard with whom I was able to get through long nights of solving problem sets with. I also must thank all of my other friends I met during graduate school; Michelle Tsui, Dustin Axman, Saransh Singh, Brain Lin, Lizzie Shimp, Chetali Gupta, Ross Cunningham, Steve Kauchr, Price Pellegren, Brian DeCost, Tim Hsu, Boopathy Kombaiah, Farangis Ram, and Kyle Arean-Rains who I could always find to talk about my work, collaborate, ask for advice or socialize with. Thanks to my other past and current group-mates Noey Munprom, Billy Frazier, Yisi Zhu, Aditi Bhattacharya, Ajay Pisat and Xiaoting Zhong.

Through all of these paths that I have taken to get to where I am now I am grateful that I have Chase Midler to persevere thorough it with me. Thank you for all of your constant support and for dealing with my daily struggles. And finally, a special thank you to Mom, Dad, Mark and Gabe for always being there for me, for pulling me up and being so supportive.

## 1.4 Abstract

Abrupt changes in grain boundary energy (GBE) and character are associated with a change in GB complexion, GB mobility and exaggerated grain growth.[1] In this thesis, complexion transitions and their effect of relative GBE and GB character distributions (GBCD) are studied for ceramics: europium doped spinel (Eu doped spinel), yttria doped (Y-doped), undoped alumina ($Al_2O_3$), and strontium titanate ($SrTiO_3$).

The population of GB planes (GBPD) of Eu doped spinel was investigated at temperatures before and after a previously identified a complexion transition. The microstructure changed from unimodal (1400 °C) to bimodal (1600 °C) and the relative area of {111} increased. This information was used to understand the GBs involved in the transition.

Atomic force microscopy was used to measure relative GBE from thermal grooves on the surfaces of $Al_2O_3$, 100 ppm Y-doped $Al_2O_3$, and 500 ppm Y-doped $Al_2O_3$ heated between 1350 °C and 1650 °C. The relative GBE of $Al_2O_3$ decreased slightly with increased temperature. When the doped samples were heated, there was an overall increase in the relative GBE, interrupted by abrupt reductions (increases) in relative GBE (mobility) between 1450 °C and 1550 °C. When the 100 ppm Y-doped sample was cooled, there was an increase in the relative GBE at the same complexion transition temperature, indicating that the transition is reversible.

Relative GBE was measured from thermal grooves on $SrTiO_3$ in a region of non-Arrhenius grain growth. Between 1350 °C and 1390 °C, an abrupt decrease in relative GBE and exaggerated grain growth indicated that a complexion transition occurred. Solidified liquid eutectic wet the boundaries at 1550 °C so these GB interfaces could not be compared to the lower temperatures.

3D microstructures of samples heated below (1350 °C), within (1390 °C), and above (1425 °C) the non-Arrhenius region in $SrTiO_3$ were measured. Internal dihedral angles indicated that slowly growing grains have lower GBE than more rapidly growing grains. Low GBE grains increased in fraction with increased temperature until 1425 °C. The GBE distribution and GBCD at 1425 °C indicated a correlated high population and low energy for the {001}, the (111) sigma 3 and $(\bar{2}21)$ sigma 9 GBs.

## 1.5 Publication Status and Plans

### 1.5.1 List of published papers related to thesis

O. Schumacher, C.J. Marvel, M.N. Kelly, P.R. Cantwell, R.P. Vinci, J.M. Rickman, G.S. Rohrer, and M.P. Harmer, "Complexion Time-Temperature Transformation (TTT) Diagrams: Opportunities and Challenges," *Curr. Opin. Solid State Mater. Sci.*, 1–8 (2016).

M.N. Kelly, S.A. Bojarski, and G.S. Rohrer, "The Temperature Dependence of the Relative Grain-Boundary Energy of Yttria-doped Alumina," *J. Am. Ceram. Soc.*, **100** [2] 783–791 (2017).

M.N. Kelly, K. Glowinski, N.T. Nuhfer, and G.S. Rohrer, "The five parameter grain boundary character distribution of α-Ti determined from three-dimensional orientation data," *Acta Mater.*, **111** 22–30 (2016).

### 1.5.2 List of other publications, completed as part of research

G.S. Rohrer, X. Liu, J. Liu, A. Darbal, M.N. Kelly, X. Chen, M.A. Berkson, N.T. Nuhfer, K.R. Coffey, K. Barmak. "The grain boundary character distribution of highly twinned nanocrystalline thin film aluminum compared to bulk microcrystalline aluminum." *Journal of Materials Science.*, **52** [16] 9819-9833 (2017).

D. Abou-Ras, N. Schäfer, T. Rissom, M.N. Kelly, J. Haarstrich, C. Ronning, G.S. Rohrer, A.D. Rollett. "Grain-boundary character distribution and correlations with electrical and optoelectronic properties of $CuInSe_2$ thin films." *Acta Mater*., **118** 244-252. (2016).

W.J. Bowman, M.N. Kelly, G.S. Rohrer, C.A. Hernandez, P.A. Crozier. "Enhanced Ionic Conductivity in Electroceramics by Nanoscale Control of Grain Boundary Composition." *Nano Letters*., (2017), in review.

### 1.5.3 Planned publications, not yet submitted

M.N. Kelly, W. Rheinmeier, M.J. Hoffman, G.S. Rohrer. "The temperature dependence of the relative grain boundary energy and distributions of internal dihedral angles of $SrTiO_3$."

M.N. Kelly, W. Rheinmeier, M.J. Hoffman, G.S. Rohrer. "The five parameter grain boundary character and grain boundary energy distributions of $SrTiO_3$ from three-dimensional orientation data."

D. Chatain, M.N. Kelly, N. Bozzolo, Gregory S. Rohrer. "The orientation relationship of Ni on the R-plane of sapphire."

S. Singh, M.N. Kelly, G.S. Rohrer, M. De Graef. "Pseudosymmetry solutions from dictionary-based indexing of electron backscatter diffraction patterns in comparison to OIM hough transform solutions."

# 2 Introduction

## 2.1 Motivation

Grain boundary complexions are distinct structural states of grain boundaries that exist at finite thicknesses and are in thermodynamic equilibrium. [2] Distinct grain boundary mobilities were observed and correlated to complexion types in doped alumina and transitions in the mobilities of the boundaries surrounding a subset of all grains can lead to bimodal grain size distributions.[3] In addition, a significant decrease in grain boundary energy has been measured in doped alumina at the temperature where the mobility changes and this decrease in mobility has been associated with a complexion transition.[1] A change in the grain boundary character distribution has also been found when there is change in mobility. [4] In this thesis, we will test the hypothesis that observed changes in the grain boundary energy and grain boundary plane distribution are assumed to be correlated to grain boundary complexion transitions. First, the change in grain boundary character distribution in Eu doped spinel was measured to detect a complexion transition. The significance of a complexion TTT diagram was also presented for Eu doped spinel as a motivation for understanding the temperature dependence of the grain boundary energy. Next, the temperature dependence of relative grain boundary energy in yttria doped alumina was measured and changes in grain boundary energy were interpreted to be the result of a complexion transition. Milling difficulty of yttria doped alumina in the Xe-ion plasma focused ion beam lead to a change in materials system studied. $SrTiO_3$ is an interesting case that has non-Arrhenius grain growth. The temperature dependence of relative grain boundary energy, internal dihedral angles, as well as temperature dependence of grain boundary character are measured in $SrTiO_3$. We hypothesize that there is a grain boundary complexion transition in $SrTiO_3$ that causes an unusual decrease in the grain growth rate.

## 2.2 Hypotheses

1. Grain boundary complexion transitions can be observed on the mesoscale by changes in the grain boundary plane and energy distributions.

2. There is a grain boundary complexion transition in $SrTiO_3$ at the same time that there is an anomalous decrease in the grain growth rate.

## 2.3 Objectives

Atomic force microscopy (AFM) will be used to analyze relative grain boundary energy and automated serial sectioning EBSD will be used to assess the effect of grain boundary character, grain boundary energy distributions and internal dihedral angles on complexion transitions. Serial sectioning will be used to collect 3D EBSD data to gather more statistically significant information in a timely fashion to analyze the character of grain boundaries, grain boundary energy distributions and internal dihedral angles in three dimensions. These results will give further understanding to the microstructural evolution of polycrystalline materials related to complexion transitions which will, in the future, allow us to predict and engineer microstructures for various applications.

# 3 Background

## 3.1 Materials Overview

### 3.1.1 Europium doped Spinel

$MgAl_2O_4$ is a cubic spinel. Its structure has space group $Fd\bar{3}m$ (no. 227 ).[5] Spinel structures are a class of materials with a typical formulation of $AB_2X_4$ where the A and B sites are cations of different sizes and the X site is an anion. In this case, magnesium (+2) takes the A site, aluminum (+4) takes the B site and oxygen (-2) sits at the X site. In a unit cell (Z = 8) of the cubic spinel configuration, the lattice constant is 8.089 Å. Because of good ballistic resistance, hardness and light transmittance capabilities, $MgAl_2O_4$ has been a material of interest for optical transparency applications such as armor for windows in vehicles, optical lenses and infrared seekers.[6–8] Doping spinel can improve the strength of the material. Doping also frequently leads to segregation.[9] Eu doping in $MgAl_2O_4$ has not been widely studied but recent observations have shown that it affects the evolution of the microstructure (see section 3.4).[10]

### 3.1.2 $Al_2O_3$

Aluminum (III) oxide, also commonly referred to as alumina, has many different forms and phases. In this study, high purity $\alpha$ alumina (Puratronic, Alfa Aesar, 99.995% pure) was used. Alpha alumina has trigonal crystal symmetry with the space group $R\bar{3}c$ (no. 167)[11]. Alumina is a stable material with good insulating properties, high temperature creep resistance and high temperature stability.[12] Several applications of alumina include ballistic armor,[13] medical prostheses (hip replacement),[14] thermocouple tubes and infrared windows on missile domes.[15] The properties mentioned above are dependent on the optimization of the microstructure. The properties of infrared windows on missile domes, for instance, must be optimized to have a dense, unimodal microstructure where the scattering mechanisms can be controlled to obtain optimal transmittance of light.[16] Single crystal sapphire has been used for infrared window applications but is expensive. Yttria doped polycrystalline alumina is a possible alternative for infrared window applications because it has many of the same properties as single crystal alumina.[15]

### 3.1.3 Effects of Yttria doping in Alumina

Yttria doping improves the sintering ability of alumina,[17] improves densification,[18] suppresses abnormal grain growth[18] and increases the creep resistance.[19–23] Therefore, yttria doped alumina is an ideal candidate for transparent ceramic manufacturing. With these properties, however, grain boundary engineering is necessary to obtain microstructures that have a high fraction of boundaries with these desirable properties. At certain concentrations of yttria, the precipitation of a second phase and presence of abnormal grains has been observed which leads to a decrease in density and a decrease in creep resistance. A detailed analysis of the mechanisms for the onset of such phenomena is imperative for successful grain boundary engineering. Yttria doped alumina has been studied with similar methods as in this thesis and is discussed in section 3.5.

### 3.1.4 $SrTiO_3$

Strontium titanate ($SrTiO_3$) has the cubic perovskite structure with space group $Pm\bar{3}m$ (no. 221). [24] Cubic perovskite structures typically are compounds in the form $ABX_3$ where the A and B sites are cations of different sizes and the X site is an anion. In this case, strontium (+2) takes the A site, titanium (+4) takes the B site and oxygen (-2) sits at the X site. In a unit cell (Z=1) of the cubic perovskite configuration, strontium sits at Wyckoff position 1b (½, ½, ½), titanium's are at the corners (0, 0, 0) in Wyckoff position 1a and oxygen's are located at Wyckoff position 3d (½, 0, 0), (0, ½, 0) and (0, 0, ½) with a lattice constant of a = 3.905 Å. The $SrTiO_3$ studied here was made by first mixing $SrCO_3$ (99.95% purity) and $TiO_2$ (99.995% purity) (Sigma Aldrich Chemie GmbH, Taufkirchen, Germany) to achieve a molar ratio (Sr/Ti) of 0.996 with further details of synthesis published elsewhere.[25] $SrTiO_3$ is a material of interest for electronic applications such as the gate dielectric for field effect transistors,[26] piezoelectric sensors for surface acoustic wave devices,[27] substrates for heteroepitaxial films (both single crystalline[28–32] and polycrystalline[33] $SrTiO_3$). With each of these applications, for polycrystalline strontium titanate, the grain boundary regions and grain size can influence its electronic properties.[34–37] In the past decade the microstructural evolution of $SrTiO_3$ from 1100 °C to 1600 °C has been an interest of research at Karlsruhe Institute of Technology (KIT) in Germany to study the processing of bulk $SrTiO_3$.[25, 38–44] This system

is unique in that they found that the grain growth rate appears to be non-Arrhenius in this temperature region which was the first ever observation reported of non-Arrhenius grain growth for bulk ceramics.[41, 45] Further details of the growth behavior is described in section 3.6. The materials studied here were synthesized by the group at KIT.

## 3.2 Grain growth and abnormal grain growth

In dense, polycrystalline materials, grains tend to grow or shrink at elevated temperature because diffusion is a thermally activated process, often following an Arrhenius relationship $D = D_0 exp\left(\frac{-Q}{RT}\right)$ where D and $D_0$ are diffusion coefficients of the current and initial states, Q is activation energy, R is gas constant and T is temperature. Therefore, at increased temperature, diffusion increases and atoms move across a boundary which results in some grains growing at the expense of shrinking grains due to mass conservation. In most cases for ceramics, the driving force for grain growth is provided by the excess energy of a grain boundary which results in total reduction of energy where the total grain boundary area per volume decreases. Grain size tends to change by a time dependent kinetic relationship, $r^2 - r_0^2 = \frac{1}{4}kt$, where $r_0$ is the initial grain size, r is the final grain size, t is time and k is the grain growth constant.[46–48] Grain growth rates have also been found to be inversely related to grain size $\left(\frac{dr}{dt} = \frac{1}{r}\right)$.[49] In addition, boundaries have been observed, during growth, to move towards their center of curvature and velocity is linearly related to their curvature. This means that as r increases, the boundary velocity decreases and thus the rate of growth decreases with increasing grain size.[49–52] Boundary velocity is also proportional to the product of mobility ($M$) and driving force ($f$) where, for curvature driven grain growth, $f = \kappa\gamma$, which is the product of mean curvature ($\kappa$) and grain boundary energy ($\gamma$).[53] When these processes occur that alter the grain size distribution of a microstructure, governed by atomic motion across a boundary, it is referred to as grain growth. With all of these terms and relationships we can begin to interpret the grain growth behavior in a material.

### 3.2.1 Abnormal grain growth

Abnormal grain growth is observed when some grains grow to be much larger than other grains in a microstructure. There are a few basic theories for the causes of this

phenomena. One is based on of particle pinning. Once a grain boundary intersects a particle, a certain amount of grain boundary area is removed. For the grain boundary to move, the "missing area" must be recreated which requires an energy increase. This is known as the Smith-Zener pinning effect.[54] Therefore, a matrix can be pinned with second phase particles and abnormal grain growth can occur when some grains escape from the pinned microstructure. [55–57] A matrix can also be pinned if a majority of grain boundaries are faceted and abnormal grains can escape by de-faceting. Often, but not always, abnormal grain growth and pinning are associated with annealing close to the solvus line.[58] Near the solvus line, some of the second phase particles can begin dissolving back into the matrix and the pinning force can be decreased due to the smaller particle size and thus abnormal grains can break away from the pinned matrix in this way. However, it has been shown by simulation that abnormal grain growth can happen in other situations such as solute-pinned microstructures without particles[59] and in particle pinned microstructures without dissolution.[60] Segregation effects to grain boundaries in terms of solute drag have also been explored as an explanation for abnormal grain growth.

An intuitive explanation of reduced grain boundary mobility leading to some grains growing more rapidly than others is solute drag. In metals it has been observed that when there is more segregation of impurities at the grain boundaries there is a lower effective mobility of those boundaries.[61] Counter-intuitively to the metallurgical explanation, in ceramics some boundaries with more segregate can be more mobile than a clean grain boundary. This is discussed further below.

Abnormal grain growth has also been explained as resulting from specific grains that have a mobility advantage over others. For example, the perimeter of a particular grain, while growing through a matrix, might have a relatively high mobility because it has a special misorientation with respect to the matrix. If if can maintain this mobility advantage, it can grow abnormally large.[62] The other possibility is that a grain boundary changes to a higher mobility complexion. As long as this complexion is sustained, it grow faster than other grains and becomes abnormally large.[2]

In doped aluminas, complexions were classified by relating the structure and chemistry at the grain boundary to mobility by extracting the product of the energy of a

grain boundary $\gamma_{gb}$ and mobility $M_b$ from the equation $V \approx 2\gamma_{gb}M_b\left(\frac{1}{G_N}-\frac{1}{G_A}\right)$ where $G_N$ is the grain size of a normal grain and $G_A$ is the grain size of an abnormal grain, V is velocity and $\gamma_{gb}$ is assumed constant.[3] Experiments showed that when multiple grain boundary complexions coexist in doped alumina, and one complexion has a much greater mobility than the other, abnormal grain growth results. This increase in mobility was correlated to increased solute adsorbed to the grain boundary and therefore may have allowed for faster transport of atoms across the boundary and thus increased mobility. In addition, a correlation to grain boundary energy was observed where the thicker adsorbed boundaries, which were found along the abnormally large grain boundaries, had lower relative grain boundary energy than adjacent thinner adsorbed boundaries along normal grains.[63] This gives evidence that, for doped aluminas, that there is a distinct relationship between grain boundary energy and microstructural evolution.

### 3.2.2 Mechanism of grain boundary motion in the absence of segregation

The currently accepted mechanism for grain boundary motion is based on theoretical models and experimental observations. Originally, a terrace-ledge-kink model was used to explain the motion.[64] Gleiter, similarly, suggested that a grain is terminated by steps and, in the absence of segregation, an atom can diffuse on a grain surface (terrace), attach to a step site and diffuse along a step, into a kink site. When more atoms are attached to one grain than another, a grain boundary migrates.[65, 66]

Many of the efforts to experimentally study this mechanism have been on bicrystals which might not be representative of real situations. Recently, the mechanisms for grain boundary motion were studied in $SrTiO_3$ using the same samples discussed in this thesis. They found that in the anti-thermal region of grain growth (1350 °C – 1425 °C), there is no change in the types of grain boundary steps on these boundaries but that a change in mobility that is observed could be due to a change in disconnections (lateral movement of interfacial line defects which can have both step and dislocation character) or the chemistry of boundaries in the vicinity of the steps.[67]

## 3.3 Grain Boundary Character Distributions

A grain boundary has five macroscopic degrees of freedom. Two are specified by the boundary plane and three are described by the rotation of the lattice. The grain boundary

plane is represented by the boundary plane normal and the angle of inclination of the boundary. The rotation of the lattice is referred to in terms of Euler angles ($\phi_1\ \Phi\ \phi_2$). Three Euler angles are used to describe the minimum set of rotations to bring one orientation into coincidence with another. Experimentally, we can use a technique called electron backscatter diffraction (EBSD) to determine the crystallographic orientation of each grain in a polycrystalline material. Each EBSD map uses a coloring scheme to highlight the differences in orientations of the grains in the map (e.g. see **Figure 3**). An inverse pole figure (IPF) key is used to correlate the colors given for each orientation in the crystallographic fundamental zone for each map. The crystallographic fundamental zone is the minimum amount of orientation space required to describe all orientations.

From measured Euler angles, to compute the transformation matrix which represents the orientation of a single grain the following equation can be used:

$$g(\phi_1\ \Phi\ \phi_2) = \begin{pmatrix} cos\phi_1 cos\phi_2 - sin\phi_1 sin\phi_2 cos\Phi & sin\phi_1 cos\phi_2 + cos\phi_1 sin\phi_2 cos\Phi & sin\phi_2 sin\Phi \\ -cos\phi_1 sin\phi_2 - sin\phi_1 cos\phi_2 cos\Phi & -sin\phi_1 sin\phi_2 + cos\phi_1 cos\phi_2 cos\Phi & cos\phi_2 sin\Phi \\ sin\phi_1 sin\Phi & -cos\phi_1 sin\Phi & cos\Phi \end{pmatrix}$$

Misorientation is the minimum rotation angle between two points or the difference in crystallographic orientation between two grains in a polycrystalline material. The misorientation can be computed from the transformation matrix of each of two grains A and B which share a grain boundary as well as corresponding rotation matrices to represent all symmetrically equivalent misorientations of each grain with the equation $\Delta g_{AB} = O_B^x g_B g_A^{-1} O_A^x$ where $O_A^x\ and\ O_B^x$ are the rotation groups for the corresponding crystal symmetry.

### 3.3.1 Disorientation angle distribution

The disorientation is the misorientation with minimum rotation angle. It can be computed by first computing all of the possible misorientations and then selecting the minimum rotation angle ($\theta$) for all of the representations $cos\theta = \frac{1}{2}(trace(\Delta g) - 1)$.

In this document, we plot a discrete histogram of the grain boundary area fraction as a function of disorientation and usually compare it to the random distribution. Any deviations from the random distribution means that that misorientation is more or less likely than random to occur.

### 3.3.2 Grain boundary plane distribution and grain boundary character distribution

The relative areas of grain boundaries as a function of grain boundary plane orientation, ignoring the misorientation, is referred to as the grain boundary plane distribution (GBPD) or the 2-parameter grain boundary character distribution. The GBPDs are plotted in the crystallographic fundamental zone. To calculate the GBPD, first, the grain boundary plane (angle of inclination) is computed from stereology for 2D EBSD data. In short[68], to infer the boundary plane inclination from a 2D EBSD map, first the boundary plane normal is taken from a trace on the orientation map, converted to crystallographic reference frame and represented as a pole on a stereogram. All possible grain boundary plane normals to that pole on the stereogram are traced and determined from all crystallographic rotations and on both sides of the boundary. The true boundary planes cannot be inferred with confidence in this manner but if enough boundaries are measured then it is more likely to be accurate. For serial sectioned data, where 2D EBSD maps are collected, material is removed at a specified thickness in an iterative process, and a final 3D volume is reconstructed, the angle of inclination is measured directly. In this document 2D GBPD means that the angle of inclination was computed from stereology but 3D GBPD refers to the distribution computed from a direct measure of the angle of inclination.

The grain boundary character distribution (GBCD) is similar to the GBPD but it is plotted at a fixed misorientation. For the GBCD or 5-parameter grain boundary character distribution, each misorientation type expands to a stereogram that shows the variation in relative areas of grain boundaries as a function of grain boundary plane orientation. The full description of the calculation can be found at reference.[69] The plotted data is given in units of multiples of random distribution (MRD) where each distribution is normalized so that any deviation from one MRD indicates that an orientation is more or less likely to occur.

### 3.3.3 Number of distinguishable grain boundaries

To determine a statistically representative grain boundary character distribution, the number of distinct grain boundary types, determined by the symmetry of the material, must be determined. This is also dependent on the resolution of the data collected. As

discussed above, there are five parameters which describe a grain boundary and each of these parameters can be resolved with a certain accuracy, $\Delta$. The number of proper symmetry operators can be written as P=M/2 where M is the number of symmetry operators in the crystal system. For materials with a center symmetry there are $2P^2$ equivalent misorientations and an arbitrary grain boundary normal pointing to the 1st or 2nd grain yields another multiplicity of 2. To compute the domain volume, the angular range of euler angles is represented as $\phi_1, \Phi,$ and $\phi_2$ where $\phi_1$ ranges from $0 \rightarrow 2\pi$, $\Phi$ from $0 \rightarrow \pi$ and $\phi_2$ from $0 \rightarrow 2\pi$. Then the spherical coordinates, are represented as $\theta$ and $\Phi$ where $\theta$ ranges from $0 \rightarrow \pi$ and $\Phi$ from $0 \rightarrow 2\pi$. In total, the complete domain volume covers $8\pi^5$. Finally, the number of distinct grain boundaries can be computed as the fraction of total volume over the volume of 1 resolved grain boundary. [70]

$$N = \frac{total\ volume}{volume\ of\ 1\ resolved\ grain\ boundary} = \frac{8\pi^5}{\Delta^5 4P^2}$$

The number of distinct grain boundaries for a cubic material with 10° resolution, for example, would then be $6x10^3$. Therefore, for a cubic system to be reliably measured for GBCD at least this many boundaries must be sampled.

## 3.4 Grain boundary mobility transitions in spinel

$MgAl_2O_4$ spinel exhibits rapid grain growth kinetics between 1400 °C and 1800 °C. Previous work, on doped alumina, has shown that changes in grain boundary mobility are linked to a change in grain boundary complexion. [3, 71, 72] Therefore, a change in grain boundary mobility can be used as an indicator for a complexion transition. Recent work in PhD thesis by Onthida Schumacher at Lehigh University characterized the complexion transition in Eu doped spinel and found that below 1500 °C a sub-monolayer type grain boundary complexion existed and above 1500 °C a bilayer type complexion existed.[10] Representative microstructures of the exaggerated grain growth behavior are represented below in **Figure 1** which is reproduced from reference.[73] This figure shows how sensitive the microstructure is to the exact thermal history. By altering the thermal history, it is possible to produce unimodal microstructures, bimodal microstructures, and microstructures with isolated near single crystals.

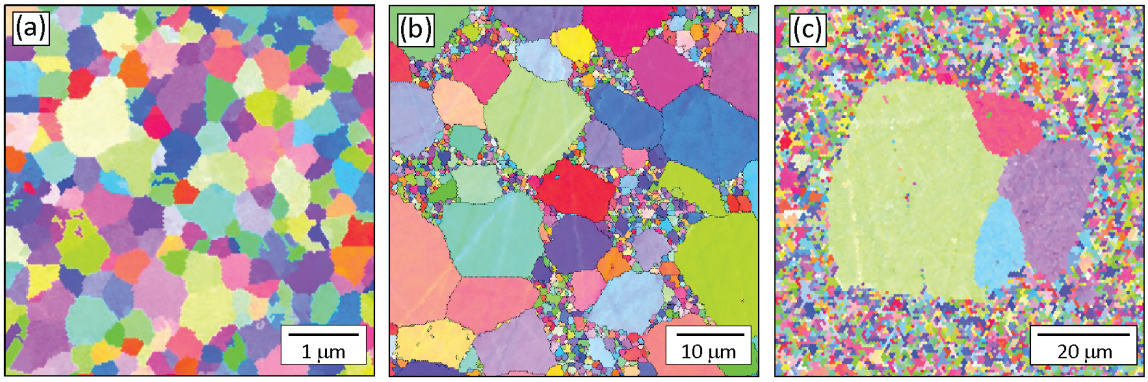


**Figure 1**: Three proof-of-concept microstructures of Eu doped spinel illustrating (a) sub-micron grains, (b) a bimodal microstructure, and (c) a near single crystal growing in the microstructure. Reproduced from reference.[73]

In Eu doped spinel, because there there is a clear transition in the grain boundary mobility with time and temperature, a TTT complexion diagram has been created to begin to understand where the complexion transition occurs. In **Figure 2**, the microstructures used to create the TTT complexion diagram are reproduced. Here we can see that the grain size distribution, stemming from changes in grain boundary mobility, varies depending on the time and temperature of annealing.

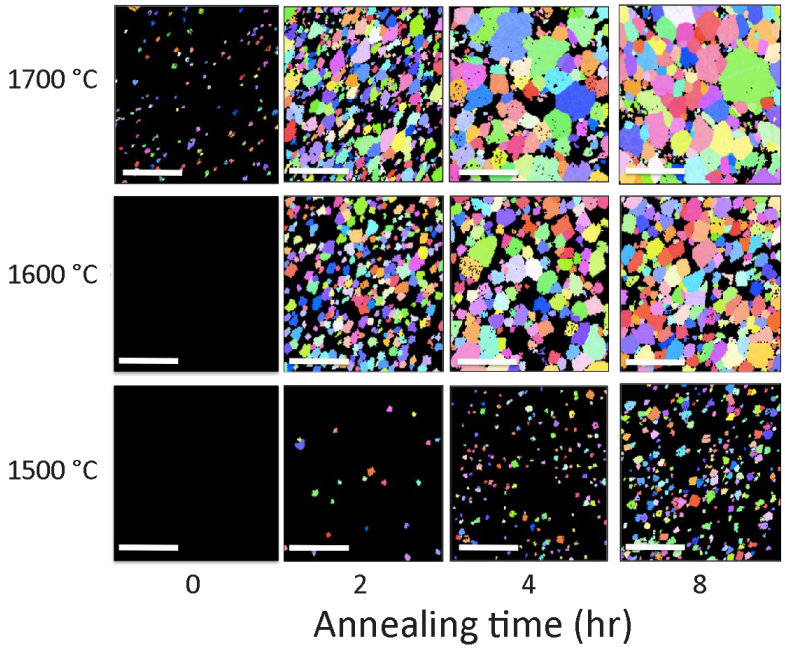


**Figure 2:** A time-temperature matrix of partitioned EBSD maps of Eu doped spinel. Small grain regions are shown in black and the scale bars represent 70 μm. Reproduced from reference.[73]

## 3.5 Mobility transition in Y doped $Al_2O_3$ related to GBCD and relative grain boundary energy

When grain boundaries with two distinct and very different mobilities coexist in a microstructure, it can be used to explain abnormal grain growth. For example, this explanation was used to explain the phenomena in doped alumina.[3, 63, 74–77] Boundaries of abnormally large grains in doped alumina tend to have a higher mobility than boundaries of normal grains and also have different amounts of solute adsorbed to the boundary.[3, 74] In yttria doped alumina, the presence of abnormally large grains has been observed between 1450 °C and 1550 °C (chapter 6). To understand the changes in mobility in relation to complexion transitions, grain boundary character distributions (defined in chapter 3.3) and relative grain boundary energies (section 3.8) have been investigated.

The grain boundary character distribution of polycrystalline 450 ppm yttria doped alumina between 1450 °C and 1600 °C was measured in previous work by Bojarksi.[4] At 1450 °C, the morphology of the grains was equiaxed with a random distribution of grain boundary planes and normal grain growth.[4] At 1500 °C, abnormal and normal grain growth occurred as well as a preference for the $(01\bar{1}2)$ orientation (*r* plane).[4] At 1600 °C, fast growing grains impinged and a coarse grained microstructure was observed with the $(11\bar{2}0)$ orientation (*a* plane) preferred.[4] Similarly, simulations by Galmarini et al.[78] of Y segregation on alumina surfaces show that Y segregates to the *a* plane and the *r* plane surfaces at 1600 °C with *a* plane having the lowest relative energy. Experimentally, Bouchet et al.,[79] showed that Y segregated to the *r* plane more than the (0001) orientation (*c* plane) at sintering temperatures of both 1450 °C and 1550 °C. Overall, Bojarksi's,[4] Galmarini's[78] and Bouchet's[79] work indicate that at temperatures above 1450 °C, Y segregates to the *r* preferred plane, which has the lowest grain boundary energy until the grain boundary mobility increases and when the abnormal grains impinge the *a* plane plane is preferred.[4]

Other work by Bojarski et al.[80] examined the distribution of the relative grain boundary energies of polycrystalline 500 ppm yttria doped alumina bonded to high and low energy single crystal sapphire interfaces. The polycrystal was sandwiched between a low energy *a* plane and a high energy *c* plane. Results by thermal groove measurements of the as-sintered state (1350 °C for 15 hours) showed that grain boundaries near the

(0001) single crystal had a higher energy (1.15) than the grain boundaries found near the $(11\bar{2}0)$ single crystal (0.55) and the bulk polycrystal had an intermediate energy (0.71).[80] This sample was then heated above the expected complexion transition temperature to observe if the high mobility complexion would nucleate at the high energy interface. In the bulk polycrystal a bimodal grain size distribution was observed and there was a distinct difference at the high and low energy interfaces. Along the high energy interface nearly all of the grains were large but along the low energy interface mostly smaller grains were observed. In addition, the relative grain boundary energy at the high energy interface (0.93) was higher than the low energy interface (0.40) and each decreased by 19% and 27%, respectively, from the as-sintered state. These results indicate that the complexion transition nucleated at high energy grain boundaries and the presence of more large grains at the high energy interface indicates that this interface transformed to a high mobility complexion.[80]

The grain boundary character distributions and relative grain boundary energy measurements in yttria doped alumina are useful to define the characteristics of the grain boundaries above, at, and below a complexion transition temperature. If these properties and mechanisms are understood, grain boundary engineering can be improved.

### 3.6 Mobility transition in $SrTiO_3$

In $SrTiO_3$ between 1100 °C and 1600 °C, microstructural evolution has been an area of interest. [25, 38–44] Interestingly, between 1350 °C and 1425 °C, grain growth appears to exhibit a non-Arrhenius behavior which is the first ever observation of this behavior for a bulk ceramic.[41, 45] A plot of the non-Arrhenius grain growth rate constant versus temperature can be found in **Figure 28**.

At 1390 °C the microstructure begins to exhibit suppressed mobility of some boundaries which causes abnormal grain growth. At 1425 °C the mobility is suppressed further which causes no apparent growth and the microstructure is unimodal. Illustrations of the changes in mobility and grain size distributions in this system are reproduced below in **Figure 3** and **Figure 4**. [43] The microstructures below are from EBSD data and are colored according to IPF color.

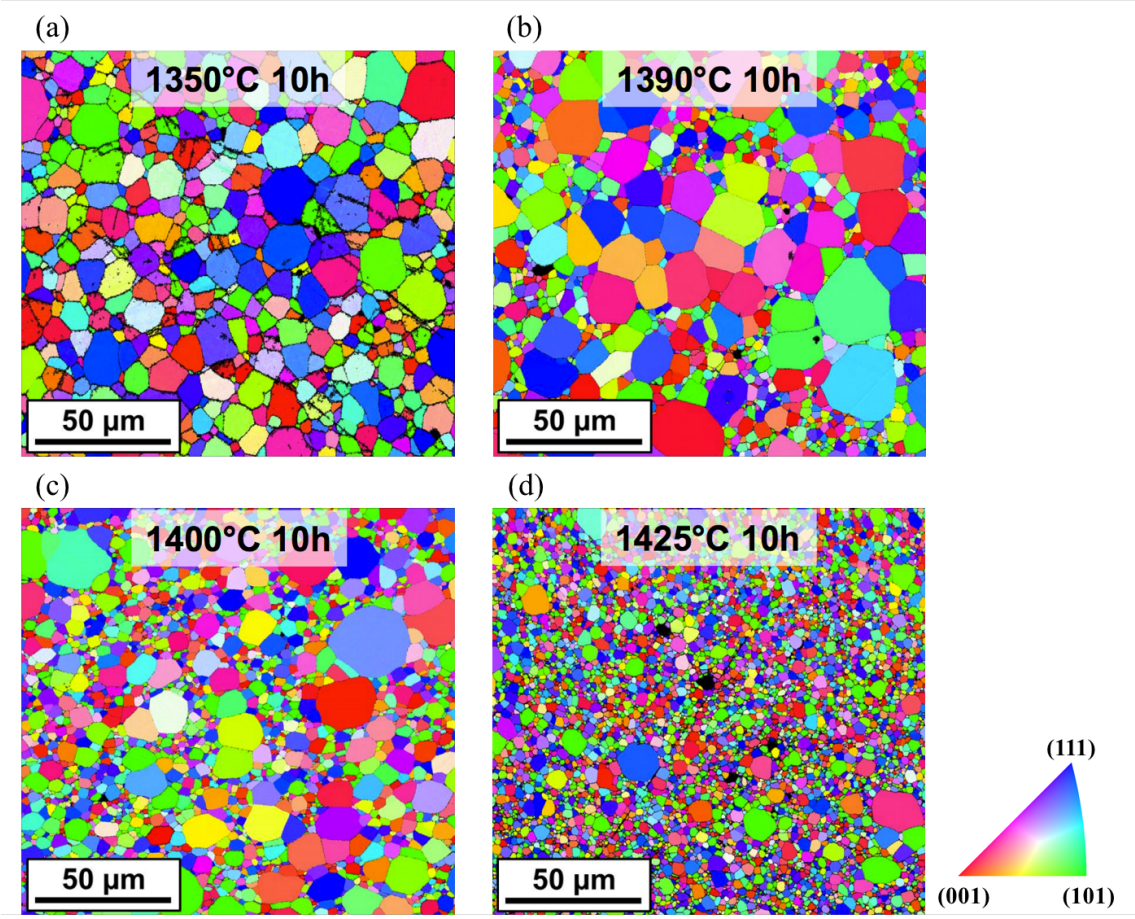


**Figure 3.** EBSD microstructures of $SrTiO_3$ after 10 h anneal at temperatures (a) 1350 °C (b), 1390 °C, (c) 1400 °C and (d) 1425 °C. Reproduced from reference.[43]

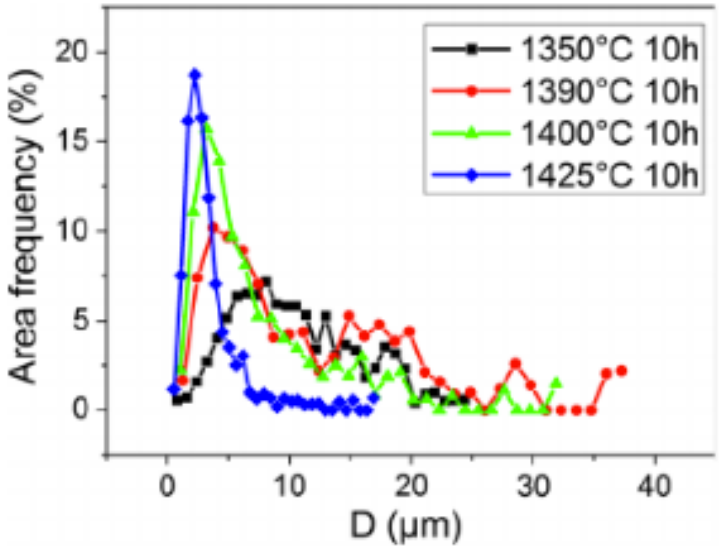


**Figure 4.** Grain size distributions corresponding to the EBSD images of **Figure 3**. Reproduced from reference. [43]

## 3.7 Surface Energy

Interfaces are created when atomic bonds are broken at the outer boundaries of a volume of crystal with uniform structure and orientation. Surfaces and grain boundaries are two types of interfaces. Energy is required to break bonds and to create these interfaces. Therefore, surface energy can be defined as the work required to create a unit area of surface and has units of energy per area, usually $J/m^2$.

### 3.7.1 Wulff Shape

Surface energy can be influenced by the type of bonds and number of bonds for any crystallographic plane in an anisotropic material. The $\gamma$-plot can be used to represent the change in surface energy as a function of crystal orientation for a single crystal. In the $\gamma$-plot, reproduced from reference[81] (Figure 5 (a)), the orientation of the interface is represented by the direction of the vector, $\gamma$, and the magnitude of this vector is the surface energy of that orientation. In Figure 5 (b), a Wulff construction is represented. Thermodynamically, systems equilibrate by minimizing their free energy. The Wulff plot is used to show the equilibrium crystal shape. To create the Wulff plot, in order to determine the equilibrium shape, lines are drawn from the origin until they intersect the $\gamma$-plot and then lines are drawn perpendicular to this intersection. Once all lines are drawn around the $\gamma$-plot, the inner shape can be realized. In this case, the equilibrium crystal shape is square, shaded in Figure 5 (b). For a perfectly isotropic crystal the Wulff plot would be a circle; this means that surface energies would all be equal with respect to crystallographic orientation. However, most materials are anisotropic and when the material is reaching its equilibrium state, the relative area of low energy interfaces, corresponding to a cusp in the $\gamma$-plot, will increase. There could also be missing orientations if the shape has facets and there are sharp edges at their intersections. However, there are no missing orientations if the facets are smoothly connected to the curved surface. In the thermal groove energy measurements presented in this document, we will consider the grain boundary to surface energy ratio. Because the surface energies are unknown, we will assume that they are constant. Surface energies vary by a few percent with orientation while grain boundary energies vary by more than 100% (see section 3.7.3).

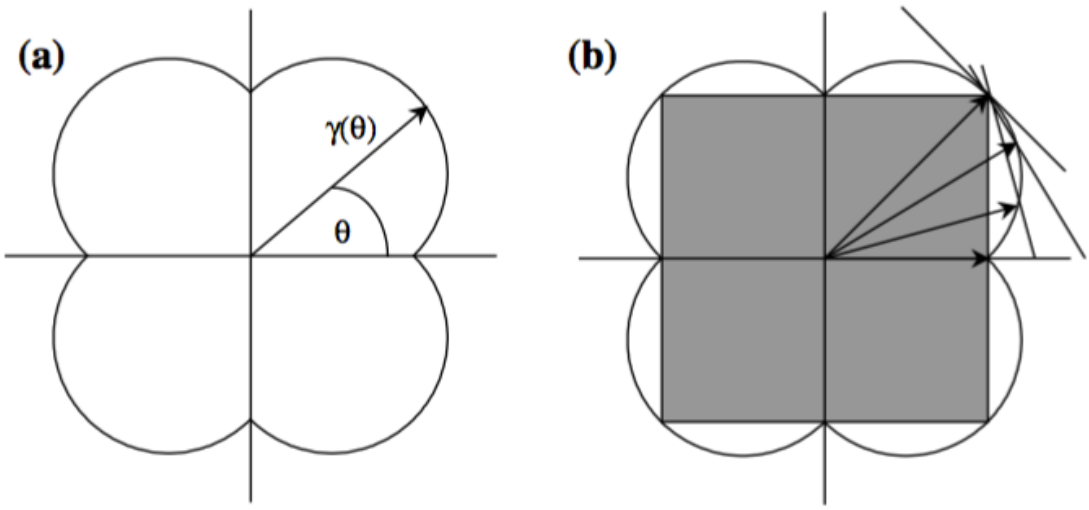


**Figure 5.** (a) $\gamma$-plot reproduced from reference[81] and (b) is the Wulff construction where the shaded shape is the equilibrium crystal shape of this example

### 3.7.2 Surface faceting and relation to the Wulff shape

For a polycrystalline material, it is possible to know which surfaces are part of the equilibrium crystal shape by examining their surface structures. Exposed surface grains will look rough with step-like features called facets, as in Figure 35. Facets form on an equilibrated surface for orientations that are not part of the equilibrium crystal shape. When a grain is not faceted, it orientation is part of the Wulff shape. It should also be noted that faceting can results from vapor transport processes, but we currently do not have enough information to distinguish between these cases.

### 3.7.3 Temperature dependence of surface energy and relation to grain boundary energy changes

It has been found that the surface energy near a material's melting point is relatively isotropic.[82, 83] With respect to a Wulff plot, as temperature is increased the cusps in the plot become more shallow and the shape becomes more rounded, eventually approaching the shape of a sphere. This was previously shown, experimentally, with Pb crystals on a graphite surface. [84] Surface energy is expected to change with increased temperature in order to reach the isotropic shape. Some experimental measurements of surface energies of particular orientations have been made with respect to temperature and are discussed in section 3.7.5 for $Al_2O_3$ and in section 3.7.7 for $SrTiO_3$. The experimental measurements of surface energy have been made from equilibrated pores in

the single crystals, from a capillarity reconstructed method (from boundary thermal grooves, surface faceting, and EBSP) as well as sessile drop studies of liquid $Al_2O_3$.[40, 85, 86] The temperature dependent surface energies measured of $Al_2O_3$ were measured well above the temperatures studied here but showed that the surface energy increased slightly with increased temperature, see section 3.7.5. The relative surface energy measurements from equilibrated pores in $SrTiO_3$ showed that the anisotropy of the surface energy decreased with increasing temperature. Overall the changes in surface energy with respect to temperature are only a few percent. No other experimental measurements of the temperature dependence of surface energy in these materials are known. Other experimental measurements in oxides in carbides report variable results of increased or decreased surface energy with increased temperature but again, vary only by a few percent. [86]

Monte Carlo simulations have been used to predict and correlate the temperature dependence of grain boundary energy and surface energy in Cu.[87] Over a 500-degree temperature range, they found that the changes in grain boundary energy were about two orders of magnitude more than the changes in surface energy. Therefore, the results reported for relative grain boundary energy here can be assumed to be mostly representative of the contributions of grain boundary energy.

### 3.7.4 Theoretical surface energy estimates in $Al_2O_3$

The surface energy of some planes in $Al_2O_3$ have been computed based on atomistic models. A first-principles calculation found the surface energy of the {0001} or *c* plane to be 1.76 J/m$^2$.[88] Two other estimations used empirical modeling and found the surface energy of the c plane to be 2.97 J/m$^2$ and 2.03 J/m$^2$. [89, 90] Using the first-principles estimate of 1.76 J/m$^2$, the relative surface energy of the *r* plane was 1.12, the *a* plane was 1.06, the *s* plane was 1.45 and *m* plane was 0.795.[88, 91] Molecular dynamics simulations by Garofallini looked at different atomic terminations of surfaces that could be formed from fracturing a bulk crystal. The "relaxed" surfaces of certain terminations varied widely. For instance, the surface energy of the *c* plane was 2.04 J/m$^2$, 2.19 J/m$^2$, and 8.04 J/m$^2$ and the surface energy of the *a* plane was 2.27 J/m$^2$, 4.77 J/m$^2$, and 8.39 J/m$^2$.[92] Approximately 2 J/m$^2$ appears to agree with other models for the *c* plane but vary for the *a* plane.

### 3.7.5 Experimental relative and actual surface energy measurements in $Al_2O_3$

Surface energy estimates in undoped $Al_2O_3$ were experimentally determined at 1600 °C and 1800 °C from the observation of cavities within single crystals produced in different ways.[83 91] The results for one type of cavity introduced lithographically and equilibrated at 1600 °C (with respect to the (0001) *c* plane) were 0.855 ± 0.017 for $\{\bar{1}012\}$ (*r* plane), 0.947 ± 0.016 for $\{10\bar{1}1\}$ (*s* plane), 0.974 ± 0.026 for $\{1\bar{2}10\}$ (*a* plane), 0.957 ± 0.026 for $\{11\bar{2}3\}$ (*p* plane), and > 1.008 for $\{10\bar{1}0\}$ (*m* plane). At 1800 °C, the results were 0.950 ± 0.030 (*r* plane), 1.042 ± 0.019 (*s* plane), 1.080 ± 0.017 (*a* plane), 1.029 ± 0.016 (*p* plane), and > 1.115 (*m* plane). [86] The results for the cavities produced by crack healing were slightly larger at 1600 °C and predicted that the *c* plane was the lowest energy plane in comparison to the *r* plane: 1.05 ± 0.04 for the *r* plane, 1.07 ± 0.06 for the *s* plane, 1.12 ± 0.07 for the *a* plane, 1.06 ± 0.05 for the *p* plane, and > 1.16 for *m* plane.[91]

Variations of the sessile and pendant drop method were used determine surface energies in $Al_2O_3$ as well.[86] Below the melting point, at 1850 °C, surface energies ranged from 0.84 - 0.91 J/m$^2$ and 0.93 J/m$^2$ at 1870 °C. At and above the melting point, surface energies ranged from 0.65 – 0.69 J/m$^2$ at 2050 °C, and 0.70 J/m$^2$ at 2080 °C. These suggest that the surface energy increases slightly with increased temperature below the melting point and that from solid $Al_2O_3$ to liquid $Al_2O_3$ the surface energy decreases slightly. However, all of these temperature dependent experimental measurements are above the maximum temperature studied in this document, 1650 °C.

### 3.7.6 Calculated surface energies of $SrTiO_3$

The energies of the (100), (110), and (111) surfaces of $SrTiO_3$ have been calculated and are summarize in Table 1.

**Table 1.** Calculated surface energies of $SrTiO_3$. Reproduced from reference.[93]

| **Surface Energy ($J/m^2$)** | | | | | |
|---|---|---|---|---|---|
| **(100)** | | **(110)** | | **(111)** | |
| SrO | $TiO_2$ | SrTiO | $O_2$ | $SrO_3$-Ti | Reference |
| 1.10 | 0.89 | | | | [94] |
| 1.33 | | | | | [95, 96] |
| | | 1.9 | | 2.4 | [97] |
| 1.27 | | | | | [98] |
| 1.40 | 1.45 | 3.1 | 2.2 | | [99] |
| 1.23 | 1.28 | | | | [100] |
| 1.39 | 1.43 | | | | [100] |
| 1.80 | | | | | [101] |

### 3.7.7 Experimental relative surface energy measurements in $SrTiO_3$ from Wulff shape

Surface energies have been measured experimentally in $SrTiO_3$ by reconstructing pore shapes. One method involves pores induced from bonding a polycrystal to a single crystal of $SrTiO_3$ between 1250 °C and 1600 °C.[40] The pore shapes were determined from SEM images of the pores and compared to a calculated pore shapes using the Wulff theorem and adjusted until the calculated shape fit the observed pore shape.[102] Calculated values of the relative surface energy were as much as 1.25 times the {100}, Figure 6. In another method, the surface energy was determined from the geometries of grain boundary thermal grooves, surface faceting, and EBSP were used to determine the inclination of a boundary and orientation of the surface plane at 1400 °C.[85] The relative surface energy by this method where reported as 0.93 ± 0.03 for {100}, 1.01 ± 0.06 for {110} and 1.02 ± 0.01 for {111} at 1400 °C in air. The values reported by this method are in good agreement with the reconstructed pore shape method for {100} but there is a difference in the results for the {111}. [85]

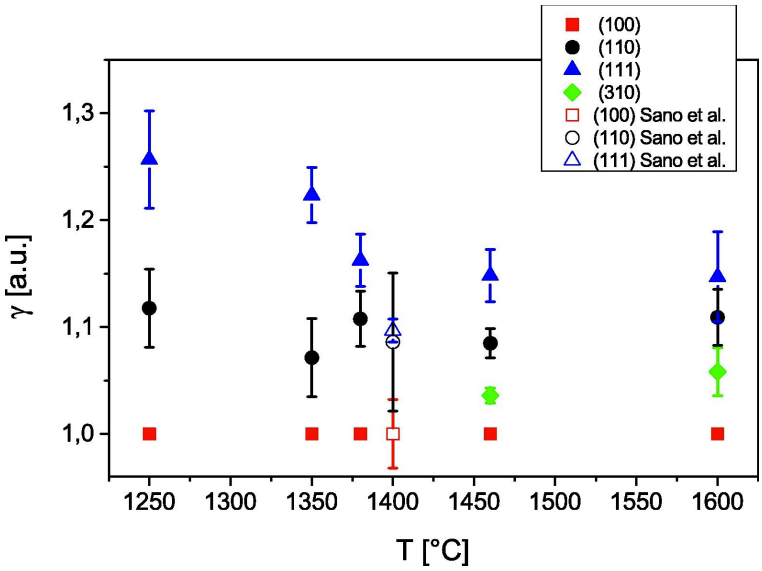


**Figure 6.** Relative surface energies of {100}, {110}, {111} and {310} of $SrTiO_3$ in air. Reproduced from reference.[40]

### 3.7.8 Surface energy estimates in metals and other elements

Surface energies have been computed in many metals by reconstructed Wulff shapes. Others have been computed using atomistic simulations. These results have been collected into a recent database called the Crystalium web application. Some typical values of surface energy are listed in **Table 2** for a few different elements.[103]

**Table 2.** Surface energy values of a variety of elements from the Crystalium web application. [103]

| Element | Surface | Surface energy ($J/m^2$) |
|---|---|---|
| Ni | (110) | 2.29 |
| | (100) | 2.21 |
| | (111) | 1.92 |
| Mg | $(10\bar{1}0)$ | 0.6 |
| | (0001) | 0.54 |
| Sr | (110) | 0.41 |
| | (100) | 0.35 |
| | (111) | 0.34 |
| Mo | (110) | 2.8 |
| | (100) | 3.18 |
| | (111) | 2.96 |
| Fe | (110) | 2.45 |
| | (100) | 2.5 |
| | (211) | 2.61 |
| | (111) | 2.73 |

## 3.8 Grain Boundary Energy

Like surface energy, grain boundary energy can be defined as the work required to create a unit area of grain boundary. It can be represented as $\gamma_{GB} = 2\gamma_S - B$ where $\gamma_S$ is the surface energy, $\gamma_{GB}$ is the grain boundary energy and $B$ is the energy returned when the two misoriented crystals join together and some of the broken bonds are reformed. It has been found, experimentally, that the grain boundary population is inversely correlated with the grain boundary energy.[104] It is often written that grain boundaries with high coincidence misorientations have lower energies. However, there is no correlation between coincident site lattice numbers and grain boundary energy.[69, 105] Grain boundary energy can also be thought of in terms of dislocation spacing. Each dislocation contains a discrete amount of excess energy so grain boundary energy can be determined from the sum of dislocations plus the energy of interaction between the dislocations. In general, the relationship between dislocation spacing and misorientation can be described as $tan\left(\frac{\theta}{2}\right) = \frac{b/2}{D}$ which reduces to $\theta = \frac{b}{D}$ if you assume $tan\left(\frac{\theta}{2}\right) \cong \frac{\theta}{2}$ where $\theta$ is misorientation, b is burgers vector and D is dislocation separation. For small misorientations ($\theta < 10°$), this model, known as the Read-Schockley model, can be used to predict how grain boundary energy varies with misorientation. However, at larger misorientations, the grain boundary can not be viewed as discrete dislocations and the Read-Shockley model is therefore not useful for misorientations greater than 10°. Therefore, we have to resort to other ways of measuring grain boundary energy.

### 3.8.1 Grain Boundary Energy from triple junctions

The geometry of a triple junction, where three interfaces meet along a triple line can be represented by a balance of forces, which was first described by Herring, Equation 1.[106] In Figure 7 (a), $\gamma$ describes the energy of the interface which is balanced by the normal (n) and tangential (t) forces. The normal terms (dashed lines) are referred to as torques and may rotate for boundary if the change in energy with respect to rotation angle ($\beta$) is large. If there is no significant torques, however, then the Herring equation can be simplified to only be a balance of the tangential forces Figure 7 (b). The balance of forces

in this case would be simplified to Young's equation $\frac{\gamma_{gb1}}{\sin\theta_{2,3}} = \frac{\gamma_{gb2}}{\sin\theta_{1,3}} = \frac{\gamma_{gb3}}{\sin\theta_{1,2}}$. With Young's equation, the grain boundary energies can be extrapolated from measuring the dihedral angles of the boundaries. When a grain boundary meets a free surface, we can assume that the surfaces have the same energy and we can estimate the grain boundary energy with respect to surface energy, as illustrated in Figure 7 (c).

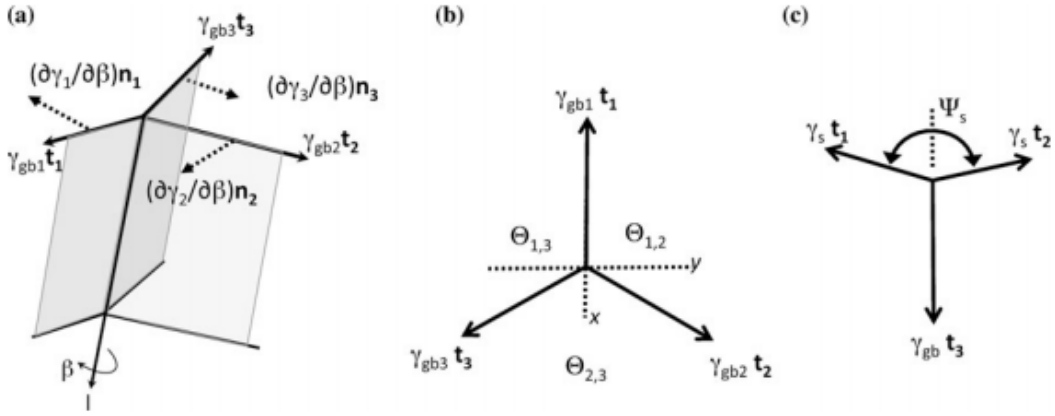


**Figure 7.** Balance of interfacial energies at triple junctions where (a) is labeled and illustrated the normal and tangential vectors of each interface as well as the rotation angle highlighted, (b) is the reduced relationship if the torque terms are ignored and (c) is a representation of a grain boundary thermal groove. Figure reproduced from reference.[105]

### 3.8.2 Grain Boundary Energy from Thermal Grooves

When a grain boundary intersects a sample surface and that polycrystal is held at an elevated temperature a thermal groove is formed by capillarity driven surface diffusion. Herring has described this as the balance of interfacial energies where $\gamma_i$ is the excess free energy of the $i$th surface, $n_i$ is the unit vector normal to the line of intersection, $t_i$ is the unit vector that lies on the $i$th interface which is normal to the line of intersection (l) of three interfaces such that $n_i$ = $t_i$ x l and $\frac{\partial\gamma_i}{\partial\beta}$ is the torque term seen in Equation 1 below.[106]

Equation 1

$$\gamma_i t_i + n_i \frac{\partial\gamma_i}{\partial\beta} = 0$$

To determine the grain boundary energy of a thermal groove, the torque term has been

assumed to be negligible such that the grain boundary energy is no longer measured as a function of its tangent plane but with respect to misorientation.[107] Therefore, Equation 1 reduces to $\frac{\gamma_{GB}}{\gamma_S} = 2\cos\left(\frac{\psi_{S1}}{2}\right) = 2\sin\beta$. In addition, this equation assumes that the surface energy is constant with orientation and assumes that the grain boundary is not affected by its orientation. More details on the calculation of grain boundary energy from thermal grooves can be found in the methods sections 4.1.5 , 4.1.6 and 4.1.7.

#### 3.8.2.1 Typical values of relative grain boundary energy in metals.

Relative grain boundary energies were measured by thermal grooving in metals and are listed here in comparison to values that will be later reported for $Al_2O_3$ and $SrTiO_3$. All of the values of relative grain boundary energy in the table are < 0.4 whereas in alumina and strontium titanate, in the temperature regions discussed in this work, are > 0.6.

**Table 3.** Relative grain boundary energies measured from thermal grooves of various metals, reproduced from reference.[108]

| Metal | Relative Grain Boundary Energy from Thermal Grooves | Reference |
|---|---|---|
| Ag | 0.35 | [109] |
| Au | 0.27 | [109] |
| Co | 0.36 | [109, 110] |
| Cu | 0.32 | [109] |
| **δ**-Fe | 0.37 | [109, 110] |
| Mo | 0.27 | [111, 112] |
| Nb | 0.34 | [109, 111] |
| Ni | 0.38 | [109, 110] |
| Pt | 0.33 | [109] |
| Sn | 0.24 | [109] |
| Ta | 0.32 | [83] |
| W | 0.38 | [109, 111] |

### 3.8.3 Expected trends of grain boundary energy with increasing temperature

One of the first studies of the thermodynamic properties of grain boundary phase transformations (a.k.a. complexions) was by Hart in 1972.[113] He used a Clausius-Clapeyron relationship to determine discontinuities in the slopes of curves of surface tension versus temperature. This theoretical thermodynamic analysis showed that pure materials would have a mean grain boundary energy decrease with an increase in temperature, which is represented by $\Delta\left(\frac{\partial\gamma}{\partial T}\right)_P = -\Delta s_\gamma$ where $s_\gamma$ is the interfacial entropy, T is temperature and P is pressure. For non-pure materials, however, there will be positive grain boundary energy temperature dependence due to impurity adsorption at the grain boundaries which is explained by adsorption and desorption models. The thermodynamics of segregation at interfaces have often been described by the Gibbs adsorption isotherm and the Langmuir-McLean isotherm.[114] The Gibbs approach[115–117] gives an explanation of the solute segregation behavior based on bulk activity and Langmuir McLean approach[118–120] describes the segregation equilibrium in terms of minimum Gibbs energy.

## 3.9 Models to describe grain boundary segregation

Many theoretical models have been developed and some compared to experimental situations for the effect of segregation on grain boundary energy. The basis for these models, some expansions, and other models used in related materials science fields are discussed below. Some more detailed models are discussed as well to be used for future that could be useful to compare the the experimental results presented here. In general, the concepts all stem from the basic thermodynamic principles of Gibbs free energy, entropy, temperature and adsorption so the results discussed will be interpreted in terms of the simplified equation $\gamma = \Delta H - T\Delta S - \Sigma\mu\Gamma$.

### 3.9.1 Gibbs adsorption isotherm

Many models have been developed to describe segregation behavior and many of them stem from the Gibbs adsorption isotherm.[117] The following descriptions of the model are paraphrased from the Wynblatt and Chatain paper cited above. The Gibbs adsorption isotherm describes segregation behavior at an interface but ignores interfacial

excess volume. The thermodynamic properties of a system can be written in terms of the extensive and intensive variables. The extensive variables are entropy $S$, volume $V$, and number of moles $n$. The energy of a single phase can be written as $dE^1 = \left(\frac{\partial E^1}{\partial S^1}\right)_{V^1,n_i^1} dS^1 + \left(\frac{\partial E^1}{\partial V^1}\right)_{S^1,n_i^1} dV^1 + \sum_i \left(\frac{\partial E^1}{\partial n_i^1}\right)_{S^1,V^1,n_{i\neq i}^1} dn_i^1$ and simplified to the standard expression of internal energy of a single phase as $dE^1 = TdS^1 - PdV^1 + \sum_i \mu_i^1 dn_i^1$ where T is temperature, P is pressure and $\mu_i$ is chemical potential of phase 1. The internal energy of the interface which does not have any volume can be written as $dE^s = TdS^s + \gamma dA + \sum_i \mu_i^s dn_i^s$. If the intensive variables T, $\gamma$, and $\mu_i$ are constant in equilibrium the interfacial equation can be integrated, $E^s = TS^s + \gamma A + \sum_i \mu_i^s n_i^s$, re-differentiated, $dE^s = TdS^s + S^s dT + \gamma dA + Ad\gamma + \sum_i \mu_i^s dn_i^s + n_i^s d\mu_i^s$. And also $dE^s = TdS^s + \gamma dA + \sum_i \mu_i^s dn_i^s$ where $0 = S^s dT + Ad\gamma + \sum_i d\mu_i^s n_i^s$. In addition, the specific surface entropy is defined as $s^s = S^s/A$ and adsorption is defined as $\Gamma_i = n_i^s/A$. The final Gibbs adsorption equation can be written from substituting these equations: $d\gamma = -s^s dT - \sum_i \Gamma_i d\mu_i$.

The Gibbs isotherm has a few shortcomings. One is that it assumes equilibrium chemical potential of the interface and the bulk. Another is that the dependence of adsorption and bulk composition must be known to compute the change in surface energy which is often unknown. Therefore, other models have been developed and explored.

### 3.9.2 Langmuir-McLean isotherm and Wynblatt and Chatain expansion

The Langmuir-McLean[118] model has been used to explain grain boundary adsorption, which can be seen in Equation 2 below where $X_{GB}$ is the grain boundary atomic fraction of solute, $X_{bulk}$ is the atomic fraction of bulk, $\Delta G_{ads}$ is the molar Gibbs free energy of adsorption (negative value for positive adsorption of solute at the grain boundary), R is the universal gas constant and T is temperature.

Equation 2

$$\frac{X_{GB}}{1-X_{GB}} = \frac{X_{bulk}}{1-X_{bulk}} e^{-\frac{\Delta G_{ads}}{RT}}$$

This model assumes segregation is constrained by a monolayer of atomic sites at the grain boundary, however.[74] There have been numerous efforts to expand the Langmuir-McLean model, one of which is derived by Wynblatt and Chatain.[117] The

following Equation 3 and Equation 4 are all duplicated from their work. The interfacial excess quantity is defined in Equation 3 below, where $\mu_i$ is the chemical potential, n is number of moles, S is entropy, T is temperature, F is Helmholtz free energy and Γ adsorption.

Equation 3

$$dF^S = -S^S dT + \gamma dA + \sum_i \mu_i dn_i^S$$

Integrating the above equation, dividing by area of surface, A, and rearranging gives the surface energy in

Equation 4

$$\gamma = f^S - \sum_i \mu_i \Gamma_i$$

Finally, rewriting the interfacial excess free energy in terms of internal energy and entropy gives Equation 5 where $e^S$ is the internal energy per unit area of surface, $s^S$ is the entropy per unit area of surface, Γ is the adsorption (surface excess number of moles of component $i$ per unit area) and T is temperature.

Equation 5

$$\gamma = e^S - Ts^S - \mu_A \Gamma_A - \mu_B \Gamma_B$$

This grain boundary energy will thus increase with increasing temperature for an impure system.

To simplify this expression of grain boundary energy change with respect to thermodynamic parameters and adsorption, Equation 5 is re-written here with more common thermodynamic symbols as $\gamma = \Delta H - T\Delta S - \Sigma\mu\Gamma$. The trends of grain boundary energy with respect to increased temperature can be predicted from this equation.

For an impure system, as temperature is increased, the adsorbed species at the grain boundary would dissolve into the bulk as long as the solubility increases with temperature. This leads to a reduction in the concentration at the grain boundary. In addition, in an impure system doped beyond its solubility limit, if a precipitate is formed as temperature is increased, the precipitation reaction may also remove excess solute from the boundaries, assuming that the boundaries were initially supersaturated. Thus, the adsorption term, Γ, would decrease and thus result in an increase in grain boundary energy with increased temperature.

For a pure system there would be no adsorption to a grain boundary so the adsorption term, Γ would be zero and the expression would read $\gamma = \Delta H - T\Delta S$. As temperature is increased for the pure system, entropy would increase and thus result in a decrease in grain boundary energy. Any deviation from this behavior would result in a change of slope in the grain boundary energy trend and may be a sign of grain boundary transition, as illustrated in **Figure 15**.

Previous measurements of relative grain boundary energy in doped alumina, as well as the data presented in chapter 6, have shown that when a complexion transition is detected there is a significant (30 %) decrease in grain boundary energy. [1, 4, 80, 121] This would cause a change in slope of the expected trend of grain boundary energy with increasing temperature of the impure system. After the transition is complete, one would expect that the mean grain boundary energy would follow the original trend from before the transition which is likely due to the result of the increasing bulk solubility of the segregate that reduces the concentration at the grain boundaries.

### 3.9.3 Schuh nanostructure segregation stability model

Stabilizing nanostructures from doping is based on the idea that the dopant can occupy all lattice sites and grain boundary sites to temper the energy effect of interfaces. The following is summarized from the Schuh model in reference.[122] Through segregation to the interface, the energy of a grain boundary $\gamma$ is reduced from the pure material $\gamma_0$ from the solute excess Γ, enthalpy $\Delta H^{seg}$, and entropy by the product of the thermal energy $kT$ and composition $X$ such that $\gamma = \gamma_0 - \Gamma(\Delta H^{seg} + kTlnX)$. The specific excess solute of boundary lowers the enthalpy and raises the entropy from the pure state. The mixing free energy was also described in terms of composition and grain size. The grain boundary volume fraction $f_{gb}$ is written with respect to grain size $d$ and boundary thickness $t$ as $f_{gb} = 1 - \left(\frac{d-t}{d}\right)^3$ where $d \geq t$. If the thickness remains constant, for increased grain size the $f_{gb}$ would decrease. The model then provides a form of the Gibbs free energy surfaces for mixing combining effects of the crystal $c$ and grain boundary, includes factors for the atomic volume Ω, interaction parameter of bond energy $\omega$, coordination number $z$, and transition bond fraction $v$ and also differentiates between solute A and solvent B: $\Delta G^{mix} = \left(1 - f_{gb}\right)\Delta G_{gb}^{mix} + f_{gb}\Delta G_{gb}^{mix} + zvf_{gb}(X_{gb} -$

$X_c)\left[(2X_{gb}-1)\omega_{gb}-\frac{1}{zt}(\Omega^B\gamma^B-\Omega^A\gamma^A)\right]$. The enthalpies of mixing and segregation were also included such that $\Delta H^{mix}=z\omega_c X(1-X)$ and $\Delta H^{seg}=z\left[\omega_c-\frac{\omega_{gb}}{2}-\frac{(\Omega^B\gamma^B-\Omega^A\gamma^A)}{2zt}\right]$.

### 3.9.4 Solute segregation models from the grain boundary embrittlement community – advances and pitfalls

The McLean isotherm[118] was derived using statistical mechanics; Fowler and Guggenheim similarly derived a model using statistical mechanics, but only for binary solutions.[123] The Fowler and Guggenheim model was an adaption of the Bragg and Williams model[124] (also known as the mean field approximation) but they extended it to be used on a surface. This model includes average adsorbate / adsorbate interactions, ignores reordering of a surface and instead replaces the occupancy of nearest neighbor sites on a surface with the average for the whole layer. Each of these adaptions are rooted from the Langmuir McLean isotherm but just include more parameters.

Other models have been developed to predict grain boundary embrittlement which include energetic predictions of solute at the surface versus a grain boundary but do not (or limitedly) consider if the solute will enrich a grain boundary in the first place.[125] More recent attempts by Lejcek have been seemingly more accurate by expanding to higher order alloy systems and by attempts to use measureable materials parameters. However, only equilibrium interfaces were taken into account and the Lejcek models are limited to open systems which do not account for changes in intrinsic concentration. [126, 127] An even more recent model by Gibson and Schuh adapts similar thermodynamic framework as past models but can consider many more conditions which were not previously combined into one model.[125]

The Gibson and Schuh model uses similar framework as previous models to interpret the thermodynamics of polycrystals such as segregation induced changes in grain boundary energy and grain boundary cohesion.[125] This model also considers solubility limit, second phase precipitation for both open and closed systems all of which are relevant subjects studied in this thesis. Although this model was developed to understand grain boundary embrittlement in metals, it appears to have applicable

scenarios to complexion transitions in ceramics. The following descriptions of the model are paraphrased from the Gibson and Schuh paper cited above.

The cohesive energy of a grain boundary, is written as, $E_{GBC} = 2\gamma_S - \gamma_{GB}$, which is a rearranged version of the model of a grain boundary energy discussed in section 3.8. For this model for grain boundary embrittlement, the equation is re-written to represent the work to create a free surface at a grain boundary: $E_{GBC} = E_{Surfaces} - E_{Grain\ Boundary}$ such that the grain boundary with the same atomic configuration has two free surfaces replacing the grain boundary. Then the cohesive energy is written as the change in the cohesive energy of the alloyed and unalloyed states: $\Delta E_{GBC} = \Delta E_{GBC}^{alloy} - \Delta E_{GBC}^{pure}$. The model is then formulated from $\Delta E_{GBC}$ for a binary alloy and takes into account surface, intergranular, and bulk regions of an alloy.

Next, this model considers a regular solution model but for nanocrystalline solutions which incorporates the nearest neighbor interactions in a polycrystal and the internal energy is written as $E_{solution}^{gb} = \sum_{r=gb,b,t} N_r^{AA}E_r^{AA} + N_r^{BB}E_r^{BB} + N_r^{AB}E_r^{AB}$ where $N_r^{XY}$ is the total number of bonds and $E_r^{XY}$ is the pairwise bonding energy between atoms of X and Y in region r where r can be the grain boundary, bulk or transitional (bulk bonds) regions. Similarly the internal energy of a surface solution can be written the same as $E_{solution}^{gb}$ except that for $E_{solution}^{s}$, r = s,b,t where s is surface, b is bulk and t is transitional regions.

The change in cohesive energy, $\Delta E_{GBC}$, can be calculated from $N_r^{XY}$ computed from the grain boundaries and surfaces. By assuming random mixing $N_r^{XY} = N_r \cdot P(XY|r)$ where $P(XY|r)$ is the probability of randomly choosing an X-Y bond in region r and $N_r$ is the total number of bonds in region r. A summary of the bond counting can be found in table 1 of the reference along with the remainder of the derivation. [125]

The final equation for cohesive energy of a crystal used for the Gibson and Schuh model is written as $\Delta E_{GBC}^{alloy} = \frac{5X_{GB}}{3[\gamma_S^B - \gamma_S^A]} - \frac{zt_{GB}}{4\Omega} X_{GB}(1 - X_{GB})\omega_{GB}$. Where $\omega_{GB}$ is a grain boundary interaction parameter for pairwise bonding energy, z is the coordination of the solvent, $t_{GB}$ is the grain boundary thickness, $X_{GB}$ is local solute concentration at the grain boundary, $\gamma_S^i$ bond energy of the surface (where $\gamma_{GB}^B = \gamma_S^B/3$ ), and Ω as the atomic volume of the solvent. This model describes changes in grain boundary cohesion with

alloying but does not employ the thermodynamic effects of changes in equilibrium of the solvent and if the solvent would segregate to the boundaries in the first place.

To quantify if segregation will change in equilibrium, the grain boundary isotherm chosen to add to this model was an adapted Fowler isotherm[123] shown by Guttmann and McLean[128] written as $\frac{X_{gb}}{1-X_{gb}} = \frac{X_b}{1-X_b} exp\left[-\frac{\Delta G_0^{seg} + z\omega_{gb} - z\omega_b - 2(X_{gb}z\omega_{gb} - X_b z\omega_b)}{RT}\right]$ where $\Delta G_0^{seg}$ is energy released upon segregation that is composition independent and proportional to the changes in grain boundary energies in the Gibson and Schuh model. This is different than the original Fowler interpretation because of the $z\omega_b$ term (interaction parameter) which accounts for mixing behavior that was previously assumed to be equal.

By including the isotherm with the original equation for cohesive energy of a crystal, Gibson and Schuh showed that there is actually a large effect on cohesive energies that influences the tendency to segregate. Next, the solubility limit was tested for this model where chemical equilibrium is maintained if the system is at compositions below the solubility limit. In this model, above the limit, the solute is assumed to be trapped in second phase and not available to affect the grain boundary cohesive energy from segregation. However, some assumptions were made which may generally not be true, such as, the temperature where the solubility limit is reached is equal to half of the melting temperature but the cohesive energy results are interesting to point out here in any case. In general, they found that the cohesive energy is lower for solute that is up to the solubility limit in the bulk as opposed to a system that is in chemical equilibrium. Future work needs to be put into emphasizing chemical equilibrium near the solubility limit and second phase precipitation.

## 3.10 Intrinsic versus extrinsic behavior in a polycrystal

In multi-component systems the amount of dissolved species of one element into the matrix of another is known as the solubility. Often, once the solubility limit is surpassed a new phase will precipitate. This is dependent on not only composition but also temperature. Solute atoms of the dissolved species in a host matrix can be accommodated within the matrix at vacancy sites, interstitial sites and substitutional sites.

Factors that influence the solubility are the atomic size of the solute / solvent, the crystal structure and the electronegativities. This is referred to as intrinsic solubility. For a single crystal there would be a single value of the solubility at any temperature, the intrinsic solubility. Solute that is not accommodated within a host matrix may reside at an interface such as a grain boundary. For a polycrystal, the excess solute accommodated at a grain boundary depends on the grain boundary area to sample volume ratio and it is therefore labeled extrinsic (it is a property of the microstructure rather than the crystal). For instance, as grain size increases there will be less grain boundary area and thus the extrinsic solubility should decrease. The sum of the intrinsic and extrinsic solubility is the total apparent solubility of a solution. Once the concentration of species is beyond apparent solubility another solid solution compound will form with a distinctly different composition. Therefore, the solubility is often qualified by searching for precipitates in a sample. Often people use energy dispersive spectroscopy to find precipitates. However, in solutions where the solubility is low (e.g. ppm concentrations in yttria doped alumina), it may be difficult to locate precipitates with this technique. Therefore, more high resolution techniques need to be used such as SIMS or EDS via TEM.

### 3.10.1 Methods to measure solubility and experimental measurements in yttria doped alumina

Solubility can be determined, experimentally, by visually searching for precipitates in samples, and identifying the sample that has the highest concentration of solute, but no precipitates. One may also measure the bulk concentration of solute in a sample that is known to be saturated because of the presence of precipitates. To do this, a systematic study of solute concentration and temperature must be employed. Many studies dope a material with a specific amount of solute and search for precipitates at a specific temperature but often do not do a systematic study of gradually and independently changing concentration and temperature to determine the highest concentration before precipitation. For instance, in yttria doped alumina, reported values of the solubility limit between 1470 °C and the melting point (2050 °C) ranged from 5 ppm up to 80 ppm (by atomic units).[18, 129–131] Determining the presence of precipitates is also limited by the detection limit of the technique.

There are a variety of analytical techniques that can be used but can be limited by the lateral resolution, the sensitivity of the analysis and sampling area. For instance, SEM / EDS is a fairly common technique but the best detection limit is only 1000 ppm. STEM / EDS and STEM / EELS provides a smaller lateral resolution but the detection limit is still only about 1000 ppm.[132] If the concentration of a single precipitate is large (> 1000 ppm) then SEM / EDS or STEM / EELS will be able to detect them. However, if there are precipitates in concentrations less than 1000 ppm these techniques will not be useful. SIMS can provide limits of at least single ppm or better and is therefore the best resolution single technique for elemental characterization to date. Due to the limited of availability of each of these techniques, many researchers will publish estimated solubility values that do not agree. For instance, in yttria doped alumina, measurement by SEM / EDS technique reported 4.52 ppm near the melting point,[129] STEM as 9.03 ppm at 1550 °C[18] and SIMS as 80 ppm at 1475 °C.[131] Again, because of the difference in resolution of the techniques it is likely that the SIMS measurement is most accurate. However, the difference in the published values of solubility could be due to an affect of microstructural evolution with temperature.

### 3.10.2 Solute accommodation at grains and grain boundaries

The concentration of solute, or extrinsic solubility, is dependent on the intrinsic solubility at a given temperature. However, grain size will change with temperature as well which will decrease the extrinsic solubility. To quantitatively determine the extrinsic solubility it can be calculated as $C_{ex} = \frac{\frac{1}{2}\Gamma A}{F_{Al}V}$ where Γ is the grain boundary excess of the solute, A is the grain boundary area of diameter D, V is the grain volume, $F_{Al}$ is the number of Al atoms per volume, and the factor of ½ that accounts for two grains which share a single grain boundary. If we assume cube shaped grains, $A = 6D^2$ and $V = D^3$. Thus, $C_{ex} = \frac{3\Gamma}{F_{Al}D}$ and clearly we can see that the extrinsic solubility will vary with grain size. The apparent solubility can then be determined by methods described above to determine if a second phase would have precipitated in the material and subtracting that apparent solubility value from extrinsic solubility to get the intrinsic solubility.

## 3.11 Grain Boundary Complexions

The idea that grain boundaries may undergo transformations in a similar way that bulk phases transform was first suggested in the 1960's-70's by Hart.[133] In later years, Cahn[134] began to describe grain boundary phase diagrams. However, grain boundary properties are dependent on other parameters like misorientation and the boundary plane normal, which is not inclusive in the fundamental definition of bulk phase diagrams. Tang et al.[2] introduced the term "complexion" in 2006 as a means of making this distinction. In 2007 Dillon and Harmer used high resolution transmission electron spectroscopy (HRTEM) and high angle annular dark field - scanning transmission electron microscopy (HAADF-STEM) to connect the structure of the boundary with its kinetics.[76] In this work, they categorized the structures (complexions) into six distinct types.[76] When an interface transforms from one complexion type to another this is known as a complexion transition and can be categorized as congruent or non-congruent.[74] These descriptions are illustrated in **Figure 8**.

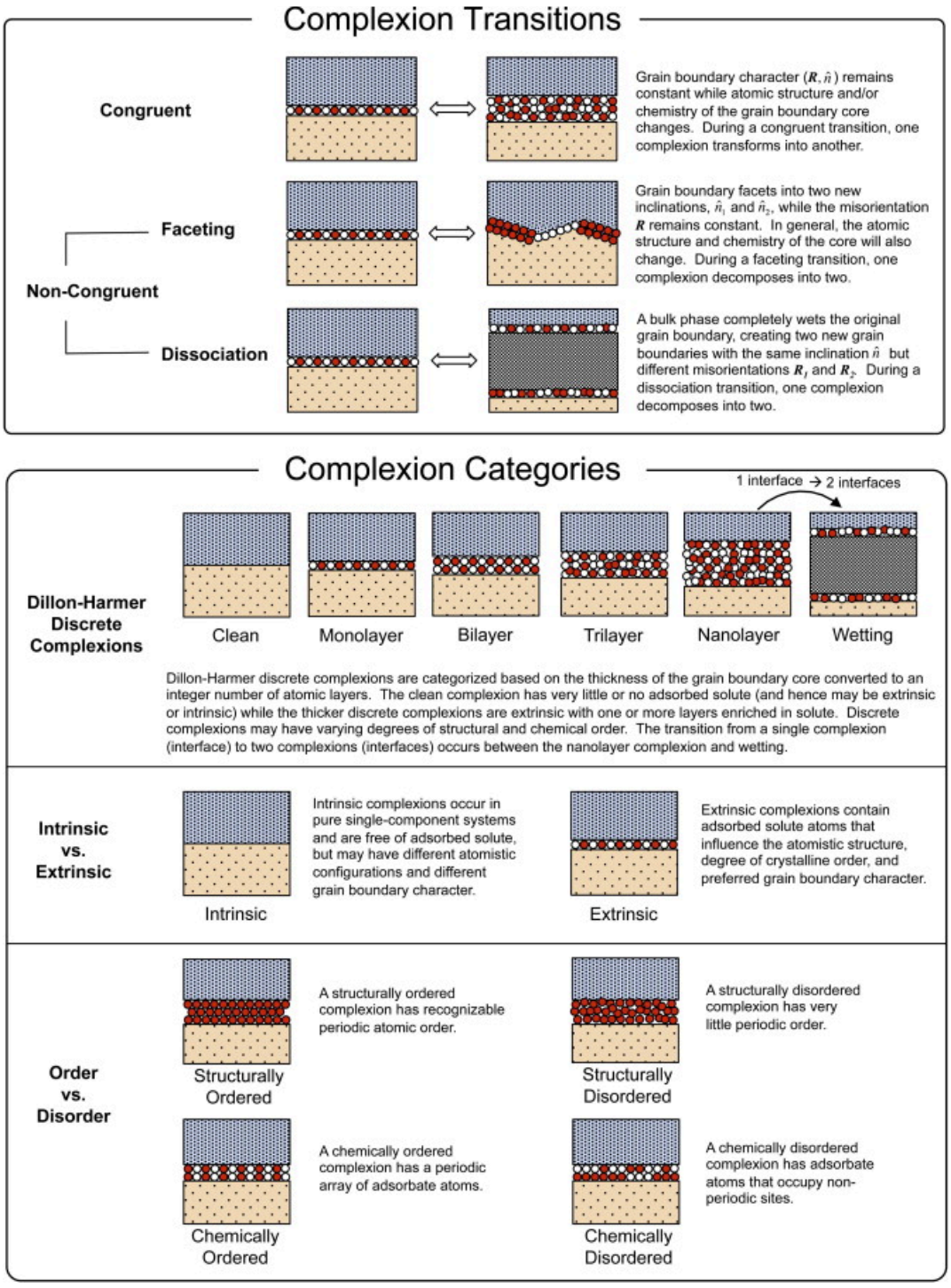


**Figure 8.** Schematic of different types of complexion transitions and different ways of categorizing complexion transitions. Reproduced from reference. [74]

HRTEM, HAADF-STEM, electron energy loss spectroscopy (EELS), transmission electron microscopy - energy dispersive x-ray spectroscopy (TEM-EDS) and atom probe tomography methods are often used to determine the type of complexion by examining

the sub-nanometer structure at grain boundaries. [3, 76] Although precise and accurate, these methods are time consuming and may only be representative of a small fraction of grain boundaries, which may not be sufficient to adequately describe the bulk characteristics. Measuring the properties (e.g. GBCD and relative grain boundary energy) of many grain boundaries makes it possible to determine representative average properties of grain boundaries. Once a complexion type is defined by looking at the sub-nanometer structure or a transition region is determined from average properties, complexion regions can be plotted in a couple of ways.

As discussed above, the term complexion was coined because grain boundary "phase" types are dependent on more parameters than bulk phases. However, bulk phase diagrams can be useful to visualize changes in grain boundary complexion types with respect to temperature and composition. If pressure and the 5 parameters used to describe a grain boundary are held constant, complexion types can be overlaid onto bulk phase diagrams.[74] Here we refer to these as grain boundary complexion diagrams (e.g. **Figure 27**). In addition, recent work has been in developing complexion time-temperature-transformation (TTT) diagrams (e.g. **Figure 14**) to map out complexion stability regions in order to engineer desirable microstructures.[135]

### 3.11.1 General Nucleation and Equation for Nucleation of a Complexion

Nucleation is the creation of a new species that can occur either homogeneously or heterogeneously. Heterogeneous nucleation occurs only on features that are not part of the ideal structure and homogeneous nucleation occurs spontaneously and randomly. Often an activation energy barrier is thought to be required for a nucleation event to occur. In addition, superheating is believed to be required for the least stable species to nucleate. Assuming spherical nucleation of a particle, the general equation for homogeneous nucleation can be written as $\Delta G = \frac{4}{3}\pi r^3 \Delta G_v + 4\pi r^2 \gamma$ where $\frac{4}{3}\pi r^3$ is the volume and $4\pi r^2$ is the area of the particle. The $\Delta G_v$ term is the change in free energy of the volume and $\gamma$ is the energy created for the area of the particle. Homogeneous nucleation of a complexion has been proposed, similar to the classical equation, but assumes a two dimensional circle nucleates on an existing complexion representing a complexion nucleating at a grain boundary. In this case, the area of the nucleating

complexion is $\pi r^2$, with circumference $2\pi r$ and energy $\lambda$ representing the energy per length of the complexion boundary. It has been shown that when a new complexion nucleates on a grain boundary the energy is decreased. Therefore, $\gamma_2$ corresponds to the new complexion and $\gamma_1$ corresponds to the existing complexion where $\gamma_2 < \gamma_1$. The proposed equation is as follows $\Delta G = -\pi r^2(\gamma_1 - \gamma_2) + 2\pi r\lambda$.[136]

### 3.11.2 Surface complexions (surficial phases) and correlation to grain boundary complexions

Similar to grain boundary complexions, surfaces (external interfaces) are known to have distinct layering transitions, such as submonolayer, monolayer, bilayer, etc. that also coexist with bulk phases.[137–139] These surface phases or surface complexions have been widely studied in the surface science community beginning with Fowler and Gugenheim's predictions in 1939.[123, 140, 141] In recent years, surface complexion diagrams have been formulated for submonolayer and monolayer[142–145] regimes as well as for nanoscale thicknesses and amorphous films.[137, 138, 146] Methods to characterize grain boundary complexions are a bit more difficult than with surface complexions because of the inherent difficulty of characterizing an internal boundary as opposed to the relative easy availability of a surface at a solid-vacuum interface.[147]

Surface complexions are believed to form from nucleation and growth, similar to the idea for grain boundary complexions. If we imagine a microstructure where there is more surface area of grain than grain boundary area, the activation energy for grain boundary nucleation should be lower than for surface nucleation simply because of the availability of sites on a surface would be larger. As temperature is increased, surfaces can become rougher. Rough surfaces have a high concentration of kinks and steps which provide sites for the addition or removal of atoms. Therefore, the number of sites for surface nucleation events should increase which should effectively decrease the activation energy for a surface complexion. However, as temperature is increased, the activation energy for each of the three events is increased and either can become the predominant nucleation event.[148] Each of these events can also be influenced by composition, particle packing, second phase precipitation and crystallographic surface reconstructions.[147] The effect of surface and grain boundary complexions nucleating simultaneously has not been studied.

# 4 Methods

## 4.1 Grain boundary energy measurements from thermal grooves

### 4.1.1 Powder processing

The yttria doped alumina samples were prepared in concentrations of 100 ppm and 500 ppm yttria in $\alpha$ alumina using spark plasma sintering. Bojarski had previously prepared the samples in the following procedure. Pure alumina powder (Puratronic, Alfa Aesar 99.995% pure) was mixed with 500 ppm and 100 ppm $Y(NO_3)_3 \cdot 6H_2O$ (Alfa Aesar, Ward Hill, MA) in two separate samples. Sapphire single crystals (MTI Corp, Richmond, CA) were thoroughly cleaned then the powder and single crystals were sandwiched. A graphite die was used and first 1.5 g of yttria-doped alumina powder was placed in the die. Next the (0001) orientation of the sapphire single crystal was placed, polished side upward following another 4 g of yttria-doped alumina powder. The $(11\bar{2}0)$ orientation of the sapphire single crystal was then placed on top of the 4 g of powder with the polished side downward and covered with another 1.5 g of powder. The ram was then inserted and the samples were spark plasma sintered (Thermal Technologies, LLC, Santa Clara, CA) using a ramp of 100 °C per minute to 800 °C for 45 minutes at 10 MPa followed by another ramp cycle of 100 °C per minute up to 1300 °C for 30 minutes at 50 MPa.[80]

Eu doped spinel samples were prepared at Lehigh university by collaborators. The general procedure is summarized here: Dense polycrystalline Eu-doped (500 wt-ppm) spinel samples were fabricated by spark-plasma sintering at 1200 °C for one hour with 40 MPa applied pressure. A cylindrical sample of ~20 mm diameter with near theoretical density was obtained, and smaller pieces (~5 $mm^3$) were sectioned and cleaned thoroughly to remove any contamination.

$SrTiO_3$ samples were prepared by Wolfgang Rheinheimer at the Karlsruhe Institut für Technologie (KIT) by first mixing $SrCO_3$ (99.95% purity) and $TiO_2$ (99.995% purity) (Sigma Aldrich Chemie GmbH, Taufkirchen, Germany) to achieve a molar ratio (Sr/Ti) of 0.996. Details on synthesis are published elsewhere.[25] To achieve high density, the green bodies were pre-sintered at 1425 °C for one hour in oxygen at 20 °C/min up.[41] Density, measured by Archimedes method, was reported as > 99% of the theoretical

density.[43] The samples were then annealed in oxygen, without cooling from the sintering step at 1425 °C, at 20 °C/min up to achieve grain growth at temperatures ranging from 1350 °C to 1550 °C as indicated in **Table 9** and subsequently air quenched.

### 4.1.2 Polishing

Each of the yttria doped alumina samples were sectioned with a 12.7 mm diamond blade (IsoMet™ Diamond Wafering Blade, Buehler) mounted on a saw (IsoMet™ Low Speed Saw, Buehler). These sectioned pieces were mounted in a cold-curing resin of 2:1 powder:liquid (813-054 (powder), 813-055 (liquid), Lecoset 7007), and polished in the procedure listed in Table 4 below. These samples were removed from the resin by soaking the entire mold in a submersion of acetone and then placed in an ultrasonic bath (Solid State Ultrasonic FS-9, Fisher Scientific). Once the samples were extracted from the mold, they were soaked in acetone, ethanol and DI water in 30-minute increments in the ultrasonic bath. In addition, each step was dried with compressed air.

**Table 4.** Polishing procedure for alumina ceramics (Buehler) (>> indicates same rotation direction of cloth and sample; >< indicates opposite rotation direction of cloth and sample)

| Cloth | Solution | Load (lbs) | Speed | Rotation | Time (mins) |
|---|---|---|---|---|---|
| Ultraprep 45 μm diamond | Water | 8 | 240-300 | >> | Until planar |
| ApexHerculese H | 9 μm MetaDi Supreme Polycrystalline diamond | 6 | 150-200 | >< | 5 |
| Verdutex | 3 μm MetaDi Supreme Polycrystalline Diamond | 6 | 120-180 | >> | 5 |
| Verdutex | 1 μm MetaDi Supreme Polycrystalline Diamond | 6 | 100-150 | >< | 5 |
| Microfloc | 0.05 μm MetaDi Supreme Polycrystalline Diamond | 6 | 100-120 | >> | 3 |

The Eu doped spinel and $SrTiO_3$ samples were prepared and polished by collaborators at Lehigh University and KIT, respectively. The $SrTiO_3$ samples were cut to ~1 mm in thickness and polished on one side in the procedure listed in **Table 5** below.

**Table 5.** Polishing procedure for $SrTiO_3$ ceramics from KIT collaborators.

| Cloth | Solution | Load (lbs) | Speed (head) | Speed (disc) | Rotation | Time (mins) |
|---|---|---|---|---|---|---|
| 30 µm Diamond disc (polymer-bonded) | Water | 6 (depending on sample area) | 150-200 | 300 | >> | Until planar |
| 10 µm Diamond disc (polymer-bonded) | Water | 6 (depending on sample area) | 150-200 | 300 | >> | 10-15 mins |
| Zeta or Texmet (Buehler) | 9 µm or 6 µm Polycrystalline Diamond (Buehler) | 6 (depending on sample area) | 150-200 | 300 | >> | 10 mins |
| Zeta or Texmet (Buehler) | 3 µm Polycrystalline Diamond (Buehler) | 6 (depending on sample area) | 150-200 | 300 | >> | 15 mins |
| Zeta (Buehler) | 1 µm Polycrystalline Diamond (Buehler) | 6 (depending on sample area) | 150-200 | 300 | >> | 20 mins |
| Zeta (Buehler) | 0.25 µm Polycrystalline Diamond (Buehler) | 6 (depending on sample area) | 150-200 | 300 | >> | 20 mins |

### 4.1.3 Thermal grooving

Each of the yttria doped alumina samples were thermally grooved in an open-air box furnace (Lindberg Blue M, Thermo Scientific Ashville, NC) in 98% pure alumina crucibles (CoorsTek Inc., Golden, CO) at 10 °C/min up to temperatures ranging from 1350 °C to 1650 °C and cooled back to room temperature at 20 °C/min. Each of the 500 ppm and 100 ppm yttria doped alumina samples were thermally grooved for 3 hours or 5 hours, respectively and the undoped samples were grooved for 3 hours each. The decreasing temperature increments, on the other hand, were mounted on a steel die with

Crystalbond™ and were hand polished from 9 μm to 0.05 μm finish, merely to accelerate the polishing, grooving and AFM process. Please note that the 45 μm step was left out in the decreasing temperature increments because the 45 μm surface is not uniform and thus difficult to polish evenly by hand.

The cut and polished $SrTiO_3$ samples were grooved at various grooving times to achieve groove widths greater than 0.5 μm and air quenched. The conditions are specified in Table 9. All of the heat treatments were performed in a furnace that had fast heating and cooling in an oxygen environment, ~20 °C/min.

### 4.1.4 AFM

To measure the topography of each surface, atomic force microscopy was used in contact mode at a set point 2, varying gain depending on sample, 10 nm step size at a 1 Hz scan frequency. All of the measurements were taken with a Solver NEXT AFM (NT-MDT, Moscow, Russia) and with silicon nitride tips (Pyrex Nitride Probes triangular shape, NanoWorld) on the smaller of the two cantilevers provided for each probe. Each image was taken at random locations around the surface to diminish any preferential analysis of specific chemical variations or abnormal grain growth areas.

### 4.1.5 Calculation of relative grain boundary energy from thermal grooves

Post processing of the AFM images was executed in Gwyddion[149] software. The tools of "leveling data by mean plane subtraction" and "correcting lines by matching height median match line correction" (to eliminate AFM artifacts) were utilized on each AFM image before the groove profiles were extracted. At each grain boundary, three representative line profiles were extracted which can be seen in **Figure 9**. The width and depth of each thermal groove was measured and further, the relative grain boundary energy ($\gamma_{GB}$) to surface energy ($\gamma_S$) ratio of each boundary was calculated (Equation 6 , Equation 7, Equation 8), according to a combination of Mullins' analysis of thermal grooves[150], assumptions from Saylor[107] and Dillon[63] as well as a groove shape correction factor from Robertson.[151] A combination of these assumptions and corrections for groove shape and AFM tip convolution is depicted in Equation 8 and further explanation of this derivation can be found in Sections 4.1.6 and 4.1.7. All of the calculations were performed in an in-house Matlab program. Due to the anisotropy of the system, the

thermal grooves are not symmetric, and therefore, measurements at either side of the groove were taken to calculate the relative grain boundary energy. **Figure 9** (a) shows a representative AFM image and **Figure 9** (b) shows a corresponding groove with the labeled parameters on one half of the groove where *w* represents width on one half of the groove, $d$ is depth on one half of the groove, $\frac{\psi}{2}$ is the half dihedral angle of the surface and $\beta$ is the groove angle.

*Ratio of grain boundary energy to free surface energy of the grains:*

Equation 6

$$\frac{\gamma_{GB}}{\gamma_S} = 2\cos\left(\frac{\psi}{2}\right) = 2\sin\beta$$

*Grain boundary groove angle (m is a constant value for groove shape see section 4.1.6):*

Equation 7

$$\beta_1 = \tan^{-1}\left(\frac{d}{2w}\right)$$

*Half angle derivation with corrections:*

Equation 8

$$\frac{\gamma_{GB}}{\gamma_S} = 2\sin\left(\beta_{gs} + \beta_{tc}\right)$$

The number of boundaries measured for each sample (concentration and temperature) is listed in **Table 8** for the yttria doped alumina samples and in **Table 11** for the $SrTiO_3$ samples. **Figure 21** depicts the cumulative distribution function for the yttria doped alumina at 1550 °C. Each point on the cumulative distribution function signifies the average of three profiles over a single grain boundary. Because two measurements were made for each groove, due to the asymmetric nature discussed above, twice as many points as grain boundaries measured are plotted on each CDF plot.

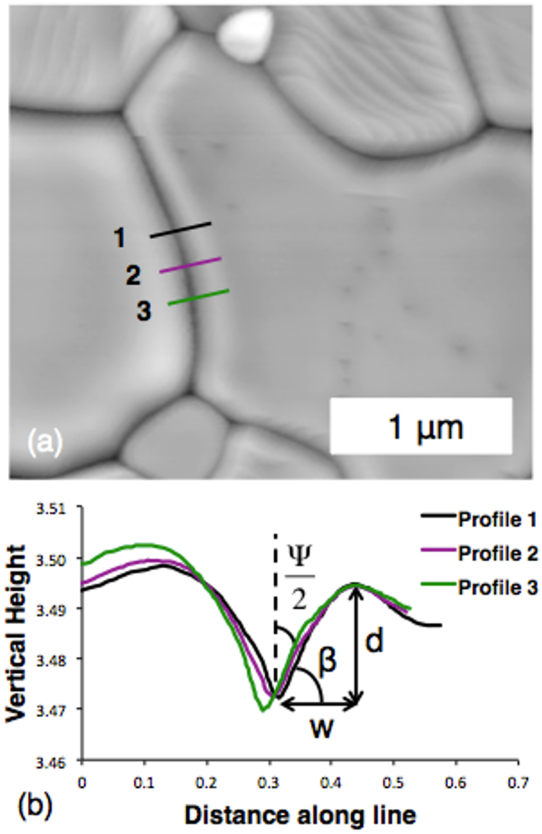


**Figure 9.** (a) Typical AFM image of a thermally grooved alumina surface. The lines indicate the positions from which the topographic traces in **Figure 9** (b) were extracted. (b) Three groove profiles from which W and d are measured. Reproduced in section 6.2.

### 4.1.6 Small Slope Approximation Correction

In Mullins initial calculation of the shape of a thermal groove due to surface diffusion he had determined a constant value of m = 4.73 that related the depth and width of the groove by small slope approximation. In this initial paper he had indicated that by private communication with Hillert they had predicted this value but didn't expand the calculation for other groove shapes. Later, Robertson[151] expanded these numerical parameters that characterize the groove shape and can be seen in Figure 10. In order to find the correct constant value of m for each type of thermal groove shape, first the value of m is determined from the depth and width of the groove (Equation 9). In Figure 10 the corresponding values to m in the curves of $d/m(Bt)^{1/4}$ and $w/(Bt)^{1/4}$ were extracted and, from this ratio, the correct value of m for the groove shape, denoted $m_{gs}$ (Equation 10),

was used as the new constant to determine beta with respect to groove shape, $\beta_{gs}$, seen in Equation 11.

Equation 9

$m = \tan(\beta_1)$ where $\beta_1 = \tan^{-1}\left(\frac{d}{2w}\right)$

Equation 10

$\mathrm{m}_{gs}\, from\, ratio\ \frac{\mathrm{w}/(\mathrm{Bt})^{1/4}}{\mathrm{d}/\mathrm{m}_{gs}(\mathrm{Bt})^{1/4}}$

Equation 11

$\beta_{gs} = \tan^{-1}\left(m_{gs}\frac{d_1}{2w_1}\right)$

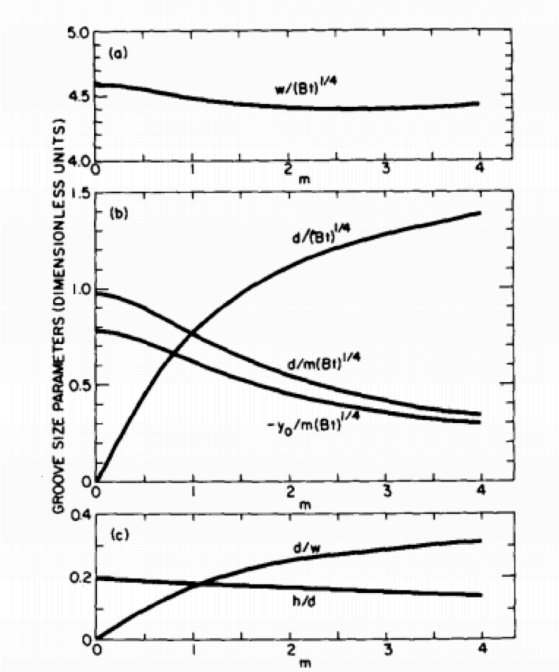


**Figure 10.** Groove shape parameters in dimensionless units. $\mathrm{w}/(\mathrm{Bt})^{1/4}$ and $\mathrm{d}/\mathrm{m}(\mathrm{Bt})^{1/4}$ used for calculations. Reproduced from reference. [151]

### 4.1.7 Groove width correction

Analyzing the groove width of the grain boundaries in each of the temperature segments we found that grooves formed at lower temperatures were frequently narrower than grooves formed at higher temperatures. Saylor and Rohrer[107] showed that small groove widths introduce a large measurement error because it is difficult for the tip to detect the actual depth of narrower grooves. As the groove width increases, the measured and actual values for groove angle converge. Therefore, to correct for an underestimation

of groove angle, Figure 11 was utilized. This figure plots the groove angle, β, with respect to groove width (μm). For values of 17.33° ≤ β < 24.81° I used the β = 20° correction line, from 24.81° ≤ β < 32.74° I used the β = 30° correction line, from 32.74° ≤ β < 40.11° I used the β = 40° correction line, and finally from 40.11 ≤ β < 48.22° I used the β = 50° correction line. For each thermal groove the correction for the AFM tip, $\beta_{tc}$, is then the distance away the value of beta is from the respective beta curve. The original equation to compute relative grain boundary energy, Equation 6, was then adjusted for the tip correction, $\beta_{tc}$ (β tip correction), which can be seen in Equation 12.

Equation 12

$$\frac{\gamma_{GB}}{\gamma_S} = 2\sin\left(\beta_{gs} + \beta_{tc}\right)$$

In addition, all grooves whose total width is less than 250 nm were not considered. The range of groove widths, based off of surface diffusion coefficient, were previously shown to be most reliable above 250 nm and these coefficients were reviewed in Saylor and Rohrer[107]. Variations of the coefficient reported were attributed to anisotropy in the surface energy and surface diffusivity for particular boundaries. The limit of 250 nm used in reference, and in this thesis, limits the extent of lower temperature data. Reduced diffusivity at lower temperature means it would take much long to make wider grooves. Therefore, data at lower temperatures, e.g. < 1450 °C for 100 ppm yttria doped alumina, could not be considered due to a majority of boundaries with narrow groove widths.

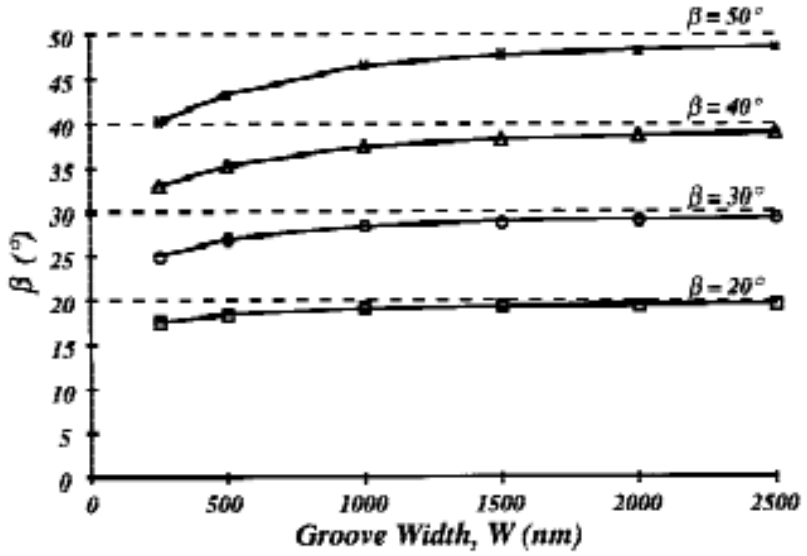


**Figure 11.** Comparison of measured values of groove angle, β, (solid lines) to actual values for the thermal groove model (dashed lines) at varying groove widths. Reproduced from reference. [107]

## 4.2 2D EBSD data collection and reconstructed boundary segment extraction

EBSD data collected for $SrTiO_3$ annealed at 1550 °C was collected using the Quanta 200 FEI microscope. The Eu doped spinel data was collected by collaborators at Lehigh University. For more details see section 5.2. In general, during data collection it was ensured that the step size was approximately 1/10 of the smallest grain boundary diameter. For EBSD data acquisition, binning was 4x4 with a varying number of frames per second depending on the contrast of the sample before acquisition began. To calculate GBPD for both Eu doped spinel (section 5.3) and $SrTiO_3$ (section 8.3) the reconstructed boundary segments were extracted using TSL software. First, before extraction, the 2D EBSD data collected were cleaned in the procedure of grain dilation, single average orientation per grain and grain CI standardization. The GBPD plots were created with Rohrer's plot_gbcd codes.

## 4.3 Serial Sectioning by PFIB – 3D EBSD data collection

EBSD data collected from serial sectioning were collected using FEI's Helios™ PFIB Dual-Beam. The FEI AutoSlice and View (EBS3 G3) software was used to control the milling and Oxford's Aztec acquisition system to collect the EBSD patterns. In this

method a fiducial mark is is milled on the front of the sample, just below the region of interest, to be used to find the region of interest when rotating the sample from the EBSD pattern collection position to the mill position, **Figure 48**. After a single EBSD map is acquired the sample is rotated so that the top face is parallel to the ion beam and a specified thickness is removed from the sample. A "rocking mill" effect was used for removal of material. With this feature the sample is milled +/- 5° about a rocking axis where the sample is fixed in one of the two positions during milling. This process is repeated until the required volume is collected, determined either by the number of distinguishable grain boundaries to compute the 5-parameter GBCD (section 3.3.3) or enough volume to compute internal dihedral angles, section 8.2.5. In addition this data is used to compute grain boundary energy distributions (GBED) described in 8.2.4. The volumes used to computed GBCD were cleaned, meshed, and reconstructed using DREAM.3D[152] and distributions computed using GBToolbox[153]. The maps for internal dihedral angles were cleaned and grain boundary segments were reconstructed using TSL OIM software for each EBSD map and then computed in in-house programs, section 8.2.5. The EBSD maps for GBED were individually cleaned and grain boundary segments were reconstructed and then computed using Rohrer_3Dprograms.[154] More details of the data collected for particular samples in this thesis can be found in chapter 7.

# 5 Population of Grain boundary planes in Europium doped Spinel – related to complexion TTT

O. Schumacher, C.J. Marvel, M.N. Kelly, P.R. Cantwell, R.P. Vinci, J.M. Rickman, G.S. Rohrer, and M.P. Harmer, "Complexion Time-Temperature Transformation (TTT) Diagrams: Opportunities and Challenges," *Curr. Opin. Solid State Mater. Sci.*, 1–8 (2016).

*Sections relevant to this thesis are taken from the paper and supporting explanation is added to the text.*

## 5.1 Introduction

Time-temperature-transformation (TTT) diagrams were first created by Davenport and Bain in 1930 to understand kinetics related to bulk phases.[155] The diagrams were so pivotal because they offered a simplistic way of understanding the complexities of kinetics associated with the processing and heat treatment of many alloys. Interfaces have also been shown to exhibit phase like behavior. In fact, this idea is not as new as one might think. It was first suggested by Hart in the 1960's-70's that grain boundaries may undergo phase transformations in a similar way that bulk phase transformations occur.[133] The transition of grain boundaries from one equilibrium state to another as a function of thermodynamic variables was finally characterized in 2006 and the term 'complexion' was coined.[2] The first detailed study of the kinetics of complexion transitions in polycrystalline $Y_2O_3$ and $Al_2O_3$ was reported in 2016.[135] Complexion TTT diagrams can be used to understand the time dependence of these transitions.

Similar to bulk phase TTT diagrams, complexion TTT diagrams can be used to engineer materials by optimizing heat treatments. This is especially useful for materials which exhibit abnormal grain growth where the nucleation and propagation of abnormal grains are not fully understood. Eu doped spinel is used here as a proof of concept because the microstructures can vary from nanocrystalline to (theoretically) single crystal and it also has the ability to have unimodal or bimodal microstructures. The ability to produce a variety of microstructures from the same starting material could be valuable technologically. For instance, each microstructure class provides useful properties: single crystal sapphire can be used for high strength armor windows [156] or substrates for LED applications [157], a bimodal microstructure in many materials can enhance toughness as

compared to a microstructure with a unimodal grain size distribution [158], and ultra-fine grain alumina can have higher strength and ductility as compared to coarse-grained alumina [159].

Although the work done in this thesis is not focused on the development of TTT diagrams, collaborative research was carried out to determine if a change in the grain boundary plane distribution – an indicator of a complexion transition – occurred at when abnormal grain growth occurred in Eu-doped spinel. Here we will highlight the determination of the grain boundary character distribution and also present the TTT diagram that resulted from the collaborative project.

## 5.2 Experimental Procedure

Samples were prepared at Lehigh University by collaborators. A summary of the experimental procedure performed by them is reproduced here: Dense polycrystalline Eu-doped (500 wt-ppm) spinel samples were fabricated by spark-plasma sintering at 1200 °C for one hour with 40 MPa applied pressure. A cylindrical sample of ~ 20 mm diameter with near theoretical density was obtained, and smaller pieces (~5 $mm^3$) were sectioned and cleaned thoroughly to remove any contamination. The samples for GBPD analysis were annealed at 1400 °C and 1600 °C f for 8 hours in a 5 % hydrogen balanced nitrogen reducing atmosphere. Following annealing, all samples were polished utilizing various diamond suspensions and cleaned thoroughly to remove residual materials from polishing. Electron backscattered diffraction (EBSD) was used to monitor the microstructure evolution of the doped spinel as a function of time and temperature. An EDAX Hikari EBSD camera that was attached to a Hitachi 4300N scanning electron microscope (SEM) was used to record the orientation maps of the microstructures by Lehigh collaborators. Cleanup, grain boundary reconstruction and GBPD calculations were performed by the author. TSL software was used for cleanup and boundary reconstruction. Grain dilation, with a grain tolerance angle of 5° and a minimum grain size of 2 pixels was used, followed by assigning a single average misorientation per grain and grain confidence index standardization. Some pseudosymmetry was present in the sample that was prepared at 1400 °C and was cleaned by removing grains with low confidence index by creating a new IPF map with a partition of 0.4 confidence index (remove all grains with confidence index less than 0.4) before exporting reconstructed

boundaries. The pseudosymmetry present in these samples showed a slight peak in the disorientation distribution at 45° which was reduced after partitioning. There was no measurable difference in the GBPD before and after pseudosymmetry cleanup. 21,000 grain boundaries were analyzed for the sample prepared at 1600 °C and 6,000 grain boundaries were analyzed for the sample prepared 1400 °C. The relative areas of different grain-boundary planes in the crystal reference frame were calculated stereologically using the conventional binning technique (with bin size of 10° for both samples [160]).

## 5.3 Results

A typical EBSD map of the bimodal microstructure and grain-size histogram are presented in **Figure 12**. At least 1000 grains in the sample annealed for 4 h at 1600 °C were measured from several EBSD maps to produce the grain size histogram. As seen in the histogram, the maximum occurs for grains that were less than 3 μm in diameter. More than half of the grains fall into this category. At the relatively low magnification of **Figure 12** (a), the small granular regions are noisy because of the choice of the EBSD step size. This data shows that this microstructure is bimodal.

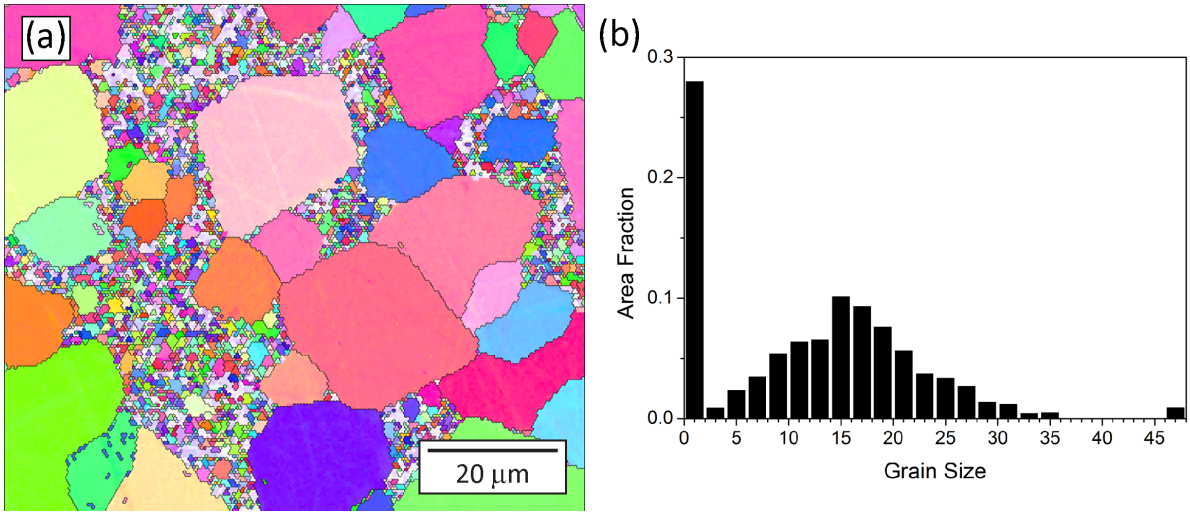


**Figure 12**: (a) A representative EBSD map, and (b) grain size histogram of bimodal Eu-doped spinel. Reproduced from reference.[73]

In **Figure 13** (a), a representative IPF map of Eu doped spinel annealed at 1400 °C is shown. This microstructure exhibits normal grain growth with a nearly isotropic grain-

boundary plane distribution. **Figure 13** (b) shows and IPF map of Eu doped spinel annealed at 1600 °C. The microstructure exhibits abnormal grain growth. Each of the images below the IPF maps in **Figure 13** (a) and (b) are GBPDs for the corresponding anneal temperature. The population of grain boundary planes for the sample annealed at 1600 °C shows that there is a significant preference for {111} grain boundary planes with a maxima of 1.7 MRD and a minima of 0.7 MRD at {001}. The GBPD of the sample annealed at 1400 °C is relatively isotropic. Changes in the grain-boundary plane distribution have previously been linked to complexion transitions and that is assumed to be the case here[77, 161].

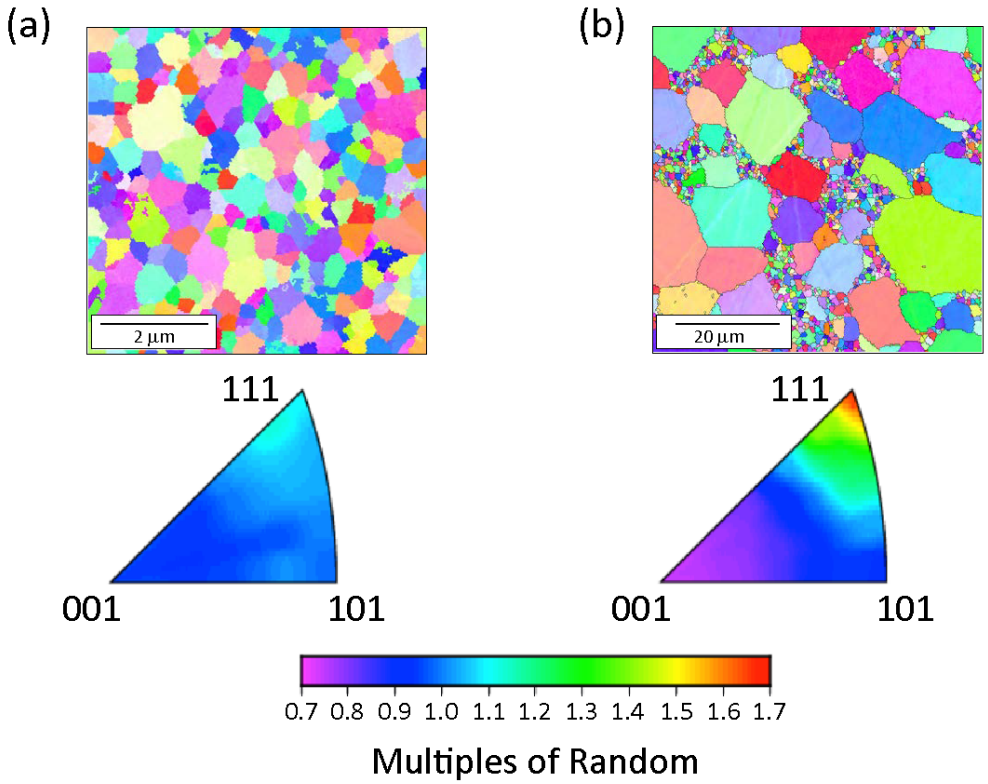


**Figure 13**: EBSD micrographs (top) and the distributions of grain-boundary planes in the crystal reference frame (bottom) of polycrystalline Eu-doped spinel annealed at temperatures of (a) 1400 °C and (b) 1600 °C. The specimen annealed at 1400 °C has a unimodal grain size distribution while the specimen annealed at 1600 °C has a bimodal grain size distribution, indicating that a grain-boundary complexion transition has occurred.

In Figure 14 the grain boundary complexion TTT diagram for Eu doped spinel is presented (this was created by our collaborators at Lehigh). Here the complexion transformation is represented as a function of temperature and time; the symbols used for each datum correspond to a fixed transformation. The diagram has three distinct time-temperature regimes:

Regime I: Grains are < 3 μm in diameter. This microstructure is represented by black squares.
Regime II: Bimodal microstructure represented by red circles.
Regime III: Grains are >> 3 μm in diameter. This microstructure is represented by blue triangles.

Regimes I and III are characterized by a unimodal grain size microstructure, with the main observable microstructure difference being the average grain size. At a given temperature in the complexion TTT diagram in Figure 14, the dashed red line (1 % line) between regime I and regime II represents the time after which grain boundary complexion transition started, while the dashed blue line (99 %) line separating regimes II and III represents the time at which nearly all grain boundaries have transitioned. The curves separating the three regimes were manually drawn to illustrate the combinations of time and temperature that separate these regimes.

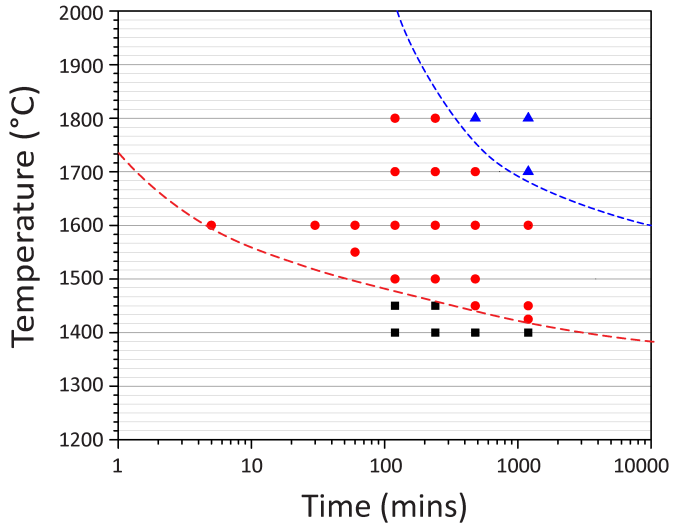


**Figure 14**. Grain boundary complexion TTT diagram of Eu doped spinel. Black squares represent microstructures with grains < 3 μm in diameter, red circles represent bimodal microstructures and blue triangles represent microstructures with grains > 3 μm in diameter.

## 5.4 Discussion

The bimodality of this microstructure, as with every other bimodal microstructure considered here, is hypothesized to be an indication that a complexion transition has occurred. The premise is that during the anneal, complexion transitions occurred along some grain boundaries and thereby enhanced the mobility of those boundaries. Thus, the grains with a sufficient number of high mobility boundaries grew at a faster rate than the rest of the matrix. Given this hypothesis, and assuming complexion transitions are first-order in nature, increasing the annealing time or temperature will increase the number of abnormally large grains at the cost of the smaller grains.

Eu-doped spinel was selected for this work because it exhibits a strong propensity for abnormal grain growth that is attributed to a grain-boundary complexion transition associated with Eu boundary segregation, and because it was observed to possess significant anisotropy in grain-boundary character. In this system, the onset of abnormal grain growth and changes in grain boundary anisotropy were identified for a range of annealing temperatures. The appearance of an abnormally large grain in the microstructure was taken as a signature of a complexion transition, indicating that the grain boundary surrounding the abnormally large grain had undergone a change in structure and chemistry that resulted in a dramatic increase in grain-boundary mobility. This interpretation of abnormal grain growth has been supported by many previous experimental studies, e.g. [74,76,162].

Using the results from many samples heated at different temperatures, the complexion TTT diagram in Figure 14 was determined by our collaborators at Lehigh. TTT complexion diagrams have also been created for 10 wt% Yb 1 wt% / Er doped $Y_2O_3$, 10 wt% Yb 4 wt% / Er doped $Y_2O_3$, undoped $Y_2O_3$ and 500 ppm Y doped $Al_2O_3$.[121] In each of these instances, the Johnson-Mehl-Avrami equation was used to extrapolate experimental data to create complexion TTT diagrams which represents overall complexion transformation kinetics of each system.[73, 135, 163] Determining when a complexion transition occurs is essential for development of these diagrams. These diagrams suggest that complexion transitions occur by a nucleation and growth method because there are regions of metastability where some boundaries transform and then spread throughout the microstructure.[135] Bojarski et al, showed that complexion

transitions occurred along the highest energy boundaries first suggesting an activation energy barrier for such a transition and showing that there are regions of metastability.[80] Although there is no experimental evidence that grain boundary complexions form by a nucleation and growth process, surface complexions have been shown experimentally to exhibit this mechanism.[164] To nucleate a transition, it is speculated that either an energy barrier must be overcome to get to its stable equilibrium or that the grain boundaries reach a critical temperature to begin a transition. Therefore, it is important to understand the energies associated with a transition.

Changes in grain boundary energy, measured by thermal grooves, have been linked to the onset of abnormal grain growth at a complexion transitions. [1] Complexion TTT diagrams give information about the kinetic behavior of these transitions but thermodynamic aspects as well as driving forces for grain growth are also factors that influence this behavior and need to be understood. Grain boundaries move at elevated temperatures because diffusion is a thermally activated process which typically follows an Arrhenius relationship. As temperature is increased, the average grain size increases, to reduce the excess grain boundary energy.

Complexion TTT diagrams are useful tools to understand the kinetic behavior of complexion transitions. However, it is a brute force way of understanding the grain boundary behavior of each materials system with each processing parameters. This thesis will highlight some experimental methods of tracking complexion transitions by measuring the grain boundary energy, which will give further insight onto the behavior of complexion transitions. Changes in the grain boundary energy with respect to increased temperature and changes in the grain boundary character distribution will be studied together because the quantities are coupled. Mobility is still another factor which needs to be measured experimentally but is not within the scope of this thesis. With the knowledge of experimental measurements of driving forces for abnormal grain growth, such as grain boundary energy, time dependent kinetic effects and thermodynamic effects will allow us to create more accurate grain boundary models in the future.

## 5.5 Conclusion

Until recently, complexion transition kinetics have been largely overlooked by the materials community, despite their strong influence on the behavior of bulk polycrystalline materials. Results from EBSD analysis and GBPD show that at 1400 °C the distribution of grain boundary planes is relatively random and at 1600 °C the population of {111} increases to 1.7 MRD. Grain boundary population has been found to be inversely correlated with grain boundary energy.[75, 81, 104, 165, 166] Therefore, this suggests that a complexion transition occurred as the grain boundary energy was reduced. This also led to abnormal grain growth. This work on Eu doped spinel also demonstrated that complexion TTT diagrams can be created which describe complexion transition time and temperature dependent kinetics. The field of complexion TTT diagrams is just beginning, and the compilation of many more complexion TTT diagrams for various materials systems will be required before the full potential of these diagrams can be realized. The complexion TTT diagram shows that complexion transitions do not occur at one particular temperature and time and the driving forces that cause these transitions need to be better understood. In the following sections, the grain boundary energies of two systems (yttria doped alumina and strontium titanate) are measured where drastic changes in grain growth are observed. In yttria doped alumina the grain boundary energies are measured before, during and after a temperature where a complexion transition was observed. The grain boundary energies were also measured in strontium titanate over a temperature region where non-Arrhenius grain growth behavior is observed. By measuring grain boundary energies throughout a transition region over which grain growth kinetics vastly change instead of at one particular temperature we can begin to understand the magnitude of the factors that influence these transitions. We also suggest that it is imperative to gather more evidence of grain boundary energies in other materials systems to aid the development of three dimensional grain growth models, which often assume energy is constant.

# 6 Temperature Dependence of Relative Grain Boundary Energy in Yttria Doped Alumina

M.N. Kelly, S.A. Bojarski, and G.S. Rohrer, "The Temperature Dependence of the Relative Grain-Boundary Energy of Yttria-doped Alumina," *J. Am. Ceram. Soc.*, **100** [2] 783–791 (2017).

Division of labor between Madeleine N. Kelly and Stephanie A. Bojarski is listed in **Table 6**.

**Table 6**. Lab work performed by Madeleine N. Kelly for acquisition of data.

| | **AFM** | **Gwyddion (line segments)** |
|---|---|---|
| ***100 ppm (T+)*** | 1350**, 1400**, 1450**, 1500**, 1525, 1650 | 1350, 1400, 1450, 1525 |
| ***100 ppm (T-)*** | 1350, 1400, 1500*, 1550* | 1400, 1500 |
| ***500 ppm (T+)*** | 1400*, 1550, 1600 | 1550, 1600, 1650 |
| ***99.995 % pure (T+)*** | 1400, 1550*, 1650* | - |

** denotes worked on together (sat together in same AFM session)
* denotes AFM sessions of the same temperature / concentration sample were split up

## 6.1 Introduction

In most models for microstructure evolution, the grain boundary energy is taken to be a constant. However, it is known from both experiments[167] and simulations [168,169] that the grain boundary energy can change with temperature and these changes have the potential to affect microstructure evolution. For example, changes in the grain boundary energy with temperature have been implicated in anti-thermal grain growth phenomena in $SrTiO_3$.[40, 41] Abrupt changes in the grain boundary energy have also been linked to complexion transitions and abnormal grain growth.[162, 1] However, there is very little available data on the temperature dependence of the grain boundary energy. The only previous study we are aware of, interpreted from grain boundary diffusion measurements made 35 years ago, indicates that the grain boundary energy of NiO increases by 14 % when the temperature is increased by 600 °C.[167, 170] Here, we experimentally examine the temperature dependence of the grain boundary energy in 99.995 % pure and Y-doped alumina.

The grain boundary excess free energy varies with temperature and there are several factors that influence the variation. First, the free energy is expected to decrease with increasing temperature because of the entropic contribution. This has been observed in a

number of pure materials.[167, 171, 172] In materials containing segregating impurities, the grain boundary energy will be affected by changes in the grain boundary composition. In most cases, the grain boundary energy decreases with increases in the grain boundary excess solute content. Because bulk solubility typically increases with temperature, solute from the intergranular regions can dissolve in the bulk as the temperature is increased, reducing the grain boundary excess (desegregation). This will lead to an increase in the grain boundary free energy with temperature. Desegregation influences the grain boundary energy in a way opposite to entropy; past studies have shown that changes from desegregation are usually more significant than those associated with entropy, so for impure materials, the grain boundary energy usually increases with temperature.[167]

Entropy and desegregation both lead to continuous changes in the grain boundary energy. One can imagine that if grain boundaries are supersaturated in solute and a second phase precipitates, the formation of a second phase would abruptly reduce the grain boundary excess and increase the energy. In polycrystals where the solvent phase has already saturated the grain boundaries, any grain growth will lead to a reduction in the intergranular area, which could supersaturate the boundaries prior to the formation of a second phase. While boundary supersaturation followed by precipitation has been reported,[173] measurements of the grain boundary energy during this series of transitions has not been reported.

An abrupt transition in grain boundary energy might also occur if there is a transition in the structure and/or chemical composition of the grain boundary; this is referred to as a complexion transition.[74] The energy changes associated with transitions have been evaluated using measurements of the grain boundary thermal groove geometry.[1, 80, 161] In this experiment, a microstructure is produced in which two grain boundary complexions are expected to co-exist, based on the presence of a bimodal grain size distribution. When the relative energies of the grain boundaries surrounding the very large grains are compared to those around the smallest grains, there is usually a significant difference. For example, in 100 ppm Y-doped alumina at 1400 °C, the energies of the boundaries around large grains were 46 % lower than around the small grains.[1]

The experiments comparing the relative energies of the different types of grain boundaries are interpreted with respect to the schematic in **Figure 15**. At low temperatures, all of the grain boundaries have a single stable complexion and a unimodal microstructure (**Figure 15**(b)). As temperature increases, one grain boundary complexion might become more stable than another. If all of the boundaries transformed immediately to the lower energy complexion, then the rate of change of the grain boundary energy with temperature will decrease at the temperature where the lines intersect, and the microstructure will remain unimodal. However, it is also possible that there is an activation barrier and the system must be superheated before the least stable boundaries transform. If so, the energy will follow the blue dashed line until the least stable boundaries transform to the lower energy complexion at the position of the vertical blue dashed line. If the high temperature, low energy complexion has a mobility advantage over the non-transformed boundaries, a microstructure with a bimodal grain size distribution will form (**Figure 15**(c)). The energy difference ($\Delta\gamma$) between the transformed grain boundaries around the large grains and the metastable boundaries around the small grains is labeled in **Figure 15**(a).

The previous experiments evaluated the energy difference between the stable and metastable boundaries at a single temperature, but they do not tell us how the grain boundary energy changes with temperature or determine the transition temperature. Therefore, the purpose of this paper is measure the temperature dependence of the relative grain boundary energy in 99.995% pure, 100 ppm Y-doped, and 500 ppm Y-doped alumina. The relative grain boundary energy is determined from AFM measurements of grain boundary thermal grooves. The measurements are made as a function of increasing temperature for all three materials. Measurements were also made with decreasing temperature for the 100 ppm Y-doped alumina sample. The measurements show that the changes in the grain boundary energy as a function of temperature are influenced by solute partitioning between the bulk and grain boundary phase, and by complexion transitions.

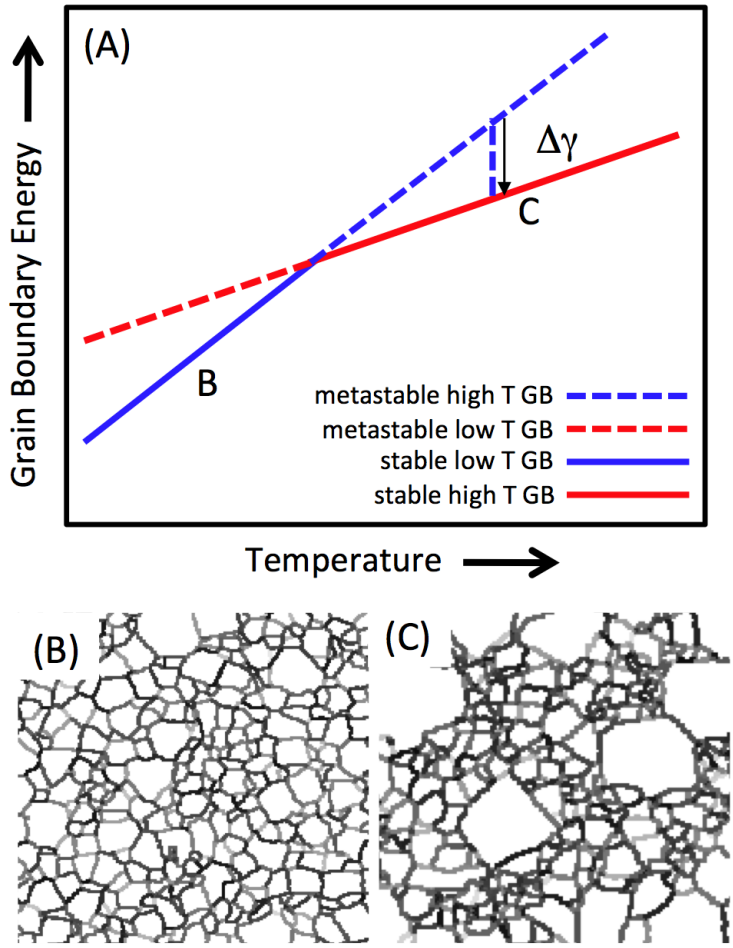


**Figure 15**. Schematic illustration of grain boundary energies (a) and microstructure (b-c) in a material with two stable grain boundary complexions that have very different grain boundary mobilities. See text for explanation.

## 6.2 Experimental Procedure

Pure alumina ceramics were prepared from 99.995 % pure alumina (Puratronic, Alfa Aesar, Ward Hill, MA). The most concentrated impurities in the starting material were Na (10 ppm), Zr (9 ppm), Ca (4 ppm), Mg (3 ppm), and Fe (2 ppm). These concentrations, supplied by the manufacturer, are in weight fractions and were determined by inductively coupled plasma emission spectroscopy. 100 ppm and 500 ppm Y-doped alumina (concentrations are Y per Al atoms) were prepared from the same alumina source, with appropriate amounts of added $Y(NO_3)_3 \cdot 6H_2O$ (Alfa Aesar, Ward Hill, MA). A micropipette was used to transfer appropriate amounts of Y (100 ppm or 500 ppm) from a 0.05 M solution of $Y(NO_3)_3 \bullet 6H_2O$ and methanol to the 99.995% pure alumina, also suspended in methanol. This solution was mixed using a PTFE magnetic

stir bar on a stirring hot plate. After evaporating the methanol from the suspension under a fume hood, the powders were dried at 100 °C in air. After drying, the doped powders were placed in plastic bags and milled with a marble rolling pin to break up agglomerates. Consolidation of the powders was carried out by spark plasma sintering. About 10 g of powder were loaded in a graphite die. The ram was then inserted and the samples were spark plasma sintered (Thermal Technologies, LLC, Santa Clara, CA) using a ramp of 100 °C per minute to 800 °C for 45 minutes at 10 MPa followed by another ramp cycle of 100 °C per minute up to 1300 °C for 30 minutes at 50 MPa. The sample was then cooled to room temperature at a maximum rate of 150 °C / min. The Archimedes method was used to measure the densities of the samples and they were found to be 96.7 %, (99.995 % pure), 98.5 % (100 ppm Y), and 95.7 % (500 ppm doped Y). Note that throughout this paper, we will refer to these samples as the 100 ppm and 500 ppm samples, based on the synthesis conditions. The actual compositions after sintering were not determined.

Each of the samples was sectioned with a 12.7 mm diamond wafering blade mounted on a low speed saw. These sectioned pieces were mounted in a cold-curing resin and polished with polycrystalline diamond, using a 0.05 micron polycrystalline diamond solution as the final step. After removing the samples from the mount, thermal grooving was carried out in a box furnace in air. The samples were placed in 98 % pure alumina crucibles and heated at 10 °C/min up to temperatures ranging from 1350 °C to 1650 °C and cooled back to room temperature at 20 °C/min. The 500 ppm and 100 ppm Y-doped alumina samples were thermally grooved for 3 hours and 5 hours, respectively, for the experiments with increasing temperature. The 99.995 % pure samples were grooved for 3 hours. For the experiments where the grooves were measured with decreasing temperature, the samples were re-polished, to remove the grooves formed at high temperature, before grooving at the lower temperature. The average grain diameters of the samples after the lowest and highest temperature annealing were measured by the linear intercept method and the results are summarized in **Table 7**.

**Table 7. Average Grains Sizes**

| Sample | Temperature | Average Grain Size |
|---|---|---|
| 99.995 % Pure | 1450 °C | 2.4 μm |
| 99.995 % Pure | 1550 °C | 4.8 μm |
| 99.995 % Pure | 1650 °C | 10.2 μm |
| 100 ppm | 1450 °C | 2.6 μm |
| 100 ppm | 1500 °C | 2.9 μm* |
| 100 ppm | 1525 °C | 3.4 μm* |
| 100 ppm | 1550 °C | 5.2 μm* |
| 100 ppm | 1650 °C | 8.8 μm |
| 500 ppm | 1350 °C | 0.9 μm |
| 500 ppm | 1400 °C | 1.4 μm |
| 500 ppm | 1450 °C | 2.8 μm |
| 500 ppm | 1500 °C | 2.4 μm* |
| 500 ppm | 1550 °C | 4.0 μm* |
| 500 ppm | 1600 °C | 6.9 μm |
| 500 ppm | 1650 °C | 6.9 μm |

*Mean values of bimodal distributions.

Atomic force microscopy (AFM) was used in contact mode to measure the groove geometry. Images were recorded with a 10 nm step size at a 1 Hz scan frequency using a Solver NEXT AFM (NT-MDT, Moscow, Russia). The pyramidal silicon nitride tips used for the measurements had a cone angle of 35°, a radius of less than 10 nm, a resonance frequency of 67 kHz, a force constant of 0.32 N/m, and a Cr / Au coating on the detector side (Pyrex Nitride Probes triangular shape, NanoWorld). The AFM images were taken at randomly selected locations on the surface, sampling all areas of the specimen.

The treatment of the AFM data followed a procedure described earlier.[107] Briefly, the images were processed to remove any overall slope. For each groove, three profiles were extracted, and the width (W) and depths (d) were measured automatically using a computer program (see **Figure 16**). Note that the groove shape is created by surface diffusion during the high temperature anneal. Because of the rapidly decreasing diffusion

rates on cooling, the high temperature groove shape is locked in, even if the grain boundary structure or composition changes at lower temperature. Because the grooves are usually asymmetric, the two sides are considered separately, as if they were two separate symmetric grooves. Knowing W and d, the ratio of the grain boundary to surface energy can be calculated using Equation 13.

Equation 13:

$$\frac{\gamma_{gb}}{\gamma_s} = 2\sin\left(\tan^{-1}\left(m\left(\frac{d}{W}\right)\right)\right)$$

Where m is a constant equal to 4.73.[150] When using AFM to measure the relative grain boundary energy, it is necessary to consider the finite size of the probe compared to the actual groove dimensions. Consideration of these factors has led to the conclusion that if the grooves are wide enough (W > 1 micron), the finite probe size should not affect the measurement.[107] The corrections for smaller grooves have been calculated and were applied to the present data. However, no grooves with widths less than 250 nm were considered; this limited the extent of the low temperature data, where reduced diffusivity means that it takes much longer to create wider grooves. It should also be noted that the value of m deviates from its ideal value of 4.73 as W/d becomes smaller. However, the relationship between m and W/d is known[151] and a correction was applied to account for this. The details of this calculation can be found in methods 4.1.5.

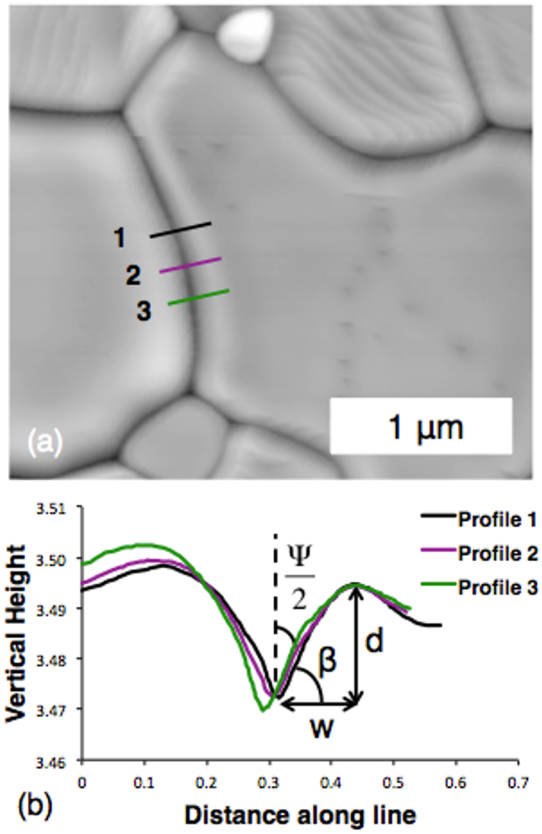


**Figure 16.** (a) Typical AFM image of a thermally grooved alumina surface. The lines indicate the positions from which the topographic traces in **Figure 16** (b) were extracted. (b) Three groove profiles from which W and d are measured.

Finally, there are a number of approximations in Equation 13 that should be recognized when applying it to measurements. First, it is assumed that the two surface energies on either side of the groove root are the same and this is, in general, not true. Second, it is assumed that the grain boundary is normal to the surface plane and, again, this is not true in general. Third, it is assumed that the differentials of the surface and grain boundary energy with respect to orientation are small enough to be ignored and this is, again, not true. Because of these approximations, the measurement of a single grain boundary groove has little meaning. Therefore, our approach is to measure many grooves and examine the distribution of values of $\gamma_{gb}/\gamma_s$, which samples variations in the unknown parameters listed above. It has been shown that if enough thermal grooves are measured, the mean value and width of the distribution are reproducible characteristics of

the sample;[151] here we will take the mean value of $\gamma_{gb}/\gamma_s$ as the quantity of interest and will refer to it as the relative grain boundary energy.

The number of measurements at each temperature varied between 48 and 311 (**Table 8**). To estimate the uncertainty of the mean value for each distribution, we tested its sensitivity to the number of measurements included in the calculation. Specifically, the mean value of $\gamma_{gb}/\gamma_s$ was calculated using randomly selected subsets of the measurements. This process was repeated 10 times and an example of this analysis is illustrated in **Figure 17**. The standard deviation of the mean values calculated using 10 random samples, each containing 50 % of the data, was taken to be the uncertainty of the mean value of $\gamma_{gb}/\gamma_s$ calculated from all of the data.

Each point on the relative grain boundary energy versus temperature plot (**Figure 22**) is the mean of a distribution of grain boundary energies. To estimate the uncertainty, we randomly selected different numbers of observations from complete sets of data and computed the means. As an example, **Figure 17** shows the mean value of the relative energy of 100 ppm Y-doped alumina sample heated at 1500 °C as a function of the number of observations, for randomly selected subsets. This was repeated 10 times. By comparing these curves, it is clear that when the mean relative energy is calculated from at least 30 % of the data, the results falls into a relatively constant band. Based on this, we used the standard deviation of the mean value of ten randomly selected subsets containing 50 % of the data as a measure of uncertainty. In this case, the 10 mean values of 105 randomly selected boundaries are (0.6887, 0.6681, 0.6617, 0.7123, 0.7013, 0.6545, 0.6810, 0.6659, 0.7173, 0.6611) and the standard deviation is 0.02.

**Table 8.** Number of grain boundaries measured for each concentration and temperature plotted in **Figure 22**. (T+) denotes measurements made while increasing the temperature and (T-) denotes measurements made while decreasing the temperature

| Concentration | Temperature (°C) | Number of boundaries |
|---|---|---|
| 99.995 % pure | 1450 | 311 |
| | 1500 | 124 |
| | 1550 | 99 |
| 500 ppm | 1400 | 65 |
| | 1450 | 109 |
| | 1500 | 172 |
| | 1550 | 57 |
| | 1600 | 48 |
| | 1650 | 99 |
| 100 ppm (T+) | 1450 | 107 |
| | 1500 | 209 |
| | 1525 | 278 |
| | 1550 | 106 |
| | 1600 | 96 |
| | 1650 | 74 |
| 100 ppm (T-) | 1350 | 82 |
| | 1400 | 136 |
| | 1450 | 120 |
| | 1500 | 95 |
| | 1550 | 110 |
| | 1600 | 76 |

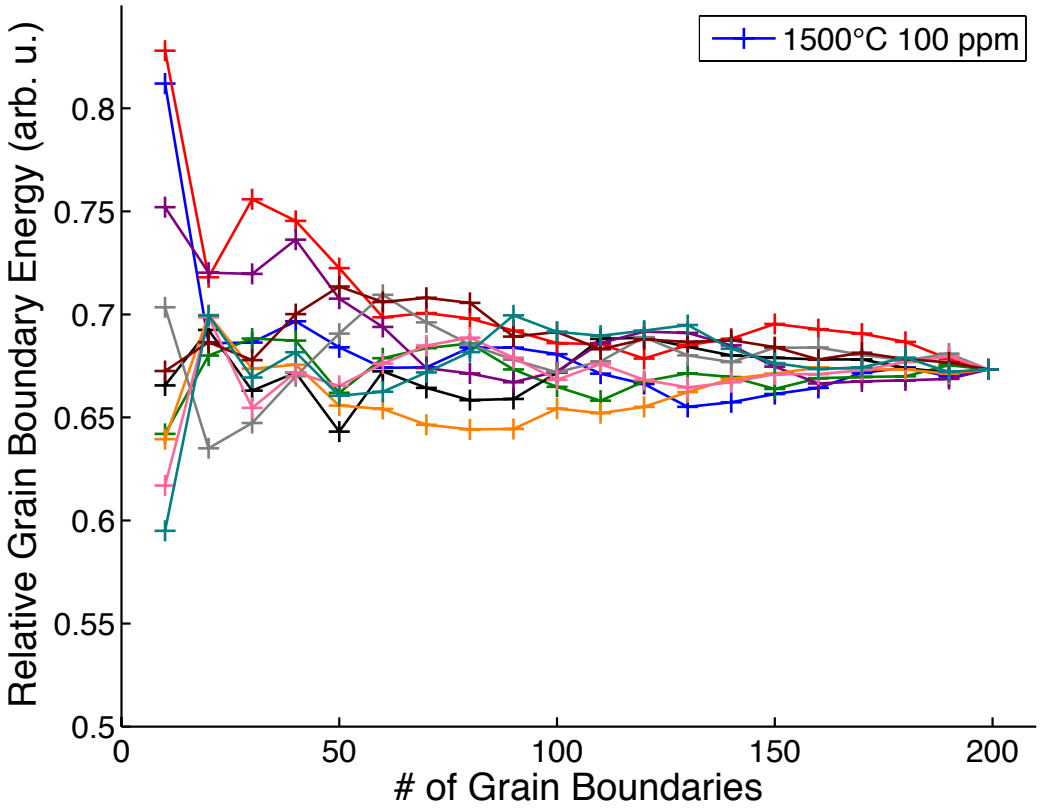


**Figure 17**. Mean values of 1500°C 100 ppm Y doped Alumina are plotted in 20 boundary increments, for the dataset randomized 10 times. Each colored curve is a different randomization of the same 100 ppm 1500°C dataset.

Violin plots were used to compare each of the distributions of relative grain boundary energies and are plotted separately according to concentration and (T+) or (T-) in Figure 23, Figure 24, Figure 25, and Figure 26. A violin plot is similar to a box plot but also includes a rotated kernel density estimation plot. The range of the y axis for each violin plot consists of quartiles, analogous to box plot quartiles, as well as whiskers which indicate the maximum and minimum values of the distribution. In the x direction on the violin plot the kernel density estimation (KDE) is plotted which, in short, is a computation of the probability density function for a random variable. Each of the violin plots were created in R.[174]

## 6.3 Results

AFM images of the microstructures of the 100 ppm Y-doped alumina samples at temperatures between 1350 °C and 1650 °C are illustrated in **Figure 18**. All images are shown with the same field of view to emphasize the changes in the grain size. It should be noted that none of the AFM images showed any evidence for the precipitation of yttrium aluminum garnet (YAG). X-ray diffraction and mapping by energy dispersive spectroscopy (EDS) also revealed no evidence for YAG precipitation. At the conclusion of the thermal treatments, the 100 ppm sample was fractured; the fracture was almost completely intergranular. Inspection by high resolution SEM, coupled with EDS mapping, yielded no evidence for the precipitation of YAG. Therefore, we conclude that the added Y remained in solution or segregated to the boundaries during this experiment. We note that studies of the solubility of Y in alumina in this temperature range cover a wide range,[17, 19, 129–131, 175–179] from less than 10 ppm[129] up to 200 ppm Y.[175]

AFM images of the microstructures of the 500 ppm Y-doped alumina samples at temperature between 1350 °C and 1650 °C are illustrated in **Figure 19**. At 1450 °C, there is clear evidence for the precipitation of YAG. Note that this image was selected for the large, obvious precipitates, which are not typical of the entire surface. Based on its EBSD pattern, the structure of this precipitate is consistent with YAG and based on EDS, its composition is consistent with YAG. The apparent second phase on the surface illustrated in **Figure 19**(c) was examined by electron backscatter diffraction (EBSD) and energy dispersive spectroscopy (EDS). The green points in the EBSD phase identification map in **Figure 20**(a) indexed as yttrium aluminum garnet and red points indexed as alumina. In the EDS map in **Figure 20**(b), the red points represent aluminum, blue represent yttrium and green represents silicon. The combination of EBSD and EDS results indicated that a second phase of Si-rich YAG is present in the 500 ppm Y-doped alumina sample. The source of the Si contamination is not known, but it is a component of the furnace insulation and heating elements. At higher temperatures, the grain size increases significantly (also see **Table 7**).

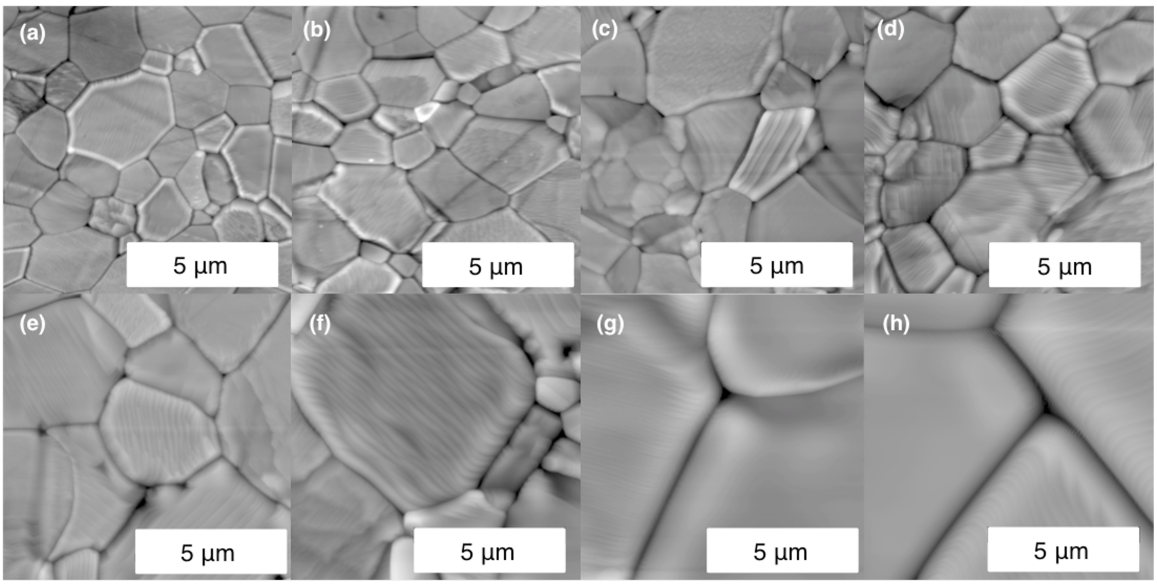


**Figure 18.** Representative AFM images of the 100 ppm Y-doped sample after grooving at (a) 1350 °C (b) 1400 °C (c) 1450 °C (d) 1500 °C (e) 1525 °C (f) 1550 °C (g) 1600 °C (h) 1650 °C.

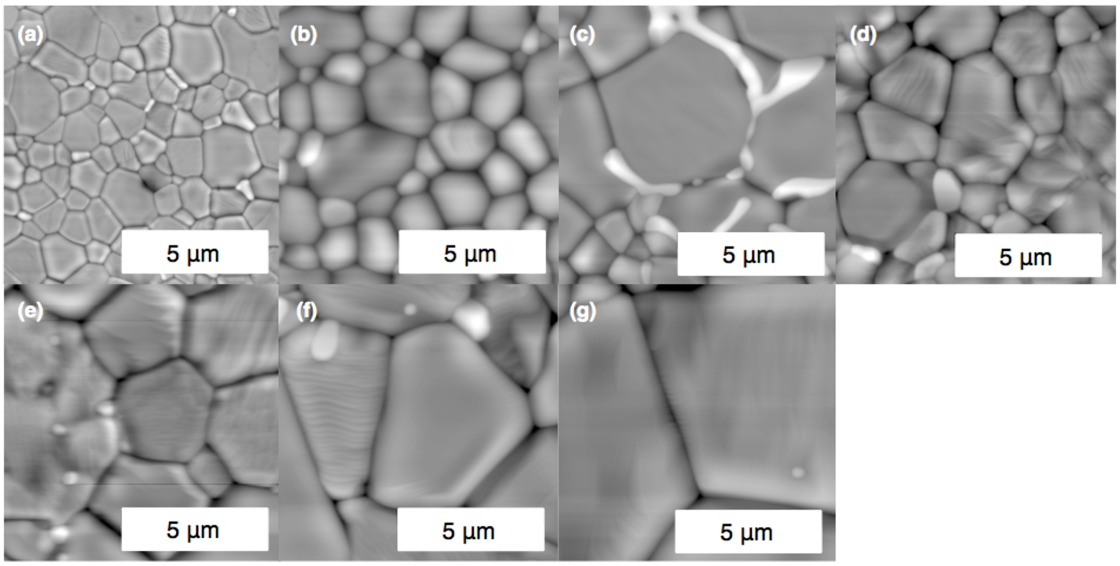


**Figure 19.** Representative AFM images of the 500 ppm Y-doped sample after grooving at (a) 1350 °C (b) 1400 °C (c) 1450 °C (d) 1500 °C (e) 1550 °C (f) 1600 °C (g) 1650 °C.

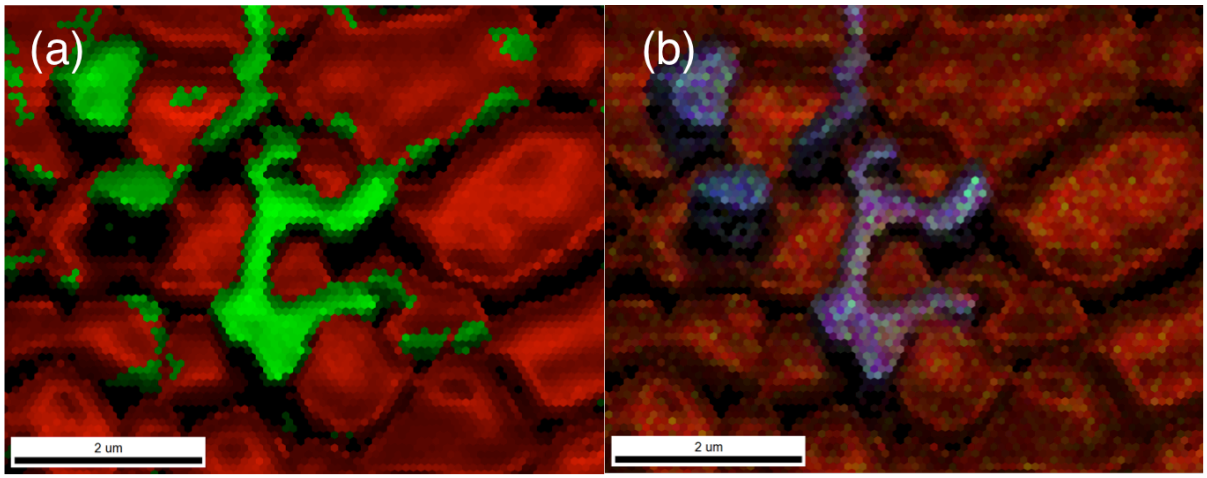


**Figure 20**. (a) EBSD map of YAG identified by green indexed points and alumina identified by red indexed points and (b) EDS map of elements aluminum (red), yttrium (blue) and silicon (green).

The images in **Figure 18** and **Figure 19** are only small areas of the samples. For each sample, large areas were imaged so that many grain boundary thermal groove profiles could be measured. **Figure 21** shows a cumulative distribution plot for all of the thermal grooves from samples annealed at 1550 °C. If we consider the median value of the relative grain boundary energy (a cumulative fraction of 0.5), then the sample with the highest concentration of dopants (500 ppm Y-doped alumina) has the lowest relative grain boundary energy and the 99.995 % pure sample has the highest median energy, as one would expect from the influence of impurities on grain boundary energies. Note that the median energies for the 100 ppm Y-doped samples (during heating and cooling) are between these two limits. Recall that YAG precipitated in the 500 ppm sample at a lower temperature, indicating that the grain boundaries in this sample are saturated with Y, in equilibrium with the YAG precipitates. Because the relative grain boundary energies of this saturated specimen are lower than in the 100 ppm doped sample, it can be surmised that the Y content in the grain boundaries is also greater. This supports the idea that the Y content of the 100 ppm sample did not exceed the solubility limit of Y in alumina at 1550 °C. When the different shapes of the distributions are compared, it appears the main effect of the dopants is to reduce the energy difference between the highest and lowest energy boundaries.

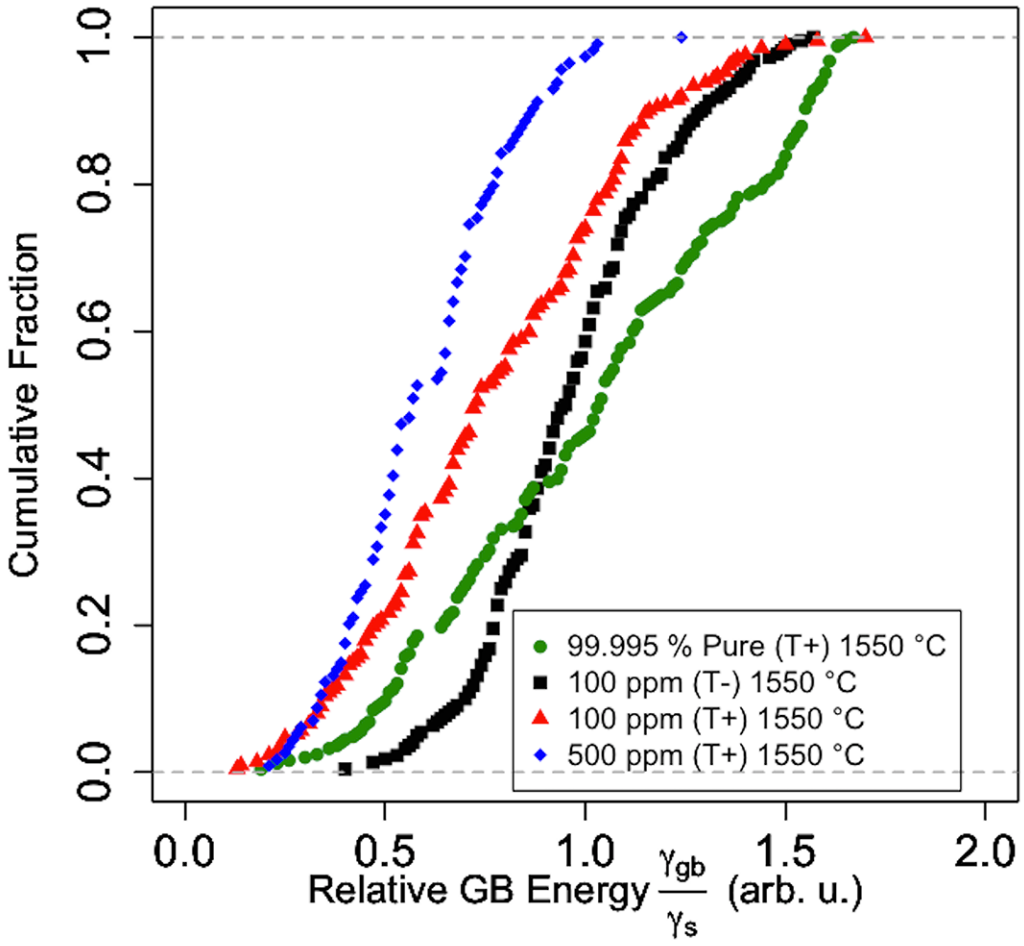


**Figure 21.** Cumulative distributions of relative grain boundary energies for the samples at 1550 °C.

The mean relative grain boundary energies for all of the samples are summarized in **Figure 22**. Note that for some of the samples, data collected at 1350 °C and 1400 °C is not included. In cases where the majority of the grooves were not wider than 250 nm, the distribution was deemed unreliable because of the convolution between the AFM tip and the groove shape, and these points are excluded.

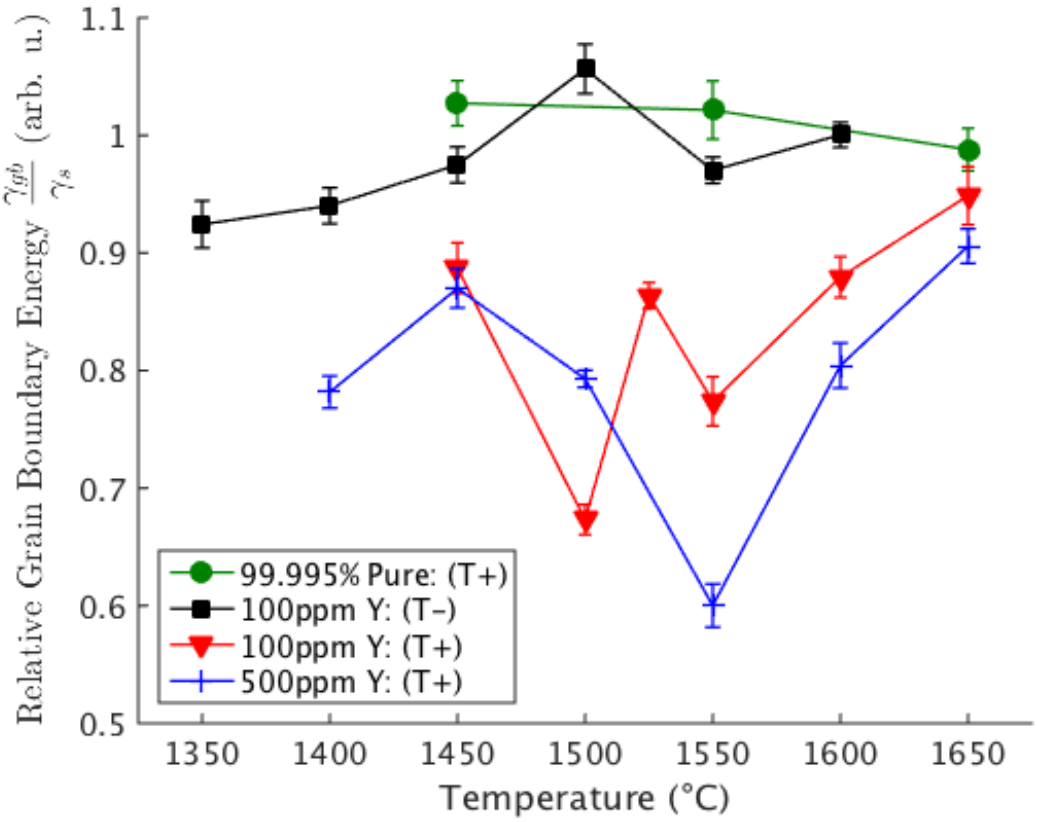


**Figure 22.** Relative grain boundary energies of doped aluminas as a function of temperature.

Thermal grooves were measured in the 99.995 % pure sample at 1450 °C, 1550 °C, and 1650 °C. Over this range of temperature, the mean values decrease slightly, consistent with the effect of entropy on the grain boundary free energy of a pure material. However, note that differences between these values are not greater than the estimated uncertainty. The mean values, which are close to 1.0, are similar to previous measurements. At 1600 °C, Handwerker et al.[180] and Saylor et al.[107] both measured $\gamma_{gb}/\gamma_s$ = 1.2; at 1400 °C, Dillon et al.[1] report a value of 1.11. The violin plots of the 99.995 % pure sample, Figure 23, also show that from 1450 °C to 1550 °C the distribution does not change much and at 1650 °C the peak in the rotated KDE function is more centered around the median value but does not change significantly.

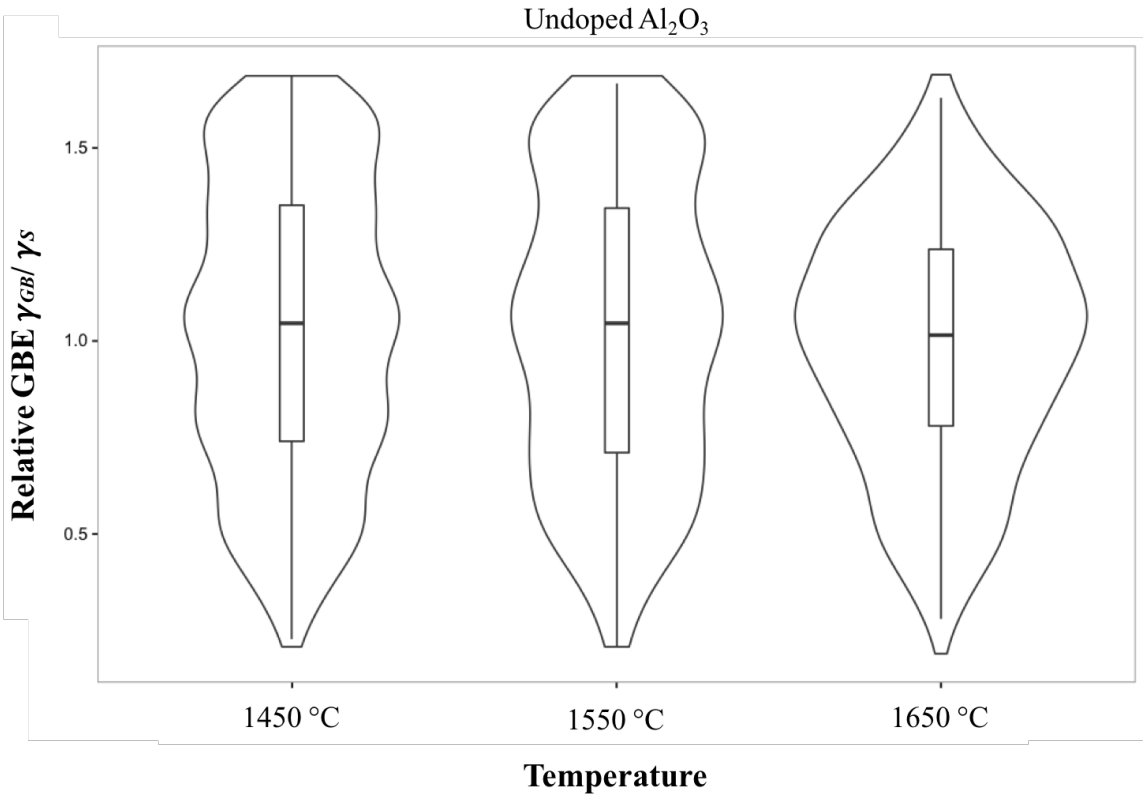


**Figure 23.** Violin plots of 99.995% pure alumina (T+).

The grain boundary to surface energy ratio of the 500 ppm Y-doped sample varies significantly with temperature. The increase in energy from 1400 °C to 1450 °C is likely the results of the depletion of Y from the grain boundaries. Note that YAG precipitates were first observed at 1450 °C and the precipitation reaction is expected to deplete excess solute from the boundaries, assuming they were initially supersaturated. Between 1450 °C and 1550 °C, there is a significant (30 %) decrease in $\gamma_{gb}/\gamma_s$. This is consistent with the previously detected complexion transition.[1, 4, 80, 121] The change occurs over a 100 °C temperature range. This is consistent with the observation that not all grain boundaries transition at the same temperature. It has previously been demonstrated that higher (lower) energy grain boundaries undergo complexion transitions at lower (higher) temperatures.[80] Finally, after the minimum grain boundary energy is reached at 1550 °C, there is a significant increase in the relative grain boundary energy. This is likely the result of the increasing bulk solubility of Y in alumina that depletes the grain boundaries.

The violin plot of 500 ppm (T+), Figure 24, exhibits similar change in average behavior. The distribution from 1400 °C to 1450 °C becomes more uniform then from 1450 °C to 1500 °C as the average energy changes the peaks in the rotated KDE distribution also becomes more centered around the lower energy values especially at 1550 °C. Then the peaks in the KDE go toward higher energy values at 1600 °C and 1650 °C, similar to the average values that increased in **Figure 22**.

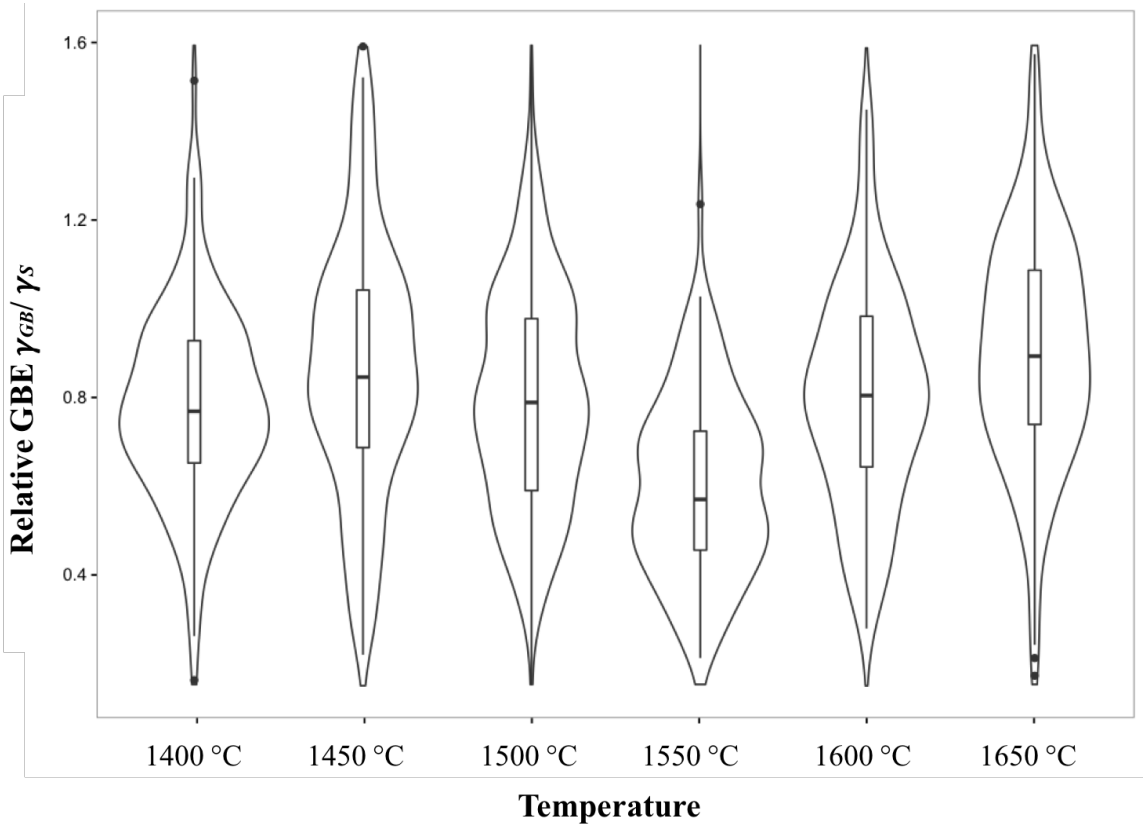


**Figure 24**. Violin plots of 500 ppm yttria doped alumina (T+).

The grain boundary to surface energy ratio of the 100 ppm Y-doped sample also decreases above 1450 °C. It then increases towards 1650 °C, where the relative energy is slightly greater than that of the 500 ppm doped sample. The points at 1525 °C and 1550 °C have an unexpected trend. It is possible there is a second boundary transition at 1550 °C that caused the decrease in energy. Between 1550 °C and 1650 °C, the energy undergoes an increase in energy similar to the 500 ppm sample. For both samples, the relative grain boundary energy is greater at the highest temperature than at the lowest temperature, which is most likely because of depletion of Y from the boundaries. The

violin plots for 100 ppm (T+), Figure 25, show similar results to the average interpreted values, **Figure 22**. The peaks in the KDE on the violin plots are more centered around lower grain boundary energies at 1500 °C, where the average GBE is lower as well, the KDE peak is at higher energy values at 1525 °C and then decreases again at 1550 °C and then the KDE peaks are centered around higher energy values again at 1600 °C and 1650 °C.

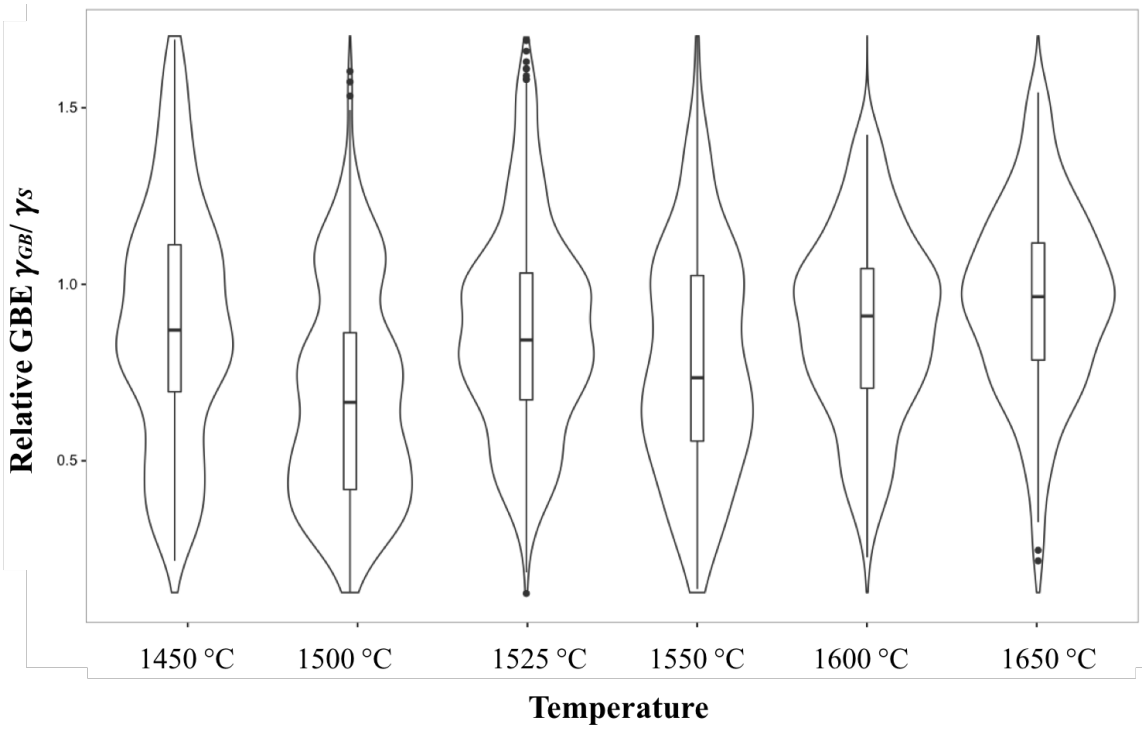


**Figure 25.** Violin plots of 100ppm yttria doped alumina (T+).

After the heat treatment at 1650 °C, the measurements on the 100 ppm Y-doped sample were repeated at successively lower temperatures. The overall trend is that there is a decrease in the relative grain boundary energy as the temperature is reduced, except for the increase that occurs at 1500 °C. The overall decrease is consistent with the increasing segregation of solute to the boundaries at lower temperature. The increase in energy at 1500 °C is consistent with a reversal of the transition that reduced the energy during heating, suggesting that the complexion transition is reversible. The absolute values of the energy are, on the other hand, quite different. It must be noted that the sample that is cooled in this experiment has a very different microstructure with respect

to grain size and grain boundary character distribution than the one that was heated and this may explain the difference. We will elaborate on this point in the next section.

The violin plots for 100 ppm (T-) are plotted in Figure 26. The KDE distribution at higher temperatures (1600 °C and 1550 °C) appear centered at the median values and then, at 1500 °C, where the average energy increased in **Figure 22**, the KDE appeared to be more smoothed. As temperature was decreased further and the grain boundary energies were measured the median value decreased at 1450 °C and 1400 °C but the KDE did not have any distinct peaks. At 1350 °C the KDE appears to be more centered around lower energies which was not clear from just the interpreted average energy so this is interesting.

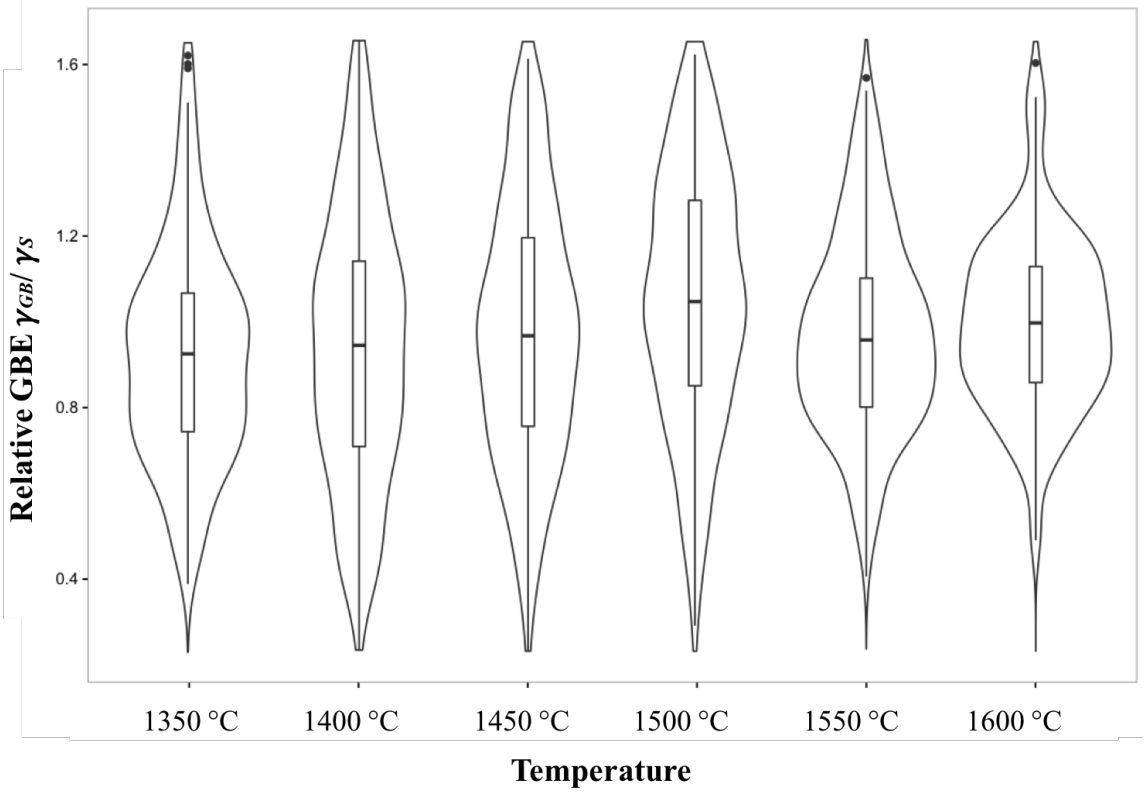


**Figure 26.** Violin plots of 100 ppm yttria doped alumina (T-).

## 6.4 Discussion

The temperature dependence of the relative grain boundary energy of 99.99 % pure alumina is consistent with expectations. The small decrease with increasing temperature is likely the result of the increasing importance of the entropic term in the free energy. More importantly, this sample serves as a "control", so that we can separate intrinsic

properties of alumina grain boundaries from extrinsic solute related effects in the Y-doped samples. The data from the 99.995 % pure sample shows that the measurements can be made consistently within a range of ± 0.05 arbitrary units and that changes in the grain boundary free energy from entropy are similar to this value. 99.995% pure alumina can be considered intrinsic even with the presence of impurities in the samples because the relative grain boundary energy trend with increased temperature decreased slightly which can be attributed to a change from the entropic term. Therefore, the much larger changes in the relative grain boundary energy found in the other samples can be attributed to the interaction of the solute with the boundary.

The data from the Y-doped samples are consistent with the overall trend that as the temperature is increased, the solute is depleted from the grain boundary and the energy increases. However, there are also significant decreases in the relative grain boundary energy in the temperature range from 1450 °C and 1550 °C. The temperature range corresponds to the point where abnormal grain growth begins. In other words, when there is a significant decrease in grain boundary energy, some of the grain boundaries have much higher velocities. This higher grain boundary velocity is indicated by some grains being significantly larger than others in the AFM images of samples heated in the 1450 °C to 1550 °C temperature range. It should be noted that, by itself, a lower grain boundary energy reduces the driving force for grain growth and boundaries should, on average, have lower velocities. Therefore, the increased grain boundary velocity with reduced grain boundary energy suggests that the grain boundary mobility must increase significantly. This transition in energy and mobility has previously been associated with a grain boundary complexion transition[1, 80] and that appears to be the best explanation for onset of abnormal grain growth at this temperature.[4, 178, 179]

The precipitation of YAG was only detected in the 500 ppm sample. As mentioned in the introduction, precipitation is expected to reduce the concentration of solute in the boundary and increase the relative grain boundary energy. As expected, when YAG precipitates in the range between 1400 °C and 1450 °C, the relative grain boundary energy increases by about 13 %. It is not clear if the increase is from desegregation alone or if the boundaries were supersaturated at 1400 °C and part of the increase is from reducing the boundary excess back to the saturated concentration.[173]

It should be noted that there are contradictory results in the literature on the solubility of Y in alumina. In this temperature range, it has been reported to be as low as 9 ppm[129] and as high as 200 ppm.[175] The available data in the literature is summarized below in **Figure 27**. Publications that describe the microstructure of Y-doped alumina were reviewed and based on the reports of phase stability and abnormal grain growth, the phase diagram highlighting the ranges of stability for different complexions was developed (**Figure 27**). The dashed solvus line between $Al_2O_3$ phase and $Al_2O_3$ + YAG phase is drawn based on reported values of the solubility limit as well as microstructural data (AGG observed). Points from studies where YAG precipitation is not mentioned are differentiated from those where it was specifically excluded. Complexion regions are also labeled as low temperature complexion region, transition region and high temperature complexion region which was determined approximately by the onset of abnormal grain growth (beginning of transition region) and development to a more unimodal microstructure after AGG (beginning of High T Complexion Region). The solidus and liquidus lines are approximations.

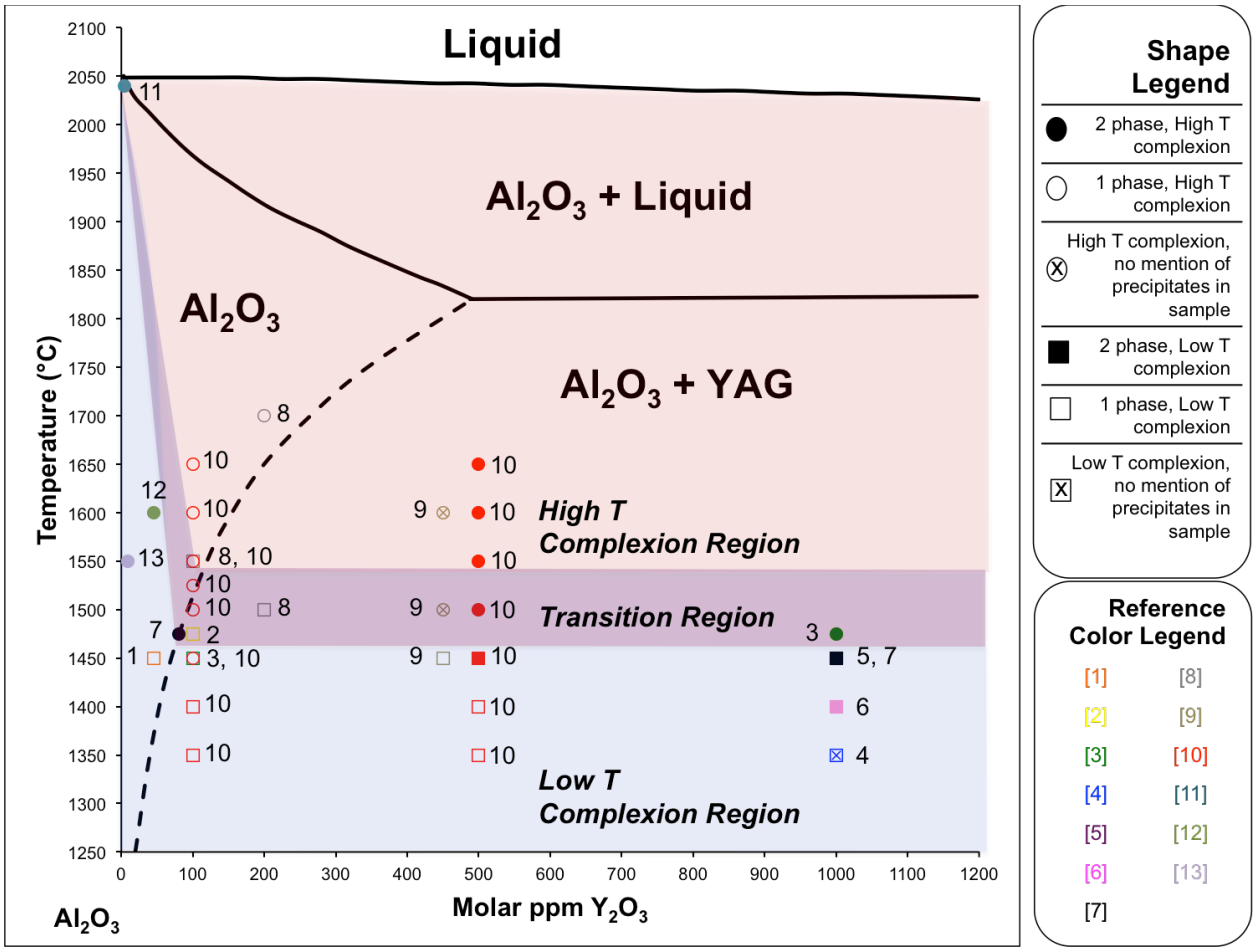


**Figure 27.** Yttria doped alumina phase diagram with overlaid complexion diagram. The current work is highlighted as reference [10] in the references for this figure. References for this figure found at the end of reference list (section 10).

It is likely that at least part of the differences in the published values of the solubility limit of Y in alumina might be explained by the microstructural effect on the apparent solubility. At any temperature, there is clearly a single equilibrium value for the solubility of Y in a single crystal of alumina. We will refer to this as the intrinsic solubility. However, in a polycrystalline ceramic, excess solute can be accommodated at the grain boundary. Because the amount of excess solute within the ceramic depends on the ratio of the grain boundary area to the sample volume, we refer to this as the extrinsic solubility. The total apparent solubility in a ceramic (the amount of solute that can be added before a second phase occurs) is then the sum of the intrinsic and extrinsic solubilities and it will vary with grain size.

To make a quantitative estimate of how the extrinsic solubility ($C_{ex}$) varies with the grain diameter, D, we define it in the following way:

$$C_{ex} = \frac{\frac{1}{2}\Gamma A}{F_{Al} V}$$

where  is the grain boundary excess of Y in alumina, in Y atoms per area, A is the grain boundary area of a grain with diameter D, V is the grain volume, $F_{Al}$ is the number of Al atoms per volume, and the factor of ½ accounts for the fact that each grain boundary is shared between to grains. If we assume cube shaped grains, $A = 6D^2$ and $V = D^3$. Based on crystallographic data for alumina, $F_{Al} = 47$ Al/nm$^3$. This leads to:

$$C_{ex} = \frac{0.064\Gamma}{D}$$

According to Gülgün et al.,[173] a typical value for Γ at saturation is 5 Y/nm$^2$. Therefore, at a grain size of 1 μm, the extrinsic solubility can be as high as 300 ppm. By the time a grain size of 10 μm is reached, the excess solubility falls to about 30 ppm. For the 100 ppm Y sample, this implies an intrinsic solubility of at least 70 ppm, which is within the range of values reported previously.[129, 175] Note that while the assumption of grain shape will affect the exact values, it will not change the order of magnitude. Considering that these are typical grain sizes in alumina ceramics, this may explain the wide range apparent solubilities that have been reported. It should be noted that there can also be another component to the extrinsic solubility associated with co-doping, especially by unintentional impurities and this might also affect the apparent solubility.

If the bulk solubility is vanishingly small, then only the grain boundaries can accommodate the dopants and changes in grain size will dramatically increase the grain boundary excess. If the bulk solubility is vanishingly small and the average grain size is 3 μm then the extrinsic solubility will be equal to 107 ppm for 5 Y/nm$^2$ adsorption. As temperature is increased and grain size increases to 9 μm, for instance, in order to accommodate for 107 ppm extrinsic solubility, the adsorption term would have to change and it would be equal to 15 Y/nm$^2$. Therefore, if bulk solubility is vanishingly small as grain size increases the adsorption at the interface would have to increase. If adsorption at

an interface increases, we would see a decrease in relative grain boundary energy with increased temperature. However, we observed an increase in relative grain boundary energy with increased temperature (except for the complexion transition range) which suggests that there is a finite solubility that increases with temperature, accommodating more solute and reducing the grain boundary excess.

Another factor that should not be ignored in the consideration of the data is the change in the types of grain boundaries in the samples as a function of temperature. In general, the populations of different grain boundary types are inversely correlated to the grain boundary energy[105, 181] and they depend on the type and concentration of segregating impurities.[182] Because of this, when Y-doped alumina goes through the complexion transition, there is a change in the grain boundary character distribution that reflects a change in the grain boundary energy anisotropy.[4] This new grain boundary character distribution is frozen in at high temperature, so the grain boundary distribution in the 100 ppm Y-doped sample is different from the distribution that existed on heating. This might partially account for the differences between the heating and cooling curves in **Figure 22**. Note that the relative grain boundary energy for the 100 ppm Y-doped sample after cooling to the lowest temperature is consistent, within experimental uncertainty, with the energy at the lowest temperature that could be measured in the sample before heating. The constancy of energy for a material with a different grain boundary character distribution and grain size is likely the result of an interplay between changes in the grain boundary excess, the specific grain boundary types, and how the excess affects the energies of those boundaries. Although we observe only an average result, the relationship between grain boundary excess and the grain boundary energy is likely to be different for each boundary.

The temperature dependence of the relative grain boundary energy of the 100 ppm Y-doped sample indicated that both the segregation of Y to the boundaries on cooling is reversible and that the complexion transition is reversible. Overall, there is a decrease in the relative grain boundary energy from 1600 °C to 1350 °C that could be explained by the segregation of Y from the grains to the grain boundary as the intrinsic solubility decreases with temperature. As noted above, the final energy is statistically indistinguishable from the initial energy suggesting that the initial and final sample have

similar grain boundary excesses. However, at 1500 °C, there is an increase in relative energy. This is at the same temperature as the complexion transition that decreases the energy upon heating. Because the change in energy is more than our estimated uncertainty, we can conclude that this is the reverse of the complexion transition that occurs on heating and leads to an increase in the grain boundary energy. Note that the reversibility of a surface complexion transition has been reported previously,[183] but this is the first indication that a grain boundary complexion transition is also reversible. The reversibility of these transitions suggests that it will be possible to define processing routes that exploit the mobility differences of the different complexions to control the microstructure.[121]

## 6.5 Conclusion

Changes in the relative grain boundary energy of Y-doped alumina, detected by the measurement of grain boundary thermal grooves, likely result from the redistribution of solute from the grain boundaries to the bulk during heating and the reverse during cooling. The relative grain boundary energy of a 99.995 % pure sample decreases slightly with increasing temperature. However, there are larger changes in the measured energies for 100 ppm and 500 ppm Y-doped samples during heating and cooling. Overall, the grain boundary energies in the Y-doped samples increased with increasing temperature and (in the case of the 100 ppm Y-doped material) decreased with decreasing temperature. This is explained by Y at the boundaries dissolving in the bulk during heating, and resegregating to the boundaries during cooling. There are also abrupt reductions in the relative grain boundary energy between 1450 °C and 1550 °C during heating that are associated with a complexion transition that increases grain boundary mobility and leads to abnormal grain growth. For the 100 ppm Y-doped sample, there is a corresponding increase in the relative energy at this temperature when the sample is cooled, suggesting that the grain boundary complexion transition is reversible.

# 7 Temperature Dependence of Relative Grain Boundary Energy in $SrTiO_3$

## 7.1 Introduction

Experimental measurements of the relative grain boundary energies in doped aluminas have shown that changes in grain boundary energy can signify a grain boundary complexion transition.[1] These transitions can significantly change microstructure evolution.[1, 162] As described in Chapter 6, the temperature dependences of relative grain boundary energy of 99.995% pure and yttria doped alumina were determined using thermal groove measurements. The measurements showed that the grain boundary energy was affected by the segregation and desegregation of solute to the grain boundaries and by grain boundary complexion transitions.[184] Similarly, here, we will measure and interpret the relative grain boundary energy in $SrTiO_3$ between 1350 °C and 1550 °C. This is of interest because grain growth in $SrTiO_3$ exhibits interesting anti-thermal behavior in the temperature range between 1350 °C and 1425 °C.

The driving force for grain growth is provided by the grain boundary excess energy. Therefore, grain growth results in a total reduction of energy and yields a reduction of the total grain boundary area per volume.[105] Grains tend to grow or shrink at greater rates as the temperature increases because diffusion is a thermally activated process. Thermally activated processes are usually Arrhenian, meaning that the logarithm of the process rate depends linearly on the inverse temperature, with a negative slope that is related to the size of the activation energy. Grain growth rates are quantified by the grain growth rate constant (k), which is the temperature dependent factor in the grain growth rate equation, $r^2 - r_0^2 = \frac{1}{4}kt$, where $r_0$ is the initial grain size, r is the final grain size, and t is time.[46–48] In most cases, the grain growth rate constant is observed to be Arrhenian; however, there are recent reports of cases where there are abrupt, non-Arrhenian changes in the grain growth rate constant. [41, 45, 74, 76, 147, 185] For example, barium titanate shows a gradual transition to faster growth, lithium lanthanum titanate exhibits an abrupt decrease of k of two orders of magnitude and in strontium titanate k decreases gradually in a transition region until faster growth commences again.[43]

The grain growth rate constant can be written as $k = 2\alpha\gamma m$, where $m$ is the mobility, $\gamma$ is the grain boundary energy, and $\alpha$ is a geometric constant close to 1.[46] The grain boundary can be thought in terms of surface energies because $\gamma_{GB} = \gamma_{S1} + \gamma_{S2} - B$ where $\gamma_{S1}$, $\gamma_{S2}$ are the surface energies of the adjacent crystals and B is the binding energy of the interface. Using cavities of equilibrium shape, the relative surface energies of $SrTiO_3$ were measured at a variety of temperatures to see if there were changes that could be used to explain the decrease of the grain growth rate constant in the temperature region between 1350 °C and 1425 °C.[40] The main conclusion was that the relative energies were less anisotropic in this temperature range. In the same study, the grain boundary plane distribution, which is known to be inversely related to the grain boundary energy, was also measured. It was observed that the relative areas of grain boundaries with {100} orientations was enhanced in the transition region, suggesting that these boundaries have a significantly lower energy than other grain boundary types.[40] If we can measure the grain boundary energy by the thermal grooving technique, it can be used to determine if there really is a decrease in the grain boundary energy in the same region where there is a decrease in the grain growth rate constant, as inferred from the grain boundary plane distribution.

The purpose of this chapter is to describe the measurement of the relative grain boundary energy in $SrTiO_3$ at several temperatures where the grain growth rate constant displays non-Arrhenian characteristics. We hypothesize that there might be a grain boundary complexion transition in this temperature range and, if so, we expect to find an abrupt decrease in the relative grain boundary energy. The measurements show that there is a decrease in grain boundary energy at the same temperature as the apparent grain boundary transition in the non-Arrhenius region.

## 7.2 Experimental Procedure

$SrTiO_3$ was prepared by first mixing $SrCO_3$ (99.95% purity) and $TiO_2$ (99.995% purity) (Sigma Aldrich Chemie GmbH, Taufkirchen, Germany) to achieve a molar ratio (Sr/Ti) of 0.996. Details of the synthesis are published elsewhere.[25] After processing the powders, ICP-OES was used to measure impurity concentrations (reported on a weight basis). The most concentrated impurities were Zr (600 ppm) and Y (35 ppm), which

were probably introduced by the yttria stabilized zirconia milling media. The sample also contained Ba (100 ppm) and Ca (250 ppm) and less than 10 ppm of Al, Cr, Mg, Fe, Nb, Ni and Mn.[25] To achieve high density, the green bodies were pre-sintered by heating at 20 °C/min to 1425 °C and holding for one hour in oxygen.[41] Before cooling, the temperature was changed at 20 °C/min to a temperature between 1350 °C to 1550 °C and the samples were annealed in oxygen for an additional 10 h before quenching in air (see Table 1). The density, measured by the Archimedes method, was > 99 % of the theoretical density.[43] Previous studies of $SrTiO_3$ with a Sr/Ti ratio of 0.996, sintered at 1400 °C, reported rutile $TiO_2$ as a minority phase.[25] The absolute concentration is unknown and may vary with grain size and annealing temperature for these samples. After heat treatment, the samples were cut into ~1 mm thick slices and polished on one side. The cut and polished samples were then annealed to create grain boundary thermal grooves. The durations of the anneals were selected to achieve groove widths greater than 0.5 μm. The samples were air quenched following grooving. The conditions are specified in **Table 9**. All of the heat treatments were performed in a furnace that had fast heating and cooling in an oxygen environment, ~20 °C/min.

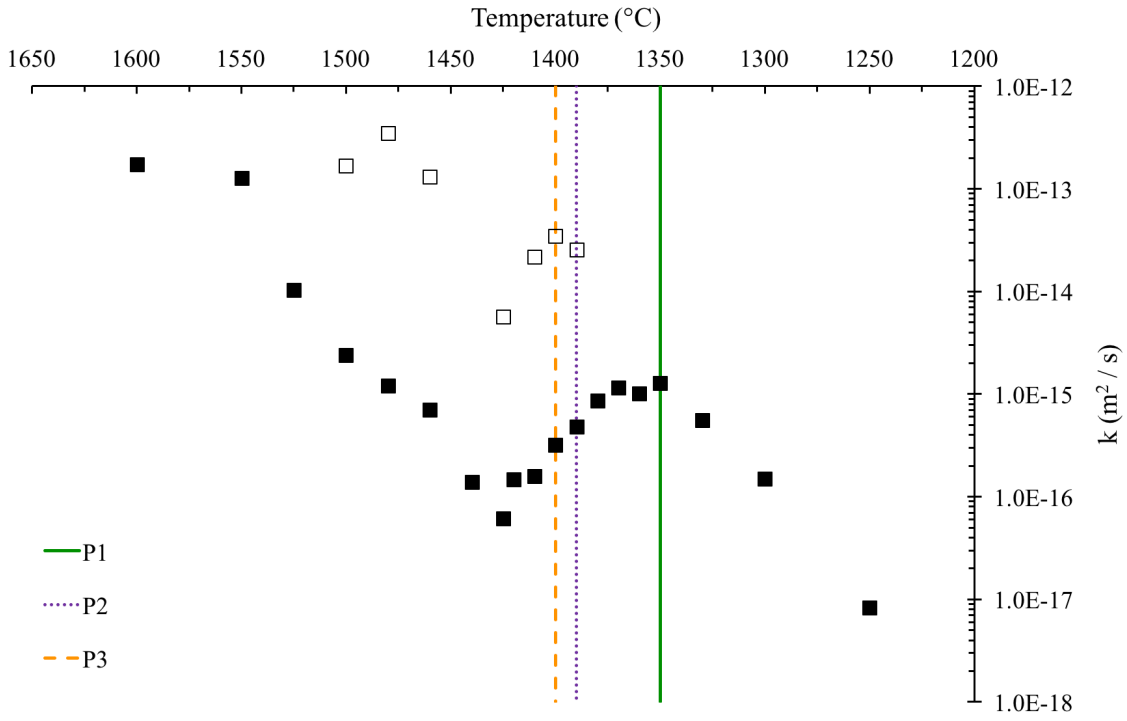


**Figure 28.** Grain growth rate constant versus temperature for $SrTiO_3$, from reference.[186] Open squares correspond to grain growth rate constants measured for the average of the largest grains in the microstructure and closed squares represent grain growth rate constants measured for the average of all grains. P1 – P3 lines correspond to the thermal treatments for the four samples used to measure the relative grain boundary energy.

**Table 9.** Thermal treatments for the four samples used to measure the relative grain boundary energy in $SrTiO_3$.

| Sample | Temperature | First anneal time | Thermal groove time |
|---|---|---|---|
| P1 | 1350 °C | 10 h | 40 min |
| P2 | 1390 °C | 10 h | 20 min |
| P3 | 1400 °C | 10 h | 20 min |

Some failed attempts to produce grain boundary grooves using other annealing treatments are listed in Table 10.

**Table 10.** Anneal and thermal groove time and temperatures for samples whose thermal grooves could not be extracted for relative grain boundary energy measurement.

| Anneal Temperature, Time | Thermal Groove Temperature, Time |
|---|---|
| 1425 °C, 10 hours | 1425 °C, 5 minutes |
| 1425 °C, 15 hours | 1425 °C, 10 minutes |
| 1425 °C, 16 hours | 1250 °C, 5 hours |
| | 1280 °C, 5 hours |
| | 1300 °C 5 hours |
| 1460 °C, 4 hours | 1300 °C, 5 hours |
| | 1325 °C, 5 hours |
| | 1350 °C, 5 hours |
| 1480 °C, 1 hour | 1300 °C, 5 hours |
| | 1330 °C, 5 hours |
| 1550 °C, 10 hours | 1550 °C, 10 minutes |

The relative grain boundary energies were measured for $SrTiO_3$ samples in a temperature range of 1350 °C to 1550 °C. In an additional experiment, the sample annealed at 1550 °C was re-annealed at 1250 °C for 48 hours, polished, and re-grooved at 1350 °C to determine if the annealing induced changes in the grain boundary energy were reversible. [184]

Relative grain boundary energy can be determined from geometric measurements of a thermal groove. Grain boundary grooves are formed by thermally activated diffusion driven by capillary driving forces and the shape was first explained theoretically by Mullins.[150] Surface height profiles perpendicular to grain boundary grooves were extracted from contact mode atomic force microscopy images using the same instrument, tips, and procedures described in previous work.[184] Using Gwyddion [149] as the post-processing software, three height profiles (see Fig. 2(a)) were extracted along lines perpendicular to a single grain boundary, as depicted in Figure 29 (b). The depth (d) and width (W) of each thermal groove was extracted using a computer program and the relative grain boundary energy (the ratio of grain boundary to surface energy) was computed using Equation 1.

$$\frac{\gamma_{gb}}{\gamma_s} = 2sin\left(tan^{-1}\left(m\left(\frac{d}{2W}\right)\right)\right) \quad (1)$$

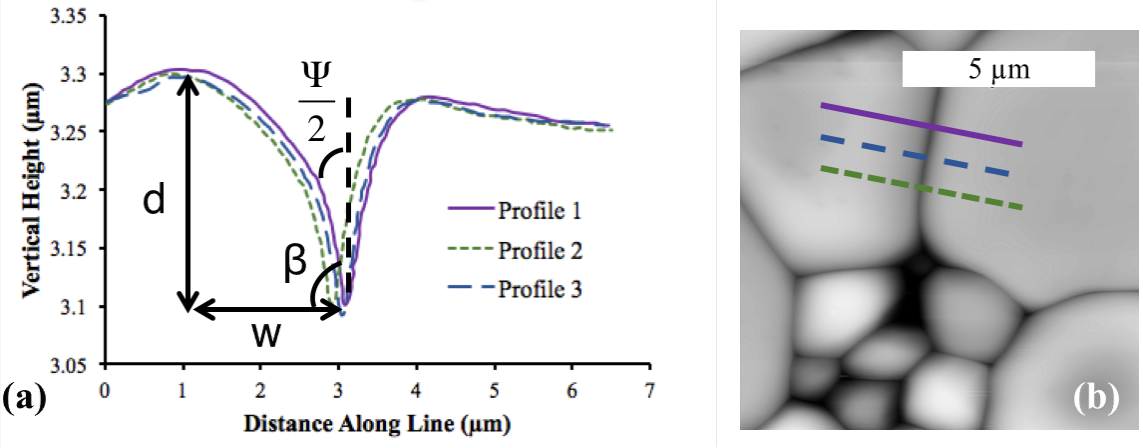


**Figure 29.** (a) Surface height profiles perpendicular to a grain boundary. (b) Topographic AFM image with three lines to indicate the positions at which the height profiles in (a) were extracted.

When the relative grain boundary energy is measured from a grain boundary thermal groove, the particular value obtained is sensitive to the particular type of grain boundary, the surfaces bounding the groove, and its inclination. Here, we measure a distribution of values and take the mean of the distribution to represent the grain boundary energy at a particular anneal temperature. Previous work has shown that the uncertainty in the mean value depends on the number of measurements in the distribution and that it is smaller than other uncertainties after about 100 measurements of randomly selected boundaries. [184] The number of boundaries measured for each $SrTiO_3$ sample is listed in **Table 11**. In this case, we will also determine the experimental uncertainty induced by wear of an AFM tip.

A persistent problem with measuring grain boundary groove profiles by AFM is that the shape of the tip can change during the measurement and influence the depth measurement, leading to inconsistent results. To obtain reproducible and accurate results, we measure a standard sample before and after data collection. If the measurements after data collection do not match the values before, the data is discarded. As a standard, we use two particular grain boundary thermal grooves on the surface of a 99.995 % pure

alumina sample annealed and thermally grooved at 1650 °C. The standard boundaries are illustrated in Figure 30. The relative grain boundary energies, computed using equation 1,[107, 151] were used for comparison. Measurements of the relative grain boundary energy were deemed acceptable if measurements of the standard before and after the acquisition of data from $SrTiO_3$ differed by less than 0.1 arbitrary units. A series of relative grain boundary energy measurements of grain boundary 1 on the standard are illustrated in Figure 31. If the relative grain boundary energies on the standard sample differed from expectations by more than 0.1, the AFM tip was replaced and, when necessary, the instrument was re-calibrated before collecting additional data.

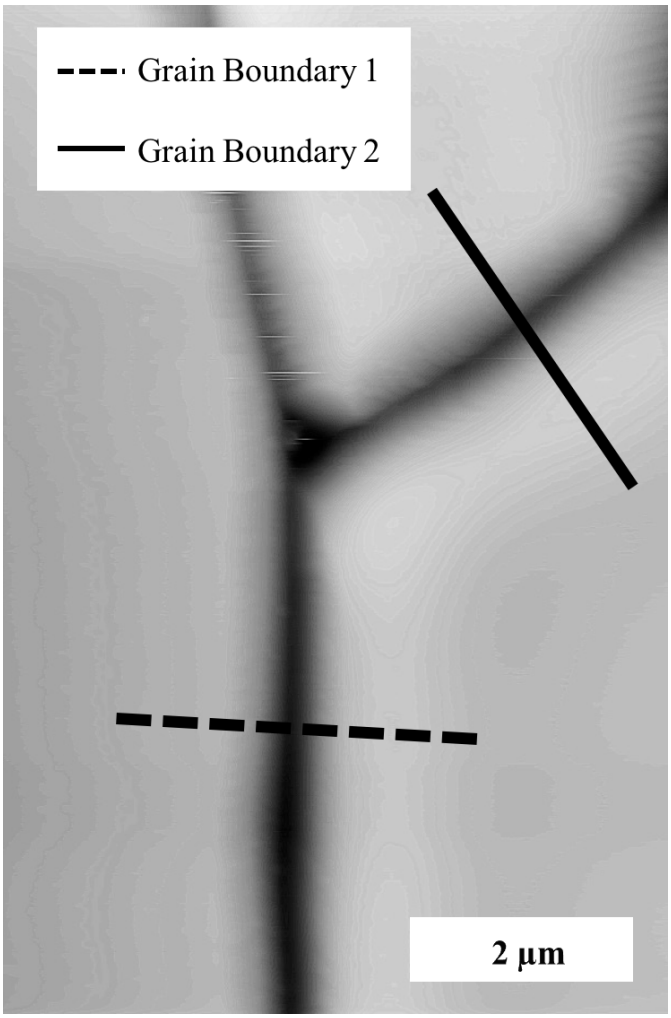


**Figure 30.** Topographic AFM image of the two grain boundaries used for standard measurement.

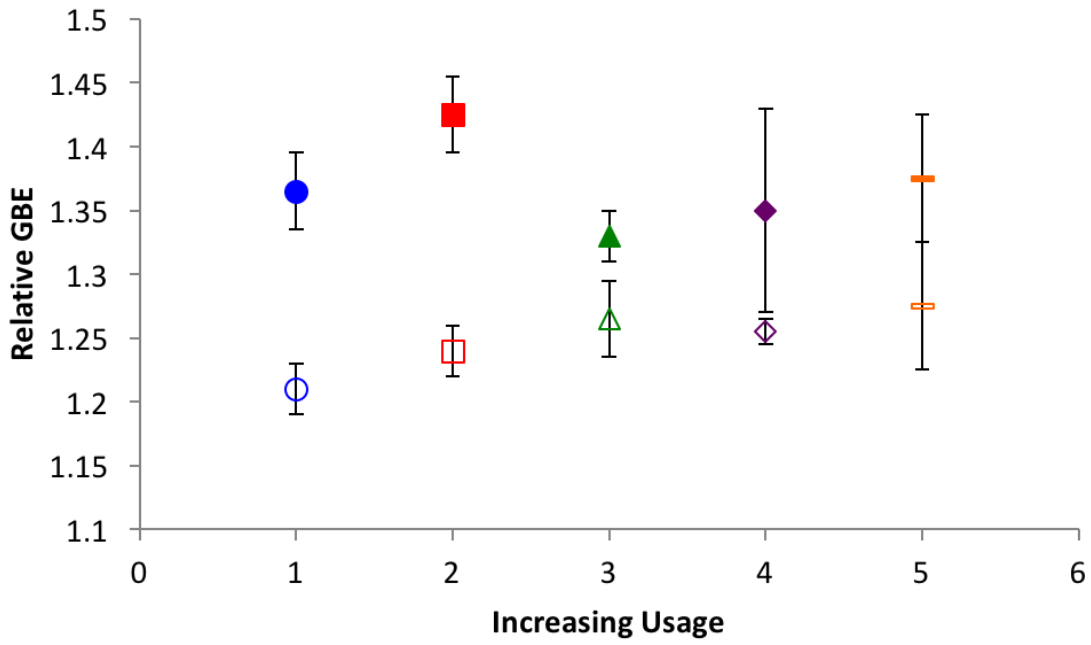


**Figure 31.** Measured relative grain boundary energies of the left (filled symbols) and right (open symbols) grooves for grain boundary 1 of the standard.

**Table 11.** Number of $SrTiO_3$ grain boundary thermal grooves measured at each temperature.

| Temperature (°C) | Number of boundaries |
|---|---|
| 1350 | 208 |
| 1390 | 200 |
| 1400 | 192 |

The microstructures of the $SrTiO_3$ samples annealed at 1390 °C and 1400 °C have bimodal grain size distributions. For the very smallest grains, the grooves from the grain boundaries overlap, and the grain surface has a single rounded shape, rather than the distinct shape of independent grain boundary grooves. In such cases, the width of the apparent groove is determined by the grain size and not the grain boundary energy and, therefore, such measurements are not useful. Therefore, grooves were only measured from grains that were larger than 3 μm in diameter where independent grooves were observed in the AFM images. **Figure 32** illustrates the difference between a profile from an acceptable grain and from a rounded grain. Considering only the height profile, **Figure 32** (b), it has the same general shape as an acceptable thermal groove. However,

in the micrograph, **Figure 32** (a) the local height maximum is simply the center of the grain. Such grooves could not be used in the analysis. There were also cases when the grain surface was so faceted that the groove shape was not apparent and these grain boundaries were also ignored.

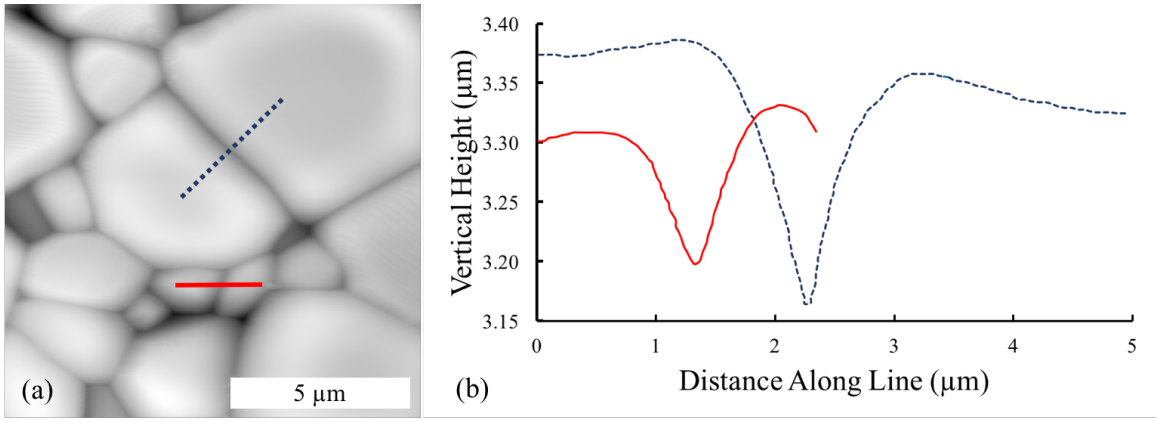


**Figure 32.** Topographic AFM image showing the microstructure of $SrTiO_3$ annealed and grooved at 1390 °C. Lines in (a) indicate the positions of the height profiles in (b) from an acceptable groove (blue) and a groove between two of the smallest grains that is unacceptable (red).

The grain boundary plane distribution for the sample annealed at 1550 °C was measured from two dimensional EBSD maps so that it could be compared to previously reported GBPDs at 1300 °C, 1350 °C and 1425 °C.[40] EBSD maps for the sample annealed at 1550 °C was collected using a Quanta 200 SEM and EDAX OIM software. An example of one of the 2D EBSD maps, before pseudosymmetry was removed, to plot the GBPD at 1550 °C is depicted in Figure 33. Grain boundary segments were extracted using the TSL post processing software (EDAX Inc, Mahwah, NJ). Orientations maps were collected with 30 kV accelerating voltage, 10 mm working distance, 70° sample tilt and step size of 0.5 µm. Cleanup was performed in TSL post processing software with grain dilation (grain tolerance angle 5°, minimum grain size 5 pixels), single average orientation per grain and grain confidence standardization (grain tolerance angle 5°). To remove the effects of pseudosymmetry the orientation data was partitioned into two groups with confidence index greater than or less than 0.07. Removing the latter group also removed the majority of the effects of pseudosymmetry in the orientation assignments. Reconstructed line segments were extracted from the partitioned maps and the grain boundary plane distribution (GBPD) was calculated using calc_gbcd_stereo.

Because two-dimensional EBSD maps only account for four of the five parameters that describe grain boundary geometry, stereology is used to estimate the distribution of grain boundary plane normals. The grain boundary plane distribution was determined from 9697 grain boundary traces extracted from orientation maps of the $SrTiO_3$ microstructure after annealing at 1550 °C. The data in **Figure 41**, at each temperature, is plotted with the same number of grain boundaries in order to accurately compare the grain boundary population at each temperature.

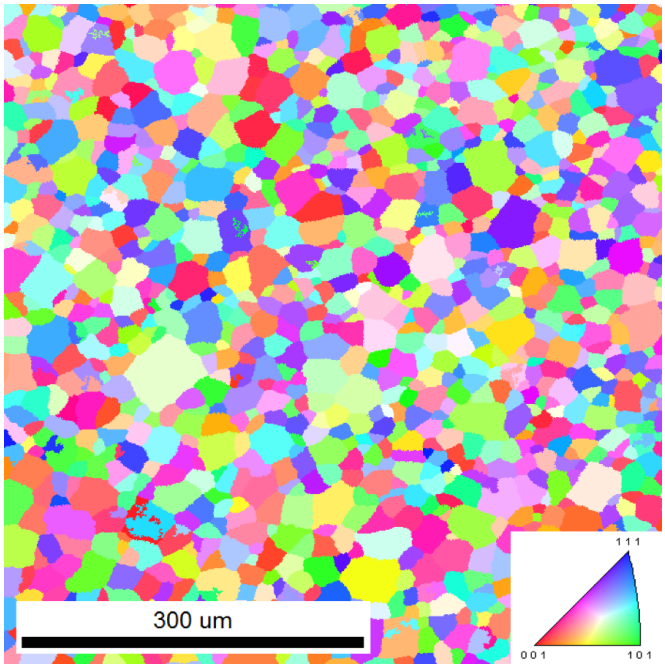


**Figure 33.** An example EBSD map for 1550 °C $SrTiO_3$ is depicted. This map and many others were used to create the GBPD at 1550 °C from 2D EBSD maps in order to compare to previously reported GBPDs at 1300 °C, 1350 °C and 1425 °C.

## 7.3 Results

AFM images of the $SrTiO_3$ surface after annealing at temperatures between 1350 °C and 1550 °C are illustrated in Figure 34. Grain size distributions of 1350 °C, 1390 °C, 1400 °C and 1425 °C were reported previously.[43] The grain size of the sample heated at 1350 °C is unimodal, as seen in Figure 34 (a). For samples heated at 1390 °C and 1400 °C, the grain sizes are bimodal and there are some very small grains whose grooves are not measurable. The microstructure of the sample heated at 1425 °C (Figure 1(d)) has a unimodal grain distribution and the grain size is much smaller than for the samples heated

at lower temperatures. The grain boundary grooves in this sample were not acceptable for interpretation. Note also that the grains surfaces are all faceted, because it was grooved at a lower temperature in an attempt to limit the groove dimensions. The average grains sizes are much larger in the sample heated at 1550 °C (Figure 34 (g)).

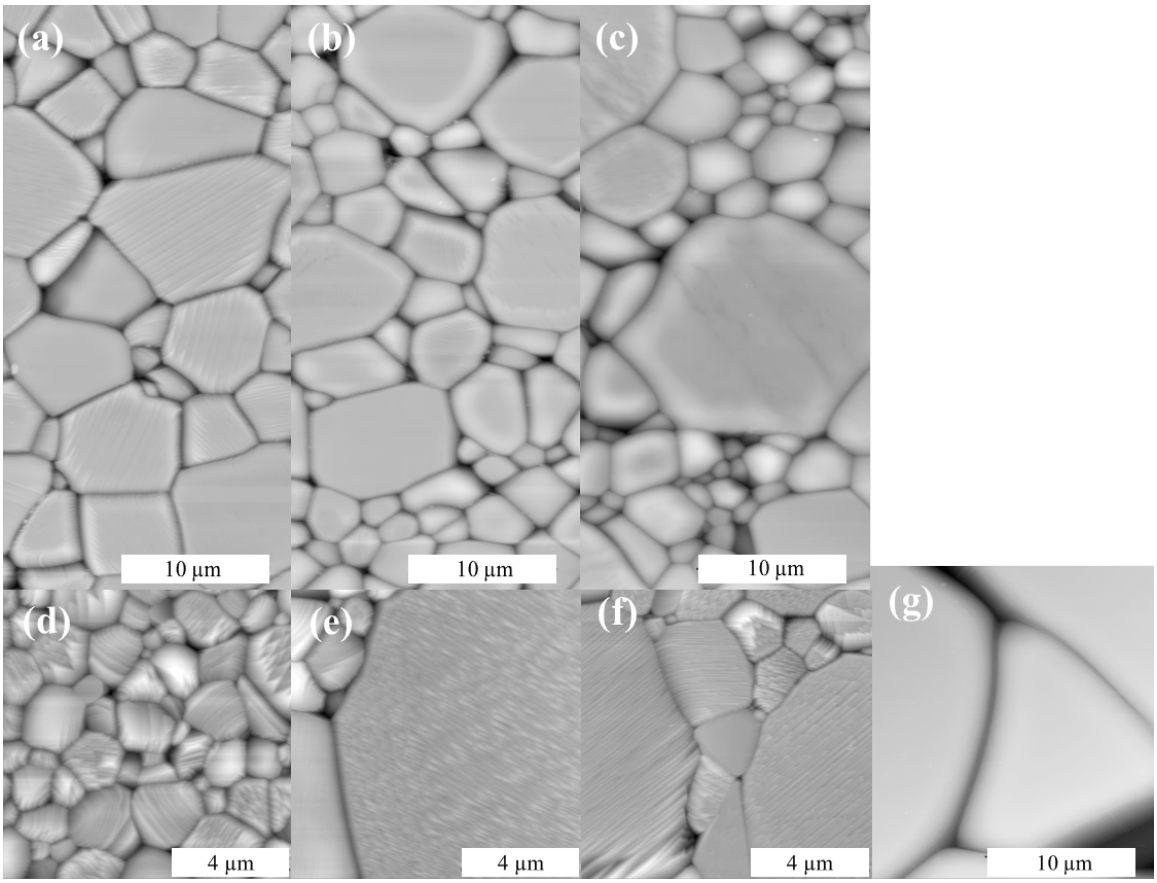


**Figure 34.** Representative AFM images of the $SrTiO_3$ samples after grooving at (a) 1350 °C (b) 1390 °C (c) 1400 °C (d) 1425 °C 16 hour anneal, 1300 °C groove 5 hours (e) 1460 °C 4 hour anneal, 1350 °C groove 5 hours (f) 1480 °C 1 hour anneal 1330 °C groove 5 hours (g) 1550 °C.

Faceting was observed in the $SrTiO_3$ samples. In Figure 35, the samples were annealed at 1425 °C for 16 hours and thermally grooved at 1300 °C for 5 hours in air in (a) and at 1390 °C for 10 hours and thermally grooved at 1390 °C for 20 minutes in air in (b). The sample in Figure 35 (a) was annealed at 1300 °C. Almost every single grain in the sample annealed at 1300 °C is faceted. This means that the orientations of these grains are not part of the Wulff shape and suggests that the Wulff shape is made up of a

few low index surfaces. In Figure 35 (b) fewer grains are faceted. In this case, the sample was annealed at 1390 °C. When a grain is not faceted, it orientation is part of the Wulff shape. The suggests that Wulff shape at 1390 °C is more isotropic than at 1300 °C, which is consistent with what is known about the temperature dependence of the surface free energy.

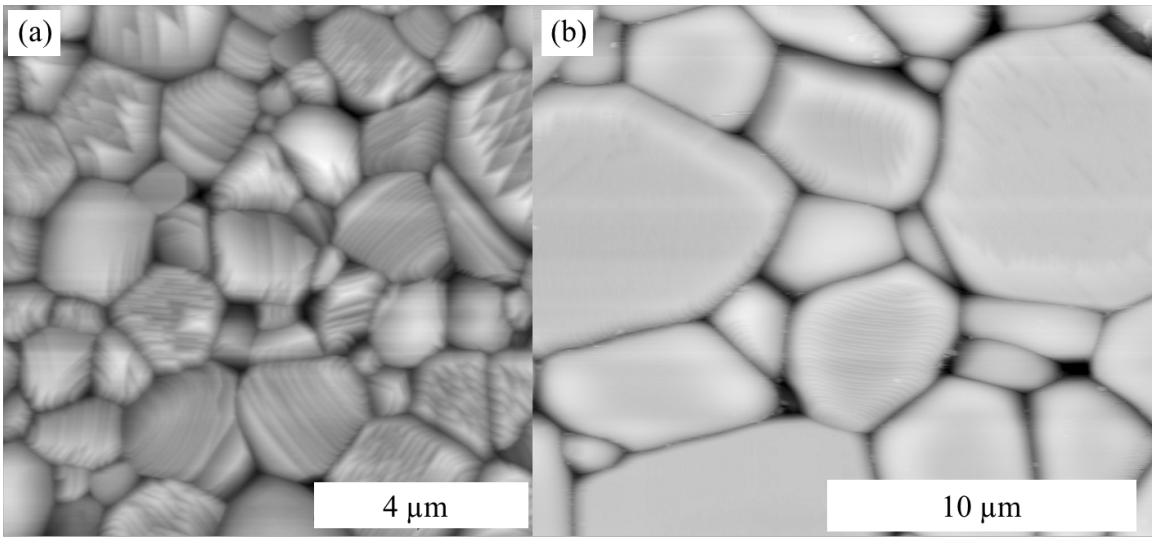


**Figure 35.** Two images of surfaces in $SrTiO_3$ that are highly faceted. (a) $SrTiO_3$ annealed at 1425 °C for 16 hours and thermally grooved at 1300 °C for 5 hours in air and (b) $SrTiO_3$ annealed at 1390 °C for 10 hours and thermally grooved at 1390 °C for 20 minutes in air.

To test for the possibility that any changes in the grain boundary energy with temperature were reversible, the sample annealed at the highest temperature (1550 °C) was later annealed for 48 h at 1250 °C and then polished and grooved at 1350 °C. When this was compared to the sample that was heated and grooved at 1350 °C without the higher temperature treatment, there was clear evidence for an irreversible change in the sample. Specifically, the microstructure showed a new phase that was identified as rutile structured $TiO_2$ (see **Figure 36** and **Figure 37**). Because of this change, we do not expect the thermal grooves formed at 1350 °C after the high temperature anneal to be the same as those formed in the sample that was not first annealed at 1550 °C and therefore were removed. The formation of rutile at high temperature is not too surprising considering the sample was initially formulated with a stoichiometric excess of titania.

Here, the reversibility of the temperature dependence of relative grain boundary energy was measured, similar to the experiments on yttria doped alumina.[184] The $SrTiO_3$ that was annealed and thermally grooved at 1550 °C was annealed at 1250 °C for 48 hours in an effort to return the boundaries to the low temperature state. It was then polished and thermally grooved at 1350 °C in the same manner as the original 1350 °C sample was grooved, for direct comparison (40 minutes in air at a rate of 20 °C/min heating and air quenched). Images of the resultant microstructure are shown in **Figure 36**. In **Figure 36** (a) an image that is representative of the majority of the microstructure is depicted, the image in (b) illustrates second phase particles on the surface, and the image in (c) shows as second phase at grain boundaries and triple junctions that appears to have solidified from a liquid that formed at high temperature. There are clear differences between the images in **Figure 36** and that of the sample annealed once at 1350 °C (Figure 34 (a)) which indicate that there were irreversible changes which include the precipitation of a second phase.

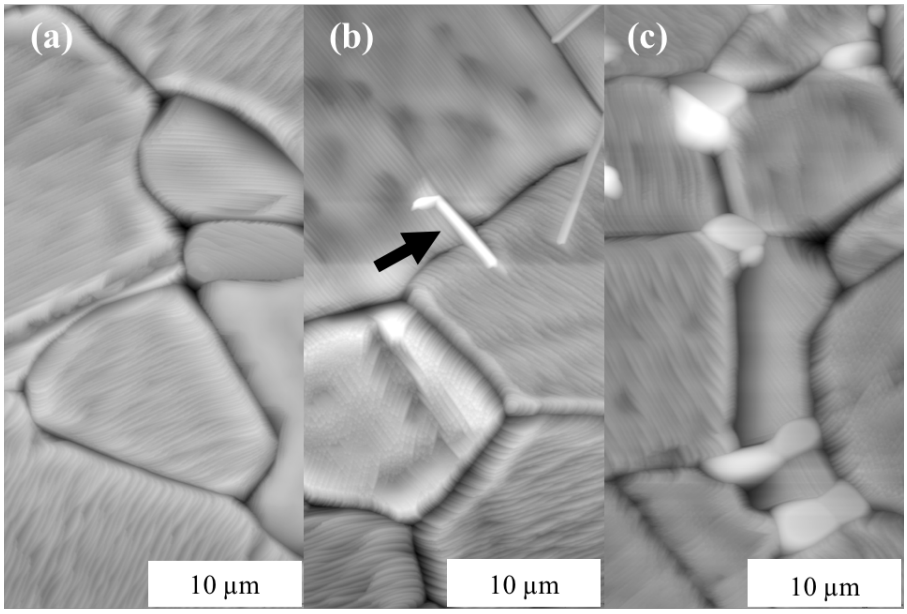


**Figure 36.** Example images of the reverse 1550 °C to 1350 °C sample. (a) is an image of the majority of the microstructure, (b) $TiO_2$ particles are found on the surface which was verified to be rutile in **Figure 37** and (c) bright smaller looking grains appear to be solidified liquid phase.

The particles in **Figure 36** (b) were investigated by electron backscatter diffraction (EBSD) and energy dispersive spectroscopy (EDS) and the results are presented in **Figure 37**. The analysis was performed using an FEI Quanta 200 field

emission scanning electron microscope at operated at 20 kV, with a spot size of 5.0, a working distance of 15 mm, and the sample tilted at the nominal 70° with respect to the camera. OIM EDAX software was used for the EBSD data collection and TSL software was used to create each independent orientation map based on phase (EDAX Inc, Mahwah, NJ). EDS was collected using TEAM software which is also provided by OIM analysis software package. In **Figure 37** (a) a secondary electron image of the area of interest is shown where there are distinct grain boundaries and elongated particles on the surface. **Figure 37** (b and c) are orientation images of the cubic $SrTiO_3$ phase and the rutile $TiO_2$ phase respectively. EDS maps of Sr, O, and Ti are shown in **Figure 37** (d-f). The intensity of the color in each of the element maps indicates the number of counts recorded by the X-ray detector at the characteristic energies of each of the elements. Brighter spots indicate the presence of that element at that location in the map and dark (or black) spots indicate that that element was not detected at that location. Here, it appears that the elongated particles contain Ti and O, but not Sr, consistent with the assignment of the EBSD patterns to rutile.

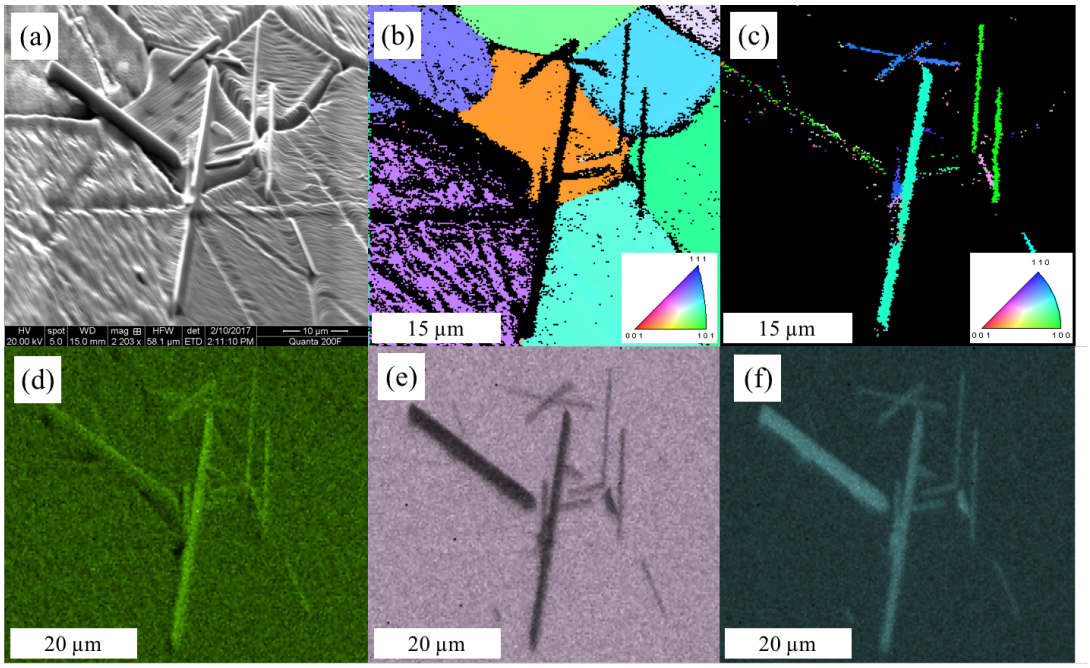


**Figure 37.** $TiO_2$ particles on the surface of $SrTiO_3$ after annealing at 1550 °C, 1250 °C, and 1350 °C. (a) SEM image, (b) the orientation map of $SrTiO_3$, (c) the orientation map of rutile, (d) EDS map of oxygen, (e) EDS map of strontium and (f) EDS map of titanium, where the brighter pixels on the EDS map represent the presence of that particular element.

The sample annealed and grooved at 1550 °C (without the subsequent lower temperature treatments) reveals evidence that these irreversible changes started during the high temperature anneal with the formation of a liquid phase at the grain boundaries. The SEM image in Figure 38 (a) and supporting STEM images of the cross section of that grain boundary Figure 38 (b and c) shows evidence of what appears to be a wetting phase at the grain boundaries. In Figure 39 the thermal groove profiles corresponding to grain boundaries containing $TiO_2$ for the 1550 °C annealed and grooved $SrTiO_3$ sample are illustrated. Because of the presence of a wetted film at the grain boundary, the depth of the groove is inhibited and therefore the shape measured does not correspond to surface diffusion assumptions for the formation of a thermal groove, Figure 39 (b). Due to the presence of second phase $TiO_2$ at many of the grain boundaries in the 1550 °C sample, the energy measurements from thermal grooving are not considered. Considering that the samples were synthesized to have excess titania, the formation of a liquid about the eutectic temperature is not surprising. However, previous studies of this material at 1550 °C did not report wetting at the grain boundaries in oxidizing atmosphere, only in reducing atmosphere so the thermal groove step could have revealed the second phase on the boundary. [187]

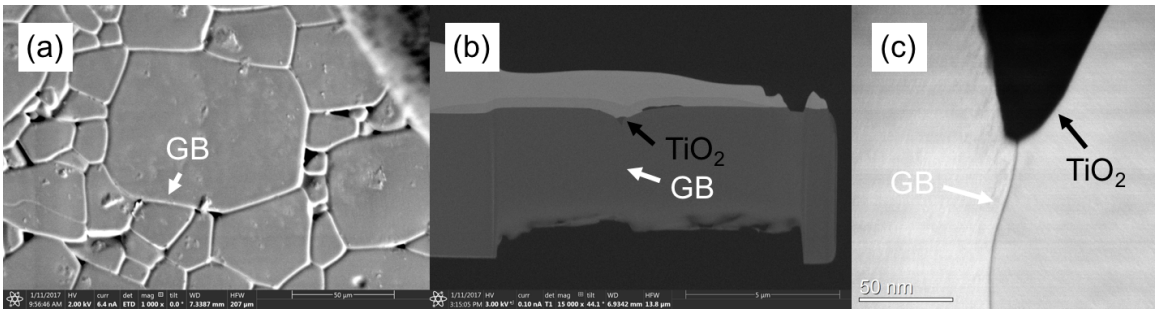


**Figure 38.** $SrTiO_3$ annealed and thermally grooved at 1550 °C. (a) SEM image of the surface with an apparent $TiO_2$ film at the grain boundary (b) BSE image of the cross section of that boundary and (c) HAADF STEM image of the grain boundary and $TiO_2$ film. *Collected by Amanda Krause, Lehigh University

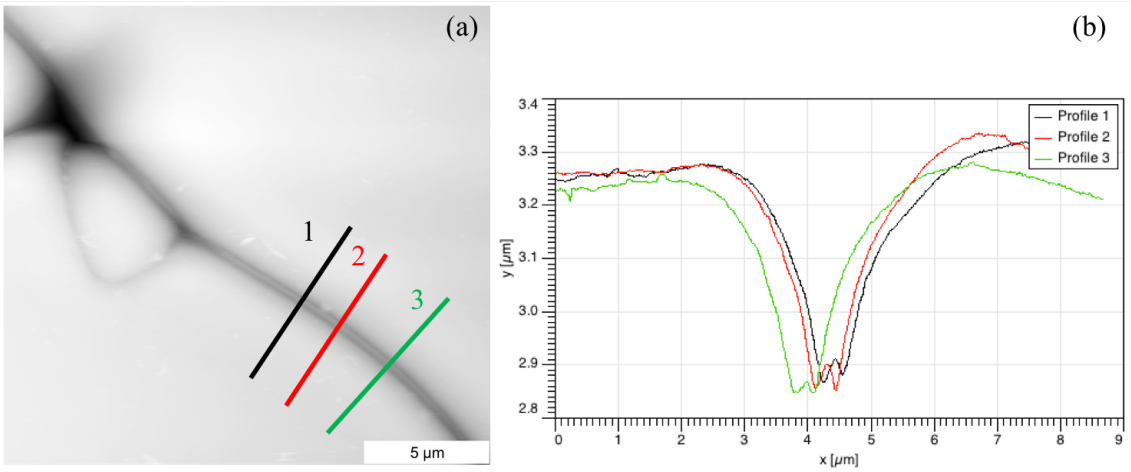


**Figure 39**. (a) AFM image of $SrTiO_3$ annealed and thermally grooved at 1550 °C and (b) corresponding thermal groove profiles of the boundary containing solidified $TiO_2$ eutectic.

In Figure 40, the sample annealed at 1425 °C for 10 hours and grooved at 1425 °C for 5 minutes shows evidence of localized second phase particles at some of the grain boundaries. It should be noted with all of the anneal times and temperature studied at 1425 °C, Table 10, this was the only region that wetting at the grain boundaries was observed.

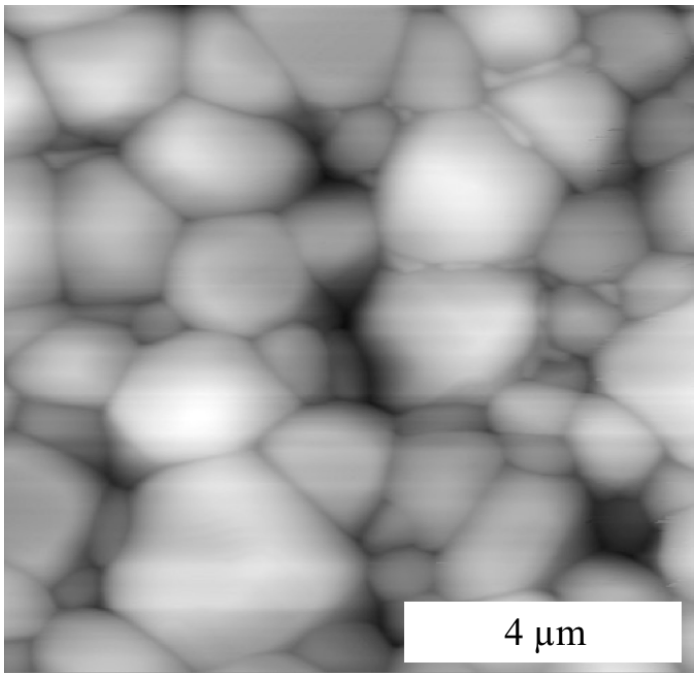


**Figure 40.** $SrTiO_3$ annealed at 1425 °C for 10 hours and grooved at 1425 °C for 5 minutes. Potential solidified liquid eutectic at the boundaries of some of the grains.

The grain boundary plane distribution for the sample annealed at 1550 °C was measured from two dimensional EBSD maps and compared to the previously reported GBPD at 1300 °C, 1350 °C and 1425 °C (see **Figure 41**). [40] The grain boundary plane distribution for the sample annealed at 1550 °C is comparable to the distributions from samples annealed at 1300 °C and 1350 °C (see **Figure 41**). The grain boundary plane distribution was plotted for two-dimensional EBSD data in a temperature range of 1300 °C to 1550 °C. The data at 1300 °C, 1350 °C and 1425 °C is reproduced from Rheinheimer et al.[40] and new data at 1550 °C is collected and presented here, in this document. From 1300 °C to 1550 °C the area fraction of {001} grain boundaries is larger than {111} and {101} type boundaries. At 1425 °C, the {001} population reaches its maximum at 1.76 MRD. Additional data not available in the previous work[40] shows that at 1550 °C, the population of {001} type boundaries is less than at 1425 °C.

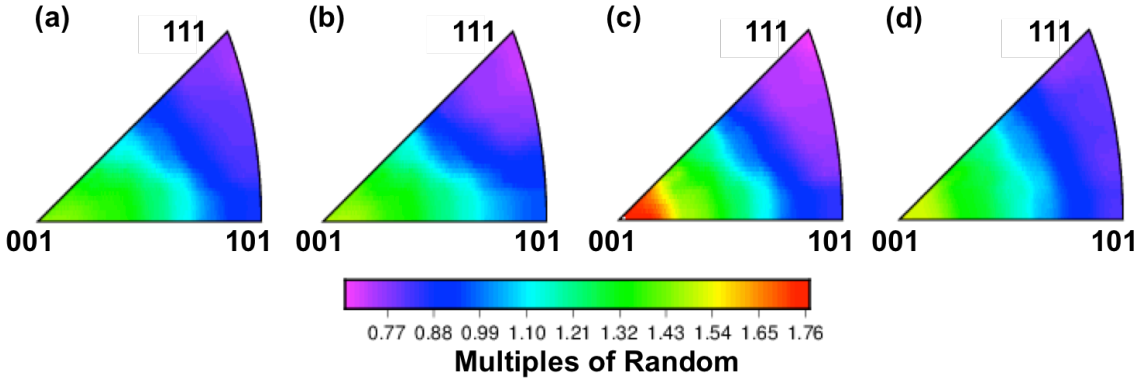


**Figure 41.** The distribution of grain boundary planes, ignoring misorientation, for samples annealed at (a) 1300 °C (b) 1350 °C (c) 1425 °C and (d) 1550 °C $SrTiO_3$. Plots a-c are reproduced from reference[40] for comparison.

The relative grain boundary energies were calculated for $SrTiO_3$ annealed and thermally grooved at 1350 °C, 1390 °C, 1400 °C, and 1350 °C (after heating to 1550 °C). **Figure 42** shows the measured distribution of relative grain boundary energies for each sample. Considering the median value (a cumulative fraction of 0.5) the sample with the highest median relative grain boundary energy is 1350 °C (after heating to 1550 °C) followed by 1350 °C, 1400 °C, and 1390 °C. The values for median and mean grain boundary energy are listed in **Table 12**.

The distribution of relative grain boundary energies at 1400 °C is similar to the distribution of relative grain boundary energies at 1390 °C, as one would expect. The

distribution at 1350 °C appears to have a different shape than at the other temperatures. The width of the distribution is more narrow at 1390 °C and 1400 °C than at 1350 °C. On average, the relative grain boundary energies at 1390 °C and 1400 °C are lower than at 1350 °C. The relative grain boundary energies of the sample annealed at 1350 °C (after heating to 1550 °C) are higher than those annealed at 1350 °C, 1390 °C and 1400 °C.

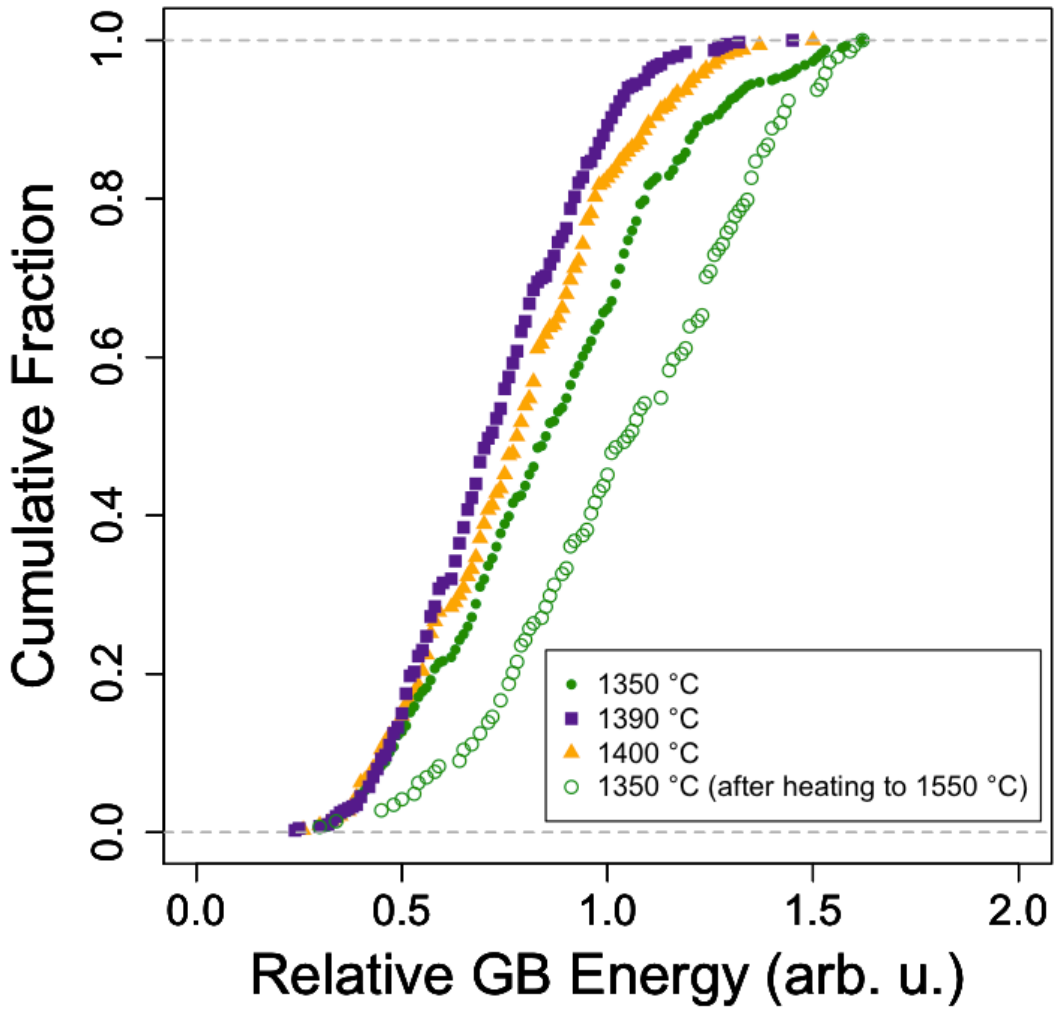


**Figure 42.** The measured distribution of relative grain boundary energies of the all boundaries measured for 1350 °C, 1390 °C, 1400 °C and 1350 °C (after heating to 1550 °C) $SrTiO_3$.

**Table 12.** Median and mean values for 1350 °C, 1390 °C, and 1400 °C.

| | 1350 °C | 1390 °C | 1400 °C | 1350 °C (after heating to 1550 °C) |
|---|---|---|---|---|
| Median | 0.86 | 0.72 | 0.80 | 1.06 |
| Mean | 0.87 | 0.73 | 0.80 | 1.05 |

The mean relative grain boundary energies for all of the grain boundaries measured for all of the samples are summarized in **Figure 43**. The mean relative grain boundary energy decreases from 1350 °C to 1390 °C / 1400 °C. The sample that was first heated to 1550 °C and later grooved at 1350 °C has the highest relative grain boundary energy. The uncertainties in **Figure 43** were calculated using a method reported previously.[184] Briefly, the mean grain boundary energies of ten randomly selected subsets of the complete set of data, each containing half of the data, were calculated. The standard deviation of these ten values was assumed to be the uncertainty of the complete set of data.

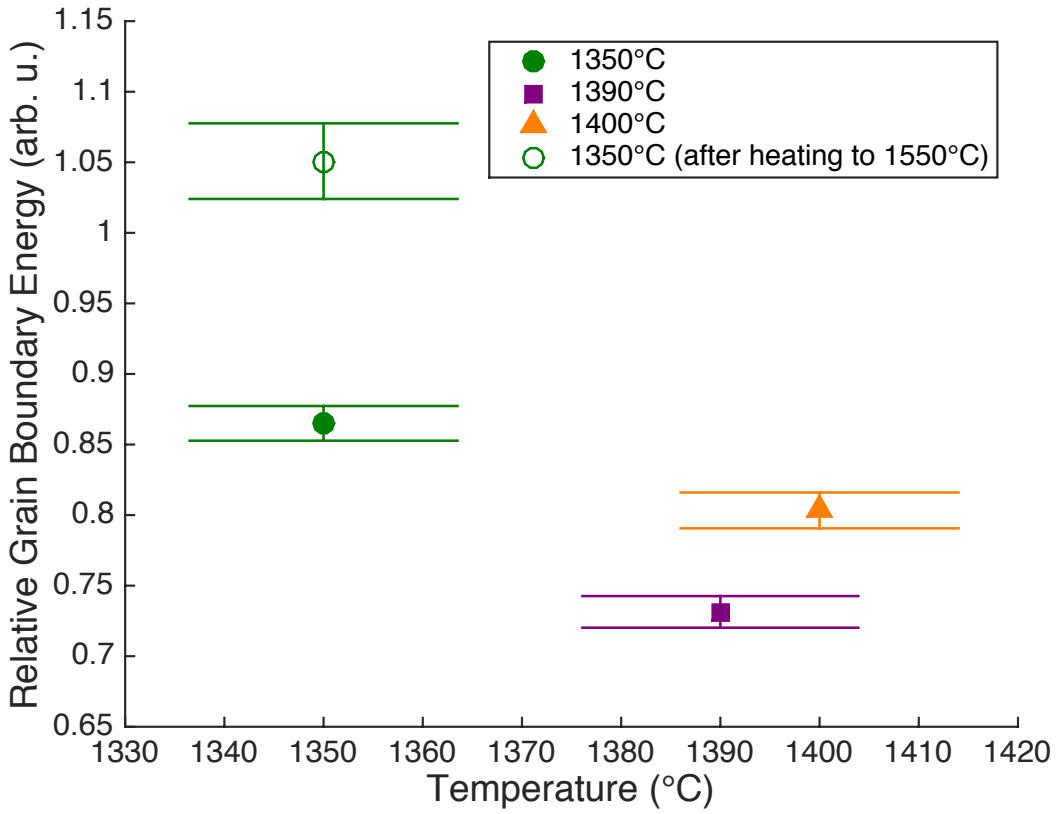


**Figure 43.** Mean relative grain boundary energies of boundaries measured in $SrTiO_3$ samples annealed at different temperatures.

The mean relative grain boundary energies in $SrTiO_3$ are overlaid on the plot of grain growth rate constant with respect to temperature in Figure 44. The shapes and colors of the relative grain boundary energy are the same as in **Figure 43** and the scale for the values of energy are on the left vertical axis. The grain growth rate constant is plotted on the right vertical axis.

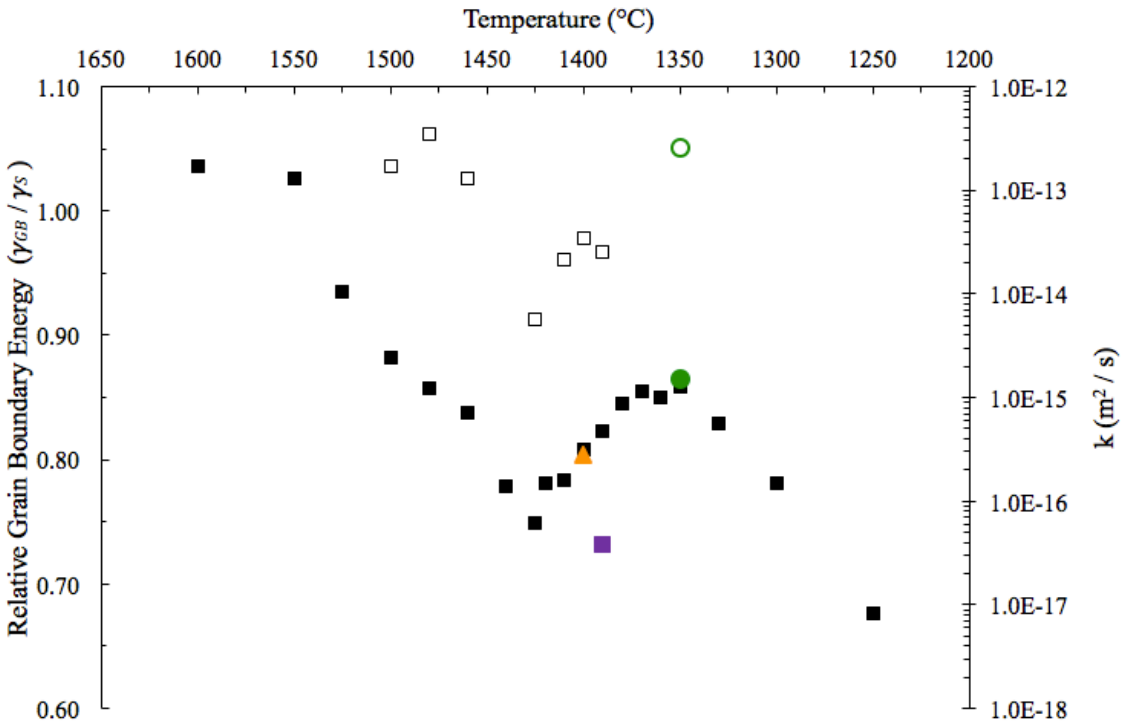


**Figure 44.** Mean relative grain boundary energies of all boundaries measured in $SrTiO_3$ overlaid with the grain growth rate constant data (grain growth rate constant data reproduced from reference[186]). Open squares correspond to grain growth rate constants measured for the average of the largest grains in the microstructure and closed squares represent grain growth rate constants measured for the average of all grains.

Violin plots corresponding to all relative grain boundary energies measured at each temperature are plotted in Figure 45. These were created using the same methods as described in section 6.2.

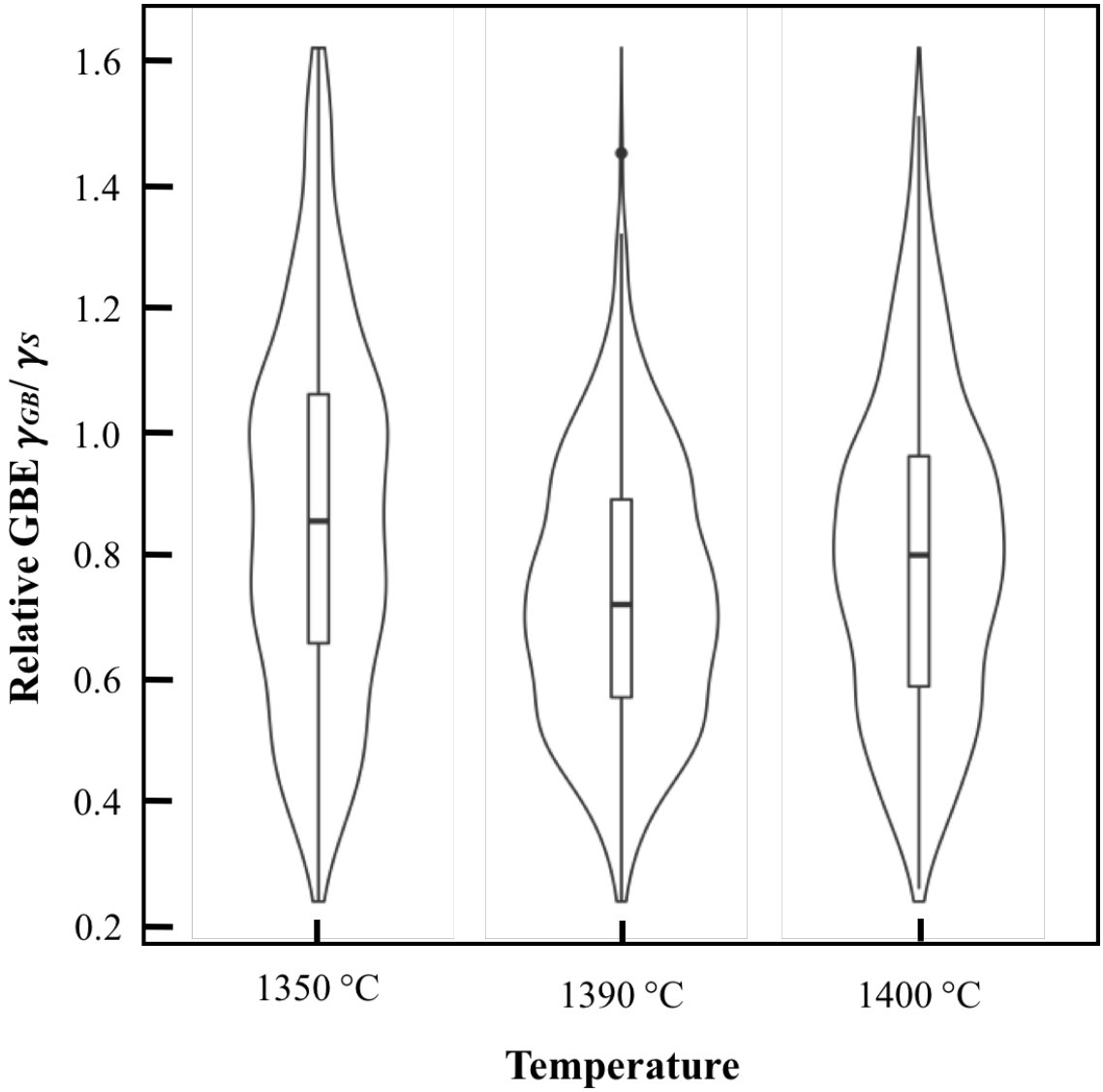


**Figure 45.** Violin plots of $SrTiO_3$ of all of the data collected for grain boundary energies at 1350 °C, 1390 °C and 1400 °C.

Violin plots of the relative grain boundary energies measured for the 1350 °C after heating to 1550 °C sample are plotted in Figure 46 as well as the 1350 °C distribution for direct comparison.

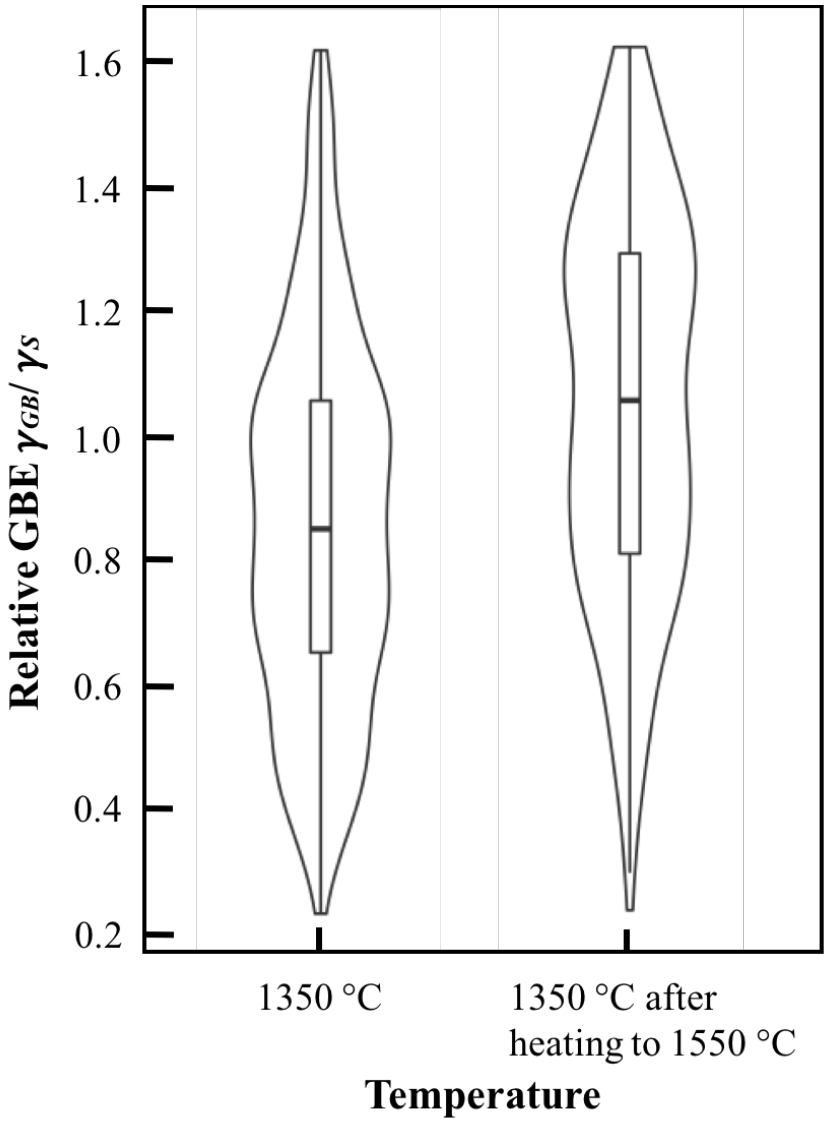


**Figure 46.** Violin plot of the relative grain boundary energies measured at 1350 °C and in comparison to the reversibility sample (1350 °C after heating to 1550 °C).

## 7.4 Discussion

The temperature dependence of the relative grain boundary energy of $SrTiO_3$ is not consistent with expectations of a pure material. These samples have slight Ti excess of Sr/Ti = 0.996, and therefore are expected to be $SrTiO_3$ + $TiO_2$ (provided by the available phase diagram, previous, and current reports) for the measured grain boundary energies presented here at 1350 °C, 1390 °C and 1400 °C .[188] In previous measurements, $TiO_2$ rutile was reported for Sr/Ti = 0.996 at 1400 °C.[25] When heated above the expected eutectic (1440 °C according to the phase diagram) another group reported Ti rich amorphous phase and Sr rich crystalline phase in the triple pockets of samples annealed

at 1440 °C and 1500 °C for Sr/Ti = 0.995.[185] Our results indicated an apparent intragranular $TiO_2$ film at the grain boundaries for the sample heated at 1550 °C, Figure 38. In addition, the 1550 °C sample annealed for 48 hours at 1250 °C and then grooved at 1350 °C for 40 minutes, $TiO_2$ crystalline particles were identified at the surface, Figure 37. In addition, one region in the 1425 °C sample appeared to have some solidified liquid eutectic. However, in the 1425 °C sample, as compared to the 1550 °C sample, the second phase appears to be localized which could be due to localized composition heterogeneity. The microstructure in other regions does not appear to have second phase, or is not obvious, so the presence of this does not appear to have an effect on the microstructure in the 1425 °C sample. If this liquid phase coated all of the boundaries in the 1550 °C sample, then the groove measurements are representative of the $SrTiO_3$/eutectic liquid interface. On the other hand, if there was a mixture of dry and wet boundaries, then the result reflects the average of those boundaries that were sampled. Our results indicate that only some of the boundaries appeared to be coated in eutectic in the 1550 °C. However, the driving force to form the grooves is no longer the $SrTiO_3$ grain boundary energy, but the energy of an interface between $SrTiO_3$ and the eutectic liquid. Therefore, the grooves cannot be used to estimate the grain boundary energy.

TEM images published for a similar stoichiometric ratio and same processing parameters of this system, annealed at 1425 °C, showed segregation of Ti or Sr at the grain boundaries with grain boundary planes oriented so that at least one of the crystals terminated on the (001) plane.[189] Four different boundary types were highlighted in this experiment. They had classified the boundary types straight and atomically flat boundaries as I, straight and disordered boundaries as II, stepped boundaries as III, and curved boundaries as IV. The composition of the boundaries were classified by STEM-EDX and were classified as either “Ti rich” which implies excess Ti or deficient Sr or “Sr-rich” which implies excess Sr or deficient Ti. [189] For types II, III and IV, neutral or Ti rich boundaries were observed by STEM-EDX and type I boundaries were neutral or Sr rich grain boundaries. In addition, more abnormally large grains in the microstructure had type I Sr rich boundaries. The matrix grains were Ti rich. [189] It is interesting to point out that similar to complexion types in doped alumina, it was reported that there appears to be different segregation behavior at the boundaries around abnormal grains than at

boundaries around normal grains. In the experiment that identifies Sr and Ti rich boundaries, no other elements besides Ti or Sr were reported as segregated to the boundaries.

In addition, previous work by the group who synthesized these samples for us at KIT identified unintentional impurities in the pre-sintered powders.[25] They reported the highest impurity as Zr with 600 ppm (by weight), 0.13% molar ratio or 1300 ppm (molar basis) from ICP-OES analysis.[25] Other trace elements of Ca, Ba and Y were also reported. Although the $SrTiO_3$ studied in this case was not intentionally doped, these reported impurity concentrations are on the same order of magnitude as impurities that caused complexion transitions in doped aluminas. The $TiO_2$ particles as well as high impurity levels in these samples possibly contribute to the anti-thermal grain growth behavior observed between 1350 °C and 1425 °C. Changes in grain growth rates are often attributed to changes in the amount of solute adsorbed at grain boundaries which we refer to as complexions.

Previous reports of the grain size distributions for these samples show primarily a unimodal distribution at 1350 °C and bimodal distributions at 1390 °C and 1400 °C with grains as small as 1 μm and as large as 37 μm in diameter. [43] The thermal grooving times for these samples, Table 10, were chosen so that the grain boundary groove widths were larger than 250 μm due to surface diffusivity issues to create a thermal groove shape, discussed in the methods 4.1.7. As a result, it was observed for the smallest grains, the grain surfaces had a single rounded shape and did not have independent grain boundary grooves. In addition, grooving for shorter times or lower temperatures, as was attempted for the 1425 °C samples that had primarily small grains (< 2.5 μm), Table 10, was not effective to create an independent shape. We found that grooves around grains larger than 3 μm had independent grooves and so measurements were made for grains sizes above this threshold. A few grains for the 1350 °C sample had the rounded shape Figure 34 (a) but were a very low area frequency of the total grain sizes in the distribution **Figure 4**. The bimodal distributions at 1390 °C and 1400 °C have a large area frequency of small grains however, so the influence of excluding the small grains must be considered. Looking at the grain size distribution in **Figure 4** the highest area frequency of grains at 1390 °C and 1400 °C is 5 μm with a high frequency of grains smaller than 10 μm as well.

The samples also contain few grains (less than 5% area frequency) larger than 10 μm. In each of the scan areas collected via AFM (20 μm x 50 μm) grain size measurements corresponding to thermal grooves measured were made from grains fully contained in the area and ranged between 4 μm and 16 μm in diameter. Many grains were cut off on the edges of the scan are so it is possible that grains larger than 16 μm were sampled over. However, a majority of the grains seemed to fully fit into the scan area. Because there is a high area frequency of grains smaller then 10 μm the measurements reported here are sampling over more of the small grains in the distribution. In addition, the grain sizes at 1350 °C are larger on average so more of the larger grains were sampled over at this temperature. The results in **Figure 43** show that the mean relative grain boundary decreases from 1350 °C to 1390 °C by 16%. The ratio of the relative grain boundary energies measured at 1350 °C, where large grains were measured, over the relative grain boundary energy of the averaged 1390 °C, 1400 °C small grains measured is $\frac{\left(\frac{\gamma_{GB}}{\gamma_S}\right)_{1350\,°C}}{\left(\frac{\gamma_{GB}}{\gamma_S}\right)_{\text{Avg of } 1390\,°C \,\&\, 1400\,°C}} = 0.89$.

For pure materials, there should be a decrease in relative grain boundary energy with increasing temperature due to the entropic contribution to the free energy. If we assume the simplified model for the grain boundary free energy, $\gamma = \Delta H - T\Delta S - \Sigma\mu\Gamma$ can be used, $\gamma$ is the interfacial free energy, $\Delta H$ is the change in enthalpy, T is the temperature, S is the change in entropy, $\mu$ is the chemical potential times and Γ is the adsorption at the interface. For a pure system, the impurity adsorption to the grain boundary should be zero so the main contributing factor to the interfacial free energy, with increasing temperature, should be the entropy. As we increase the temperature of the system, the grain boundary free energy should decrease. For an impure system, the adsorption term should dominate and as temperature is increased the solute accommodated at the grain boundaries should go back into the bulk and the adsorption term should decrease, yielding an increase of grain boundary energy with increased temperature. As discussed above, it is speculated that $SrTiO_3$ studied here is impure due to excess titania and impurities. Unfortunately, here, it is difficult to interpret the trend from 1350 °C to 1550 °C because an intergranular second phase was seen at 1550 °C so the results were deemed unreliable. No intermediate samples were taken to discover if the

second phase formed earlier. In previous reports of the temperature dependence of yttria doped alumina, for 500 ppm yttria, a second phase formed but it was not coating all of the grain boundaries, it was in isolated particles. Here, the liquid eutectic seems to coat many of the grain boundaries.

Trends of the temperature dependence of grain boundary energy for doped and 99.995 % pure alumina were previously measured and the expected trends were observed.[184] For both pure and doped materials, one expects the temperature dependence of grain boundary energy to be continuous. However, if there is a discontinuous change, it is likely that an abrupt transition in the structure or composition of the boundary has occurred, for example a complexion transition.[74] The 16 % reduction in the grain boundary energy of $SrTiO_3$ measured between 1350 °C 1390 °C is thought to be the result of a grain boundary complexion transition. Previous work has shown that the anisotropy of surface energy, determined using the Wulff construction from the equilibrium shapes of pores, appears to decrease with increasing temperature. [44] Because relative grain boundary energy is the ratio of grain boundary energy to surface energy, changes in the surface energy will affect the energy ratio. However, the magnitude of that change could not account for the 16 % reduction in the average of the relative grain boundary energy. This is consistent with changes previous observed for complexion transitions. While past structural studies do not show evidence of a structural transition, the impurity content of these materials (up to $10^3$ ppm) are the same order of magnitude as other materials where complexion transitions. In addition, it has been shown that changes in grain boundary character distribution are indicators of complexion transitions.

Results from previous measurements of the GBPD in these $SrTiO_3$ samples between 1300 °C and 1425 °C indicated an increase in the population of grain boundary planes with {001} orientations, Figure 38. [40] It has been observed that GBPD is inversely correlated to grain boundary energy.[105, 181] Therefore, in addition to the thermal groove measurements showing the relative grain boundary energy decreases from 1350 °C to 1390 °C, the grain boundary energy continues to decrease with increasing temperature until 1425 °C. New GBPD measurements at 1550 °C show that the population of grain boundary planes with {001} orientations are similar to fractions of those of the lower temperatures (1300 °C and 1350 °C), **Figure 41**. However, solidified liquid eutectic was

found to wet the boundaries at 1550 °C so the distributions cannot be directly compared to the lower temperature data. This is due to the dissociation of single $SrTiO_3$ grain boundaries to two interfaces adjoining the solidified liquid phase (see **Figure 8**). The EBSD technique, used to make GBPDs, can only capture orientations of crystalline materials and unfortunately the solidified liquid phase observed must be considered in order to interpret the misorientation between crystalline $SrTiO_3$ and the solidified liquid eutectic. Therefore, the GBPD plotted at 1550 °C is not representative of $SrTiO_3$ / solidified liquid eutectic interfaces and cannot be directly compared to the lower temperature GBPDs.

A TEM study of grain boundary faceting in $SrTiO_3$ yielded results consistent with the GBPD observations. When observing grain boundary planes in $SrTiO_3$, annealed at 1300 °C, Bäuer et al. did not find any grain boundary planes parallel to {100} but at 1425 °C almost 50 % of the grain boundary planes were oriented parallel to {100}.[39] The GBPD results show that in samples annealed at 1300 °C **Figure 41** (a), there was a lower area fraction of {001} than at 1425 °C **Figure 41** (c). In $SrTiO_3$, the mobility has also been measured previously for single crystal / polycrystal interfaces to determine relative mobility. [44] The correlation of mobility of specific orientations to grain boundary energy can give us some insight onto which orientations are most influential in the non-Arrhenius region.

In a similar temperature region (1250 °C to 1600 °C) for $SrTiO_3$, the relative mobilites of specific orientations were previously measured by observing the migration of a single crystal into an adjacent polycrystalline matrix at specific annealing times and temperatures. [44] Results showed that at 1375 °C the mobility of grain boundary planes with (100) orientations decreased the most while all other orientations increased in mobility. This is interesting in comparison to the GBPD results at a close temperature (1425 °C) and the grain growth rate constants reported. [41] The GBPD showed that the grain boundary planes with (100) orientations had the highest relative area which also correspond to low energy. [40] This could indicate that the grain boundary planes with (100) orientations, are transitioning to the slow grain boundary type more than other orientations. Because of the decrease in mobility this also gives some initial indication that the grain boundaries are transitioning to slower boundaries. This is contrary to what

happened in doped alumina, where higher temperature grain boundary complexions are increasingly more mobile.

The figure overlaying the grain growth rate constant and average grain boundary energies, Figure 44, indicates that the grain boundary energies measured in the transition region, at 1390 °C, have reduced energies in the same temperature region where the mobility is reduced. This indicates, again, that the grain boundaries could be transitioning to the slow type boundaries in the non-Arrhenius region. On a similar note, the boundary velocity is the product of driving force and mobility.[53] The reduced grain boundary energy would reduce the driving force for growth in the non-Arrhenius grain growth region.

The sintering temperature of 1425 °C was chosen because of the stability of grain size with sintering time. In comparison to other temperatures attempted for sintering (1300 °C to 1600 °C) 1425 °C had the least amount of grain growth between 0 and 20 hours of sintering.[45] This suggests that the grain boundaries are in their low mobility state during the initial sintering. After this treatment, when heated at lower temperatures, we believe that the grain boundaries transform back to the fast (high mobility) state. Then, once the temperature exceeds 1350 °C some boundaries stay fast and some boundaries transform to the slow type which was observed by a reduction in grain boundary energy of the small grains. When heated to 1425 °C again, after initial sintering, almost all of the grain boundaries transform to the slow state and thus results in a microstructure with little to no grain growth as compared to the initial sintered state.

Similarly, in doped alumina the grain size distribution begins unimodal, is bimodal at higher temperatures, and then unimodal again at even higher temperatures except an increased average grain size is observed for increased temperature, **Table 7**. In the bimodal distributions (e.g. Nd doped alumina), abnormal grains had a higher mobility complexion type, low in energy and the small grains had a low mobility complexion type, high in energy.[1] Because the grain size distribution began unimodal, the reduction in energy observed with abnormal grain growth is believed to cause the change in low to high mobility complexion. After abnormal grain growth, the average grain size increases, likely from the high mobility boundaries of the large abnormal grains "eating up" the small, low mobility grains. In $SrTiO_3$, a similar concept is observed. The primary

difference is that the grains in $SrTiO_3$, we believe, begin with high mobility and transition to low mobility in fractional increments until most are in the low in mobility state at 1425 °C. In doped alumina the boundaries begin in the low mobility state and transition to high mobility and a fraction of these grains transition but eat up the small grains so those boundaries do not have to transition. In both doped alumina and $SrTiO_3$ the transitions are induced by a reduction in grain boundary energy.

In alumina, the coexistence of different structured grain boundaries lead to abnormal grain growth. Here, for $SrTiO_3$, the similar coexistence of two properties, (1) structurally distinct segregation at the grain boundaries and (2) abrupt changes in microstructure, such as abnormal grain growth, suggests a similar grain boundary transition and is occurring in this system. This suggests that the grain boundary transition is a complexion transition and increases the fraction of lowest energy grain boundary types. The temperature dependence of the relative grain boundary energy appears to behave like the temperature dependence of yttria doped alumina system, which is not surprising from the impurities reported in this system.[184]

## 7.5 Conclusion

Liquid eutectic was found to wet grain boundaries of samples annealed and grooved at 1550 °C. GBPD plotted at 1550 °C is not representative of the structure due to solidified liquid eutectic at the interfaces that could not be captured by EBSD. Relative grain boundary energies were measured between 1350 °C and 1400 °C, a region where anti-thermal grain growth was observed. There was an abrupt, 16 %, decrease in relative grain boundary from 1350 °C to 1390 °C. Abnormally large grains were also observed at 1390 °C and 1400 °C. The GBPD of the sample annealed at 1550 °C was measured using stereology.

# 8 GBCDs and Internal Dihedral angles from 3D volumes of $SrTiO_3$ by PFIB

Portions of introduction and methods:
M.N. Kelly, K. Glowinski, N.T. Nuhfer, and G.S. Rohrer, "The five parameter grain boundary character distribution of α-Ti determined from three-dimensional orientation data," *Acta Mater.*, **111** 22–30 (2016).

## 8.1 Introduction

In recent years, several techniques have been used to determine the three-dimensional (3D) microstructure of metallic and ceramic polycrystals.[190–195] These studies make it possible to measure the quantitative characteristics of microstructures that can only be estimated from two-dimensional sections. In particular, they can be used to define all five of the crystallographic parameters of grain boundaries, which are known to influence materials properties such as corrosion resistance[196], electrical resistance[197], and strength[198]. The most common technique for 3D microstructure studies has been focused ion beam (FIB) serial sectioning in a scanning electron microscope (SEM)[75, 104, 165, 199–201]. In this experiment, the crystal orientations are mapped in a section plane, a Ga-ion beam is used to remove a thin layer, and the orientation mapping is repeated. A 3D orientation map can then be constructed from the resulting set of parallel layers. The main limitation of the FIB SEM experiment is the time it takes to remove the material with the Ga-ion beam. Collecting a volume of data 1 x $10^5$ μm$^3$ (a typical volume in past studies) requires several continuous days of automated data collection. Assuming a grain diameter of about 5 μm, this volume contains approximately $10^3$ grains and 7 x $10^3$ grain faces. This is approximately the number of distinguishable grain boundary types in a cubic material, when the boundary parameters are resolved with an accuracy of 10°.[70] The recent availability of commercial Xe plasma focused ion beams (PFIBs) makes it possible to remove material at a faster rate and, in comparable times, characterize a much greater volume of material.[202] Compared to Ga FIBs, the PFIB has a greater current and the ion has a greater mass. As shown in recent work on the Xe plasma FIB, this instrument makes it possible to characterize a volume of at least 4.3 x $10^6$ μm$^3$ , which is more than ten times greater than the volume that has been characterized by the Ga FIB, in a similar amount of time.[203]

For this project, the greater data acquisition speed will make it feasible to collect multiple 3D volumes of cubic $SrTiO_3$ equilibrated at different temperatures. The only known 3D microstructural data of $SrTiO_3$ are from samples annealed at 1470 °C [204] and 1650 °C [205]. In addition, some initial measurements of the GBPD calculated from stereology were published at some of the temperatures[40] of interest but more data is collected and analyzed here for higher anneal temperatures (1550 °C). The purpose of this chapter is to analyze the grain boundary populations related to the anti-thermal region found in $SrTiO_3$ with the goal of understanding how changes in the GBCD, GBED and internal dihedral angles correlate with the grain growth transitions and the relative grain boundary energy measurements made in section 6. The internal dihedral angles measured from the 3D volumes will be used to infer energy changes in the microstructure for boundaries that could not be measured by thermal grooving in 6.

We hypothesize, again, that there might be a grain boundary complexion transition in this temperature range. If so, we expect to find a difference in the internal dihedral angles (grain boundary energies) of grain boundaries that have transformed to the lower energy, lower grain growth rate constant complexion and those that have not. We also hypothesize that at the end of the anti-thermal region, 1425 °C, the most frequent grain boundary planes will have minima in the GBED. Measurements of internal grain boundary dihedral angles for bimodal microstructures in the transition region demonstrate the coexistence of higher energy grain boundaries around grains with a high grain growth rate constant and lower energy grain boundaries around grains with a low grain growth rate constant. The Xe plasma FIB will be used to characterize the 3D microstructure of sample annealed at a temperature before grain growth transitions are detected (1350 °C), during the transition (1390 °C), and at the end of the transition (1425 °C). The GBPD, GBCD and GBED are plotted at the end of the transition and dihedral angles of all three 3D microstructures are compared. These grain boundary populations and grain boundary character distributions are calculated and compared to 2D GBPDs and new 2D GBPD of $SrTiO_3$ at 1550 °C anneal temperature.

## 8.2 Experimental Procedure

### 8.2.1 Data Acquisition

Three-dimensional serial sectioning was used to study the internal grain boundary structure of the $SrTiO_3$ sample annealed at 1350 °C, 1390 °C and 1425 °C. Each sample was synthesized by the same methods described in 7.2. The samples annealed at 1390 °C and 1425 °C were prepared for 3D Xe Plasma-FIB SEM by first fracturing the material with a razor blade and selecting the sharpest piece with tweezers. The pointed piece, approximately 30 μm wide, was adhered with silver paint onto the 36° side of a 36° / 54° pre-tilted holder. The sample annealed at 1350 °C was polished flat so that the polished side was parallel to the tilted holder and material behind the pillar was milled away to create a rectangular shape. This made it possible to accurately measure the amount of material that was milled away from recorded images before and after milling. We found that on the polished surface the milled amount was correct but on pyramidal shaped pillars the amount removed is less accurate because the fiducial mark can become distorted from the rocking positions. Figure 47 shows images of the pillar. Figure 46 (a) is the ion image collected to place the cut position and (b) is the electron image collected at the rotated position used to collect EBSD data.

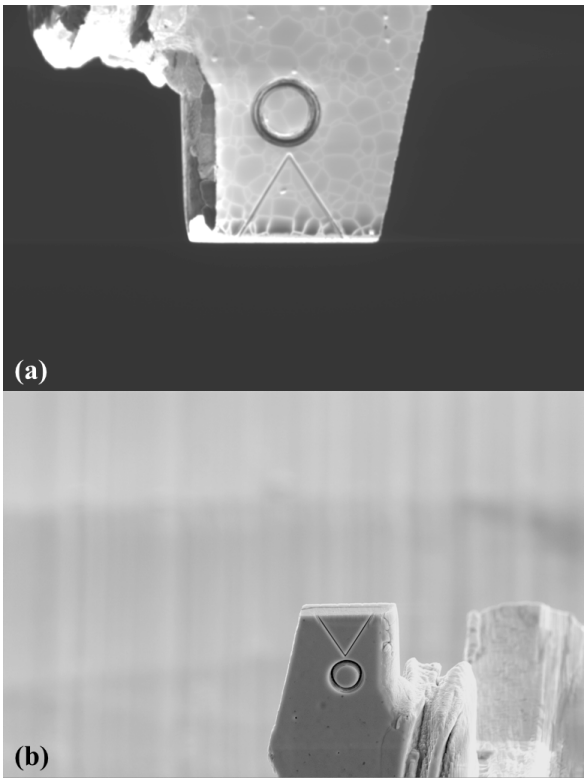


**Figure 47.** Images of the pillar used to collect the 1350 °C dataset. The top image (a) is at the mill position which was collected from the ion beam and the bottom image (b) is at the EBSD position which was collected from the electron beam.

FEI's Helios$^{TM}$ PFIB Dual-Beam was used to collect the data. The FEI AutoSlice and View (EBS3 G3) software was used to control the milling and Oxford's Aztec system was used to obtain orientation mapping for each slice. A schematic of the system is provided in **Figure 48**, illustrating the geometry of the specimen and beams. The specimen was mounted onto a 36° angle pre-tilted holder and the horizontal axes of the sample holder and stage were aligned (these axes are perpendicular to the page in **Figure 48**). The vertical position was adjusted so that the region of interest was 4 mm from the pole piece. The stage was then tilted to 16°, which brings the region of interest to an inclination of 70° with respect to the electron beam for electron backscatter diffraction (EBSD) pattern collection; this is referred to as the EBSD position (see **Figure 48**(a)). For milling with the Xe-ion beam, the stage is rotated 180° around the z-axis of the stage, so that the region of interest is parallel to the ion beam; this is referred to as the milling position (see **Figure 48**(b)). The region of interest (ROI), which is perpendicular to the

page in **Figure 48**(a) and (b), is shown in an oblique projection of the sample in **Figure 48**(c).

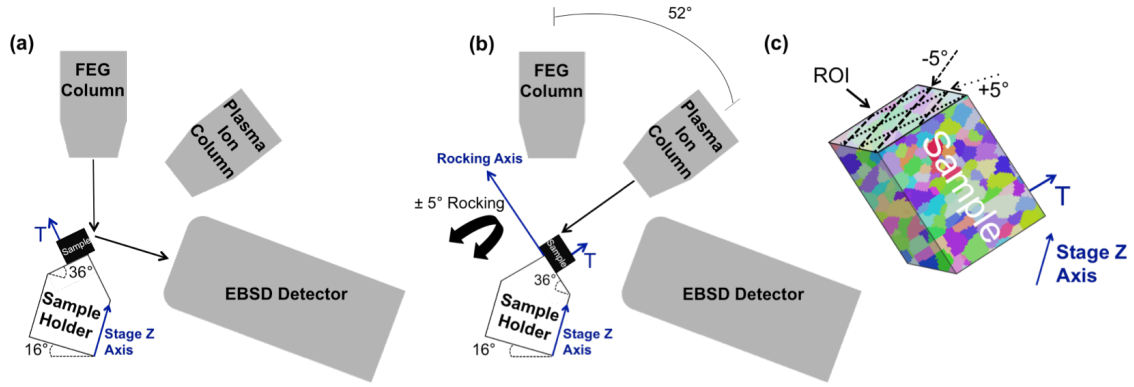


**Figure 48.** Schematic of the Xe-ion PFIB. (a) In the EBSD position, the region of interest (ROI) makes a 70° angle with the electron beam. (b) In the milling position, the ROI is parallel to the Xe-ion beam. The change from the EBSD position to the milling position is accomplished by a 180° rotation around the z-axis. (c) In oblique projection, the ROI is visible and the paths of the ions in the two different positions are shown by the dashed lines.

An X-shaped fiducial mark was milled into the pillar at a position just below the region of interest. Typically, a Pt layer is deposited over the region of interest before milling a fiducial mark to reduce charging and increase the contrast of the fiducial mark. In this case, however, it was found that the contrast between the sample and the fiducial mark was sufficient and a Pt layer was not needed. The increased contrast is important because the AutoSlice and View software must recognize the fiducial mark to re-align the pillar with each mill step so that the amount of material removed and the position of each EBSD scan is consistent. The through-the-lens detector performed better than the Everhart-Thornley detector for imaging the fiducial mark. For the AutoSlice and View (EBS3 G3) software to be initialized, it is necessary for the following conditions to be met; the *Z* position is linked to working distance, the horizontal field width less than 450 μm, and the third party detector interface (Oxford Aztec) is ready. The milling parameters were set up. In this case, the image resolution for the ion beam was set to yield pixels sizes of at least half of the thickness used for cutting to ensure cut placement by the program would be as accurate as possible. We found that if the pillar took up a majority of the width of the electron image, the auto contrast brightness function would more successfully recognize the fiducial mark.

The $SrTiO_3$ 1350 °C data set is made up of a single volume, the 1390 °C dataset is made up of two volumes and the 1425 °C data set is made up of a two volumes as well. The samples were ion milled at 30 kV and either 15 nA or 6.7 nA (6.7 nA was used if the 15 nA lens was too worn) using the PFIB. The EBSD data were collected using a 30 kV and 5.5 nA beam. A "rocking mill" with a 5° angle was used to minimize curtaining. In this procedure, the sample is milled at two different angles, +/- 5° about the rocking axis in **Figure 48**(b). This is accomplished by a compound stage tilt. While the manufacturer's term, rocking, suggests continuous motion, the sample is actually fixed in one of the two positions during milling. The paths of the ions in the two positions are illustrated by the lines on the region of interest in **Figure 48**(c). For EBSD pattern collection, the camera was set to 4x4 pixel binning, an integration time of 4 ms (2.3 ms for 1390 °C data collected at the University of Manchester), camera gain of 15, and two frames were averaged for each point. For indexing, we used band center detection, refined accuracy, auto and static background collection, a Hough resolution of 80, and orientations were determined from 12 bands.

Three-dimensional serial sectioning was also used to study the internal grain boundary structure of the $SrTiO_3$ sample annealed at 1350 °C. The 3D volume collected of $SrTiO_3$ annealed at 1350 °C was a single volume consisting of 342 parallel sections of 60 μm x 17 μm area EBSD scans sliced at 100 nm separation. Each of the EBSD maps contained unindexed area beyond the edge of the pillar. Therefore, in the 3D volume depicted in Figure 49, the edges were cropped so that only the rectangular volume is in view. An example image of one of the 2D maps is illustrated in Figure 50 where the grains are numbered and the regions of unindexed pixels beyond the edge of the pillar are colored black.

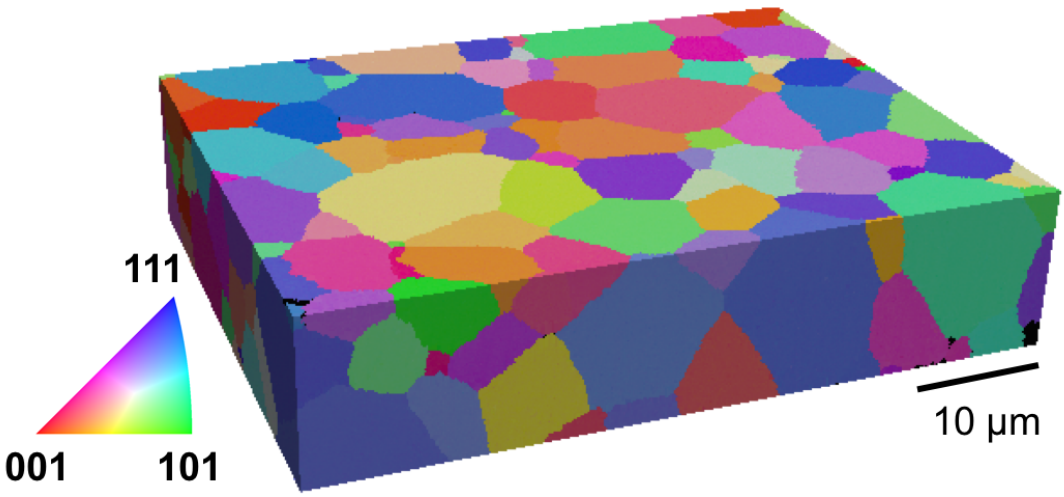


**Figure 49.** Three-dimensional orientation maps after cleanup and reconstruction of the sample annealed at 1350 °C. Maps are color coded by orientation according to the legend.

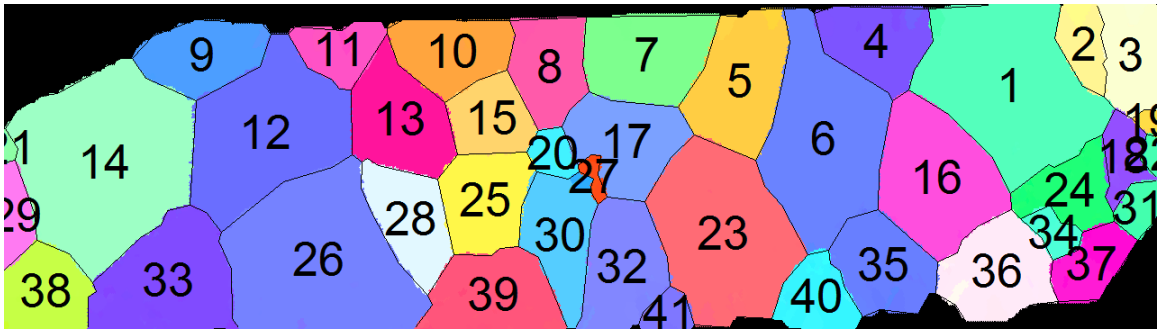


**Figure 50.** EBSD map of a section of the 1350 °C 3D volume. The solid colors represent grains which are indexed and included in the volume. The black areas are empty space beyond the edge of the pillar. Each number labels a grain encompassed by the grain boundaries which are outlined in black.

Three-dimensional serial sectioning was used to study the internal grain boundary structure of the $SrTiO_3$ sample annealed at 1390 °C. Two parallel but discontinuous volumes were sampled. The larger of the two consisted of 28 parallel layers, each 29 µm x 44 µm, and separated by 100 nm (see Figure 51 (a)). The smaller of the two volumes consisted of 13 parallel layers with the same dimensions and spacing as the first volume (see Figure 51 (b)). Three-dimensional orientation maps were reconstructed from the data using DREAM.3D.[152] The data were exported from the Aztec software in the CTF

file format that could be imported by DREAM.3D. The reconstruction was used only to produce the images for 1350 °C Figure 49, 1390 °C in Figure 51, and 1425 °C **Figure 52**.

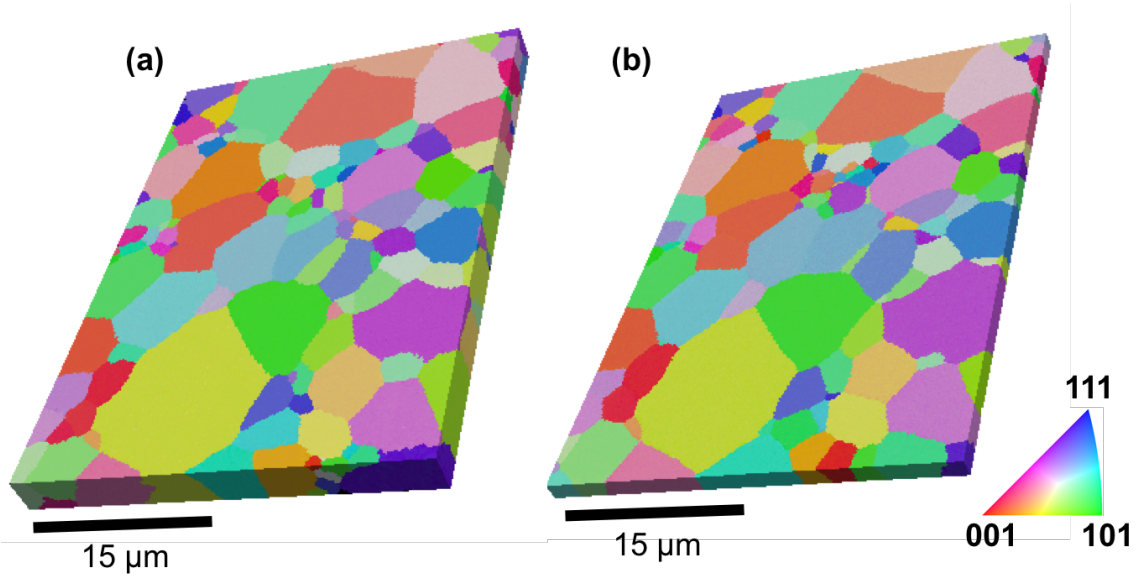


**Figure 51.** Three-dimensional orientation maps after cleanup and reconstruction of the larger (a) and smaller (b) volumes of the $SrTiO_3$ sample annealed at1390 °C. Maps are color coded by orientation according to the legend.

Three-dimensional serial sectioning was used to study the internal grain boundary structure of the $SrTiO_3$ sample annealed at 1425 °C. The analyzed volume of $SrTiO_3$ annealed at 1425 °C was 6,300 $\mu m^3$ as illustrated in **Figure 52**. Two parallel but discontinuous volumes were sampled. The larger of the two consisted 46 parallel layers. of 23.5 µm x 22 µm separated by 200 nm **Figure 52** (a) and the smaller consisted of 27 parallel layers of 24 µm x 24 µm separated by 100 nm. The grains in the reconstructed three dimensional orientation maps are color coded by orientation according to the legend. These two volumes contained a total of 3,049 grains, 20,729 grain faces and 2,725,756 triangular segments. This 1425 °C volume contained enough distinguishable grain boundaries to analyze the five parameter grain boundary character distribution.

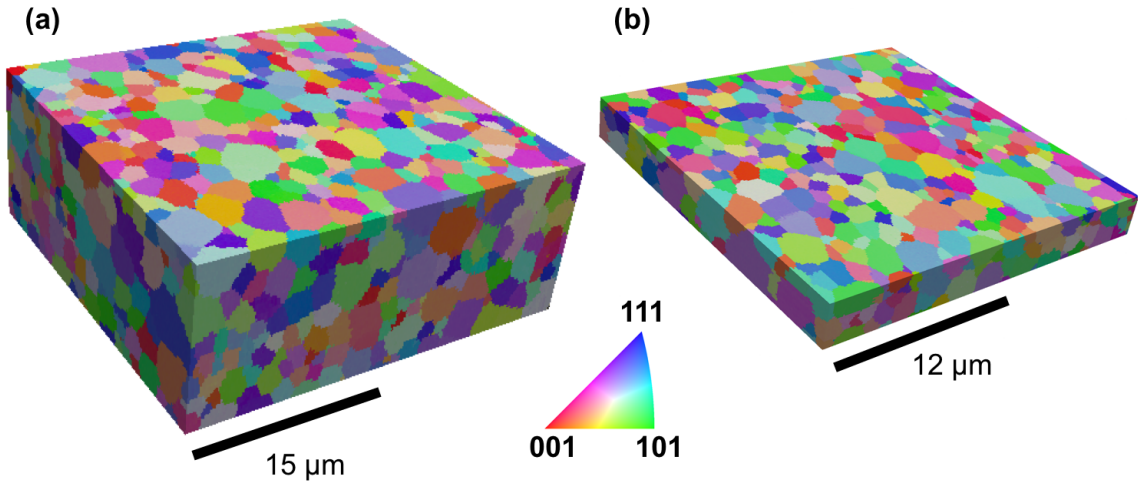


**Figure 52**. Three-dimensional orientation maps after cleanup and reconstruction of the larger (a) and smaller (b) volumes of the $SrTiO_3$ sample annealed at 1425 °C. Maps are color coded by orientation according to the legend.

### 8.2.2 Post Processing and Reconstruction

Once the data were collected, the default Oxford 3D file type (CPR) was converted to the CTF file type first by exporting as individual CPR files in Aztec software. Then each individual file had to be read into Oxford's Project Manager software and exported as a CTF file. The CTF files were used for subsequent reconstruction and clean-up procedures in DREAM.3D [152]. The steps used in this process, known as a 'pipeline', were essentially the same as the pre-set reconstruction and clean-up pipelines provided in DREAM.3D, except for the parameters that were particular to this dataset. Briefly, the stacks of 2D EBSD maps were aligned such that the overlap of pixels of similar orientations, belonging to adjacent slices and differing by no more than 5°, was maximized. The EBSD data were first aligned with a misorientation tolerance of 5°. The data was cropped so that the grains were all within a rectangular volume. Then the data was cleaned, first, by iteratively ascribing the parameters (orientations, image quality, etc.) of the most reliable neighbors to all voxels with undetermined orientations. Clusters of at least 16 voxels, whose orientations deviated from one another by less than 5°, were grouped into grains and average orientations were assigned to each grain. In addition, grains with fewer than three neighbors were removed. The reconstructed three

dimensional orientation maps, after clean-up, are shown in Figure 50, Figure 51, and **Figure 52**. Note that the orientations are colored with respect to the normal of the surface analyzed by EBSD. The surfaces of boundaries separating the grains were reconstructed in the form of meshes of planar triangular segments using Laplacian smoothing. For the Laplacian smoothing, 100 iteration steps were used, default lambda of 0.25, triple line lambda of 0.2 and quadruple points lambda of 0.15. For each triangular segment, its normal, area, and misorientation between grains on its sides were determined.

### 8.2.3 Computational Methods: Disorientation distribution, GBPD and GBCD

In this analysis, the Grain Boundary Character Distributions (GBCDs) were computed using the Kernel Density Estimation (KDE) technique which, it has been suggested, leads to more accurate distributions [206] as compared to the conventional partitioning method.[207] In this method the reconstructed and meshed volumes from DREAM.3D[152] can be directly imported into the GBToolbox[208] program. The conventional technique involves counting boundaries within assigned bins of the partitioned boundary space and in the KDE technique, the boundary space is probed at assigned points and the areas of boundaries close to these points are summed. Two limiting radii are used to define the bin shapes in the KDE method. First, the misorientation ($\rho_m$) is chosen and then the boundary plane resolution ($\rho_p$) is chosen. An illustration of the angular dimensions with respect to binning for each method is in **Figure 53** which is reproduced from K. Glowinski's dissertation.[208] In **Figure 53** (a) is an illustration of the partitioning method with 10° bins. In **Figure 53** (c) is an illustration of the KDE method with limiting radius of the boundary planes set to $\rho_p$= 7°. From these two figures we can see that with the KDE method the boundary space can be sampled over more evenly than with conventional binning because spherical domains are used to sample the boundary space. **Figure 53** (b) and (d) are plots of the grain boundary character distributions of the sigma 5 grain boundary type of the partition and KDE methods, respectively. For **Figure 53** (b) 10° bins were used to partition the space and for **Figure 53** (d) $\rho_m$= 5° = $\rho_p$ was used to bin by the KDE method. In these figures we can see that there is less spreading of the dominant peaks for the KDE method, resulting in more accurate GBCDs.

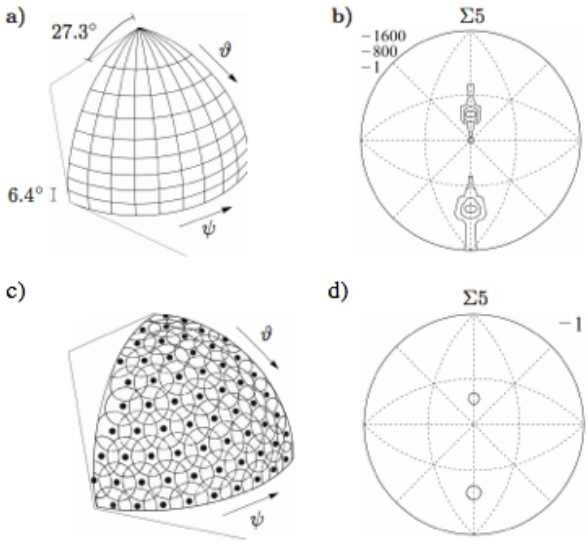


**Figure 53.** (a) Representation of 10° binning by conventional technique and (b) the associated GBCD for sigma 5 grain boundary type. (c) Representation of $\rho_p$= 7° for the KDE technique and (d) GBCD for the sigma 5 grain boundary type with $\rho_m$= 5° = $\rho_p$. Figures are reproduced from K. Glowinski's dissertation.[208]

For the new method, two separate functions are used to define the boundary space instead of one. This is reasonable because the boundary space parameter is comprised of two factors, the boundary normal subspaces and the misorientation. The distance between boundaries, in the boundary normal subspace, is quantified as $min\left[\sqrt{(\chi_L^2+\chi_R^2)/2}\right]$ (L = left grain; R = right grain) where $\chi_i = \cos^{-1}(m_i \cdot m_i')$ ($m_i$ = normal to the first boundary and $m_i'$ = normal to the second boundary). The distance between boundaries, in misorientation subspace, is $min\{\cos^{-1}[(trM'M^T-1)/2]\}$ over all symmetrically representations ($M$ = misorientation matrix of the first boundary and $M'$ = misorientation matrix of the second boundary). The boundary parameter space is computed as a Cartesian product of the boundary normal and the misorientation subspaces.

To calculate a GBCD by this method, the boundary space is probed at the misorientation of interest and vectors are pointed from the center towards evenly scattered points on the hemisphere, which can be visualized in **Figure 53** (c). First, boundary segments that fall within the radius of the specified misorientation tolerance, $\rho_m$, are gathered. Then, the limiting radial distance for boundary plane subspace, $\rho_p$, is used to identify boundary segments whose normal fall within this limiting distance. The

boundary segments (meshed triangles) that fall within each $\rho_p$ and $\rho_m$ are summed, assigned to bins and normalized to be expressed in units of multiples of random distribution (MRD).

The volume of each bin can affect the uncertainty of each distribution. We can estimate this uncertainty by using $v$, the fractional volume of subspace limited by the radii $\rho_p$ and $\rho_m$, $n$, the number of distinct grain boundaries (number of grain faces), the distribution value, $f$, at a given point and $c$ as a coefficient defining correlations in the data. The minimum number of measurements required for relative error can be represented as $n \approx (c/(\varepsilon^2 vf)$ .[208, 209] The data appears to be weakly correlated (comparing the number of distinct grain boundaries (number of grain faces) to the number of segments in a meshed sample (see **Table 13**)) so we can assume $c \approx 1$. The relative error can then be represented as $\varepsilon = (nvf)^{-1/2}$.[208] To determine the absolute error, applicable to the data represented in this document, absolute error is represented as $\sigma = \varepsilon f = \sqrt{\frac{f}{nv}}$ where the distribution value f is $f = f \pm \varepsilon f$.[203]

To compute the distribution of boundary planes, independent of misorientation, mesh triangles corresponding to normals of boundary planes within the limiting radius, $\rho_p$, are summed. This distribution is probed in the same manor that the GBCD is calculated and units are represented as MRD. The Grain Boundary Plane Distribution (GBPD) is then plotted in the standard stereographic triangle for the crystal frame.

The values for limiting radii $\rho_p$ and $\rho_m$ are selected based on experimental resolution of boundary parameters. Previously, it has been found that the resolution of grain boundary planes is about 7.5° [206, 207] so $\rho_p$ was selected as 7° for both the GBPD and GBCDs. For misorienations, the threshold during reconstruction was selected as 5°. For computing GBCDs, $\rho_m$ was selected as 3° which is a higher resolution than the experimental 5° threshold but should yield the same result as choosing 5° because the minimum threshold was 5°.[204]

### 8.2.4 Grain boundary energy computation and TSL data extraction

The data used to compute grain boundary energy from the five parameter distribution was extracted differently than it was for the GBPD and GBCDs. Each of the individual 2D EBSD maps were cleaned in TSL OIM software using grain dilation, single average orientation per grain and grain confidence index standardization each with a tolerance angle of 5° and minimum grain size of 3 pixels. After each of the individual maps were cleaned, the reconstructed segments were exported as individual text files where the boundaries were reconstructed with a tolerance of 2 pixels. In addition, grain identification maps were exported to correspond with each reconstructed segments file for each map to later to be used for the dihedral angle computation.

A set of programs were used to compute the grain boundary energies.[154] Each set of reconstructed segments all belonging to the same 3D volume were first sorted to find where the triple junctions meet on consecutive layers. To do this, each set of line segments were searched to find which end points shared the same coordinates to form a triple point then they were compared to the consecutive layers. The closest 5 coordinates of triple points on the next layer were searched to see if orientations matched and for those that deviated by disorientation angle of less than 5° a triple line was assumed to connect the layers. This data is saved into a new file where the vectors of each layer are saved but also the vector of the connecting triple line and are sorted so they are listed counter clockwise. The cross product of the triple line and the vector tangent to the grain boundary is used to specify the grain boundary normal. The magnitude of the cross product is the area of the boundary plane. The misorientation and boundary normal are used to discretize the grain boundary types. The sum of all of the triangle areas make up the GBCD by the Rohrer method.[154] The GBCDs plotted here are by the Glowinski method[208] but later the normals will be used to compute dihedral angles. There are 6 total triangles for each triple line, 3 for the normals of the three vectors on the top layer and 3 for the normals of the three vectors on the bottom layer.

One would expect a random distribution of orientation of triple lines in the sample reference frame in an equiaxed microstructure. Previous reports have shown that this is not the case, however, and that the distributions are biased which is likely due to an

alignment error.[165] Therefore, a ridged shift is applied to the coordinates so that the triple line direction is not biased.

The grain boundary energies are then computed using a method developed by Morawiec[210] which uses the capillarity vector by looking at the interfacial geometry at equilibrium of a triple line, as described by Herring.[211] This method assumes, as with many other methods to determine grain boundary energy, that the interfacial junctions are at local thermodynamic equilibrium. This technique to measure grain boundary energy has been previously described and applied to different materials but will be summarized briefly here. [165, 207, 210]

The Herring equation involves three capillarity vectors ($\xi$) and a triple line ($l$) which describe three grain boundaries that meet at a triple line. In the expression, $(\xi^1 + \xi^2 + \xi^3)\, X\, l = 0$, $\xi^1$, $\xi^2$ and $\xi^3$ are associated with each of the three grain boundaries. Each vector has a component tangent to the boundary and a component perpendicular to the grain boundary. The magnitude of the tangent vector is the differential of the energy with right handed rotation about $l$ and the magnitude of the normal vector is the relative grain boundary energy. To solve these equations, the normal and tangent directions are known but the magnitudes are unknown and must be solved by iteratively finding the set of capillarity vectors which will satisfy the equations. The number of equations is equal to the number of triple junctions in the dataset. A smoothing parameter is also ascribed to the equations by averaging the vector and adjacent vectors of $\xi$ and replacing $\xi$ with the averaged values. Then the relative grain boundary energy is computed as $\gamma = \xi \cdot n$ where $n$ is the grain boundary normal. It was shown that this method, when compared to simulated data of energy functions that the trends in the data were reproducible but the depth of the cusps were not. Therefore this method may not be quantitatively precise and the actual energy values may be more anisotropic than the results by the capillarity method suggest.[166, 210]

### 8.2.5 Dihedral angle analysis

To compute dihedral angles from the three-dimensional volume, the triple lines and adjoining grain boundaries were reconstructed using in house developed code that has been described in earlier publications.[104, 212] In the first step, the TSL OIM software was used to cleanup the data. The clean-up procedure started with of a grain dilation

operation with a minimum grain size of 5 pixels and minimum misorientation angle of 5°. This was followed by assigning a single average orientation per grain and a grain confidence index standardization. The grain boundaries were then approximated as line segments in each plane, such that the approximate boundary position differed from the true position by no more than two pixels. An example orientation map with the approximated grain boundary line segments overlayed is illustrated in Fig. 7. At the end of this procedure, the coordinates of each line segment were exported with the orientations, sizes, and numerical grain identifier (ID) of the grains on either side of the segment.

The first step of the triple line reconstruction is to identify all of the triple points on each layer by finding those segments with shared coordinates. The triple points on each layer are then compared to determine which are likely connected by a triple line. The connected triple junctions are identified according to two criteria. First, the triple point on the second layer must be one of the five spatially closest to the triple point on the first layer. Second, all three grain orientations at a junction on one layer are misoriented by less than 5° from the grains on the next layer. At the end of this procedure, the set of triple lines in three-dimensions consists of three coplanar grain boundary line segments on one layer, a triple line that originates at the intersection of the boundaries and ends at the intersection of three boundaries on a parallel layer. In addition, each of the three grains is associated with a size parameter. In this case, grains were identified as having diameters smaller than 5 μm or larger than 5 μm for 1390 °C and 1425 °C datasets or smaller than 7 μm or larger than 7 μm for 1350 °C dataset.

The coordinates of the grain boundaries and triple lines define the end points of vectors. The vector perpendicular to each of the three grain boundary planes is determined by the vector product of each grain boundary line segment and the triple line vector. The grain boundary dihedral angles, $\psi_i$, were computed from the scalar product of the grain boundary normal vectors. Following the hypothesis that the grain boundaries surrounding the smallest and largest grains had distinct energies, the dihedral angles were classified as belong to junctions of three small grains (diameter < 5 μm or 7 μm), three large grains (diameter > 5 μm or 7 μm), or a mixture of the two. This means that there are four distinguishable types of junctions. Using the notation '1' for the small grains and

'2' for large grains, the four junction types are 111, 112, 122, and 222. This notation will be used throughout the paper and examples of each type are shown in **Figure 54**.

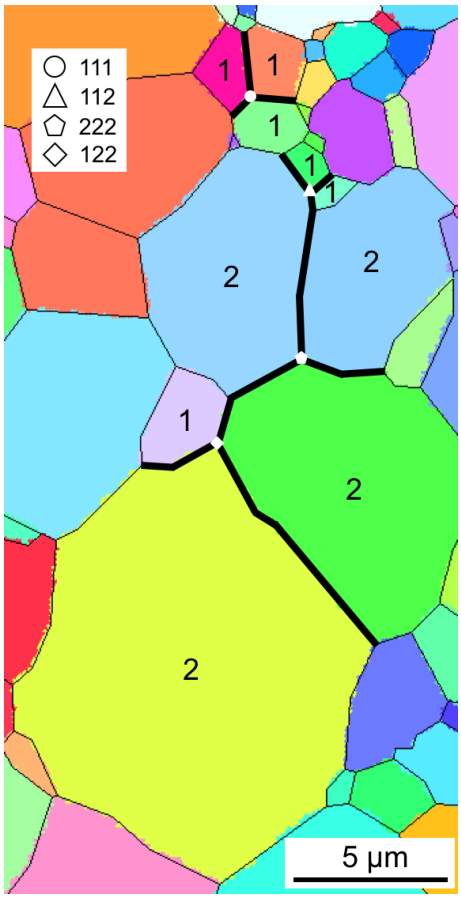


**Figure 54.** Example of an orientation map illustrating the four types of triple junctions: 111 (circle), 112 (triangle), 122 (diamond), 222 (pentagon).

As described above, the normals for each grain boundary can be determined and the data must be shifted to correct for alignment. At each triple junction the dihedral angles can be computed, which was described in the previous chapter. There were four types of junctions studied and are illustrated in Figure 54. First, the grain size distributions were analyzed at each temperature by combining parallel maps from layers throughout the 3D volume. The grain sizes were ordered from smallest to largest and plotted with respect to number of grains where number of grains is just the number of the grain in the ordered list. The distribution for 1350 °C is in Figure 55 and the distribution for 1390 °C is in Figure 56. The cutoff for a large / small grain at 1350 °C was 7 µm because that is where the distribution began to deviate from linear behavior and for 1390

°C was 5 µm because that is where the distribution deviated from linear behavior. At 1425 °C the cutoff was 5 µm, all of the grains were smaller than 5 µm.

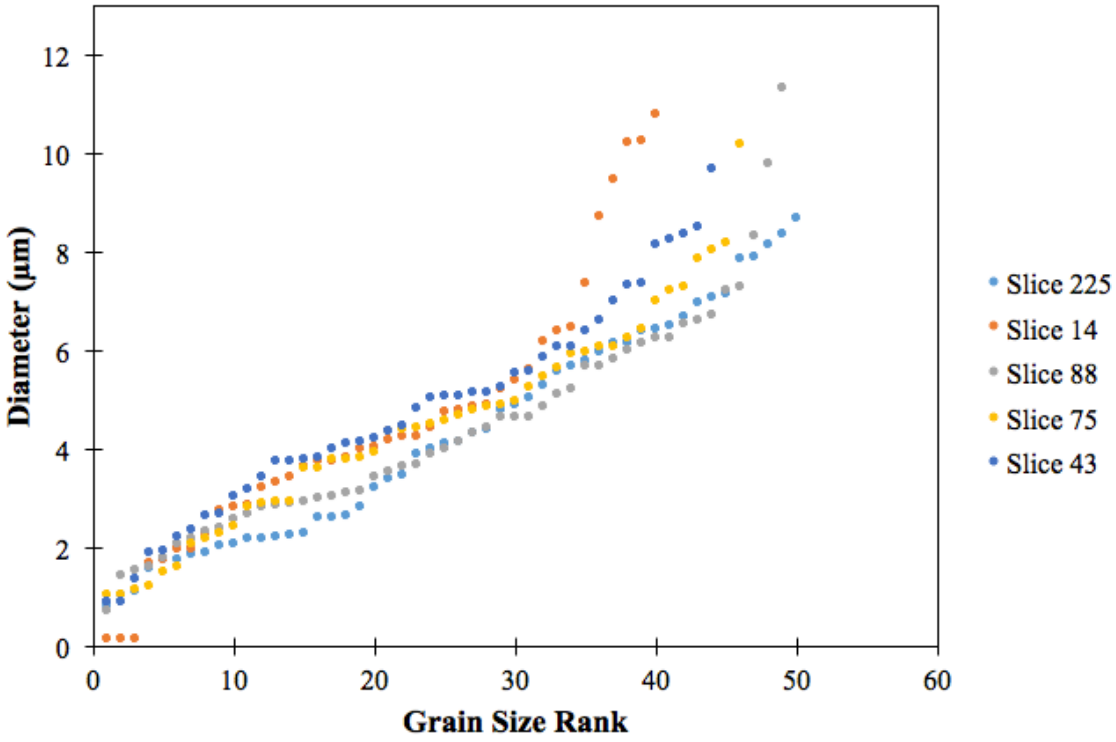


**Figure 55.** Example grain size versus number of grains for 1350 °C STO. The grain size cutoff for dihedral angle analysis was at 7 µm where the grain size distribution seemed to begin to deviate from linear behavior with increased number of grains.

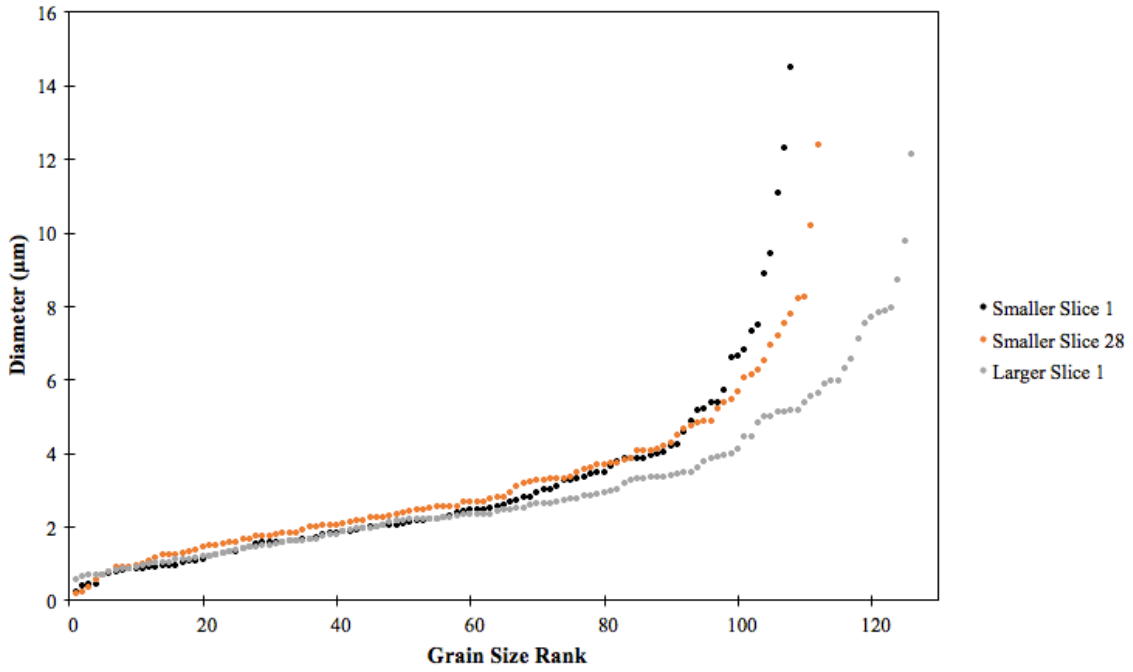


**Figure 56.** Example grain size versus number of grains for 1390 °C STO. The grain size cutoff for dihedral angle analysis was at 5 µm where the grain size distribution seemed to begin to deviate from linear behavior with increased number of grains.

Once each grain was classified as large (2) or small (1) the triple junctions were grouped. In Figure 54 the four different types of triple junctions are illustrated. Three small grains meeting at one junction is illustrated by a circle, three large grains meeting is illustrated by a pentagon, two small grains and a large grain where the dihedral angle measured is the large grain is illustrated by a triangle and two large grains and a small grain meeting where the small grain is the measured dihedral angle is illustrated by a diamond. In addition, all of the edge grains, grains that touch the outer rectangular perimeter of the acquired area, were removed from the analysis because some of the grains were cut off so the size estimates will not be accurate.

## 8.3 Results

The size (volume), number of grains, number of distinct grain boundaries (number of grain faces) and the number of meshed triangular segments for the $SrTiO_3$ sample annealed at 1425 °C are listed in **Table 13** for the two datasets separate and combined. Here, the number of grains, grain faces and number of triangular segments are all included for the entire reconstructed volume in DREAM.3D. The grain size distributions later on, removed edge grains

**Table 13.** Number of grain faces and number of meshed triangular segments are listed for each $SrTiO_3$ sample annealed at 1425 °C.

| | Volume | # Grains | # Grain Faces | # Triangular Segments |
|---|---|---|---|---|
| 1425 °C 100 nm slices, 200 nm separation | 23.5 x 22 x 9.2 = 4,756.4 $\mu m^3$ | 2,241 | 16,999 | 1,772,154 |
| 1425 °C 50 nm slices, 100 nm EBSD separation | 24 x 24 x 2.7 1,555.2 = $\mu m^3$ | 1,012 | 7,521 | 953,602 |
| Sum | 6,311.6 $\mu m^3$ | 3,049 | 20,729 | 2,725,756 |

The disorientation distribution was plotted for the combined 1425 °C data and compared to the random distribution in **Figure 57**. There are slight deviations from random but do not appear to deviate significantly.

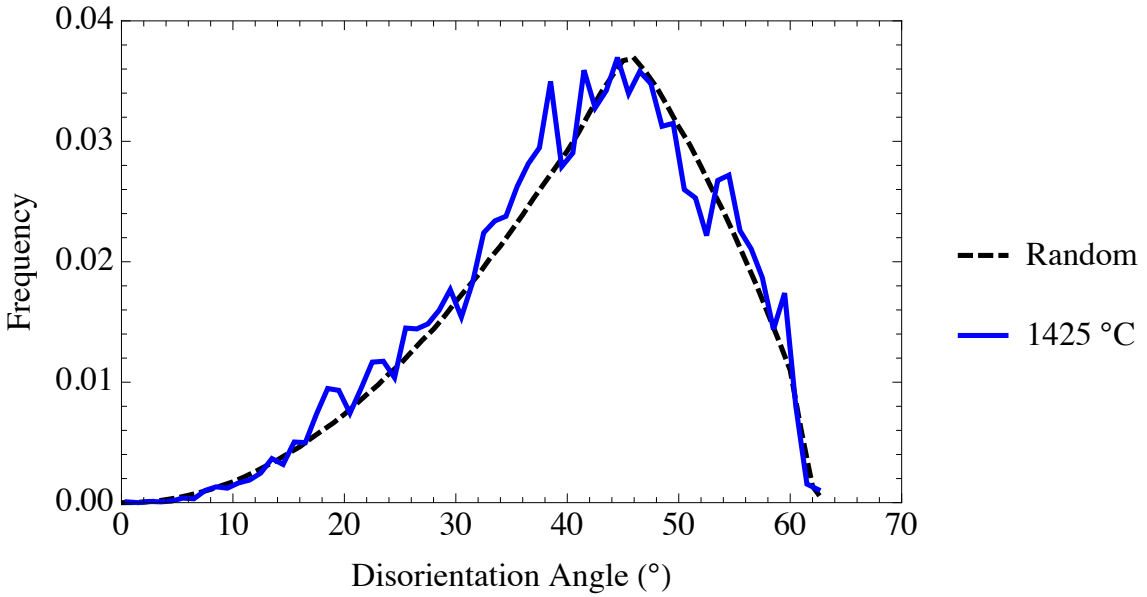


**Figure 57.** Distribution of disorientation angles at 1425 °C.

The grain boundary plane distribution, averaged over all misorientations, is plotted in **Figure 58**. These distributions indicate that, on average, the population of {001} type grain boundaries make up a greater fraction of total grain boundary area. These results appear to be consistent with grain boundary plane distributions plotted for two-dimensional EBSD of $SrTiO_3$, which can be seen in Chapter 7, **Figure 41**.

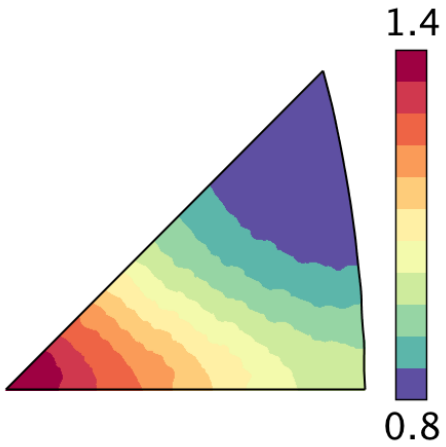


**Figure 58**. 3D grain boundary plane distribution of 1425 °C $SrTiO_3$.

After analyzing the data from disorientation distribution to determine which angles deviated from random and grain boundary plane distributions to determine which orientations deviated from random we then analyzed the grain boundary character distributions in terms of the relative areas of grain boundaries as a function of grain boundary plane orientation at specific misorientations. In this case we focused on a few select misorientations that were well above 1 MRD. We choose to compare GBCD's for the sigma 3 (60°/ [111]), sigma 9 (39° / [110]) and 40°/[100] boundaries. The 1425 °C dataset contained enough grain boundaries to be analyzed via the five parameter grain boundary character distribution but the datasets at 1390 °C and 1350 °C did not contain enough data. The GBCDs at 1425 °C are in the top row and the uncertainties associated with each GBCD are in the bottom row of **Figure 59**.

In **Figure 59** (a), for the sigma 3 grain boundary, there was a single peak at the symmetric twist (111) of 104.3 ± 9.3 MRD. For sigma 9, in **Figure 59** (b), there was also a single peak at symmetric twist $(\bar{2}21)$ of 63.1 ± 7.3 MRD. For 40°/[100], **Figure 59** (c), there were a few peaks. At the twist $(\bar{1}00)$ and at (100) there were peaks of 15.6 ± 3.6 MRD. In addition, for 40°/[100] there were peaks along a tilt axis at the $(0\bar{1}0)$, $(0\bar{1}1)$, $(001)$ and (011) of 9.9 ± 1.8 MRD and at (010) of 8.5 ± 1.5 MRD.

The highest area fraction of grain boundary planes independent of misorientation has the {100} orientation. Although there were not any distinct angles that deviated from random in the disorientation distribution, a few fixed misorientations had significantly

non-random grain boundary plane distributions. Corresponding to the high fraction of {100} observed, 40°/[100] had a high fraction at (100) and $(\bar{1}00)$ orientations. In addition, the highest area fraction of grain boundary planes at fixed misorientation is the (111) orientation for the sigma 3 grain boundary. The sigma 9 also had a high fraction of boundary planes at $(\bar{2}21)$ orientation. These are both high symmetry grain boundaries that, in some representations, are symmetric tilt grain boundaries.

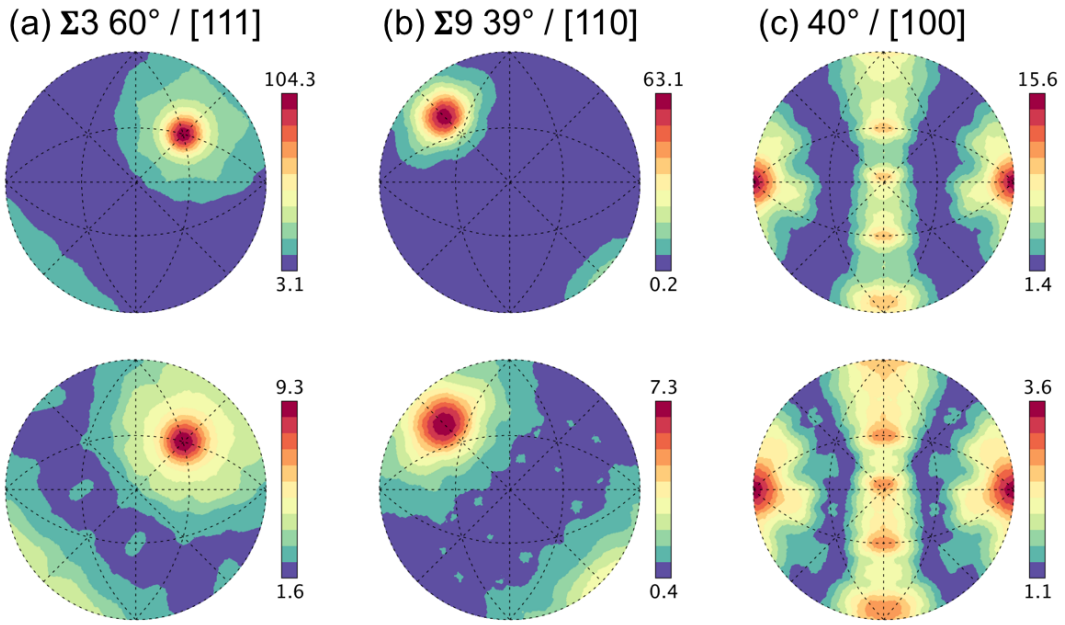


**Figure 59.** Grain boundary character distributions for 1425 °C $SrTiO_3$ at fixed misorientations.

It is possible to identify the crystallographic characteristics of the maxima in Figure 58 by referring to Figure 60. For each of the three types of fixed misorientations studied, the tilt grain boundaries (teal), twist grain boundaries (red), symmetric grain boundaries (blue) and improper quasi-symmetric grain boundaries (green) are indicated in the figures.

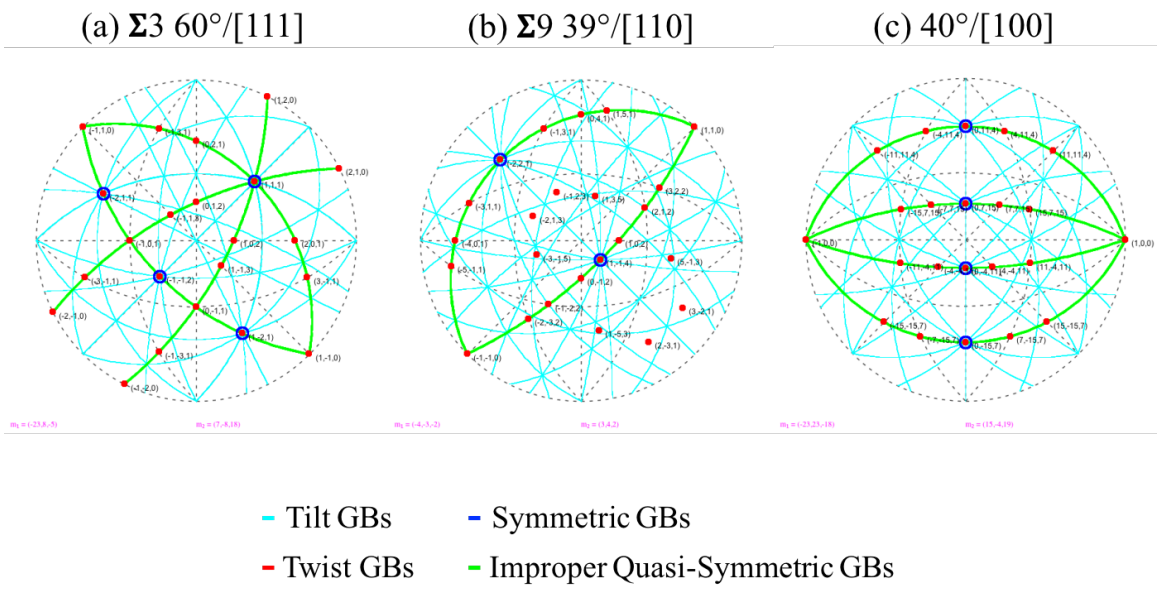


**Figure 60.** Grain boundary plane crystallography for a fixed misorientations with m$\bar{3}$m crystal symmetry. Reproduced from GBToolbox software.

Relative grain boundary energies were measured for the three dimensional volume at 1425 °C. Grain boundaries with {100} oriented grain boundary planes have the lowest average energy, while grain boundaries with {110} and {111} are higher in energy, as illustrated in Figure 61. The lower relative energy at the {100} orientation is consistent with the relatively higher area of these planes shown in Figure 57.

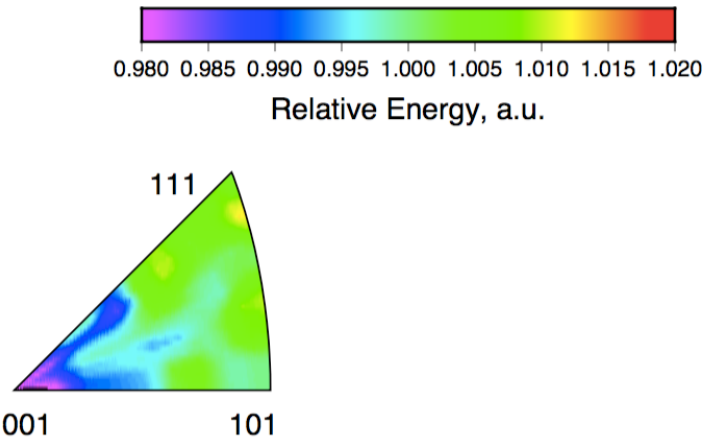


**Figure 61.** Distribution of grain boundary energies of $SrTiO_3$ at 1425 °C independent of misorientation.

The relative grain boundary energy for different grain boundary plane orientations at two fixed misorientations is illustrated in Figure 62. The sigma 3 grain boundary has

relatively high energies for the symmetric tilt $(\bar{2}11)$, $(\bar{1}\bar{1}2)$ and $(1\bar{2}1)$ orientations and the lowest energy near (111). For the sigma 9 grain boundary, the lowest energies are at the symmetric tilt positions: $(\bar{2}21)$ and $(1\bar{1}4)$. The low energy at $(\bar{2}21)$ is consistent with the high population at this orientation in Figure 58. However, the $(1\bar{1}4)$ orientation is not a local maximum in the grain boundary area distribution (Figure 58).

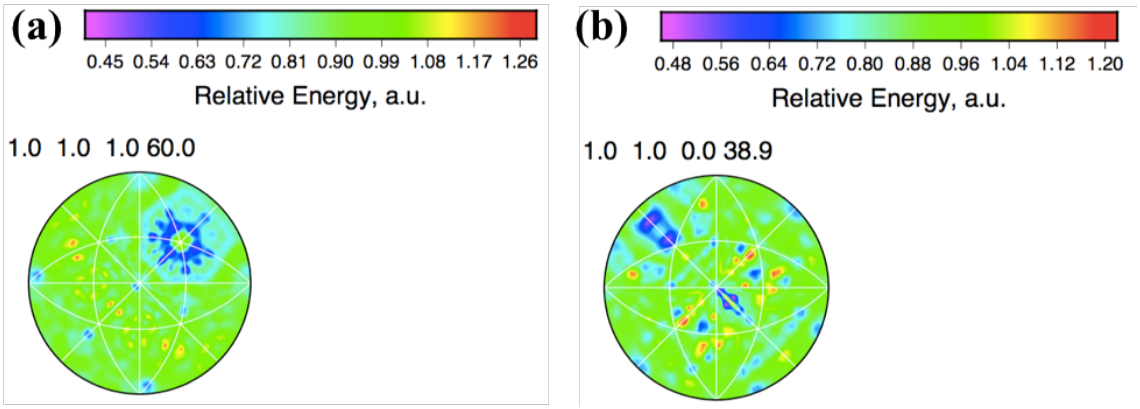


**Figure 62.** Distribution of grain boundary energies of $SrTiO_3$ at 1425 °C for the sigma 3 (a) and sigma 9 (b) grain boundaries.

The grain size distributions and the number of faces per grain were computed for the 1425 °C 3D data. The average grain size is 1.35 m and the grains had and average of 12.5 sides per grain. **Figure 63** shows histograms of the numbers of grains with particular sizes (a) and numbers of grain with particular numbers of grain faces (b). Figure 64 illustrates the correlation between the number of faces per grain and the corresponding grain size.

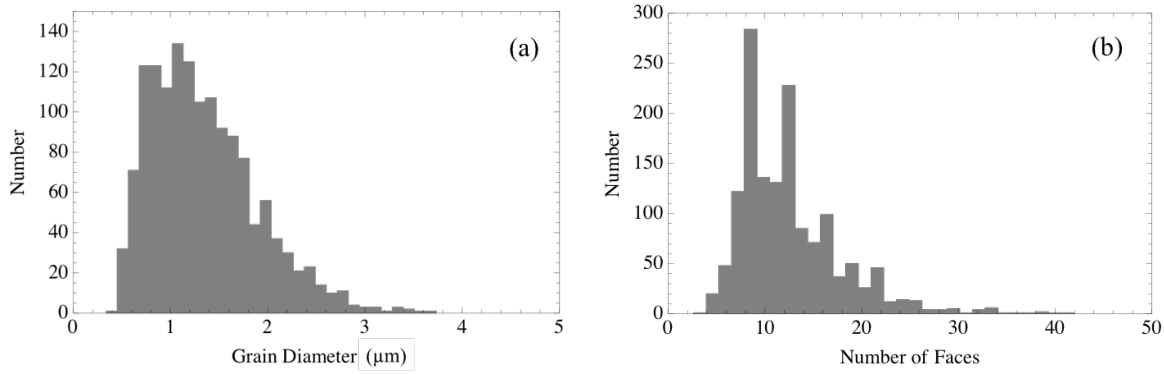


**Figure 63.** Number of the sizes of grains (a) and number of the number of faces per grain (b) for $SrTiO_3$, annealed at 1425 °C with 30 total bins for each figure.

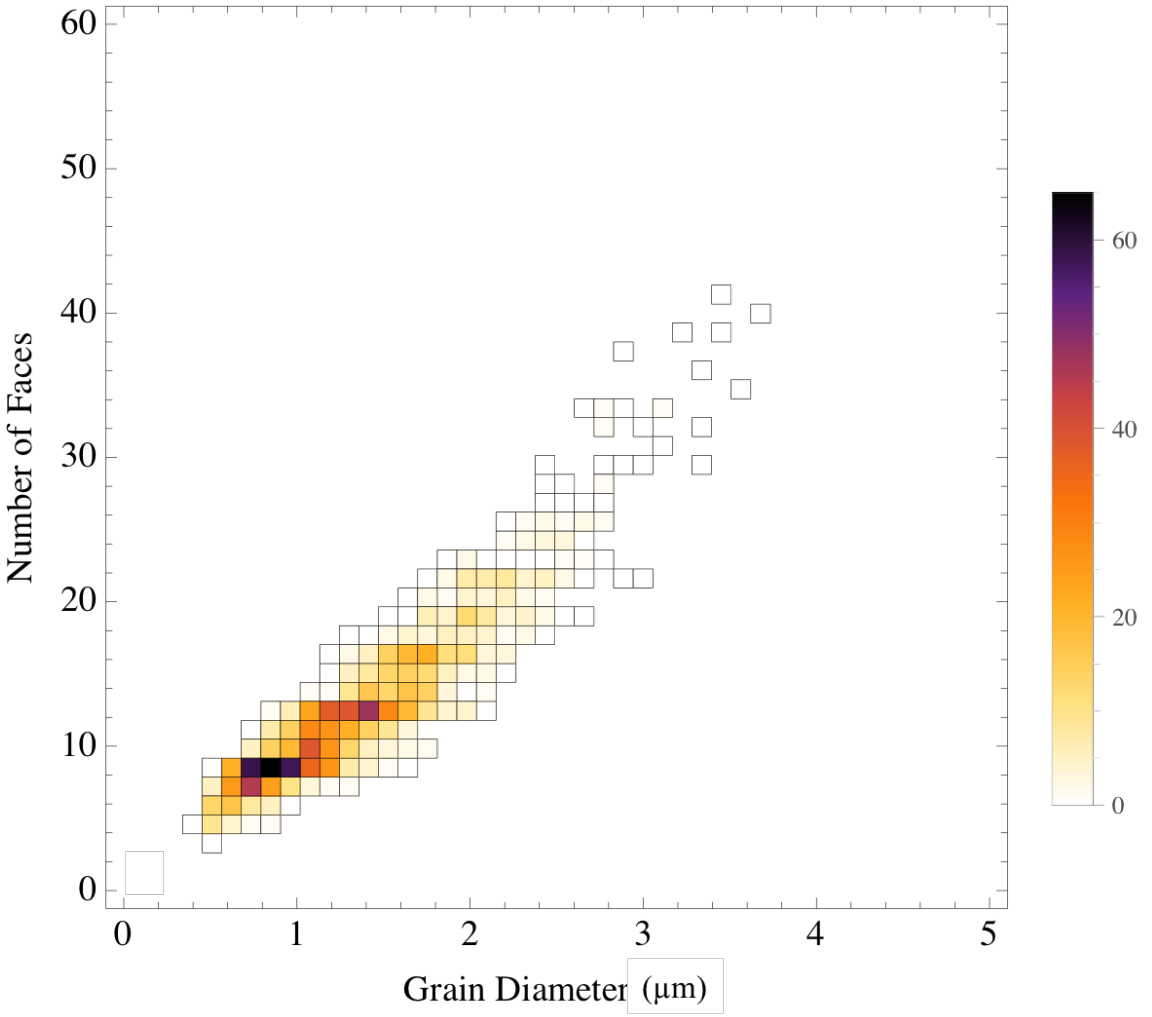


**Figure 64.** Number of faces versus grain diameter (μm) for $SrTiO_3$, annealed at 1425 °C with 30 bins in the x direction and 30 bins in the y direction.

Triple junction dihedral angles were calculated for the sample annealed at 1350 °C for triple junctions of types 111, 112 and 122 (there was no 222 grouping). Here, 1 corresponds to a grain smaller than 7 μm and 2 corresponds to a grain larger or equal to 7 μm. For the 111 junctions, we are considering all three dihedral angles. For the 112 and 122 types, we are considering only the dihedral angles between the two boundaries that separate small and large grains. The distributions are shown in Figure 65. The average dihedral angle for 111 grouping is 120° with 6,396 triple junctions, 112 is 123° with 499 triple junctions and 111° with 34 triple junctions totaling 6,929 triple junctions analyzed. Each of the three groupings had similar standard deviations 111 was 28°, 112 was 28°, and 122 was 30°.

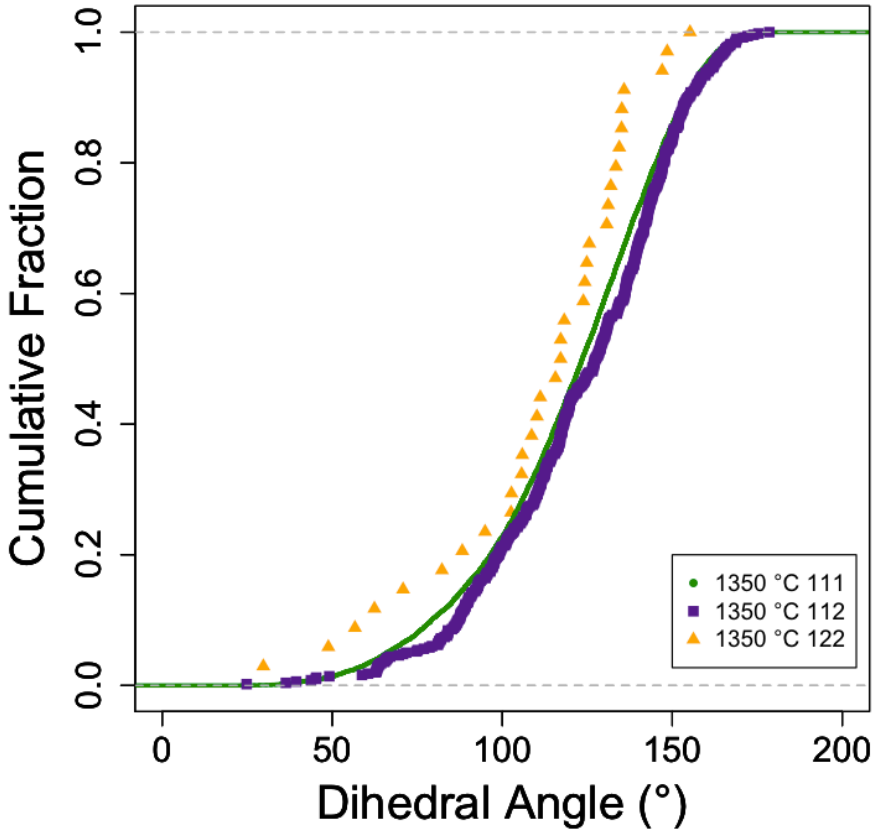


**Figure 65.** Distribution of dihedral angles for the sample annealed at 1350 °C where 111 represents the junction of all small grains (green circle), 112 is the dihedral angle of the large grain that meets at a junction of two other small grains (purple square), 122 is the dihedral angle of the small grain that meets at the junction of two large grains (orange triangle). 112 and 122 junctions are plotted with single points because of few data and the 111 junctions are plotted with the fitted CDF curve.

The distributions of internal grain boundary dihedral angles of the sample annealed at 1390 °C are plotted Figure 66. If one averages over enough triple junctions of equivalent grain boundaries, one would expect a mean of 120°. In fact, the average dihedral angles for the 8,778 triple junctions of the 111 and 222 types is 120° with a standard deviation of 29°. The average dihedral angle for the boundary between two small grains in the 1,743 112 junctions is 125° with a standard deviation of 28°. In other words, these dihedral angles are systematically larger than the expected value of 120°. Similarly, the average dihedral angle for the boundary between two large grains in the 529 122 type junctions is 115°, with a standard deviation of 26°. Note that there is an uncertainty in the sizes of grains on the periphery of the field of view. Therefore, any

junctions containing grains that intersected the boundary of the image were excluded from the analysis. However, when they were included, the trends were the same.

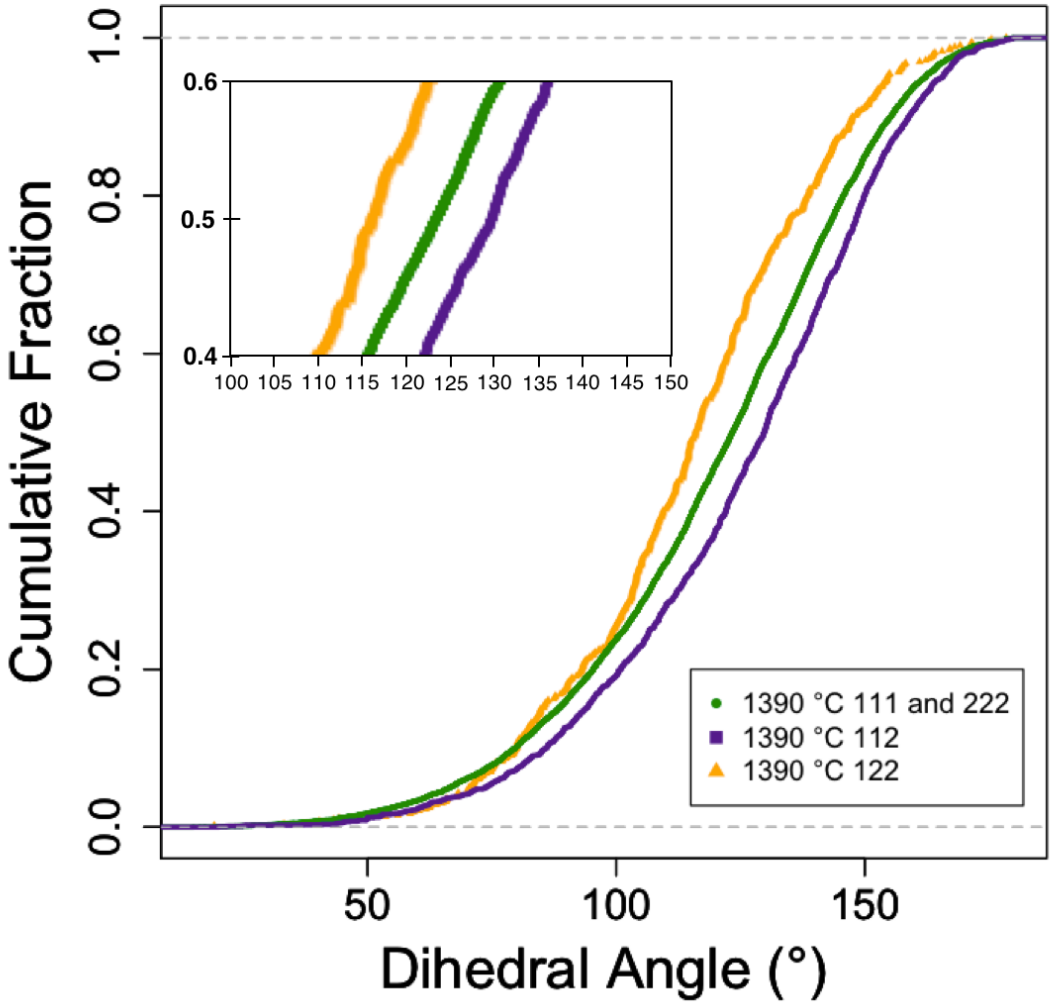


**Figure 66.** The distribution of dihedral angles for 111 and 222 type lines (green circle), 112 type junctions (purple square) and 122 type junctions (orange triangle) for $SrTiO_3$ annealed at 1390 °C.

For the 1425 °C data there were two datasets, one with each layer separated by 100 nm and another with each layer separated by 200 nm. In Figure 67 the distributions of each of the separated datasets separately and combined are plotted. In Table 14 the average values are reported as well. For the 100 nm dataset the average dihedral angle is 120° for 37,602 triple junctions, for the 200 nm dataset it is 120° for 46,596 triple

junctions an 120° for 84,198 combined. As you can see, the averages do not deviate significantly but the distributions appear to change slightly.

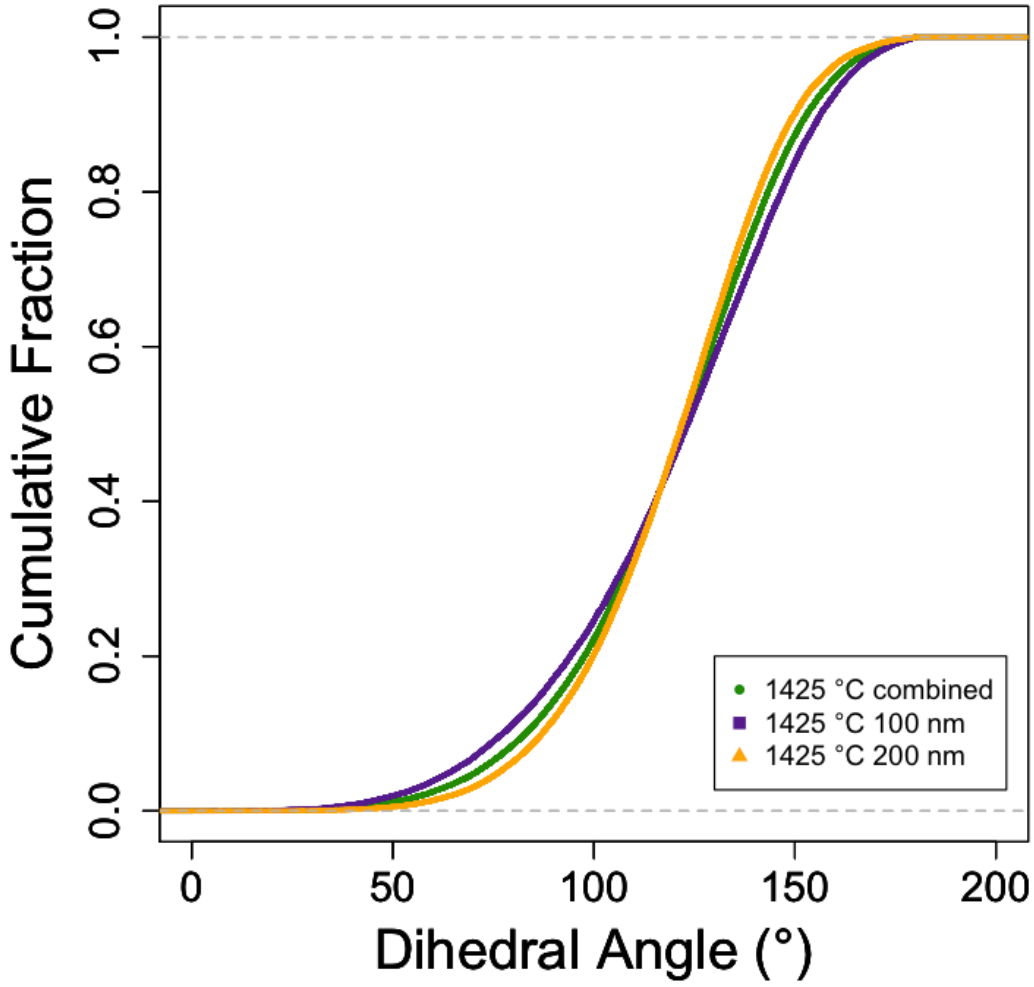


**Figure 67.** Distribution of dihedral angles for all 1425 °C data where the edges are removed and the data of the two volumes is plotted separately and combined for comparison.

At 1425 °C the data was all grouped into 111 where 1 corresponds to grains smaller than 5 μm. The distributions can be found in Figure 68. The average dihedral angle for 111 grouping is 120° with 84,198 triple junctions and standard deviation of 27. For the separated 100 nm and 200 nm datasets the mean dihedral angle was also 120° for the 100 nm separation dataset and 120° for the 200 nm separation dataset. To directly compare to the 1350 °C and 1390 °C dataset only the 100 nm separation data was used.

In Figure 68 the three different temperatures (1350 °C, 1390 °C and 1425 °C) data of 111 junctions all overlap almost exactly.

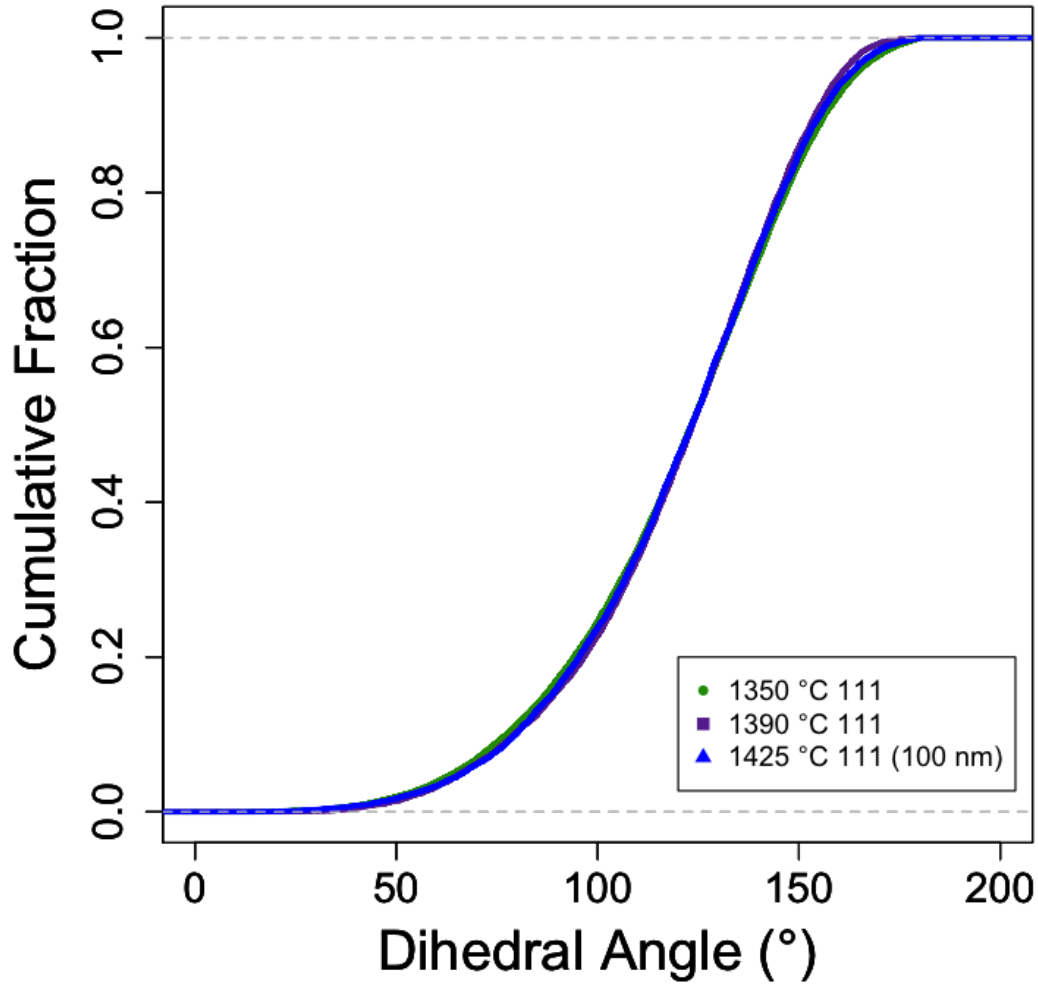


**Figure 68.** Distribution of dihedral angles for all 111 junctions for 1350 °C, 1390 °C and 1425 °C where only the data for the same 100nm separation is included.

The statistics for the dihedral angles measured at each temperature and of each of the types of junctions is listed in Table 14.

**Table 14.** Statistics on the distribution of dihedral angles, with edge grains removed, for 1350 °C, 1390 °C and 1425 °C.

| **Triple Junction Type** | | **1350 °C** | **1390 °C** | **1425 °C** | **1425 °C 100 nm layer separation** | **1425 °C 200 nm layer separation** |
|---|---|---|---|---|---|---|
| **111** | Average Dihedral Angle (°) | 120 | 120* | 120 | 120 | 120 |
| | Standard Deviation | 28 | 29* | 27 | 30 | 25 |
| | # of Triple Junctions | 6,396 | 8,778* | 84,198 | 37,602 | 46,596 |
| **112** | Average Dihedral Angle (°) | 123 | 125 | - | | |
| | Standard Deviation | 27 | 28 | - | | |
| | # of Triple Junctions | 499 | 1,743 | - | | |
| **122** | Average Dihedral Angle (°) | 111 | 115 | - | | |
| | Standard Deviation | 30 | 26 | - | | |
| | # of Triple Junctions | 34 | 529 | - | | |
| **222** | Average Dihedral Angle (°) | - | - | - | | |
| | Standard Deviation | - | - | - | | |
| | # of Triple Junctions | - | - | - | | |
| **Total Triple Junctions** | | 6,929 | 11,050 | 84,198 | | |

*denotes 222 combined with 111

## 8.4 Discussion

The number of distinguishable grain boundaries in a polycrystalline cubic material is 6.5 x $10^3$ for 10° resolution and 2.5 x $10^5$ for 5° resolution.[70] With the new method of binning we choose $\rho_m$= 3° and $\rho_p = 7°$. This, by volume is about two times smaller than conventional 10° binning so approximately 1.3 x $10^4$ boundaries are required. Estimation of the number of distinguishable boundaries for experimental data is not elementary. **Table 13** lists the number of faces and the number of triangular segments for each sample. The number of distinguishable boundaries lies somewhere between the two

because each grain face is composed of a set of triangular segments which usually have similar plane orientations. Therefore, in the 1425 °C dataset, 2 x $10^4$ grain faces and 2.7 x $10^6$ triangular segments should be sufficient to uphold the minimum number of distinguishable boundaries in a polycrystalline cubic material for $\rho_m = 3°$ and $\rho_p = 7°$ resolution. In addition, the uncertainty for each of the grain boundary types probed at 1425 °C is smaller than the maxima of the distribution function. So we can still say with confidence that these boundaries, statistically, deviate from random and thus indicate that real changes in the grain boundary plane population are observed.

The distribution of disorientation angles for 1650 °C annealed $SrTiO_3$ has been measured previously from two dimensional EBSD data.[205, 213] It has also been measured for three dimensional data of $SrTiO_3$ annealed at 1600 °C by means of X-ray diffraction contrast tomography.[195] All of the distributions showed no significant disorientation texture. However, each of the disorientation distributions in the previous work $SrTiO_3$ studied samples annealed at temperatures above 1600 °C. The disorientation distributions at the temperature studied here, 1425 °C, had not been plotted previously. The distributions in **Figure 57** indicate that the there is no significant disorientation texture at these temperatures either.

The GBPD had been measured by Rheinheimer et al. by 2D EBSD data in $SrTiO_3$ at 1300 °C, 1350 °C and 1425 °C.[40] Comparing other measurements from the literature, at 1650 °C anneal temperature, Saylor et al. found that the {001} type boundaries had the highest relative area (1.53 MRD) and the {111} had the lowest (0.70 MRD) .[205] Another paper published by Saylor et al. indicated that with this same sample the {001} boundaries, again, had the highest relative area (1.75 MRD) and the {111} had the lowest (0.60 MRD).[214] There appears to be some discrepancy with these previous measurements. This could be due to different computational methods of the calc_gbcd program and different versions of the program that may have changed from the first publications in 2004. In addition, Saylor et al. computed the GBPD from three-dimensional data and Rheinheimer et al. compared two-dimensional data. In any case, the data published here, in **Figure 41**, all of the data at 1300 °, 1350 °C, 1425 °C and the new data collected at 1550 °C was computed with the same version of calc_gbcd and is directly comparable. These results indicate that the population of {001} type boundaries increase for samples

heated at 1425 °C and then the population decreases for samples heated at even higher temperature, 1550 °C. This is interesting, considering the grain growth transitions in this system. Going back to the grain growth constant versus temperature plot in **Figure 28**, the transition from grain boundary type 1 begins at 1350 °C which is when the population of {001} type boundaries begins to increase. At the end of the transition region, at 1425 °C, the population of {001} is at its highest. At 1550 °C, in grain boundary type 2 region, the {001} population decreases and the distribution is similar to what it was before the transition, in the GB type 1 regime.

The GBPDs from three-dimensional data at 1425 °C were computed from data collected on the Xe-ion plasma FIB. The only published, reconstructed orientation data thus far, on the Xe-ion plasma FIB is from alpha-Titanium.[203] This new instrumentation allows for faster and larger volume of data collection than was ever possible with the Ga FIB for metals,[203] but for the ceramics studied here, it should be noted that the milling speeds, in order to maintain indexing quality above 80%, is approximately the same as with the Ga FIB. A previous computation of GBPD of three-dimensional data for the same materials system studied here, $SrTiO_3$, was collected on the Ga FIB by H. Miller for $SrTiO_3$ annealed to 1470 °C.[204] At 1470 °C they had found that the {001} population in the GBPD was above random but the maxima cannot be directly compared to the current results because of the different data collection methods used. [204] Here, we measured the GBPD for 3D data for $SrTiO_3$ at the end of the Non-Arrhenius grain growth transition region, 1425 °C **Figure 58**. Measurements of the GBPD from 3D EBSD at 1425 °C showed that the {001} boundaries were dominant with 1.4 MRD. Comparing the 3D GBPD, **Figure 58**, to the GBED Figure 61, independent of misorientation, an inverse trends was observed. In the GBED there was a minima of 0.98 MRD at the {001} and maxima of 1.20 MRD at the {111}. This indicates that the {001} grain boundary planes are low in energy. The 2D GBPD data also showed a high fraction of {001}. The relative area of {001} was 1.76 MRD, **Figure 41** (c). The stereology method to compute GBPD from 2D EBSD observations infers the boundary normal but from 3D EBSD we have a direct measure of the boundary normal. Unfortunately, the uncertainties in the normal derived from 3D data are thought to be large and are currently unquantified, so it is impossible to say which is more accurate.

The GBCDs, at fixed misorientation, have not been calculated before for the $SrTiO_3$ system using the KDE method. With the conventional method (counting boundaries within assigned bins) some GBCDs were computed from 2D EBSD data from samples annealed at 1650 °C. In this reference, the grain boundary plane distributions for 20°, 30°, and 40° about the [100], 20°/[110], 20°/[111], 20°/[952], sigma 3, sigma 5, sigma 7 and sigma 9 were presented.[205] They found that there was no significant misorientation texture but there was an enhanced number of low-misorientation angle grain boundaries with a maximum population of 2.43 MRD. For 20°, 30° and 40° about the [100] Saylor et al. found peaks at the {100}. For sigma 3, sigma 5, sigma 7 and sigma 9 boundaries Saylor et al. found the maximum peaks at the (111), (100), (111) and (110) respectively. These results cannot be directly compared, in terms of the relative area of boundary planes, to the results here because of the different methods in the data analysis. However, Glowinski's work focused on these differences and showed that peaks tend to be in the same locations as binning method but the maxima MRD in the KDE method tends to be larger.[208] However, it is interesting to note which boundaries the previous study were found as most frequent and to compare peaks which may be similar to the data here, although analyzed at different temperatures. $SrTiO_3$ 3D data annealed at 1470 °C, was previously acquired by Miller and was also analyzed for a few select misorientations and published in his thesis.[204] Miller found the maxima for the sigma 3 boundary as 12.5 MRD at the (111) orientation. In addition, the grain boundary plane distribution for the 20°/[111] misorientation was plotted and had a peaks at the {001} orientations of 3.22 MRD. [204]

Examining the GBCD for the sample annealed at 1425 °C, we found that the sigma 3, sigma 9 and 40°/[100] boundaries had the highest area fraction and were significantly larger than the uncertainty. At the sigma 3 grain boundary, the (111) had a significantly higher relative area of 104.3 ± 9.3 MRD. Compared to the partition based method of computing GBCDs, 104 MRD seems like a very large value. In previous measurements from 3D data in nickel where 20% of the data was estimated to be twin boundaries, the (111) for the sigma 3 grain boundary had 1,100 MRD by the partition based method.[165] The KDE method compared this data and measured 1,600 MRD.[208] The sigma 7 showed 8 MRD by partition method[165] and 29 MRD by KDE in nickel. [208] The sigma 9 showed 2

MRD by partition method[165] and 15 MRD by KDE in nickel. [208] Therefore, it is not surprising that the values for the relative area are significantly larger by the KDE method than by the partition method in $SrTiO_3$ as well. In a direct comparison, with this dataset, $SrTiO_3$ at 1425 °C, the sigma 3 grain boundary in the 200 nm separation dataset alone by the KDE method yielded 126.7 ± 19.3 MRD and by the partition method (through DREAM.3D filter) yielded 18 MRD. The main cause for these differences is that the relative area value is sensitive to the size of the partition and when one uses the KDE method with a smaller acceptance range for the data, the numerical value will always be greater.

Previous work has shown that there is an inverse relationship between grain boundary population and grain boundary energy.[104] Here, for the sigma 3 we see that there is a high area fraction of (111) of 104.3 ± 9.3 MRD in **Figure 59** (a) and in Figure 62 (a) the relative area of (111) is low at about 0.54 a.u. in the energy distribution. Therefore, it is likely that (111) in the sigma 3 grain boundaries have the lowest grain boundary energy at 1425 °C.

The sigma 9 and 40°/[100] showed high area fractions of high symmetry boundaries in the GBCD. At sigma 9, the $(\bar{2}21)$ symmetric tilt grain boundary had 63.1 ± 7.3 MRD in **Figure 59** (b) and in Figure 62 (b) the GBED showed a minima of less than 0.48 a.u. near the $(\bar{2}21)$ as well. Near another symmetric tilt position, $(1\bar{1}4)$, for the sigma 9, a minima of 0.48 a.u. is observed but did not have a corresponding maxima in the GBCD. The observation that the $(\bar{2}21)$ symmetric tilt grain boundary was low in energy and high in population is consistent with the expected correlation among these quantities.

For 40°/[100] in the GBCD there are peaks at a the orientations of twist grain boundaries. At $(\bar{1}00)$ and (100) the area fraction of these grain boundary planes is 15.6 ± 3.6 MRD and along a tilt axis the $(0\bar{1}0)$, $(0\bar{1}1)$, $(001)$ and (011) is 9.9 ± 1.8 MRD and at (010) it is 8.5 ± 1.5 MRD. Because there were so few boundaries with this misorientation, the grain boundary energy distribution was not expected to be reliable.

The results in chapter 7 show that in the transition region the relative grain boundary energy decreases at 1390 °C and suggest that the energy is even lower at 1425 °C because the mobility continues to decrease. Therefore, the high population of {100} orientations observed with corresponding low energy can be considered the pervasive

orientations transitioning to a lower energy state in the non-Arrhenius region. In addition, although there are not many sigma 3 or sigma 9 boundaries, the (111) for the sigma 3 misorientation and $(\bar{2}21)$ for the sigma 9 show a high area fraction and corresponding local minima in the GBED so these grain boundary planes could be transitioning to a low energy state at 1425 °C as well.

The grain size distribution and number of faces per grain for 1425 °C are in **Figure 63** and combined plot in Figure 64. The distributions of the number of faces per grain to grain size appear to correspond to previous 3D distributions of beta-brass[215] as well as alpha-titanium[203].

It was not possible to compute GBCDs and GBEDs for all of the samples, because in some cases there was not enough data. In these cases, internal dihedral angles were analyzed and compared to infer the changes in grain boundary energy. For grain boundaries that are high in energy one would expect that the dihedral angle would be smaller and for a grain boundary low in energy that the dihedral angle to be larger. This was quantified by Young's equation: $\frac{\gamma_{gb1}}{\sin\theta_{2,3}} = \frac{\gamma_{gb2}}{\sin\theta_{1,3}} = \frac{\gamma_{gb3}}{\sin\theta_{1,2}}$ where $\theta_{x,y}$ are the dihedral angles and $\gamma_{gbi}$ are the grain boundary energies, Figure 69. In addition, energy ratios were computed from the dihedral angle measurements using this equation. For instance, the average dihedral angle for the 112 junction at 1350 °C is 123°. Assuming that the other two grain boundaries meeting at the triple junction are equal to one another the ratio of the slow to fast grain boundary energies can be computed by the following equation $\frac{\gamma_1}{\sin(123°)} = \frac{\gamma_2}{\sin(\frac{1}{2}*(360°-123°))}$.

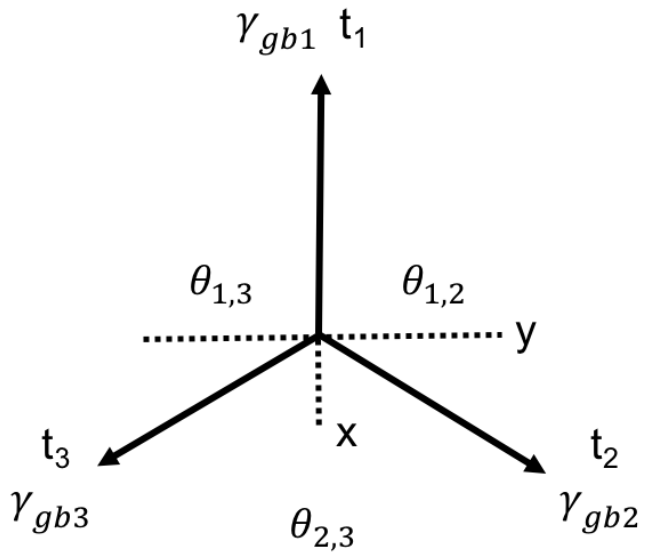


**Figure 69.** Diagram of a triple junction, corresponding dihedral angles $\theta_{x,y}$, and balance of forces of each grain boundary $\gamma_{GBi}$.

This can also be thought of qualitatively. If three grain boundaries meet at a triple junction each of the boundaries have three different forces that all balance to form an equilibrium, $t_1$, $t_2$, and $t_3$ in Figure 69. To create a dihedral angle which is small, e.g. for dihedral angle $\theta_{2,3}$ the force at the opposing junction, $t_1$, must be large which would require a large energy $\gamma_{gb1}$ to create a small dihedral angle. For a larger dihedral angle, less force would be required and would thus have a lower energy to create a large dihedral angle. If one averages over enough triple junctions of equivalent grain boundaries, one would expect a mean of 120°. The data was grouped into '1' corresponding to a grain smaller than 5 μm (1390 °C and 1425 °C) or 7 μm (1350 °C) or '2' corresponding to a grain larger than 5 μm (1390 °C and 1425 °C) or 7 μm (1350 °C). At the 112 junction the dihedral angle measured is the one corresponding to the boundary between two, '1' grains. At the 122 junction the dihedral angle measured is the one corresponding to the boundary between two, '2' grains. The 111 junctions are combined with the 222 junction data because the distributions yielded the same averages (120°). Note that there is an uncertainty in the sizes of grains on the periphery of the field of view. Therefore, any junctions containing grains that intersected the boundary of the image were excluded from the analysis. However, when they were included, the trends were the same.

At 1350 °C, the data was grouped into '1' corresponding to a grain smaller than 7 μm or '2' corresponding to a grain larger than 7 μm. For the 111, 112 and 122 type junctions there were many grain boundaries grouped into 111, few in 112 and barely any in 122. Looking at the grain size distributions previously published at 1350 °C, it is not surprising that most of the junctions are in the 111 grouping.[43] At 1350 °C, the grain size distribution is basically unimodial. The distributions of dihedral angles can be found in Figure 65. The average dihedral angle for 111 grouping is 120° with a standard deviation of 28° and 6,396 triple junctions. For the 112 types the average dihedral angle is 123° with a standard deviation of 28° and 499 triple junctions, inferring that these are low energy boundaries along the two small ("slow") grains. The 122 type only had 34 triple junctions average dihedral angle of 111° and standard deviation of 30° inferring these are high energy boundaries along the grain boundary that divides two large ("fast") grains. The ratio of the fast (122) to slow (112) grain boundary energies at 1350 °C $\left(\frac{\gamma_{fast}}{\gamma_{slow}}\right)_{\mathbf{1350\,°C}} = 0.88$.

The distributions of internal grain boundary dihedral angles of the sample annealed at 1390 °C are plotted Figure 66. Similar to the result at 1350 °C the 112 grain boundaries had larger dihedral angles and the 122 grain boundaries had a smaller dihedral angles. At 1390 °C however, there was a different classification for large ('2') versus small ('1') grains. 5 μm was used as the cutoff to distinguish between the two. In addition, the grain size distribution at 1390 °C is clearly bimodal with a more drastic distinction between large and small grains. The average dihedral angles for the 8,778 triple junctions of the 111 and 222 types is 120° with a standard deviation of 29°. The average dihedral angle for the boundary between two small ("slow") grains in the 1,743 112 junctions is 125° with a standard deviation of 28°. In other words, these dihedral angles are systematically larger than the expected value of 120°. Similarly, the average dihedral angle for the boundary between two large ("fast") grains in the 529 122 type junctions is 115°, with a standard deviation of 26°. The ratio of the fast (122) to slow (112) grain boundary energies at 1390 °C $\left(\frac{\gamma_{fast}}{\gamma_{slow}}\right)_{\mathbf{1390\,°C}} = 0.89$.

Comparing the grain boundary energy ratios of fast to slow energies, of internal dihedral angles, at 1350 °C and 1390 °C the values measured are exactly equal to the

ratio of the fast to slow relative grain boundary energies measured from thermal grooves in chapter 7. This indicates that the measurements made from thermal grooving agree with the method of internal dihedral angles presented in this chapter.

The dihedral angles at 1425 °C all fell into the same category of 111 type junctions for a grain size cutoff of 5 μm. This grain size distribution was found to be unimodal as well with an average grain size of 1.35 μm for the 3D volume. The average dihedral angle at 1425 °C was 120°, standard deviation of 27° for 84,000 junctions. In Figure 68 all 111 type junctions were plotted to compare the distributions at 1350 °C, 1390 °C and 1425 °C for the data that was collected with the same in plane spacing (100 nm). The distributions almost perfectly overlap, indicating that this method of measuring dihedral angles is robust and can be comparable to other temperatures if the methods are the same. This also indicates that any changes in the distributions of other junctions studied (112 and 122) will infer a change in dihedral angle and thus a change in grain boundary energy.

From the dihedral angle data there is a distinct difference between boundaries between two small grains and boundaries between two large grains when they meet boundaries between large and small grains. For microstructures which have a unimodal distribution the dihedral angles are isotropic at 120°. When grouped the same way for bimodal distributions the dihedral angles become more anisotropic. Grains which all have the same size in the bimodal distribution show 120° dihedral angle average as well but the junctions which have a mixture of small and large grains deviate from 120°. The grain boundaries of two small grains adjacent to a large grain have large dihedral angles and thus lower energy. The grain boundaries of two large grains adjacent to a small grain have small dihedral angles and thus larger energy. This was evident at both 1350 °C, where the distribution was mostly unimodal but even more pronounced at 1390 °C where the distribution is clearly bimodal. At 1350 °C only 7% of the boundaries were of the 112 type (low energy), 0.5% were of the 122 type (high energy) and 92% were of the 111 type. At 1390 °C 16% were 112 type, 5% were 122 type and 79% were either the 111 or 222 type. At 1425 °C 100 % of the boundaries were of the 111 type. This shows that a fraction of the grain boundaries can transition, like the fraction of grain sizes but this data indicates that the energies are changing as well. Because the fraction of large dihedral

angles increases from 1350 °C to 1390 °C our interpretation is that the small grain boundaries transition to a lower energy during annealing and the large grains are at a high energy state until they all transition to slow type at 1425 °C. Because all of the grains are small at 1425 °C the average dihedral angles are 120° but looking at the 3D data we see that there are low energy types here, specifically those grain boundaries with {001} grian boundary plane orientations.

## 8.5 Conclusion

Internal dihedral angles, GBEDs, and the populations of grain boundary planes, independent and dependent of misorientation provided insight onto the grain boundary evolution in the non-Arrhenius grain growth region in $SrTiO_3$. As compared to chapter 7, this chapter samples over all grain boundaries in 3D volumes at 1350 °C, 1390 °C and 1425 °C whereas in chapter 7, not all boundaries could be measured.

Internal dihedral angles showed that the fraction of types of triple junctions changed with temperature. '1' was used to describe small grains in the microstructure and '2' was used to describe large grains. Using this numbering scheme, triple junctions were divided into four categories, 111, 112, 122 and 222. 111 and 222 type junctions yielded an average dihedral angle of 120°, 112 junctions yielded an average dihedral angle >120° and 122 had an average <120°. At 1350 °C, 7% of the boundaries were of the 112 type (low energy), 0.5% were of the 122 type (high energy) and 92% were of the 111 type. At 1390 °C, 16% were 112 type, 5% were 122 type and 79% were either the 111 or 222 type. At 1425 °C 100 % of the boundaries were of the 111 type. This suggests that the fraction of 112 type (low energy) grain boundaries increases with increasing temperature until all boundaries are in the slow state at 1425 °C. In addition, the ratio of fast to slow relative grain boundary energies calculated from internal dihedral angles, at 1350 °C and 1390 °C, agree with the ratio of fast to slow relative grain boundary energies measured from thermal grooves in chapter 7.

GBCDs and GBEDs were measured at the end of the non-Arrhenius transition, 1425 °C. At 1425 °C, the GBPD, independent of misorientation, and corresponding GBED showed that the {001} had the highest area fraction and lowest energy. For the sigma 3 grain boundary, there was a single peak at the symmetric twist (111) of 104.3 ± 9.3 MRD and corresponding minima in the GBED at the (111) of 0.54 a.u. indicating that the (111)

is highest in population at the sigma 3 and lowest in energy. At 1425 °C the sigma 9 showed a high area fraction of $(\bar{2}21)$ and corresponding minimum in the GBED of 0.48 a.u., again indicating that the $(\bar{2}21)$ for sigma 9 is high in population and low in energy.

# 9 Conclusions

In this thesis, the temperature dependence of grain boundary energy and grain boundary character were measured for three materials. Each of these materials have interesting microstructures that change in the temperature regions studied. In Eu doped spinel, the microstructure ranges from nanocrystalline to nearly single crystal. In doped alumina, the microstructure begins with a unimodal grain size, then abnormal grain growth begins, and after the abnormally large grains impinge, the microstructure becomes unimodal again. In $SrTiO_3$, non-Arrhenius grain growth is observed with increased temperature. In each of these materials a complexion transition was previously found to be associated with the changes in microstructure or is hypothesized to be the case (e.g. in $SrTiO_3$). Relative grain boundary energies were measured from thermal grooves, GBCDs were measured from both 2D and 3D grain orientation volumes, internal dihedral angles of triple junctions were measured and GBEDs were measured from 3D volumes. The temperature dependence of relative grain boundary energies, internal dihedral angles, or GBCDs had not been studied and correlated before.

The results from GBPDs of Eu doped spinel indicated that the distribution of grain boundary planes at 1400 °C was relatively random until the population of {111} increased to 1.7 MRD at 1600 °C. Based on results from other materials, the grain boundary population is inversely correlated to grain boundary energy. Therefore, the changes in the GBPD suggest that a change in grain boundary energy is associated with a change in complexion type. The increase in the relative areas of grain boundaries with {111} orientations at 1600 °C indicates that these orientations are low in energy. The microstructural data was used to create a complexion TTT diagram that describes the kinetics of the microstructural changes in Eu doped spinel.

The changes in the relative grain boundary energies of pure and Y-doped alumina as a function of temperature were measured from grain boundary thermal grooves. The changes of relative grain boundary energy observed with respect to temperature are likely from an interplay of solute segregation and desegregation between the grain boundaries and the bulk. The relative grain boundary energies of 99.995% pure alumina decrease slightly with increasing temperature which is explained by the entropic component of the grain boundary free energy. In the doped samples, overall, the relative grain boundary

energy increased with increased temperature (and decreased with decreasing temperature, for 100 ppm Y-doped alumina (T-)). The increase in relative grain boundary energy is explained by solute dissolving in the bulk during heating. Abrupt reductions in the grain boundary energy are associated with a complexion transition between 1450 °C and 1550 °C that increases the mobility of a fraction of the grain boundaries and leads to abnormal grain growth. The decrease in relative grain boundary energy in this temperature region indicates that the relative area of the lowest energy grain boundaries increases when a complexion transition occurs. For the 100 ppm Y-doped alumina (T-) sample there is an abrupt increase in grain boundary energy when the sample is cooled indicating that the grain boundary complexion transition is reversible. This is the first indication of reversibility of a grain boundary complexion transition.

$SrTiO_3$ exhibits non-Arrhenius grain growth behavior. Grain boundary thermal grooves, internal dihedral angles, GBCDs and GBEDs were measured to better understand this behavior. The relative grain boundary energies decreased in the temperature range where the anti-thermal grain growth was observed. In addition, liquid eutectic was found in samples annealed above the non-Arrhenius region; the relative grain boundary energies could not be evaluated for these samples and the GBPD measured from stereology cannot be compared to lower temperatures due to the new $SrTiO_3$ / solidified liquid eutectic interfaces created at this temperature. The relative grain boundary energies measured from 1350 °C to 1390 °C indicate that an abrupt decrease in energy in this temperature region which indicates that a complexion transition occurred and is contributing to the anti-thermal behavior.

Xe-ion plasma FIB 3D microstructures were collected of $SrTiO_3$ at the beginning (1350 °C), middle (1390 °C), and end (1425 °C) of the anti-thermal region, chapter 8. At all of the temperatures internal dihedral angles showed that triple junctions with all the same size grains had an average dihedral angle of 120°. For junctions with two small grains meeting a large grain the average internal dihedral angle was > 120°, indicating these grain boundaries are low in energy. For two large grains meeting a small grain the average internal dihedral angle was < 120° and therefore high in energy on average. At 1350 °C 7% of the boundaries were low energy, 0.5% were high energy, and 92% were isotropic (average = 120°). At 1390 °C, in the middle of the anti-thermal region, the

percentages of low and high energy grain boundary types increased. 16% of the grain boundaries were low in energy, 5% were high in energy and 79% isotropic at 1390 °C. At the end of the anti-thermal region, 1425 °C, all of the grain boundaries were grouped into the the isotropic case (average = 120°). These results suggest that small grains (slow boundaries) are lower in energy than the large grains (fast boundaries) and that the fraction of low energy grain boundaries increases with increasing temperature until all of the grain boundaries are in the slow state at 1425 °C.

GBCDs and GBEDs were measured at the end of the anti thermal region, 1425 °C. The GBPD and corresponding GBED showed that the {001} orientations had the highest area fraction and lowest energy. Again the increase in area fraction of {001} orientations as well as corresponding low values in GBED indicate that the complexion transition increases the relative area of the lowest energy grain boundary types. Also at 1425 °C the (111) orientation of the sigma 3 was high in area fraction and low in energy. At the sigma 9 the $(\bar{2}21)$ was high in area fraction and low in energy.

Results from Eu doped spinel, yttria doped alumina and $SrTiO_3$ indicate that complexion transitions can be detected by a reduction in grain boundary energy either from directly measuring grain boundary energies from thermal grooves, internal dihedral angles, or GBEDs from 3D volumes or from inferring the reduction in energy from the inverse correlation to population in the GBPD. In addition, the anomalous anti-thermal behavior observed in $SrTiO_3$ can be explained by changes in grain boundary energy and character all associated with a complexion transition.

# 10 References


[1] S.J. Dillon, M.P. Harmer, and G.S. Rohrer, "The relative energies of normally and abnormally growing grain boundaries in alumina displaying different complexions," *J. Am. Ceram. Soc.*, **93** [6] 1796–1802 (2010).

[2] M. Tang, W.C. Carter, and R.M. Cannon, "Grain boundary transitions in binary alloys," *Phys. Rev. Lett.*, **97** [7] (2006).

[3] S.J. Dillon and M.P. Harmer, "Multiple grain boundary transitions in ceramics: A case study of alumina," *Acta Mater.*, **55** [15] 5247–5254 (2007).

[4] S.A. Bojarski, M. Stuer, Z. Zhao, P. Bowen, and G.S. Rohrer, "Influence of y and la additions on grain growth and the grain-boundary character distribution of alumina," *J. Am. Ceram. Soc.*, **97** [2] 622–630 (2014).

[5] *Space group 227*, *Int. Tables Crystallogr.*, ch 7.1 (2006).

[6] M. Rubat du Merac, H.J. Kleebe, M.. Muller, and I.E. Reimanis, "Fifty years of research and development coming to fruition; unraveling the complex interactions during processing of transparent magnesium aluminate (MgAl2O4) spinel," *J. Am. Ceram. Soc.*, **96** 3341–3365 (2013).

[7] A. Krell, E. Strassburger, T. Hutzler, and K. J., "Single and polycrystalline transparent ceramic armor with different crystal structure," *J. Am. Ceram. Soc.*, **96** 2718–2721 (2013).

[8] J.-M. Kim, H.-N. Kim, Y.-J. Park, J.-W. Ko, J.-W. Lee, and H.-D. Kim, "Microstructure and optical properties of transparent MgAl2O4 prepared by Ca-infiltrated slip-casting and sinter-HIP process," *J. Eur. Ceram. Soc.*, **36** [8] 2027–2034 (2016).

[9] W. Cao, A. Kundu, Z. Yu, M.P. Harmer, and R.. Vinci, "Direct correlations between fracture toughness and grain boundary segregation behavior in ytterbium-doped magnesium aluminate spinel," *Scr. Mater.*, **69** 81–84 (2013).

[10] S. Onthida, "Thermodynamics and kinetics of complexion transitions in europium-doped MgAl2O4;" Lehigh University, 2016.

[11] *Space Group 167*, *Int. Tables Crystallogr.*, 548–551 (2006).

[12] E.R. Dobrovinskaya, L.A. Lytvynov, and V. Pishchik, "Properties of Saphire;" pp. 55–176 in *Sapphire Mater. Manuf. Appl.* Springer Science, 2009.

[13] R. Chi, A. Serjouei, I. Sridhar, and G.E.B. Tan, "Ballistic impact on bi-layer alumina/aluminum armor: A semi-analytical approach," *Int. J. Impact Eng.*, **52** 37–43 (2013).

[14] J.L. Tipper, P.J. Firkins, A.A. Besong, P.S.M. Barbour, J. Nevelos, M.H. Stone, E. Ingham, and J. Fisher, "Characterisation of wear debris from UHMWPE on zirconia ceramic, metal-on-metal and alumina ceramic-on-ceramic hip prostheses generated in a physiological anatomical hip joint simulator," *Wear*, **250–251** [PART 1] 120–128 (2001).

[15] M. V Parish, M.R. Pascucci, and W.H. Rhodes, "Aerodynamic IR domes of polycrystalline alumina," *Proc. SPIE 5786, Wind. Dome Technol. Mater. IX*, 195–205 (2005).

[16] D.C. Harris, "Optical Properties / Performance of Infrared Windows;" pp. 1–82 in *Mater. Infrared Wind. Domes Prop. Perform.*, PM70. SPIE Press, 1999.

[17] J. Fang, A.M. Thompson, M.P. Harmer, and H.M. Chan, "Effect of Yttrium and Lanthanum on the Final-Stage Sintering Behavior of Ultrahigh-Purity Alumina," *J. Am. Ceram. Soc.*, **12** [1997] 2005–2012 (2005).

[18] R. Voytovych, I. MacLaren, M.A. Gülgün, R.M. Cannon, and M. Rühle, "The effect of yttrium on densification and grain growth in α-alumina," *Acta Mater.*, **50** [13] 3453–3463 (2002).

[19] J. Cho, M.P. Harmer, H.M. Chan, J.M. Rickman, and A.M. Thompson, "Effect of Yttrium and Lanthanum on the Tensile Creep Behavior of Aluminum Oxide," *J. Am. Ceram. Soc.*, **80** [4] 1013–1017 (1997).

[20] J.P. Buban, K. Matsunaga, J. Chen, N. Shibata, W.Y. Ching, T. Yamamoto, and Y. Ikuhara, "Grain boundary strengthening in alumina by rare earth impurities.," *Science*, **311** [January] 212–215 (2006).

[21] S. Lartigue-Korinek, C. Carry, and L. Priester, "Multiscale aspects of the influence of yttrium on microstructure sintering and creep of alumina," *J. Eur. Ceram. Soc.*, **22** [9–10] 1525–1541 (2002).

[22] K. Matsunaga, H. Nishimura, H. Muto, T. Yamamoto, and Y. Ikuhara, "Direct measurements of grain boundary sliding in yttrium-doped alumina bicrystals," *Appl. Phys. Lett.*, **82** [8] 1179–1181 (2003).

[23] H. Yoshida, Y. Ikuhara, and T. Sakuma, "High-temperature creep resistance in rare earth-doped fine-grained Al 2 O 3," *J. Mater. Res.*, **13** [9] 2597–2601 (1998).

[24] *Space group 221*, *Int. Tables Crystallogr.*, 672–674 (2006).

[25] M. Bauer, H. Kungl, and M.J. Hoffmann, "Influence of Sr/Ti Stoichiometry on the Densification Behavior of Strontium Titanate," *J. Am. Ceram. Soc.*, **92** [3] 601–606 (2009).

[26] R.A. McKee, F.J. Walker, and M.F. Chisholm, "Crystalline Oxides on Silicon: The First Five Monolayers," *Phys. Rev. Lett.*, **81** [14] 3014–3017 (1998).

[27] F. Sun, H. Khassaf, and S.P. Alpay, "Strain engineering of piezoelectric properties of strontium titanate thin films," *J. Mater. Sci.*, **49** [17] 5978–5985 (2014).

[28] M. Kawasaki, T. Kazuhiro, T. Maeda, R. Tsuchiya, M. Shinohara, O. Ishiyama, T. Yonezawa, M. Yoshimoto, *et al.*, "Atomic control of the SrTiO(3) crystal surface," *Science (80-. ).*, **266** [5190] 1540–1542 (1994).

[29] B. Stauble-Pumpin, B. Ilge, V.C. Matijasevic, P.M.L.. Scholte, A.J. Steinfort, and F. Tuinstra, "Atomic force microscopy study of (001) SrTiO3 surfaces," *Surf. Sci.*, **369** [1–3] 313–320 (1996).

[30] T. Matsumoto, H. Tanaka, T. Kawai, and S. Kawai, "STM-imaging of a SrTiO3 (100) surface with atomic-scale resolution," *Surf. Sci. Lett.*, **278** L153–L158

(1992).

[31] Y. Liang and D.A. Bonnell, "Structures and chemistry of the annealed SrTiO3 (001) surface," *Surf. Sci.*, **310** [1–3] 128–134 (1994).

[32] K. Szot, W. Speier, J. Herion, and C. Freiburg, "Restructuring of the surface region in SrTiO3," *Appl. Phys. A*, **64** [1] 55–59 (1996).

[33] A.M. Schultz, Y. Zhu, S.A. Bojarski, G.S. Rohrer, and P.A. Salvador, "Eutaxial growth of hematite Fe2O3 films on perovskite SrTiO3 polycrystalline substrates," *Thin Solid Films*, **548** 220–224 (2013).

[34] Y.-M. Chiang and T. Takagi, "Grain-boundary chemistry of barium titanate and strontium titanate: I, High-temperature equilibrium space charge," *J. Am. Ceram. Soc.*, **73** [11] 3278–3285 (1990).

[35] S.B. Desu and D.A. Payne, "Interfacial segregation in perovskites: I-IV," *J. Am. Ceram. Soc.*, **73** [11] 3391–3421 (1990).

[36] S. Chung, B. Lee, and S.L. Kang, "Core-shell structure formation in Nb2O3-doped SrTiO3 by oxygen partial pressure change," *J. Am. Ceram. Soc.*, **81** [11] 3016–3018 (1998).

[37] M. Fujimoto and W.D. Kingery, "Microstructures of SrTiO3 internal boundary layer capacitors during and after processing and resultant electrical properties," *J. Am. Ceram. Soc.*, **68** [4] 169–173 (1985).

[38] M. Baurer, S.-J. Shih, C. Bishop, M.P. Harmer, D. Cockayne, and M.J. Hoffmann, "Abnormal grain growth in undoped strontium and barium titanate," *Acta Mater.*, **58** [1] 290–300 (2010).

[39] M. Bauer, H. Stormer, D. Gerthsen, and M.J. Hoffmann, "Linking Grain Boundaries and Grain Growth in Ceramics," *Adv. Eng. Mater.*, **12** [12] 1230–1234 (2010).

[40] W. Rheinheimer, M. Bäurer, H. Chien, G.S. Rohrer, C.A. Handwerker, J.E. Blendell, and M.J. Hoffmann, "The equilibrium crystal shape of strontium titanate

and its relationship to the grain boundary plane distribution," *Acta Mater.*, **82** 32–40 (2015).

[41] W. Rheinheimer and M.J. Hoffmann, "Non-Arrhenius behavior of grain growth in strontium titanate: New evidence for a structural transition of grain boundaries," *Scr. Mater.*, **101** 68–71 (2015).

[42] M. Bauer, S.-J. Shih, C. Bishop, M.P. Harmer, D. Cockayne, and M.J. Hoffmann, "Abnormal grain growth in undoped strontium and barium titanate," *Acta Mater.*, **58** 290–300 (2010).

[43] W. Rheinheimer and M.J. Hoffmann, "Grain growth transitions of perovskite ceramics and their relationship to abnormal grain growth and bimodal microstructures," *J. Mater. Sci.*, **51** 1756–1765 (2016).

[44] W. Rheinheimer, M. Baurer, C.A. Handwerker, J.E. Blendell, and M.J. Hoffmann, "Growth of single crystalline seeds into polycrystalline strontium titanate: Anisotropy of the mobility, intrinsic drag effects and kinetic shape of grain boundaries," *Acta Mater.*, **95** 111–123 (2015).

[45] M. Baurer, D. Weygand, P. Gumbsch, and M.J. Hoffmann, "Grain growth anomaly in strontium titanate," *Scr. Mater.*, **61** 584–587 (2009).

[46] J.E. Burke and D. Turnbull, "Recrystallization and grain growth," *Progr. Met. Phys.*, **3** 220–292 (1952).

[47] J.D. Powers and A.M. Glaeser, "Grain boundary migration in ceramics," *Interface Sci.*, **6** 23–39 (1998).

[48] M. Hillert, "On the theory of normal and abnormal grain growth," *Acta Met.*, **13** 227–238 (1965).

[49] J.D. Burke, "Some factors affecting the rate of grain growth in metals," *Trans. Met. Soc. AIME*, **180** 73–91 (1949).

[50] R.C. Sun and C.L. Bauer, "Measurements of grain boundary mobilities through magnification of capillary forces," *Acta Met.*, **18** 635–648 (1970).

[51] R.C. Sun and C.L. Bauer, "Tilt boundary migration in NaCl bicrystals," *Acta Met.*, **18** [639–647] (1970).

[52] R.C. Sun and C.. Bauer, "Kinetics of grain boundary migration in copper bicrystals with [001] rotation axes," *Acta Met.*, **21** 1099–1109 (1973).

[53] D. Turnbull, "Theory of grain boundary migration rates," *Trans. AIME*, **191** [8] 661 (1951).

[54] C. Zener, "Private communication to C.S. Smith," *Trans. Met. Soc. AIME*, **175** [15] (1948).

[55] J. Calvet and C. Renon, "Discontinuous grain growth in Al-Cu alloys," *Mem. Sci. Rev. Metall.*, **57** [3] (1960).

[56] D.A. Porter and K.E. Easterling, "Phase Transformations in Metals and Alloys," *Van Nostrand Reinhold Co. New York*, (1981).

[57] P.A. Manohar, M. Ferry, and T. Chandra, "Five Decades of the Zener Equation," *ISIJ Intl.*, **38** 913 (1998).

[58] A. Gangulee, "Effect of Cu concentration on the temperature at which AGG starts in Al-Cu films," (1972).

[59] S.G. Kim and Y.B. Park, "Grain boundary segregation, solute drag and abnormal grain growth," *Acta Mater.*, **56** 3739–3753 (2008).

[60] C. Roberts, "Grain growth and the Zener pinning phenomenon: A computational and experimental investigation;" 2008.

[61] K. Detert and K. Lucke, "The influence of defined small amounts of impurities on the recrystallization of aluminium," *Brown Univ. Report. AFOSR-TS-56-103*, [AD-S2016] (1956).

[62] E.A. Holm, M.A. Miodownik, and A.D. Rollett, "On abnormal subgrain growth and the origin of recrystallization nuclei," *Acta Mater.*, **51** [9] 2701–2716 (2003).

[63] S.J. Dillon, M.P. Harmer, and G.S. Rohrer, "Influence of interface energies on solute partitioning mechanisms in doped aluminas," *Acta Mater.*, **58** [15] 5097–

5108 (2010).

[64] W.K. Burton, N. Cabrera, and F.C. Frank, "The Growth of Crystals and the Equilibrium Structure of Their Surfaces," *Philos. Trans. R. Soc. London*, **243** 300–58 (1951).

[65] H. Gleiter, "Mechanism of grain boundary migration," *Acta Metall.*, **17** [5] 565–573 (1969).

[66] H. Gleiter, "Theory of grain boundary migration rate," *Acta Metall.*, **17** [7] 853–862 (1969).

[67] H. Sternlicht, W. Rheinheimer, M.J. Hoffmann, and W.D. Kaplan, "The mechanism of grain boundary motion in SrTiO3," *J. Mater. Sci.*, (2015).

[68] D.M. Saylor and G.S. Rohrer, "Determining crystal habits from observations of planar sections," *J. Am. Ceram. Soc.*, **85** [11] 2799–2804 (2002).

[69] D.M. Saylor, B.S. El Dasher, A.D. Rollett, and G.S. Rohrer, "Distribution of grain boundaries in aluminum as a function of five macroscopic parameters," *Acta Mater.*, **52** 3649–365 (2004).

[70] G.S. Rohrer, D. Saylor, B. El Dasher, B. Adams, A. Rollett, and P. Wynblatt, "The distribution of internal interfaces in polycrystals," *Z. Met.*, **95** 197–214 (2005).

[71] S.J. Dillon and M.P. Harmer, "Relating grain boundary complexion to grain-boundary kinetics I: Calcia-doped alumina," *J. Am. Ceram. Soc.*, **91** [7] 2304–2313 (2008).

[72] S.J. Dillon and M.P. Harmer, "Relating grain boundary complexion to grain boundary kinetics II: Silica-doped alumina," *J. Am. Ceram. Soc.*, **91** [7] 2314–2320 (2008).

[73] O. Schumacher, C.J. Marvel, M.N. Kelly, P.R. Cantwell, R.P. Vinci, J.M. Rickman, G.S. Rohrer, and M.P. Harmer, "Complexion Time-Temperature Transformation (TTT) Diagrams: Opportunities and Challenges," *Curr. Opin. Solid State Mater. Sci.*, 1–8 (2016).

[74] P.R. Cantwell, M. Tang, S.J. Dillon, J. Luo, G.S. Rohrer, and M.P. Harmer, "Grain boundary complexions," *Acta Mater.*, **62** 1–48 (2014).

[75] S.J. Dillon and G.S. Rohrer, "Characterization of the Grain-Boundary Character and Energy Distributions of Yttria Using Automated Serial Sectioning and EBSD in the FIB," *J. Am. Ceram. Soc.*, **92** 1580–1685 (2009).

[76] S.J. Dillon, M. Tang, W.C. Carter, and M.P. Harmer, "Complexion: A new concept for kinetic engineering in materials science," *Acta Mater.*, **55** [18] 6208–6218 (2007).

[77] S.J. Dillon, H. Miller, M.P. Harmer, and G.S. Rohrer, "Grain boundary plane distributions in aluminas evolving by normal and abnormal grain growth and displaying different complexions," *Int. J. Mater. Res.*, **101** [1] 50–56 (2010).

[78] S. Galmarini, U. Aschauer, P. Bowen, and S.C. Parker, "Atomistic Simulation of Y-Doped alpha-Alumina Interfaces," *J. Am. Ceram. Soc.*, **91** [11] 3643–3651 (2008).

[79] D. Bouchet, F. Dupau, and S. Lartigue-Korinek, "Structure and Chemistry of Grain Boundaries in Yttria Doped Aluminas," *Microsc. Microanal. Microstruct.*, **4** 561–573 (1993).

[80] S.A. Bojarski, M.P. Harmer, and G.S. Rohrer, "Influence of grain boundary energy on the nucleation of complexion transitions," *Scr. Mater.*, **88** 1–4 (2014).

[81] D.M. Saylor, "The Character Dependence of Interfacial Energies in Magnesia;" Carnegie Mellon University, 2001.

[82] D. Saylor, D. Mason, and G. Rohrer, "Experimental method for determining surface energy anisotropy and its application to magnesia," *J. Am. Ceram. Soc.*, **83** 1226–32 (2000).

[83] M. Kitayama and A.M. Glaeser, "The Wulff Shape of Alumina: III, Undoped Alumina," *J. Am. Ceram. Soc.*, **85** [3] 611–22 (2002).

[84] J.C. Heyraud and J.J. Metois, "Equilibrium shape and temperature - lead on

graphite," *Surf. Sci.*, **128** 334–342 (1983).

[85] T. Sano, D.M. Saylor, and G.S. Rohrer, "Surface Energy Anisotropy of SrTiO3at 1400°C in Air," *J. Am. Ceram. Soc.*, **86** [11] 1933–39 (2003).

[86] S.H. Overbury, P.A. Bertrand, and G.A. Somorjai, "The Surface Composition of Binary Systems. Prediction of Surface Phase Diagrams of Solid Solutions," *Chem. Rev.*, **75** [5] 547–560 (1975).

[87] S.M. Foiles, "Evaluation of harmonic methods for calculating the free energy of defects in solids," *Phys. Rev. B*, **49** [21] 14930–14938 (1994).

[88] I. Manassidis, A. De Vita, and M.J. Gillan, "Structure of the (0001) surface of alpha-Al2O3 from first principles calculations," *Surf. Sci. Lett.*, **285** L517–L521 (1993).

[89] P.W. Tasker, "No Title," *Adv. Ceram.*, **10** 176 (1988).

[90] W.C. Mackrodt, "No Title," *J. Chem. Soc. Faraday Trans.*, **II** [85] 54 (1989).

[91] J.-H. Choi, D.-Y. Kim, B.J. Hockey, S.M. Wiederhorn, C.A. Handwerker, J.E. Blendell, W.C. Carter, and A.R. Roosen, "Equilibrium Shape of Internal Cavities in Sapphire," *J. Am. Ceram. Soc.*, **80** [1] 62–68 (1997).

[92] S. Blonski and S.H. Garofalini, "Molecular dynamics simulations of alpha-alumina and gamma-alumina surfaces," *Surf. Sci.*, 263–274 (1993).

[93] T. Sano, "Interface Anisotropy and its Effect on Microstructural Evolution During Coarsening;" Carnegie Mellon University, 2005.

[94] W.C. Mackrodt, "Atomistic Simulations of Oxide Surfaces," *Phys. Chem. Min.*, **15** [3] 228–237 (1988).

[95] J. Padilla and D. Vanderbilt, "Ab Inito Study of SrTiO3 Surfaces," *Surf. Sci.*, **418** [1] 64–70 (1998).

[96] B. Meyer, J. Padilla, and D. Vanderbilt, "Theory of PbTiO3, BaTiO3, and SrTiO3 Surfaces," *Faraday Discuss., Surf. Sci. Met. Oxides*, **114** 395–405 (1999).

[97] A. Pojani, F. Finocchi, and C. Noguera, “Polarity on the SrTiO3 (111) and (110) Surfaces,” *Surf. Sci.*, **442** [2] 179–198 (1999).

[98] C. Cheng, K. Kunc, and M.H. Lee, “Structural Relaxation and Longitudinal Dipole Moment of SrTiO3 (001) (1x1) Surfaces,” *Phys. Rev. B.*, **62** [15] 10409–10418 (2000).

[99] E. Heifets, A. Kotomin, and J. Maier, “Semi-empirical Simulations of Surface Relaxation for Perovskite Titanates,” *Surf. Sci.*, **462** [1–3] 19–35 (2000).

[100] E. Heifets, R.I. Eglitis, E.A. Kotomin, J. Maier, and G. Borstel, “Ab Initio Modeling of Surface Structure for SrTiO3 Perovskite Crystals,” *Phys. Rev. B.*, **64** [23] 235417–235422 (2001).

[101] X. Zhang and A. Demkov, “Steps on the (001) SrTiO3 Surface,” *J. Vac. Sci. Technol. B*, **20** [4] 1664–1670 (2002).

[102] W. Rheinheimer, “Zur Grenzfla¨chenanisotropie von SrTiO3;” Karlsruhe Institut fu¨r Technologie (KIT), 2013.

[103] R. Tran, Z. Xu, B. Radhakrishnan, D. Winston, W. Sun, K.A. Persson, and S.P. Ong, “Surface energies of elemental crystals,” *Sci. Data*, **3:160080** (2016).

[104] J. Li, S.J. Dillon, and G.S. Rohrer, “Relative grain boundary area and energy distributions in nickel,” *Acta Mater.*, **57** [14] 4304–4311 (2009).

[105] G.S. Rohrer, “Grain boundary energy anisotropy: A review,” *J. Mater. Sci.*, **46** [18] 5881–5895 (2011).

[106] C. Herring, “The Physics of Powder Metallurgy;” p. 143 in *Phys. Powder Metall.* Edited by W.. Kingston. McGraw-Hill, New York, 1951.

[107] D.M. Saylor and G.S. Rohrer, “Measuring the Influence of Grain-Boundary Misorientation on Thermal Groove Geometry in Ceramic Polycrystals,” *J. Am. Ceram. Soc.*, **82** [6] 1529–1536 (1999).

[108] W.R. Tyson and W.. Miller, “Surface free energies of solid metals. Estimation from liquid surface tension measurements,” *Surf. Sci.*, **62** 267–276 (1977).

[109] Hondros, "Energetics of Solid-Liquid Interfaces," *Interfaces, Ed RC Gitkins*, [Butterworths, London] 77 (1969).

[110] T.A. Roth, "No Title," *Mater Sci Eng*, **19** 183 (1975).

[111] E.. Hodkin, M.G. Nicholas, and D.M. Poole, "No Title," *J. Less-Common Met.*, **20** 93 (1973).

[112] B.C. Allen, "No Title," *Trans. Met Soc AIME*, **245** 1621 (1969).

[113] E.W. Hart and H. Hu, "The nature and behavior of grain boundaries," *New York Plenum*, 155 (1972).

[114] P. Lejcek and S. Hofmann, "Thermodynamics of Grain Boundary Segregation and Applications to Anisotropy, Compensation Effect and Prediction," *Crit. Rev. Solid State Mater. Sci.*, **33** 133–163 (2008).

[115] A.P. Sutton and R.W. Balluffi, "Interfaces in Crystalline Solids, Clarendon," *Oxford*, (1995).

[116] "The Scientific Papers of J. Willard Gibbs. Bol. I: Thermodynamics," *Longmans, Green Co*, (1906).

[117] P. Wynblatt and D. Chatain, *Anisotropy of segregation at grain boundaries and surfaces*, *Metall. Mater. Trans. A Phys. Metall. Mater. Sci.*, **37** [9] 2595–2620 (2006).

[118] D. McLean, *Grain boundaries in metals*. Oxford, Clarendon Press, 1957.

[119] P. Lejcek and S. Hofamnn, "Thermodynamics and structural aspects of grain boundary segregation," *Crit. Rev. Sol. State Mater. Sci.*, **20** [1] (1995).

[120] E.D. Hondros, M.P. Seah, S. Hofmann, and P. Lejcek, "Interfacial and surface microchemistry," *Phys. Metall.*, **R. W. Cahn** [4th ed.] 1201 (1996).

[121] P.R. Cantwell, S. Ma, S.A. Bojarski, G.S. Rohrer, and M.P. Harmer, "Expanding time-temperature-transformation (TTT) diagrams to interfaces: A new approach for grain boundary engineering," *Acta Mater.*, **106** 78–86 (2016).

[122] T. Chookajorn, H.A. Murdock, and C.A. Schuh, "Design of Stable Nanocrystalline Alloys," *Science (80-. ).*, **337** 951–954 (2012).

[123] R.H. Fowler and E.A. Guggenheim, "Stastistical thermodynamics," *Cambridge Cambridge Univ. Press*, (1939).

[124] W.L. Bragg and E.J. Williams, "No Title," *Proc. R. Soc. A*, **145** [699] (1934).

[125] M.A. Gibson and C.A. Schuh, "Segregation-induced changes in grain boundary cohesion and embrittlement in binary alloys," *Acta Mater.*, **95** 145–155 (2015).

[126] P. Lejcek, "Effect of solute interaction on interfacial segregation and grain boundary embrittlement in binary alloys," *J. Mater. Sci.*, **48** 2574–2580 (2013).

[127] P. Lejcek, "Effect of ternary solute interaction on interfacial segregation and grain boundary embrittlement," *J. Mater. Sci*, **48** 4965–4972 (2013).

[128] M. Guttmann and D. McLean, "Grain boundary segregation in multicomponent systems, in: W.C. Johnson, J.M. Blakely (Eds.)," *ASM Semin. Interfacial Segreg. ASM, Chicago, USA*, 261–348 (1977).

[129] J.D. Cawley and J.W. Halloran, "Dopant distribution in nominally yttrium-doped sapphire," *J. Am. Ceram. Soc.*, **69** [8] C195–C196 (1986).

[130] C.R. Koripella and F.A. Kröger, "Electrical-conductivity of Al2O3-Fe+Y," *J. Am. Ceram. Soc.*, **69** [12] 888–896 (1986).

[131] A.M. Thompson, K.K. Soni, H.M. Chan, M.P. Harmer, D.B. Williams, J.M. Chabala, and R. Levi-Setti, "Dopant distributions in rare-earth-doped alumina," *J. Am. Ceram. Soc.*, **80** 373–376 (1997).

[132] T. Wirtz, P. Philipp, J.-N. Audinot, D. Dowsett, and S. Eswara, "High-resolution high-sensitivity elemental imaging by secondary ion mass spectrometry: from traditional 2D and 3D imagining to correlative microscopy," *Nanotechnology*, **26** [434001] 1–22 (2015).

[133] E.W. Hart, "Grain Boundary Phase Transformations;" pp. 155–170 in *Nat. Behav. Grain Boundaries*. Edited by H. Hu. TMS-AIME Fall Meeting, Detroit, 1971.

[134] J.W. Cahn, “Transitions and Phase Equilibria among Grain Boundary Structures,” *J. Phys. Colloq.*, **43** [C6] 199–213 (1982).

[135] P.R. Cantwell, S. Ma, S.A. Bojarski, G.S. Rohrer, and M.P. Harmer, “Expanding time-temperature transformation (TTT) diagrams to interfaces: A new approach for grain boundary engineering,” *Acta Mater.*, **106** 78–86 (2016).

[136] G.S. Rohrer, *Personal Correspondence*, (2015).

[137] J. Luo and Y.-M. Chiang, “Existence and Stability of Nanometer-Thick Disordered Films on Oxide Surfaces,” *Acta Mater.*, **48** 4501–4515 (2000).

[138] J. Luo, Y.-M. Chiang, and R.M. Cannon, “Nanometer-Thick Surficial Films in Oxides as a Case of Prewetting,” *Langmuir*, **21** 7358–7365 (2005).

[139] G.A. Somorjai and J.Y. Park, “The Impact of Surface Science on the Commercialization of Chemical Processes,” *Catal. Letters*, **115** [3] 87–98 (2007).

[140] T.L. Hill, “Statistical mechanics,” *New York McGraw-Hill*, (1956).

[141] de B. J.H., “The dynamical character of adsorption,” *London Oxford Univ. Press*, (1953).

[142] M. Baram, S.H. Garofalini, and W.D. Kaplan, “Order in nanometer thick intergranular films at Au-sapphire interfaces,” *Acta Mater.*, **59** [14] 5710–5715 (2011).

[143] U. Diebold, S.-C. Li, and M. Schmid, “Oxide Surface Science,” *Annu. Rev. Phys. Chem.*, **61** 129–48 (2010).

[144] A. Fujishima, X.T. Zhang, and D.A. Tryk, “TiO2 photocatalysis and related surface phenomena,” *Surf. Sci. Rep*, **64** [12] 515–582 (2008).

[145] C.R. Henry, “Surface studies of supported model catalysts,” *Surf. Sci. Rep*, **31** [7–8] 231–233, 235–325 (1998).

[146] J. Luo and Y.-M. Chiang, “Equilibrium-thickness Amorphous Films on {11-20} surfaces of Bi2O3-doped ZnO,” *J. Eur. Ceram. Soc.*, **19** [6–7] 697–701 (1999).

[147] M.P. Harmer, “Interfacial kinetic engineering: how far have we come since Kingery’s inaguaral Sosman address?,” *J. Am. Ceram. Soc.*, **93** 301–317 (2010).

[148] H. Zhang and J.F. Banfield, “Phase transformation of nanocrystalline anatase-to-rutiel via combined interface and surface nucleation,” *J. Mater. Res.*, **15** [2] 437–448 (1999).

[149] “Open Source, Gwyddion. Free SPM (AFM, SNOM/NSOM, STM, MFM, ...) data analysis software,” *Available: Gwyddion.net*, (2014).

[150] W.W. Mullins, “Theory of Thermal Grooving,” *J. Appl. Phys.*, **28** [3] 333–339 (1957).

[151] W.M. Robertson, “Grain-boundary grooving by surface diffusion for finite surface slopes,” *J. App. Phys*, **42** [1] 463–467 (1971).

[152] M.A. Groeber and M.A. Jackson, “DREAM.3D: A Digital Representation Environment for the Analysis of Microstructure in 3D,” *Integr. Mater. Manuf. Innov.*, **3** [5] 1–17 (2014).

[153] K. Glowinski, *GBToolbox*, (n.d.).

[154] G.S. Rohrer, “Index of /~gr20/stereology/3Dprograms,” (2017).

[155] E.S. Davenport and E.. Bain, “Transformation of austenite at constant subcritical temperatures,” *Trans. AIME*, **90** 117–144 (1930).

[156] C.P. Khattak and F. Schmid, “Growth of the world’s largest sapphire crystals,” *J. Cryst. Growth*, **225** [2–4] 572–579 (2001).

[157] M.S. Akselrod and F.J. Bruni, “Modern trends in crystal growth and new applications of sapphire,” *J. Cryst. Growth*, **360** 134–145 (2012).

[158] B. Raeisinia, C.W. Sinclair, W.J. Poole, and C.N. Tomé, “On the impact of grain size distribution on the plastic behaviour of polycrystalline metals,” *Model. Simul. Mater. Sci. Eng.*, **16** [2] 25001 (2008).

[159] M.A. Meyers, A. Mishra, and D.J. Benson, “Mechanical properties of nanocrystalline materials,” *Prog. Mater. Sci.*, **51** [4] 427–556 (2006).

[160] D.M. Saylor, B.S. El-Dasher, B.L. Adams, and G.S. Rohrer, "Measuring the five-parameter grain-boundary distribution from observations of planar sections," *Metall. Mater. Trans. A*, **35** [7] 1981–1989 (2004).

[161] S.A. Bojarski, S. Ma, W. Lenthe, M.P. Harmer, and G.S. Rohrer, "Changes in the grain boundary character and energy distributions resulting from a complexion transition in Ca-Doped yttria," *Metall. Mater. Trans. A*, **43** [10] 3532–3538 (2012).

[162] S.J. Dillon and M.P. Harmer, "Demystifying the role of sintering additives with 'complexion,'" *J. Eur. Ceram. Soc.*, **28** [7] 1485–1493 (2008).

[163] M. Avrami, "Kinetics of Phase Change. | General Theory," *J. Chem. Phys.*, **7** 1103 (1939).

[164] J.B. Hannon, H. Hibino, N.C. Bartelt, B.S. Swartzentruber, T. Ogino, and G.L. Kellogg, "Dynamics of the silicon (111) surface phase transition," *Nature*, **405** 552–554 (2000).

[165] G.S. Rohrer, J. Li, S. Lee, A.D. Rollett, M. Groeber, and M.D. Uchic, "Deriving grain boundary character distributions and relative grain boundary energies from three-dimensional EBSD data," *Mater. Sci. Technol.*, **26** [6] 661–669 (2010).

[166] D.M. Saylor, A. Morawiec, and G.S. Rohrer, "The relative free energies of grain boundaries in magnesia as a function of five macroscopic parameters," *Acta Mater.*, **51** 3675–3686 (2003).

[167] D. Gupta, "Diffusion, solute segregations and interfacial energies in some material: An overview," *Interface Sci.*, **11** [1] 7–20 (2003).

[168] S.M. Foiles, "Temperature dependence of grain boundary free energy and elastic constants," *Scr. Mater.*, **62** [5] 231–234 (2010).

[169] R. Najafabadi, D.J. Srolovitz, and R. Lesar, "Thermodynamic and structural properties of [001] twist boundaries in gold," *J. Mater. Res.*, **6** [5] 999–1011 (1991).

[170] A. Atkinson and R.I. Taylor, "The diffusion of 63 Ni along grain boundaries in

nickel oxide," *Philos. Mag. A*, **43** [4] 979–998 (1981).

171 G. Barreau, G. Brunel, G. Cizeron, and P. Lacombe, "Diffusion in copper-silver system: Heterodiffusion and chemical diffusion. Influence of low Cr, Te, Ti and Zr additions to copper," *Mem. Sci. Rev. Met.*, **68** 357–366 (1971).

172 W. Lange, A. Hässner, and G. Mischer, "Messung der korngrenzendiffusion von Nickel-63 in nickel und gamma-eisen," *Phys. Status Solidi*, **5** [1] 63–71 (1964).

173 M.A. Gülgün, R. Voytovych, I. Maclaren, M. Rühle, and R.M. Cannon, "Cation segregation in an oxide ceramic with low solubility: Yttrium doped alpha-alumina," *Interface Sci.*, **10** [1] 99–110 (2002).

174 R.C. Team, *R: A Language and Environment for Statistical Computing*, (2016).

175 S.K. Behera, "Atomic structural features of dopant segregated grain boundary complexions in alumina by EXAFS;" Lehigh University, 2010.

176 J. Cho, H.M. Chan, M.P. Harmer, and J.M. Rickman, "Influence of yttrium doping on grain misorientation in aluminum oxide," *J. Am. Ceram. Soc.*, **81** [11] 3001–3004 (1998).

177 J. Cho, C.M. Wang, H.M. Chan, J.M. Rickman, and M.P. Harmer, "Improved tensile creep properties of yttrium- and lanthanum-doped alumina: a solid solution effect," *J. Mater. Res.*, **16** [2] 425–429 (2001).

178 C.M. Wang, G.S. Cargill, H.M. Chan, and M.P. Harmer, "X-ray absorption near-edge structure of grain-boundary-segregated Y and Zr in creep-resistant alumina," *J. Am. Ceram. Soc.*, **85** [10] 2492–2498 (2002).

179 C.M. Wang, G.S. Cargill, M.P. Harmer, H.M. Chan, and J. Cho, "Atomic structural environment of grain boundary segregated Y and Zr in creep resistant alumina from EXAFS," *Acta Mater.*, **47** [12] 3411–3422 (1999).

180 C.A. Handwerker, J.M. Dynys, R.M. Cannon, and R.L. Coble, "Dihedral angles in magnesia and alumina: distributions from surface thermal grooves," *J. Am. Ceram. Soc.*, **73** [5] 1371–1377 (1990).

[181] S.J. Dillon and G.S. Rohrer, "Mechanism for the development of anisotropic grain boundary character distributions during normal grain growth," *Acta Mater.*, **57** [1] 1–7 (2009).

[182] F. Papillon, G.S. Rohrer, and P. Wynblatt, "Effect of segregating impurities on the grain-boundary character distribution of magnesium oxide," *J. Am. Ceram. Soc.*, **92** [12] 3044–3051 (2009).

[183] H. Qian and J. Luo, "Vanadia-based equilibrium-thickness amorphous films on anatase (101) surfaces," *Appl. Phys. Lett.*, **91** [6] 61909-1-61909–3 (2007).

[184] M.N. Kelly, S.A. Bojarski, and G.S. Rohrer, "The Temperature Dependence of the Relative Grain-Boundary Energy of Yttria-doped Alumina," *J. Am. Ceram. Soc.*, **100** [2] 783–791 (2017).

[185] L. Amaral, M. Fernandes, I.M. Reaney, M.P. Harmer, A.M.R. Senos, and P.M. Vilarinho, "Grian Growth Anomaly and Dielectric Response in Ti-rich Strontium Titanate Ceramics," *J. Phys. Chem.*, **117** 24787–24795 (2013).

[186] W. Rheinheimer and M.J. Hoffmann, "Grain growth in perovskites: What is the impact of boundary transitions?," *Curr. Opin. Solid State Mater. Sci.*, **20** [5] 286–298 (2016).

[187] W. Rheinheimer, M. Bauer, and M.J. Hoffmann, "A reversible wetting transition in strontium titanate and its influence on grain growth and the grain boundary mobility," *Acta Mater.*, **10** 80–89 (2015).

[188] E.M. Levin, C.R. Robbins, and H.F. McMurdie, "Phase diagrams for ceramists 1969 Supplement," *Am. Ceram. Soc.*, **M. K. Rese** Figure 2334 (1969).

[189] S.-J. Shih, S. Lozano-Perez, and D.J.H. Cockayne, "Investigation of grain boundaries for abnormal grain growth in polycrystalline SrTiO3," *Mater. Res. Soc.*, **25** [2] 260–265 (2010).

[190] D.M. Saylor, A. Morawiec, and G.S. Rohrer, "Distribution and Energies of Grain Boundaries in Magnesia as a Function of Five Degrees of Freedom," *J. Am. Ceram. Soc.*, **85** [12] 3081–3083 (2002).

[191] M.A. Groeber, B.K. Haley, M.D. Uchic, D.M. Dimiduk, and S. Ghosh, "3D reconstruction and characterization of polycrystalline microstructures using a FIB-SEM system," *Mater. Charact.*, **57** [4–5] 259–273 (2006).

[192] D.J. Rowenhorst, A.C. Lewis, and G. Spanos, "Three-dimensional analysis of grain topology and interface curvature in a β-titanium alloy," *Acta Mater.*, **58** [16] 5511–5519 (2010).

[193] M.P. Echlin, A. Mottura, C.J. Torbet, and T.M. Pollock, "A new TriBeam system for three-dimensional multimodal materials analysis," *Rev. Sci. Instrum.*, **83** [2] (2012).

[194] C.M. Hefferan, J. Lind, S.F. Li, U. Lienert, A.D. Rollett, and R.M. Suter, "Observation of recovery and recrystallization in high-purity aluminum measured with forward modeling analysis of high-energy diffraction microscopy," *Acta Mater.*, **60** [10] 4311–4318 (2012).

[195] M. Syha, W. Rheinheimer, M. Baurer, E.M. Lauridsen, W. Ludwig, D. Weygand, and P. Gumbsch, "Three-dimensional grain structure of sintered bulk strontium titanate from X-ray diffraction contrast tomography," *Scr. Mater.*, **66** [1] 1–4 (2012).

[196] T. Watanabe, "Grain boundary engineering: Historical perspective and future prospects;" pp. 4095–4115 in *J. Mater. Sci.* 2011.

[197] T. Sun, B. Yao, A.P. Warren, K. Barmak, M.F. Toney, R.E. Peale, and K.R. Coffey, "Surface and grain-boundary scattering in nanometric Cu films," *Phys. Rev. B - Condens. Matter Mater. Phys.*, **81** [15] (2010).

[198] C.S. Kim, A.D. Rollett, and G.S. Rohrer, "Grain boundary planes: New dimensions in the grain boundary character distribution," *Scr. Mater.*, **54** [6] 1005–1009 (2006).

[199] S.J. Dillon, L. Helmick, H.M. Miller, L. Wilson, R. Gemman, R. V. Petrova, K. Barmak, G.S. Rohrer, *et al.*, "The orientation distributions of lines, surfaces, and interfaces around three-phase boundaries in solid oxide fuel cell cathodes," *J. Am.*

*Ceram. Soc.*, **94** [11] 4045–4051 (2011).

[200] H. Beladi and G.S. Rohrer, "The relative grain boundary area and energy distributions in a ferritic steel determined from three-dimensional electron backscatter diffraction maps," *Acta Mater.*, **61** [4] 1404–1412 (2013).

[201] H. Beladi, N.T. Nuhfer, and G.S. Rohrer, "The five-parameter grain boundary character and energy distributions of a fully austenitic high-manganese steel using three dimensional data," *Acta Mater.*, **70** 281–289 (2014).

[202] T.L. Burnett, R. Kelley, B. Winiarski, L. Contreras, M. Daly, A. Gholinia, M.G. Burke, and P.J. Withers, "Large volume serial section tomography by Xe Plasma FIB dual beam microscopy," *Ultramicroscopy*, **161** 119–129 (2016).

[203] M.N. Kelly, K. Glowinski, N.T. Nuhfer, and G.S. Rohrer, "The five parameter grain boundary character distribution of α-Ti determined from three-dimensional orientation data," *Acta Mater.*, **111** 22–30 (2016).

[204] H.M. Miller, "Influences of Processing and Composition on the Grain Boundary Character Distribution;" Carnegie Mellon University, 2008.

[205] D.M. Saylor, B. El Dasher, T. Sano, and G.S. Rohrer, "Distribution of grain boundaries in SrTiO3 as a function of five macroscopic parameters," *J. Am. Ceram. Soc.*, **87** 670–676 (2004).

[206] K. Glowinski and A. Morawiec, "Analysis of Experimental Grain Boundary Distributions Based on Boundary-Space Metrics," *Met. Mater. Trans. Phys. Met. Mater. Sci.*, **45A** 3189–3194 (2014).

[207] D.M. Saylor, A. Morawiec, and G.S. Rohrer, "Distribution of grain boundaries in magnesia as a function of five macroscopic parameters," *Acta Mater.*, **51** 3663–3674 (2003).

[208] K. Glowinski, "Methods for quantitative characterization of three-dimensional grain boundary networks in polycrystalline materials;" Polish Academy of Sciences, 2015.

[209] K.G. van den Boogaart, "Statistics for individual crystallographic orientation measurements;" Aachen, 2002.

[210] A. Morawiec, "Method to Calculate the Grain Boundary Energy Distribution over the Space of Macroscopic Boundary Parameters from the Geometry of Triple Junctions," *Acta Mater.*, **48** [13] 3525–3532 (2000).

[211] C. Herring, "Surface Tension as a Motivation for Sintering," *Phys. Powder Metall.*, **Edited by** 143–79 (1951).

[212] S.J. Dillon and G.S. Rohrer, "Characterization of the Grain Boundary Character and Energy Distributions of Yttria Using Automated Serial Sectioning and EBSD in the FIB," *J. Am. Ceram. Soc.*, **92** [7] 1580–1585 (2009).

[213] D.C. S.J. Shih, K. Dudeck, S.Y. Choi, M. Bäurer , M.J. Hoffmann, "No Title;" p. 94 in *J. Phys. Conferece Ser.* 2008.

[214] D.M. Saylor, B. El Dasher, Y. Pang, H. Miller, P. Wynblatt, A.D. Rollett, and G.S. Rohrer, "Habits of Grains in Dense Polycrystalline Solids," *J. Am. Ceram. Soc.*, **87** [4] 724–726 (2004).

[215] F.C. Hull, "Plane section and spatial characteristics of equiaxed β-brass grains," *Mater. Sci. Technol.*, **4** [9] 778–785 (1988).

**Supplement References Cited for Figure 27**

[1] J. Cho, C.M. Wang, H.M. Chan, J.M. Rickman, M.P. Harmer. "Improved tensile creep properties of yttrium- and lanthanum-doped alumina: a solid solution effect." *J Mater Res*, **16** [2] 425-429 (2001). http://dx.doi.org/10.1557/JMR.2001.0064

[2] C.M. Wang, G.S. Cargill III, H.M. Chan, M.P. Harmer. "X-ray Adsorption Near-Edge Structure of Grain-Boundary-Segregated Y and Zr in Creep-Resistant Alumina." *J Am Ceram Soc*, **85** [10] 2492-2498 (2002). DOI: 10.1111/j.1151-2916.2002.tb00486.x

[3] C.M. Wang, G.S. Cargill III, M.P. Harmer, H.M Chan, J. Cho "Atomic structural environment of grain boundary segregated Y and Zr in creep resistant alumina

from EXAFS." *Acta Mater*, **47** [12] 3411-3422 (1999). doi:10.1016/S1359-6454(99)00210-4

[4] J. Fang, A.M. Thompson, M.P. Harmer, H.M. Chan. "*Effect of Yttrium and Lanthanum on the Final-Stage Sintering Behavior of Ultrahigh-Purity Alumina*." *J Am Ceram Soc*, **80** [8] 2005 2012 (1997). DOI: 10.1111/j.1151-2916.1997.tb03084.x

[5] J. Cho, M.P. Harmer, H.M. Chan, J.M. Rickman, A.M. Thompson. "Effect of Yttrium and Lanthanum on the Tensile Creep Behavior of Aluminum Oxide." *J Am Ceram Soc*, **80** [4] 1013-1017 (1997). DOI: 10.1111/j.1151-2916.1997.tb02936.x

[6] J. Cho, H.M. Chan, M.P. Harmer, J.M. Rickman. "Influence of Yttrium Doping on Grain Misorientation in Aluminum Oxide." *J Am Ceram Soc*, **81** [11] 3001-3004 (1998). DOI: 10.1111/j.1151-2916.1998.tb02726.x

[7] A.M. Thompson, K.K. Soni, H.M. Chan, M.P. Harmer, D.B. Williams, J.M. Chabala, R. Levi-Setti. "Dopant Distributions in Rare-Earth-Doped Alumina." *J Am Ceram Soc*, **80** [2] 373-376 (1997). DOI: 10.1111/j.1151-2916.1997.tb02840.x

[8] S.K Behera. "Atomic structural features of dopant segregated grain boundary complexions in alumina by EXAFS." *PhD dissertation, MSE, Lehigh*. 1-223 (2010). 3389944 http://gradworks.umi.com/33/89/3389944.html

[9] S.A. Bojarski, M. Stuer, Z. Zhao, P. Bowen, G. S. Rohrer. "Influence of Y and La Additions on Grain Growth and the Grain-Boundary Character Distribution of Alumina**."** *J. Am. Ceram. Soc.*, **97** [2] 622-630 (2014). DOI: 10.1111/jace.12669

[10] M. Kelly, S. Bojarski, G.S. Rohrer Thermal groove data (current work).

[11] J.D. Cawley, J.W. Halloran. "Dopant Distribution in Nominally Yttrium-Doped Sapphire." *J. Am. Ceram. Soc*., 69 [8] Pages C-195–C-196 (1986). DOI: 10.1111/j.1151-2916.1986.tb04838.x

[12] C.R. Koripella, F.A. Kröger. "Electrical Conductivity of $A1_2O_3$: Fe + Y." J. Am. Ceram. Soc., **69** [12] 888-96 (1986). DOI: 10.1111/j.1151-2916.1986.tb07389.x

[13] M.A. Gülgün, R. Voytovych, I. Maclaren, M. Rühle. "Cation Segregation in an Oxide Ceramic with Low Solubility: Yttrium Doped α-Alumina." *Interface Science,* **10** [1] 99-110 (2002). DOI: 10.1023/A:1015268232315